

# Strongly Interacting Fermi-Fermi and Fermi-Bose Mixtures: From Polarons to a Bose-Condensed Impurity Cloud

ISABELLA FRITSCHÉ, MSc

Doctoral thesis submitted to the faculty of  
Mathematics, Computer Science and Physics  
at the University of Innsbruck

In partial fulfillment of the requirements for the degree of  
DOCTOR OF PHILOSOPHY

Carried out at the Institute for Quantum Optics and Quantum Information and  
the Institute of Experimental Physics under the supervision of

UNIV.-PROF. DR. RUDOLF GRIMM

with the co-supervisors

UNIV.-PROF. DR. ROLAND WESTER

PROF. DR. JOOK T. M. WALRAVEN

May 2021



# *Abstract*

In this thesis, I discuss measurements to study strongly interacting Fermi-Fermi and Fermi-Bose mixtures with strong population imbalance. We use a mixture of fermionic  ${}^6\text{Li}$  in combination with either fermionic  ${}^{40}\text{K}$  or bosonic  ${}^{41}\text{K}$ , the latter species being the minority component and thus acting as an impurity in a large Fermi sea of noninteracting lithium atoms. First, we conduct measurements on the Fermi-Fermi mixture where we investigate the real-time evolution of the Fermi polaron after an interaction quench. We find that the metastable repulsive polaron and the attractive polaron coexist if the interspecies interaction is strong. In addition, we observe a slight change in the measured signal when we increase the density of the minority species. As a next step, we change from a Fermi-Fermi system to a Fermi-Bose system by exchanging  ${}^{40}\text{K}$  with the bosonic isotope  ${}^{41}\text{K}$ . We find that we can use the condensed K atoms as a tool for thermometry and probe the temperature of our fermions. In studying an interspecies Feshbach resonance, we find that in the case of moderate repulsive interactions and when the bosons are condensed, the two species separate spatially. We characterize the static and dynamic behavior of phase separation, where the physics of an entire system is governed by a thin interface between the two species. Finally, we add a dilute sample of bosons to the Fermi sea and investigate the Fermi polaron with bosonic impurities. As we increase the density of the minority component to the point where the bosons condense, we observe an additional branch in the polaron spectrum indicating coexistence of the Fermi and Bose polaron.

# *Kurzfassung*

In dieser Arbeit werden Messungen besprochen, die zur Untersuchung von stark wechselwirkenden Fermi-Fermi- und Fermi-Bose-Gemischen mit starkem Populationsungleichgewicht durchgeführt wurden. Wir verwenden eine Mischung aus fermionischem  ${}^6\text{Li}$  in Kombination mit entweder fermionischem  ${}^{40}\text{K}$  oder bosonischem  ${}^{41}\text{K}$ . Die letztere Spezies stellt die Minoritätskomponente dar und kann entsprechend als Verunreinigung in einem großen Fermi-See aus nichtwechselwirkenden Lithiumatomen angesehen werden. Zunächst untersuchten wir mit unserer Fermi-Fermi-Mischung die Echtzeitentwicklung des Fermi-Polarons, wobei wir die Koexistenz des metastabilen repulsiven Polarons und des attraktiven Polarons beobachteten. Außerdem beobachteten wir eine leichte Veränderung des Kontrasts des Systems, als wir die Dichte der Minoritätsspezies veränderten. Als nächster Schritt wechselten wir das Isotop von K und begannen, das neue Fermi-Bose-System zu untersuchen. Wir fanden heraus, dass wir die kondensierten K-Atome als Thermometer für eine Untersuchung der Temperatur unserer Fermionen verwenden können. Bei der Erforschung der Interspezies-Feshbach-Resonanz fanden wir heraus, dass sich die beiden Spezies im Falle moderater repulsiver Wechselwirkungen, und wenn die Bosonen kondensiert sind, räumlich trennen. Wir charakterisierten das statische und dynamische Verhalten dieser Phasentrennung, wobei die Physik des gesamten Systems durch eine dünne Grenzfläche zwischen den beiden Spezies bestimmt wird. Schließlich fügten wir eine verdünnte Probe von Bosonen in das Fermi-See ein und untersuchten das Fermi-Polon mit bosonischen Verunreinigungen. Wir fanden eine erstaunliche Übereinstimmung zwischen unseren Messungen mit einer endlichen Dichte der Minoritätskomponente und den theoretischen Voraussagen im Falle einer einzelnen Verunreinigung. Als wir allerdings die Dichte der Minoritätskomponente bis zu dem Punkt erhöhten, an dem die Bosonen kondensierten, beobachteten wir einen zusätzlichen Zweig im Polaronenspektrum, der auf eine Koexistenz des Fermi- und des Bose-Polarons hindeutet.

# Contents

<b>Abstract</b>	<b>iii</b>
<b>Kurzfassung</b>	<b>iv</b>
<b>1 Introduction</b>	<b>1</b>
<b>2 Overview of the work presented in this thesis</b>	<b>5</b>
<b>3 Polarons in ultracold atom experiments</b>	<b>9</b>
3.1 Introduction to the FeLiKx experiment . . . . .	9
3.2 The polaron . . . . .	20
<b>4 Publication: Ultrafast many-body interferometry of impurities coupled to a Fermi sea</b>	<b>31</b>
4.1 Abstract . . . . .	32
4.2 Introduction . . . . .	32
4.3 Main results . . . . .	33
4.4 Conclusion . . . . .	38
4.5 Acknowledgments . . . . .	39
4.6 Supplemental Material . . . . .	39
<b>5 Publication: Thermometry of a deeply degenerate Fermi gas with a Bose-Einstein condensate</b>	<b>63</b>
5.1 Abstract . . . . .	64
5.2 Introduction . . . . .	64
5.3 Bosons as a Fermi gas thermometer . . . . .	65
5.4 Experimental procedures . . . . .	67
5.5 Cooling and thermometry results . . . . .	72
5.6 Conclusion . . . . .	79
5.7 Acknowledgments . . . . .	80
5.8 Appendix: ‘Magic’ levitation trap . . . . .	80
<b>6 Publication: Probing the Interface of a Phase-Separated State in a Repulsive Bose-Fermi Mixture</b>	<b>83</b>
6.1 Abstract . . . . .	84
6.2 Introduction . . . . .	84
6.3 General idea . . . . .	85
6.4 Main results . . . . .	87
6.5 Conclusion and Outlook . . . . .	91
6.6 Acknowledgments . . . . .	91
6.7 Supplemental Material . . . . .	92

---

<b>7</b>	<b>Publication: Breathing mode of a Bose-Einstein condensate repulsively interacting with a fermionic reservoir</b>	<b>113</b>
7.1	Abstract . . . . .	114
7.2	Introduction . . . . .	114
7.3	Experimental procedure and results . . . . .	115
7.4	Acknowledgment . . . . .	121
7.5	Supplemental Material . . . . .	121
<b>8</b>	<b>Publication: Stability and breakdown of Fermi polarons in a strongly interacting Fermi-Bose mixture</b>	<b>127</b>
8.1	Abstract . . . . .	128
8.2	Introduction . . . . .	128
8.3	Bosonic Impurities in a fermionic environment . . . . .	129
8.4	Experimental procedures . . . . .	132
8.5	Experimental results . . . . .	136
8.6	Summary and conclusion . . . . .	146
8.7	Acknowledgment . . . . .	148
8.8	Appendix: Accurate determination of the Feshbach resonance center . . .	148
8.9	Appendix: Quasiparticle properties of Fermi polarons . . . . .	150
<b>9</b>	<b>Outlook</b>	<b>155</b>
	<b>Bibliography</b>	<b>159</b>
	<b>Acknowledgements</b>	<b>177</b>

# 1

## Chapter 1

### Introduction

Strongly interacting quantum many-body systems form the basis of complex problems that describe groundbreaking new physics and exotic states such as spintronic devices [Hir20] or superconductors [Kau21]. They range from problems involving the origin of the universe, the quark-gluon plasma, to observable systems with high temperatures and large spatial extent such as neutron stars, to small structures with low temperatures such as superconductors. Or as Richard D. Mattuck put it in his introductory book about Feynman diagrams [Mat92]:

*“The many-body problem has attracted attention ever since the philosophers of old speculated over the question of how many angels could dance on the head of a pin.”*

Apart from rather controversial debates amongst theologians, this question offers an intuitive picture of what many-body problems are about. If we consider the situation of many angels and a pinhead, we are dealing with a system of many bodies, or alternatively: a many-body system. However, the problem arises when interactions between angels are introduced into the system. This step transfers many single-body problems into a single many-body problem. The complexity becomes apparent when considering that the former reduces to individually solvable problems whereas the latter increases exponentially with the number of angels, rendering the search for analytic or numeric solutions impossible. The challenging task of predicting the multifariousness of physical phenomena that arise from strongly interacting quantum many-body systems demands combined effort of experimentalists and theoreticians. One approach to tackle such cumbersome tasks is to view a simpler problem by applying approximations and truncations to the system. A rather simple scenario is considered first and slowly scaled up until a similar level of complexity is reached as in the desired system. This is the point where ultracold atom experiments show their strength. Considering, for example, the many-body problem of many angels where each one of them attracts all of the others and the whole group accumulates on the head of a pin. One could use a heavy atom to simulate the unmovable pin head and a few light atoms as being the angels. The fact that the atoms are ultracold helps in a sense that they will practically stand still. Then add a short-range attractive interspecies interaction to simulate the attraction of the angels towards the pin and an attractive long-range intraspecies interaction to take care of the interaction amongst the angels. As the experiment is set up one can watch the system evolve in real time<sup>1</sup>. The platform of ultracold atoms enables researchers to simulate a

---

<sup>1</sup>Note that the realization of such a scenario, including the build up of the experiment, will probably take three years and a budget of about two million euros. However, if the simulation are done on an existing experiment with the right tools, such a measurement is a matter of minutes.

vast manifold of problems, from the manipulation of single atoms up to the realization of billions of trapped degenerate atoms of different species, which is possible due to the technological developments within the last 30 years.

The development of ultracold-atom experiments took place at the end of the 20<sup>st</sup> century and peaked around 1997 when Steven Chu, Claude Cohen-Tannoudji, and Bill Phillips were awarded the Nobel prize in physics “*for development of methods to cool and trap atoms with laser light*” [Chu97]. At that moment it was possible to cool a sample of dilute atoms in the gaseous phase down to degeneracy, a point in which the interparticle distance becomes comparable to the spatial extension of the particle itself. This achievement opened the door to the world of quantum physics with ultracold atoms. Theoretical predictions of the novel state of Bose-Einstein condensation (BEC) [Bos24, Ein24] were confirmed with the first experimental verification and awarded by the Nobel prize for Eric A. Cornell [And95], Wolfgang Ketterle [Dav95] and Carl E. Wieman [And95] in 2001 [Cor01]. The challenges of creating a degenerate Fermi gas (DFG) [Hol00, Sch01a, Tru01], due the fermions’ unfavourable thermalization dynamics, were overcome soon after and the famous BEC-BCS crossover [Bar04a, Bou04, Gre05] was observed and investigated. The two achievements of BEC and DFG opened the doors to creating degenerate Bose-Bose, Fermi-Fermi and Bose-Fermi mixtures, which enabled the investigation of new methods, such as ultracold polar molecules [Sag05, Dei08, Vit08, Lan08, Ni08, Dan08], artificial gauge fields [Dal11, Gal19] as well as the observation of novel phenomena such as superfluidity [Zwi05] or supersolidity [Tan19, Böt19, Cho19]. Ultracold-atom experiments offer the ability of trapping a single- (or multiple-) species dilute atom cloud with tunable interactions, temperature, and density and the ability of manipulating them globally or on a single-atom basis. Furthermore the atoms can be imaged with a precision ranging from a single atom to billions of atoms. Due to their vast controllability, diversity and tunability, ultracold atoms offer promising platforms for many research topics such as quantum simulations [Blo13], quantum computation [Sch12b, Par17], atomtronics [Ami21] and precision measurements [Ye06].

In the experiments presented in this thesis, ultracold atoms are utilized to investigate quasiparticles. The description of such quasiparticles goes back to a famous many-body problem originated in the field of condensed matter physics: the motion of an electron in a crystal. Here a single impurity (the electron) is moving in a lattice of atom cores. Interspecies interactions influence the impurity, as well as the environment, which leads to a situation that can neither analytically nor numerically be solved exactly. Considering this problem, L.D. Landau developed his celebrated idea of quasiparticles [Lan33], in which he describes a renormalization of the properties of the minority species caused by its surrounding Fermi sea. In this picture the impurity is described by a dressed impurity that polarizes its environment [Lan48], hence the name *polaron*. This quasiparticle plays a crucial role in many systems, e.g. for charge transport in condensed matter systems [Wöl18], or coherence times in superconducting circuits [Cat19]. However, to study the polaron and its temporal evolution in systems where it occurs, probes would need to be developed that operate on the time scales on which such a quantum process occurs, which in conventional condensed matter systems is in the attosecond range. Another and at the moment possible (but still non-trivial) approach is to change to a system with

more favourable time scales. This can be done using ultracold atoms. The fact that the trapped atoms are diluted and degenerate results in energy scales that are about twelve orders of magnitude lower, compared to a condensed-matter system. This allows physical processes to occur on the microsecond scale, enabling their observation with state-of-the-art detectors. With the aid of Feshbach resonances [Chi10] the interaction between neutral atoms can be tuned to an arbitrary strength, which enabled the experimental observation of the Fermi polaron [Sch09], an impurity attractively interacting with its fermionic environment. The investigation of the metastable repulsive Fermi polaron was possible by utilizing fast excitation methods [Koh12]. Later on different configurations as the Bose polaron [Hu16, Jør16, Yan20a], different mass ratios [Mas12, Sch18], different dimensional systems [Kos12, Taj21, DO19], and the polaron-to-molecule transition [Nes20] were and still are investigated. Theoretical calculations about the Fermi polaron using the variational approach [Che06] and the T-matrix approach [Com07] based on the assumption of a single impurity show remarkable agreement with experimental findings even in the regime of strong interactions and finite concentration. This conundrum provoked the question of the limits of Landau's quasiparticle theory, which can be probed by increasing the temperature or the density of the constituents. This highly non-trivial task is currently being investigated in Fermi-Fermi mixtures [Sca17, Yan19, Muk19] and Bose-Bose mixtures [Pap08, Ada21, Lev17], however, still lacks a description in the case of a Fermi-Bose mixtures.

The measurements, carried out in the laboratory of Rudi Grimm at the Institute for Quantum Optics and Quantum Information (IQOQI), are conducted with a mixture of ultracold lithium and potassium. A sample of fermionic  ${}^6\text{Li}$  is evaporatively cooled to degeneracy, which sympathetically cools a sample of either fermionic  ${}^{40}\text{K}$  or bosonic  ${}^{41}\text{K}$ , using an all-optical approach [Wil09, Spi10]. This experiment presented one of the first mass-imbalanced Fermi-Fermi mixtures in the world and consequently offered to investigate rich physics, and still does to this day. First measurements focused on the search for interspecies Feshbach resonances [Wil08]. Subsequently the stability of a three-fermion mixture at strong interspecies interactions [Spi09] and the observation of the corresponding hydrodynamic expansion of the atomic cloud [Tre11] was investigated. In 2012, the team working on this experiment explored the lifetime of the repulsive polaron [Koh12], a metastable state that had not been observed at that time. The ground state of this system at strong repulsive interactions is represented by a shallow dimer state, which holds one peculiar feature due to the fermionic nature of the atoms and the mass imbalance: The interaction between the dimer and the surrounding  ${}^{40}\text{K}$  atoms is attractive [Jag14], in contrast to expectations from pure s-wave scattering. Furthermore, the lifetime of those shallow molecules and their decay channels were investigated in Ref. [Jag16], in which a suppression of loss processes due to the fermionic nature of the dimers' constituents was found. During this thorough investigations of the bound state, the polaron was investigated further as well by measuring its decoherence in the vicinity of the interspecies Feshbach resonance [Cet15]. Within this last publication a nifty technique was developed. By optically shifting the center of the Feshbach resonance the interaction between the Li and K atoms could be tuned on the timescale of hundreds of nanoseconds. This fast interaction switch enabled us to study the real-time evolution

of the Fermi polaron. These measurements are presented as the first publication in this thesis (see Ch. 4).

# 2

## Chapter 2

# Overview of the work presented in this thesis

In this Chapter, I provide an overview of the work I have done in the FeLiKx experiment over the past six years, which is mainly represented by the publications presented in Chapters 4-8. I joined the team during the measurements of the first publication (see Chapter 4) in the summer of 2015. Previous investigations, in which the Fermi polaron was observed and characterized [Koh12, Cet15] opened many new questions on this intriguing particle and suggested the main research line of my thesis to be on Fermi polarons in our Li-K system with the focus on interacting Fermi-Bose mixtures.

### Chapter 3: Introduction to polarons in ultracold-atom experiments

This Chapter presents a short introduction into the setup of the FeLiKx experiment and the methods with which the atoms are manipulated and probed. Furthermore the Fermi polaron and its properties are introduced on the basis of the polaron spectrum, which reflects the energy of the dressed impurity in dependence of the interspecies interaction. After that, in a brief theoretical summary, common tools for describing Fermi polarons in particular regimes are presented. The Chapter concludes with a general discussion of various ultracold atomic systems in which polarons can occur.

### Chapter 4: Ultrafast dynamics of Fermi polarons

In the work published in [Science 354 6308 \(2016\)](#) we performed a spectroscopic Ramsey sequence to determine the contrast of a Fermi polaron after an ultrafast quench from a non-interacting into a strongly interacting system. One intriguing feature of this measurement is the fact that this quench is more than an order of magnitude faster than the fastest time scale of the system, which is determined by the Fermi time (see Supplemental Material of Ref. [Cet15]). This enabled us to observe the temporal evolution of a quantum many-body system for positive and negative inter-particle scattering lengths in real-time: the birth of the repulsive and the attractive Fermi polaron. In the case of resonant interactions we observed a rapid decay of the contrast followed by an oscillatory behavior, which we interpreted as a beat of the two polarons coexisting in this special situation. By comparing these measurements with two different theoretical approaches<sup>1</sup>, we found that finite-temperature effects play a crucial role in our experiment

---

<sup>1</sup>Recently the truncated-basis approximation (TBA), utilizing the variational Ansatz, was extended for finite temperatures in Ref. [Liu19] and striking agreement with our data was achieved. This illustrates once more the remarkable accuracy of the single particle-hole approximation at strong interactions.

and would diminish the possibility of observing the Anderson orthogonality catastrophe [And67, Kna12] in our system. However, we saw a different intriguing effect, namely eventual polaron-polaron interactions. If investigated further, such interactions can lead to the break down of Fermi-liquid theory and it can lead to insight into systems beyond Landaus famous theory.

## Chapter 5: Introducing bosons to our system

So far we worked with a Fermi-Fermi mixture of  $^6\text{Li}$  and  $^{40}\text{K}$  and already saw hints on polaron-polaron interactions, which we wanted to investigate further. One method to do this is to increase the concentration of the minority species and observe the response of the system. However, since the density of a single spin-state Fermi gas is limited by Fermi pressure, we decided to introduce the bosonic isotope  $^{41}\text{K}$  into our setup. We implemented a cooling and trapping sequence for the bosonic isotope  $^{41}\text{K}$  into our setup and successfully generated our first Bose-Einstein condensate in 2016. After this we found that this BEC can be used as a tool for thermometry and published the results in *Phys. Rev. A* **95**, 053627 (2017). The determination of the temperature in a degenerate Fermi gas can pose a challenge due to the fact that it is usually determined by the wings of a polylog function and is therefore subject to large error bars. With our novel method, we carefully ensure that the small BEC is only partially condensed and fully thermalized with the surrounding Fermi gas. Then we determine the BEC fraction and calculate the temperature of the fermions, via a simple mathematical relation. With the aid of this thermometric method, we could determine our temperature to be as low as  $T/T_F = 0.059$  with a remarkably small error of  $\pm 0.005$ .

Just before we started these measurements, we implemented a novel D1 cooling stage in our Li system [Fri15] in order to further decrease the temperature. This and the different preparation schemes explain the low temperatures, relative to the previous polaron measurements where  $T/T_F \approx 0.1$ . With this new method and the low temperatures, we went in search of suitable FR for the new  $^6\text{Li}$ - $^{41}\text{K}$  mixture.

## Chapter 6: Phase separation in the $^6\text{Li}$ - $^{41}\text{K}$ system

By immersing a thermal bosonic sample into a Fermi sea, scanning the magnetic field, and looking for loss features, we found a suitable FR around  $B_0 \approx 335$  G. The next step was to repeat this loss measurements around 335 G with a condensed sample of K in order to to characterize the environment of the Feshbach resonance for future high-precision measurements. By comparing both loss measurements we found a peculiar behavior. The measurement, in which the bosonic density was greatly increased due to condensation, showed a strong suppression of three-body recombination loss in the presence of strong repulsive interparticle interactions. After careful analysis, we found that this is due to the fact that the fermions are almost completely removed from the spatial region of the BEC. The investigation of phase separation (PS) was published in *Phys. Rev. Lett.* **120** 243403 (2018). The intriguing thing about such a phase-separated state is that the physics of the whole system is governed in a small region, the interface,

where bosons and fermions can still overlap. We found an elegant way to quantify the PS by measuring the dependence of the three-body recombination loss on the interaction strength. A comparison with numerical calculations, in which we minimize the energy functional in order to obtain the densities, shows that the influence of the kinetic-energy term is responsible for the smoothening of this phase transition.

Naturally we also investigated the region of attractive interaction around the FR and observed enhanced loss features in the presence of the BEC. This occurrence is referred to as the mean-field collapse and results from Li particles inside the BEC, attracting K atoms, and leading to the subsequent collapse of the condensate [Osp06a, Zac06]. After observing and characterizing the process of phase separation from a static perspective we were wondering how such a system behaves as collective modes are excited, for example due to an interaction quench. Therefore the next step was to investigate the dynamical behavior of a phase-separated sample.

## Chapter 7: Dynamics of phase separation

In order to test the influence of PS on the dynamics of our system we excited collective modes and measured its oscillation frequency for different interaction strengths. We published the results in *Phys. Rev. A* **99** 041602(R) (2019). Since, in the PS regime, the small interface between  $^6\text{Li}$  and  $^{41}\text{K}$  is the only region where the two species interact, we decided to excite a volume changing mode of K, the breathing mode. As the name suggests, after excitation the interface will inflate and deflate and the influence of PS will become apparent in a change of the oscillation frequency. Indeed we saw a strong increase in the frequency of the breathing mode of the BEC, as we approached the center of the Feshbach resonance, until the value stagnated. We interpret this behavior as an effect of increased Fermi pressure, which leads to an increase of the frequency until, at a certain interaction strength, full phase separation is reached. The two species are separated as they can be and the frequency does not change any further.

With our observations of PS and BEC collapse, we have characterized the  $^6\text{Li}$ - $^{41}\text{K}$  Feshbach resonance. This enables us to start precision measurements, such as the investigation of Fermi polarons with bosonic impurities, in which we can tune the interspecies interaction strength of our new Fermi-Bose system.

## Chapter X: Breakdown of FeLiKx

After the measurements for the publication presented in Chapter 7 were finished the experiment revealed its age and collapsed. The FeLiKx lab repairs took up one-third of my time as a PhD student. Within the next, almost, two years we did not conduct a single measurement. After we repaired/replaced many broken lasers, TA chips, laser diodes, control units, broken bus systems, broken power supplies, broken computers, a broken air conditioning system and burned oven parts, we fixed almost every part of the lab. In 2020, we recovered the experiment and were able to continue our measurements. Note, however, that despite the repairs and improvements, as of now we are working

with atom numbers that are reduced by a factor of two compared to previous polaron measurements. After a careful check of the entire experiment, we believe that a clogging of the oven is the reason for the low atomic numbers. Therefore we are currently working on a new oven design, in order to recover old conditions and hopefully even get better atom numbers.

## **Chapter 8: Stability and breakdown of Fermi polarons**

After repairing the main issues of the experiment we focused again on the investigation of the Fermi polaron with bosonic impurities (PRA **103**, 053314 (2021)). We found that a thermal cloud of bosons, immersed in a large Fermi sea matches the theoretical description of a single impurity, as in the case of fermionic impurities. However, as the bosons formed a partial Bose-Einstein condensate an additional branch evolved in the spectrum for repulsive interspecies interactions. We interpret the situation to be such that the BEC serves as an environment for the few fermions that are located within its spatial extent. This conjecture is strengthened by the good qualitative agreement between the observed energy shift of the BEC and a theoretical description in terms of Bose polarons. Therefore, our partially condensed K sample immersed into the Li Fermi sea provides a platform in which both the Fermi polaron and the Bose polaron can coexist. In addition to that we probed the regime of intermediate concentration  $\mathcal{C} \approx 1$  and found hints towards eventual polaron-polaron interactions in this regime. When conducting Rabi-oscillation measurements we discovered that the resonance frequency of the condensed K sample, in the presence of Li, is dependent on the applied RF power and therefore on the number of possibly transferred atoms. This feature underlines once more the presence of density-dependent effects that lead to the break down of the Fermi polaron picture.

With this we have investigated the Fermi polaron with fermionic and bosonic impurities and observed the transition to a system with Bose polarons. Our near- and far-future projects are discussed in Chapter 9.

# 3

## Chapter 3

# Polarons in ultracold atom experiments

Ultracold atom experiments provide a platform for quantum simulations, which can be used to tackle challenging many-body problems. Landau's celebrated Fermi-liquid theory presents a description of an interacting Fermi gas, which paved the way to the investigation of such problems. One famous problem is to understand the behavior of an electron in a crystal lattice, which can be simulated by an impurity particle immersed in a degenerate quantum gas. The focus of this Chapter lies on impurities and how their strong interaction with their fermionic environment leads to the formation of Fermi polarons. These quasiparticles [Lan33] emerged from Landau's famous Fermi-liquid theory. In Section 3.1, I introduce the experimental setup and two working tools, which are utilized to produce a sample of strongly interacting ultracold atoms, namely Feshbach resonances and radio-frequency pulses. Furthermore I explain a method that is used to probe this many-body system, which is commonly known as radio-frequency spectroscopy. After this the polaron is introduced in Section 3.2. First, the properties on the basis of the spectral response will be discussed, after which two theoretical models, to calculate certain parameters of the polaron, are introduced. Since the explanations will be tightly bound to the experiments presented in Chapters 4-8, I will finally discuss further systems around open questions in the field of polaron physics.

### 3.1 Introduction to the FeLiKx experiment

In this Section, the basic working principle and the setup of the FeLiKx experiment, in which the measurements presented in this thesis were conducted, is discussed. This is followed by a brief overview on Feshbach resonances, atoms, radio-frequency pulses and the interaction between the atoms and these pulses. Finally, all of these topics can be merged and a radio-frequency spectrum of an atomic species in the vicinity of a Feshbach resonance is introduced. Table 3.1 provides an overview of a few important quantities, which will be used later in the text. Note that the basics of Bose and Fermi gases, ultracold scattering processes and Feshbach resonances are explained in several excellent reviews and text books [Ket08, Ket99, Pit16, Gre17b, MW03, Chi10] and shall therefore not be treated in detail in this thesis. The abbreviation FeLiKx stands for **F**ermionic **L**ithium and **K**alium<sup>1</sup>. The last letter **x** serves as a placeholder for the, still up-to-date, future plan to implement a third atomic species. This dual-species, mass-imbalanced experiment was designed using an all-optical approach to cool and trap the two fermionic species <sup>6</sup>Li and <sup>40</sup>K [Wil09, Spi10]. In 2016 an extension to work

---

<sup>1</sup>Kalium is the german name for potassium. The name is derived from the arabic word **قلوي** for alkali.

TABLE 3.1: Table of commonly used quantities in ultracold-atom experiments. The example values in the second column show typical working conditions of the FeLiKx experiment.

symbol	typ. value	parameter	description
$d = n^{-1/3}$	$10^{-6}$ m	interparticle distance	defined through the density $n$ of the sample and reveals the typical distance between particles in a thermal atomic sample.
$\lambda_{\text{dB}} = \sqrt{\frac{h^2}{2\pi m k_{\text{B}} T}}$	$10^{-7}$ m	de Broglie wavelength	indicates the wavelength of the matter wave associated to the atoms, with $h, m, k_{\text{B}}$ and $T$ being the Planck constant, the atomic mass, the Boltzmann constant and the temperature of the sample, respectively. The typical value is calculated for a temperature of 200 nK
$a$	$ a  \lesssim 10^5 a_0$	scattering length	usually given in units of the Bohr radius $a_0$ and represents the scattering amplitude at low temperatures. The scattering length diverges at the pole of a Feshbach resonance.
$E_{\text{F}}$	20 kHz $\times h$	Fermi energy	presents the highest possible energy a fermion can possess at $T = 0$ . Consequently, the fastest time scale in a Fermi system is proportional to the inverse $\tau_{\text{F}} \propto 1/E_{\text{F}}$
$T_{\text{F}}$	1 $\mu\text{K}$	Fermi temperature	temperature derived by dividing $E_{\text{F}}$ by the Boltzmann constant $k_{\text{B}}$ . Commonly used in combination with the temperature $T/T_{\text{F}}$ to signalize degeneracy in the sample. Nowadays values of down to $T/T_{\text{F}} \approx 0.05$ can be reached in ultracold samples.
$k_{\text{F}} = \frac{\sqrt{2mE_{\text{F}}}}{h}$	$1/(4500 a_0)$	Fermi wave vector	wave vector derived from Fermi energy. This inverse of $k_{\text{F}}$ indicates the inter-particle distance in a degenerate Fermi gas.
$R^*$	2000 $a_0$	range parameter	The range parameter is used to express the effective range of a Feshbach resonance and needs to be considered in calculating the scattering length for a certain class of Feshbach resonances.
$k_{\text{F}} R^*$	0.5, 1	characteristic width	The combination of the range parameter and the Fermi wave vector provides a dimensionless parameter that is used to classify Feshbach resonances.
$ \text{K} \alpha\rangle,  \text{Li} \beta\rangle$	$\alpha, \beta = 1, 2, 3$	Zeeman sublevels	the letter indicates the species and the number indicates the corresponding sublevel with ascending energy, e.g. $ \text{Li} 1\rangle$ corresponds to lithium atoms in the energetically lowest hyper-fine state $F = 1/2, m_{\text{F}} = 1/2$
$X = -1/(k_{\text{F}} a)$	$-1 < X < 1$	interaction parameter	dimensionless quantity that indicates the interaction strength between two species with inter-particle scattering length $a$

with the bosonic isotope  $^{41}\text{K}$  was added to the experiment. Now the system can be used as either Fermi-Fermi ( $^6\text{Li}$ - $^{40}\text{K}$ ) or a Fermi-Bose ( $^6\text{Li}$ - $^{41}\text{K}$ ) mixture. In order to reach quantum degeneracy certain length scales of the system play a crucial role. As the temperature decreases and therefore the thermal de Broglie wavelength approaches values that are on the order of the interparticle distance  $\lambda_{\text{dB}} \approx d$  (see Table 3.1) the fundamental nature of the atoms, leading to quantum statistics, starts to play a crucial role. Bosons will start to occupy the lowest momentum state and form a Bose-Einstein condensate (BEC), whereas for fermions, due to the Pauli exclusion principle, only one atom can occupy one quantum state. Thus at very low temperatures  $T \ll T_{\text{F}}$  many accessible momentum states of a Fermi gas are occupied and therefore s-wave scattering processes are strongly suppressed. Since cooling processes rely on the thermalization of the ensemble, which requires the single atoms to scatter off of each other, a single spin state Fermi gas cannot be cooled efficiently to very low temperatures by its own. However, in the FeLiKx experiment the Li atoms are distributed in two of the three energetically lowest Zeeman sublevels, denoted Li|1> ( $F = 1/2$ ,  $m_{\text{F}} = 1/2$ ), Li|2> ( $F = 1/2$ ,  $m_{\text{F}} = -1/2$ ) and Li|3> ( $F = 3/2$ ,  $m_{\text{F}} = -3/2$ ). The K atoms are prepared, via spin relaxation, almost fully polarized in the third to lowest K|3> ( $F = 1$ ,  $m_{\text{F}} = -1$ ) and lowest K|1> ( $F = 9/2$ ,  $m_{\text{F}} = -9/2$ ) Zeeman sublevel in the case of the bosonic and fermionic isotope, respectively. They are then sympathetically cooled with the other species through thermalizing collisions. For more details on the preparation stage of the FeLiKx experiment I refer to [Wil09, Spi10] and the Supplemental Material of [Lou18b]. Typical atom numbers  $N$  and temperatures at the end of a cooling sequence are  $N_{\text{Li}} \approx 4 \times 10^5$ ,  $N_{\text{K}} \approx 3 \times 10^4$  and  $T \approx 100$  nK. Compared to the corresponding Fermi energy this results in  $T/T_{\text{F, Li}} \approx 0.1$  and  $T/T_{\text{F, K}} \approx 0.3$  and, in the Fermi-Bose case, a BEC fraction of  $\beta \approx 0.5$ .

### 3.1.1 Feshbach resonance

A Feshbach resonance (FR) is a very important and commonly used tool in ultracold-atom experiments to magnetically tune the interspecies or intraspecies interaction strength. Its detailed mechanism is explained in the review of Ref. [Chi10] and shall only be briefly explained here. The basic idea of the occurrence of a FR can be captured in a two-channel model. Figure 3.1(a) presents a sketch of a FR between Li and K. The black solid line (lower potential curve) asymptotically connects to two free particles and describes therefore the energetically accessible channel or “open channel” for two particles scattering with collisional energy  $E_c$ . Note that due to the low energy of the constituents in ultracold atom experiments, collisions are reduced to s-wave scattering [MW03] and  $E_c \approx 0$ . The upper potential curve (green solid line) depicts an energetically forbidden channel, or “closed channel”, and exhibits bound states. The one that is in the vicinity of the scattering state is marked as the horizontal line. If the bound state energetically approaches  $E_c$ , the colliding atoms resonantly couple to this bound state and their scattering length diverges. If the magnetic moment of the closed and open channel differ  $\delta\mu \neq 0$  the energy of the scattering state and the molecular state vary with an applied magnetic field  $\Delta E = B\delta\mu$ , as illustrated by the dashed black and green lines in the inset of Fig. 3.1(a). Due to the resonant mixing of the two channels, the crossing of the scattering and the

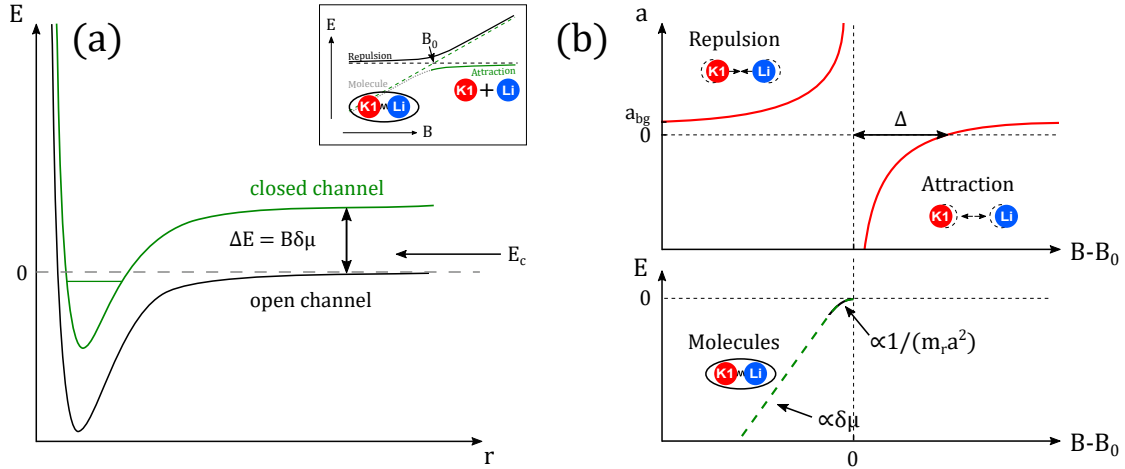


FIGURE 3.1: Two channel model describing the occurrence of a Feshbach resonance. Panel (a) depicts the energies  $E$  as a function of the interparticle distance  $r$ . The green and black solid lines represent the closed and open channel, respectively. The former of the two potential curves exhibits a bound state (green horizontal line), which lies energetically close to the collisional energy  $E_c$  of the two incoming particles. Due to the fact that the dimer state and the scattering state possess a different magnetic moment, the coupling between them can be tuned by changing the magnetic field  $B$ . The inset depicts the molecular and the atomic channel as the dashed green and black lines, respectively. Due to the mixing of the channels an avoided crossing appears. Panel (b) shows the dependence of the scattering length on the magnetic field detuning, measured relative to the pole of the resonance  $B_0$ , where  $a$  diverges. The green dashed line in the lower panel illustrates the molecular branch of the FR. For large magnetic detunings its slope is determined by the difference of the magnetic moment of the two channels  $\delta\mu$ . In contrast, close to the center of the FR the solid black line indicates the increasing influence of the open channel. The quadratic dependence of the energy of these shallow, dressed molecules on the magnetic field marks the universal regime. This figure is based on [Chi10].

molecular state becomes an avoided crossing and two separated branches evolve [Ket08]. The repulsive branch, where two atoms scatter and repel each other (upper solid line) and the energetically lower lying attractive branch (solid green line). The latter shows weak attraction on the very right side of the sketch, where no bound state can exist in three dimensions. As the attraction grows up to the point where the scattering length diverges and the center of the resonance  $B_0$  is reached, molecules, illustrated by the grey dotted line can form and represent the new ground state of the system<sup>2</sup>. In an experiment, such molecules are typically produced by adiabatically ramping the magnetic field from the weakly attractive regime via the avoided crossing to the molecular state [Fer08]. Since the repulsive branch is energetically higher than the molecular state and therefore does not represent the ground state of the system, one can as well create a strongly repulsive mixture and wait until the atoms decay into the lower lying molecular state. However, such a decay is accompanied by a severe gain in kinetic energy and

<sup>2</sup>Note that in the case of two degenerate Fermi gases, even weak attraction can indeed lead to weakly bound states. This peculiar effect caused by a many-body phenomenon, in which a Fermi surface can be viewed as a two-dimensional entity and in two-dimensional systems bound states do exist for weak attractive interactions. This many-body effect led to the investigation of the description of Cooper pairs and the topic of BEC-BCS crossover [Ket08].

consequently with significant heating and atom loss, since cold atom traps are usually shallow.

A sketch of the dependence of the scattering length  $a$  on the magnetic field  $B$  around the point of resonant coupling  $B_0$  is shown as the red solid line in the upper panel of Fig. 3.1(b). It is commonly described by the equation [Moe95]

$$a = a_{\text{bg}} \left( 1 - \frac{\Delta}{B - B_0} \right), \quad (3.1)$$

with  $\Delta$  representing the distance between the pole of the resonance and the zero-crossing of  $a$ . Positive and negative scattering lengths mark the regions of repulsive and attractive interactions, respectively. The background scattering length  $a_{\text{bg}}$  and the width of the FR  $\Delta$  can be found theoretically, via coupled-channel calculations, or experimentally, via radio-frequency spectroscopy [Chi10]. Note that these two quantities can also take negative values. As the energy of the bound state lies below the energy of the scattering state in the open channel,  $B - B_0 < 0$  in Fig. 3.1, a molecule can be formed. The resulting binding energies are sketched in the lower panel of Fig. 3.1(b). In the case of large negative detuning, the binding energy is proportional to the differential magnetic moment  $\delta\mu$  and calculations via a two-channel model, where both the open and the close channel are considered, are necessary to describe the situation. However, the region of resonant coupling is of particular interest. In this regime the open channel contribution dominates the interaction process and leads to the occurrence of a *universal regime*. The characteristic feature of such a regime is that a detailed knowledge of the scattering potential is not required, since the scattering length is much bigger than the interatomic potential. The green/black solid line in the lower panel of Fig. 3.1(b) depicts this universal regime, where the binding energy  $E_b = \hbar^2/(2m_r a^2)$  is solely dependent on the inter-particle scattering length  $a$  and the reduced mass  $m_r$ . The width of this regime varies between resonances and determines the physics that can be experimentally observed. For this reason, Feshbach resonances are divided into the two classes of open-channel and closed-channel dominated resonances, respectively. The former, in contrast to the latter, possesses an extension of the universal regime over a large range of the width of the resonance  $\Delta$  and is therefore experimentally better (or at all) accessible. Note that in the field of ultracold atoms the two different classes of FR are often sloppily referred to as *broad* and *narrow* resonances, which can be misleading, since the width of a FR,  $\Delta$ , is not the only parameter that is important for this classification.

In order to distinguish between an open-channel and a closed-channel dominated FR it is useful to introduce a characteristic length scale, which depends on the parameters that define the width of the universal regime of the particular FR and compare it to a typical length scale of the system. Many different notations can be found in literature, such as  $\eta$  [Köh06] and  $s_{\text{res}}$  [Chi10] as dimensionless interaction parameters, or  $a_{\text{res}}$  [Bru04] and  $R^*$  [Pet04, Mas12, Tre12] as length scales. For the experiments presented in this thesis the length parameter

$$R^* = \frac{\hbar^2}{2m_r \delta\mu a_{\text{bg}} \Delta}, \quad (3.2)$$

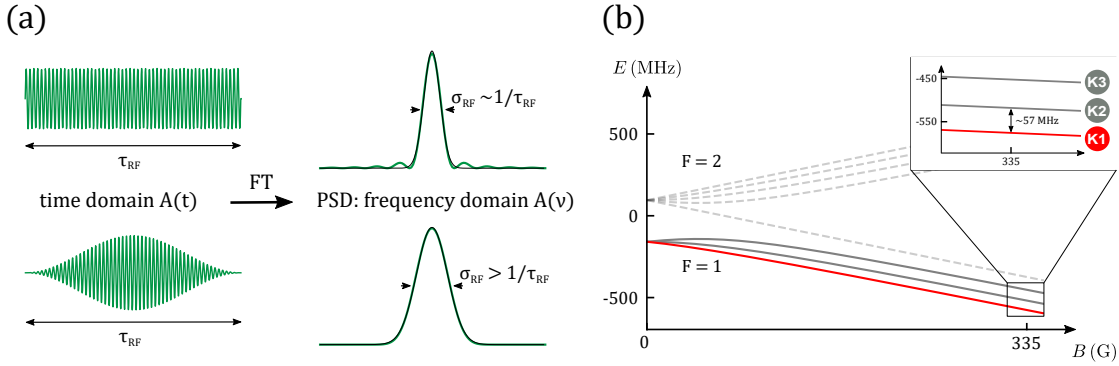


FIGURE 3.2: Light and atom - radio frequency pulse (a) and Zeeman sublevels of an atom (b). The left upper panel in (a) depicts a sinusoidal RF signal with a rectangular envelope of length  $\tau_{\text{RF}}$  oscillating at a frequency  $\nu_{\text{RF}}$ . The power-spectral density (PSD) is obtained by a Fourier transformation, indicated by the horizontal arrow (FT). It represents the RF power at each frequency, and depicts a *sinc*-function with distinct side lobes. In comparison, the lower panel depicts the time dependent signal  $A(t)$  of a Blackman pulse with frequency  $\nu_{\text{RF}}$ . A gaussian fit to the dominant frequency peak for both pulse shapes is shown as the black solid line and serves to compare their widths  $\sigma_{\text{RF}}$ . (b) Zeeman sublevels of the  $^2S_{1/2}$  ground state of a  $^{41}\text{K}$  atom in dependence of the magnetic field. The two levels  $F = 2$  and  $F = 1$  at  $B = 0$  depict the finestructure. Higher B-fields lead to the hyperfine splitting illustrated by the dashed and solid lines, where the latter are used in the FeLiKx experiment. The particular states and their energy differences at a field of  $B \approx 335$  G are emphasized in the Inset. The energy splittings on the order of 60 MHz are conveniently accessible, by commercial electronic devices.

which combines all relevant parameters of the FR that are influencing its universal regime, is compared to the typical length scale in strongly interacting fermionic systems ( $a \rightarrow \pm\infty$ ), namely the interparticle distance. In an ultracold Fermi gas this quantity is given by the inverse of the Fermi wave vector  $k_{\text{F}}$ . Different characters of FRs can lead to different physical phenomena. In early experiments broad resonances, defined to be in the regime where  $k_{\text{F}}R^* \ll 1$ , were common since they occur in homonuclear alkali-atom experiments. These types of FR present ideal conditions to investigate the BCS-BEC crossover [Ket08]. On the other hand narrow resonances, where  $k_{\text{F}}R^* \gg 1$ , are coincidentally more common in hetero-nuclear mixtures and enable a more diverse platform of physical effects, such as view-body bound states [Joh17].

The FR used in the experiments presented in this thesis reach values for the dimensionless interaction strength of  $k_{\text{F}}R^* \lesssim 1$ , which can be viewed as narrow resonances. Reference [Mas12] discusses the influence of the effective range and the mass imbalance of the two scatterers on the effective shape of the FR in the case of a single impurity immersed into a Fermi sea. One intriguing outcome of this calculations is that the transition of the ground state of a system can be significantly changed when considering the effective range of a narrow FR. Examples for such an effect are discussed in Sec. 3.2.

### 3.1.2 Light-atom interactions

Spectroscopy describes the measure of the response of a system to an applied electromagnetic (EM) radiation field that is varied in frequency. The resulting spectrum can be used to analyze the EM source by a known medium and, in the case of a known source, it can reveal information about the composition of the system. This method has a wide range of applications. Two prominent examples for spectroscopic methods are the diffraction of light on a prism and the determination of the composition of stars by EM radiation in the field of astronomy. For this reason, it is divided into many different classes, according to frequency ranges. In ultracold-atom experiments we use, amongst others, radio-frequency (RF) spectroscopy, which covers a frequency range of  $10^6$  Hz- $10^9$  Hz. Due to its fitting frequency range, this very powerful tool allows to probe and manipulate atomic and molecular states on a tremendously level of precision [Mar88, Sch10]. In a nutshell, as the frequency of the (monochromatic) RF probe is varied it will couple to and manipulate the system as the frequency is in resonance with the atom that is probed. The principle of this probing technique relies on the details of the RF pulse, the composition of the single atoms being probed, and, consequently, on the interaction between the atom and the EM field. These three topics shall now briefly be discussed before an example-spectroscopy measurement is introduced.

In order to create an RF pulse, suitable to manipulate ultracold atoms, the signal of an RF generator is, if necessary, amplified and then connected to an antenna. In the case of the FeLiKx experiment the antenna consists of a copper wire soldered to a BNC connector with some capacitors in order to tune its resonance frequency and match its impedance [Tie99]. The simplest form of an RF pulse consists of a sinusoidal signal with frequency  $\nu_{\text{RF}}$  and a rectangular envelope with length  $\tau_{\text{RF}}$ , as depicted in the upper panel of Fig. 3.2(a). The envelope is obtained by simply switching the frequency generator on, applying the pulse  $A(t) = A \sin(2\pi\nu_{\text{RF}}t)$  with amplitude  $A$  for a duration of  $\tau_{\text{RF}}$  and ensure that the latter is much longer than the switching time. However, the simplicity of the pulse has a drawback, which becomes apparent when considering the frequency domain, obtained by the Fourier transform (FT) of the signal. The transformed signal is not monochromatic (singly peaked), but has the shape of a  $\text{sinc}(\nu) = \sin(\nu)/\nu$  function (FT of a square pulse) with distinct side lobes. If such a pulse is applied to an unknown system, multiple states can be excited at the same time and the resulting spectrum can be misinterpreted. Note that a pulsed RF signal can, in contrast to a continuous wave, never be truly monochromatic, since the finite duration will always lead to a finite width in the frequency domain. However, side lobes can be suppressed. A good alternative to the rectangular pulse is the Blackman-shaped pulse [Bla], as illustrated in the lower panel of Fig. 3.2(a), which is widely used in ultracold-atom experiments. It is described by

$$A(t) = \left[ 0.42 - 0.5 \cos\left(2\pi \frac{t}{\tau_{\text{RF}}}\right) + 0.08 \cos\left(4\pi \frac{t}{\tau_{\text{RF}}}\right) \right] \times \sin(2\pi\nu_{\text{RF}}t) \quad (3.3)$$

and has the advantage that the side lobes in the frequency domain are strongly suppressed<sup>3</sup>. Both spectral functions  $A(\nu)$  in Fig. 3.4(a) can now, for the sole reason to discuss the two functions, be approximated by a gaussian and correspondingly associated to a standard deviation  $\sigma_{RF}$ , which is proportional to the inverse of  $\tau_{RF}$ . If compared to the rectangular RF pulse, it becomes apparent that the width of the Blackman shaped pulse is increased. This fact reveals a disadvantage of the latter, since the width in the frequency domain is related to the resolution of the measurement and the transfer probability, as discussed later. In the case where neither the antenna, nor the atom can be changed and the resonance frequency is fixed (resembling a natural situation in a laboratory), the largest possible power of the RF generator determines the shortest possible pulse duration for an atom transfer. In other words, the limit of the fastest atom manipulation is given by the power of the RF signal. As an example, in the FeLiKx experiment, a 100 W RF amplifier is used to drive pulses at  $\nu_{RF} = 57$  MHz in order to excite an atom with a minimum possible duration of  $\tau_{RF} = 56 \mu s$ . If the same power is applied for a Blackman as for a pulse with rectangular envelope, the latter will be faster. Both pulse shapes have their advantages and disadvantages and are therefore used in the according situations. The Blackman pulse is used when complicated and unknown structures, as for example a polaron spectrum, need to be investigated, whereas the rectangular pulse is applied when short pulses are crucial, e.g. in the presence of fast loss processes.

The second ingredient to RF spectroscopy in ultracold-atom experiments, besides the RF pulse, are atoms. Figure 3.2(b) shows the fine- and hyperfine-structure of the  $^2S_{1/2}$  ground state of a  $^{41}K$  atom. As an external B-field is applied,  $B > 0$ , the degeneracy of the finestructure  $F = 2$  and  $F = 1$  is lifted and the Zeeman sublevels appear in the spectrum. Atoms occupying different sublevels possess different angular momenta with respect to the quantization axes. Therefore, when applying an RF pulse with the right polarization (given by the orientation and profile of the antenna), such that angular momentum conservation is fulfilled, an atom can be transferred into a neighbouring spin state, provided that the frequency of the pulse matches the difference of the two states  $h\nu_{RF} = h\nu_{HFS}$ . The measurements presented in this thesis are conducted in the three lowest hyperfine states of potassium,  $|K|1\rangle$ ,  $|K|2\rangle$ , and  $|K|3\rangle$ , emphasized in the inset of Fig. 3.2. This example shows that an RF pulse with a frequency of about  $\sim 57$  MHz must be applied in order to transfer an atom from the state  $|K|2\rangle$  into the state  $|K|1\rangle$ .

The detailed knowledge of the interactions between atoms and light (RF pulse) is crucial in order to identify a suitable method to probe one's system. The situation of a K atom in the state  $|K|2\rangle$  that is transferred into the state  $|K|1\rangle$ , which itself can undergo interactions with the surrounding Li Fermi sea, can be described by a two-level system with damping. The excited state,  $|K|1\rangle$ , can be subject to decay with a rate  $\Gamma$ , which is coupled to a near-resonant radiation field with detuning  $\Delta\nu = \nu_{RF} - \nu_0$  from the resonance frequency  $\nu_0$  of the two states. The coupling strength is expressed via the Rabi frequency  $\Omega_0 = \boldsymbol{\mu}_{12}\mathbf{E}_0$ , with  $\boldsymbol{\mu}_{12}$  and  $\mathbf{E}_0$  being the transition dipole moment of

<sup>3</sup>In an ideal scenario a gaussian envelope would be used, because its Fourier transformation is simply another gaussian. However, rather expensive arbitrary waveform generators would be necessary in order to realize such a modulation. For many applications, such a precision is not necessary since residual side lobes in a Blackman pulse are negligibly small.

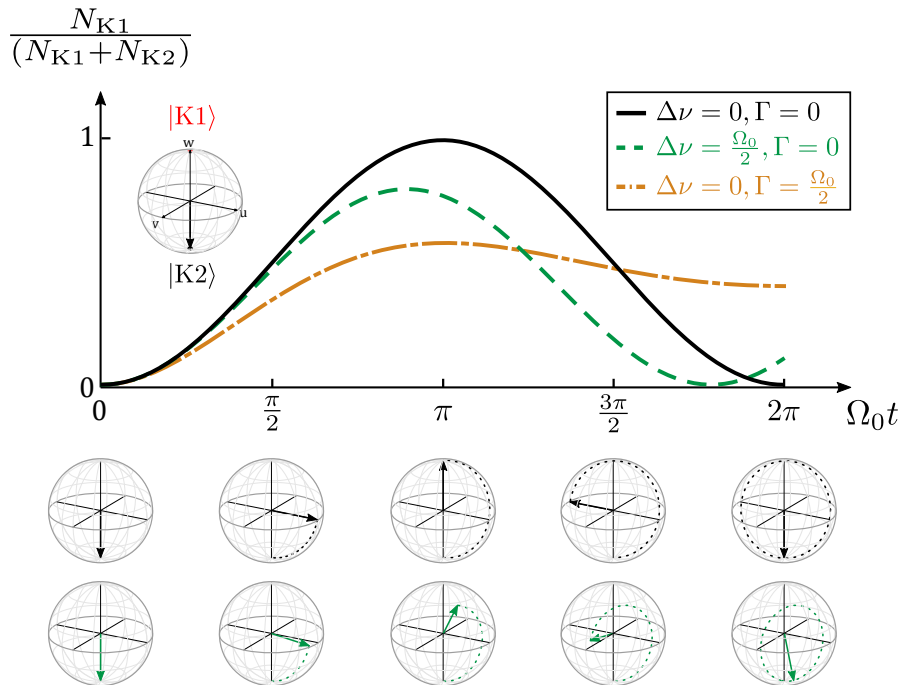


FIGURE 3.3: Rabi oscillations and the Bloch sphere. The black line shows the number of transferred atoms from  $|K|2\rangle$  into  $|K|1\rangle$  as an RF pulse is applied with Rabi frequency  $\Omega_0$  for pulse durations of up to  $\tau_{\text{RF}} = 2\pi/\Omega_0$ , which corresponds to a  $2\pi$ -pulse. The second curve with slightly lower amplitude, green solid line, shows Rabi oscillations for a slightly detuned radio frequency and therefore a generalized Rabi frequency of  $\Omega > \Omega_0$ . The upper panel also shows an example Bloch sphere, where the states are defined as  $|K|2\rangle$  and  $|K|1\rangle$  being on the bottom and top of the sphere, respectively. The lower panel illustrates the movement of the Bloch vector on the sphere for the corresponding Rabi oscillation (upper row:black, lower row: green). The black and green dots in the spheres shall help the reader to track the movement of the Bloch vector.

the two atomic states and the applied RF field, respectively. Following the derivations of [Tan], the Bloch equations can be obtained as:

$$\dot{u} = \Delta\nu v - \frac{\Gamma}{2}u, \quad (3.4)$$

$$\dot{v} = -\Delta\nu u - \Omega_0 w - \frac{\Gamma}{2}v, \quad (3.5)$$

$$\dot{w} = \Omega_0 v - \frac{\Gamma}{2}(1 + 2w). \quad (3.6)$$

They describe the time dependence of the coordinates of the Bloch vector in its corresponding Bloch sphere, as depicted in the left upper side of Fig. 3.3. The Bloch sphere is used to provide an intuitive geometrical representation of the evolution of the population in the two states. The three axes  $u, v, w$  span the coordinate system and the arrow indicates that the  $K$  atoms are in the state  $|K|2\rangle$ , which is the starting condition at  $t = 0$ . The Bloch spheres in the lower part of Fig. 3.3 visualize the rotation of the Bloch vector. The upper row illustrates a textbook Rabi oscillation of a two level system, coherently driven by an external radiation field. After a time  $\Omega_0 t = 0, \pi/2, \pi, 3\pi/2, 2\pi$  the atom has been transferred from  $|K|2\rangle$  into  $(|K|1\rangle + |K|2\rangle)/\sqrt{2}$ ,  $|K|1\rangle$ ,  $(|K|1\rangle - |K|2\rangle)/\sqrt{2}$  and back to  $|K|2\rangle$ , which corresponds to a  $0, \pi/2, \pi, 3\pi/2$  and  $2\pi$  rotation of the sphere

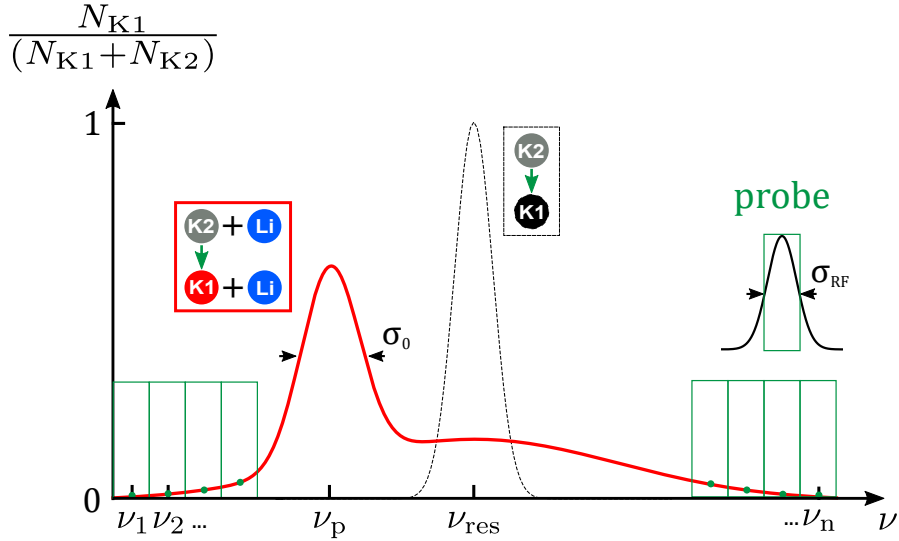


FIGURE 3.4: Radio frequency spectroscopy of the  $K|2\rangle$ - $K|1\rangle$  transition. Illustration of the frequency dependent transfer amplitude  $A(\nu)$  after  $K|2\rangle$  is transferred into  $K|1\rangle$  by a Blackman shaped probe pulse of width  $\sigma_{\text{RF}}$ . The green rectangles show single measurements in which the probe pulse frequency is varied from  $\nu_1$  to  $\nu_n$  and their corresponding averaged transfer amplitudes are indicated as green circles. The red solid and black dashed lines depict the spectral response as  $K$  is transferred from an initially non-interacting into an interacting  $K|1\rangle\text{Li}|1\rangle$  and a non-interacting  $K|1\rangle$  system, respectively. The former shows a doubly peaked signal consisting of two contributions centered around the frequencies  $\nu_p$  and  $\nu_{\text{res}}$ , representing the combination of a sharp quasiparticle-like excitation and a broad background, respectively.

around the  $\nu$ -axis. However, as a finite detuning is introduced an additional rotation of the  $u$ -axis guides the Bloch vector on another path on the sphere's surface, which cannot reach the maximum transfer amplitude. The black solid and green dashed lines show the corresponding evolution of the population in units of  $\Omega_0\tau_{\text{RF}}$  in the case of a resonant  $\Delta\nu = 0$  and an off-resonant  $\Delta\nu = \Omega_0/2$  driving field. It is clearly visible that, with non-zero detuning, the transfer amplitude is decreased and the Rabi frequency increased. The orange dash-dotted curve is added for completion and pictures the situation as a decoherent process of the upper state is introduced  $\Gamma \neq 0$ . In this case the absolute value of the Bloch vector shrinks in time, while the vector rotates around the  $\nu$ -axis until the system is fully decohered. In this case the excitation probability is 0.5. In an experiment it is convenient to define a reference pulse in a well-known scenario. Here, this corresponds to the case of  $\Delta\nu = 0$ ,  $\Gamma = 0$  and  $\Omega_0 = \tau_{\text{RF}}$ , which represents the  $\pi$ -pulse condition. Note that the discussion of the Bloch sphere in this thesis is limited to the specific applications in the FeLiKx experiment. Other cases and detailed discussions can be obtain e.g. from Ref. [Tan].

In order to understand a standard spectroscopic measurement in the FeLiKx experiment, consider a Blackman pulse fulfilling the  $\pi$ -pulse condition being applied to an atomic sample initially prepared as a non-interacting mixture of atoms in the state  $K|2\rangle$ . The magnetic field is adjusted to the vicinity of a FR between  $K|1\rangle$  and  $\text{Li}|1\rangle$ . The aim of this measurement is to transfer  $K|2\rangle$  into  $K|1\rangle$  and find the resonance  $\nu_{\text{res}}$  where maximum transfer occurs by varying the frequency of the RF pulse. Such a scenario is depicted in Fig. 3.4. The black dashed line illustrates the transferred fraction  $N_{K1}/N_{K2}$

in dependence of  $\nu_{\text{RF}}$  for the reference  $\pi$ -pulse. At resonance  $\Delta\nu = \nu_{\text{RF}} - \nu_{\text{res}} = 0$  the atoms are fully transferred into  $\text{K}|1\rangle$ . For finite detuning, as discussed in Fig. 3.3, the transfer amplitude decreases. However, as Li is added to the sample the situation gets more complex. Since the final state is a strongly interacting mixture of  $\text{Li}|1\rangle$  and  $\text{K}|1\rangle$  the spectrum undergoes interaction-induced shifts and new states, e.g. molecular states, can appear. In order to investigate this we use RF spectroscopy. The green rectangles in Figure 3.4 symbolize single measurements and the corresponding green circles show the transferred amplitude obtained for different radio frequencies from  $\nu_1$  to  $\nu_n$ . The duration of the RF pulse is chosen such that its width is smaller than the estimated smallest structure in the final spectrum  $\sigma_{\text{RF}} < \sigma_0$  to make sure that the resolution is sufficient. As all  $n$  measurements are conducted, the green circles represent a discretized version of the full spectrum. An interpolation of these points is illustrated by the red solid line. In order to determine the effect of strong interactions on the  $\text{K}|1\rangle$  energy, the two measurements (red solid and black dashed lines) can now be compared. It is evident that the resonance frequency of a particle like respond shifted towards lower frequencies  $\nu_{\text{p}} < \nu_{\text{res}}$  and a broad background signal, centered around the initial resonance frequency, appeared. For detailed physical interpretations of such spectra see Ch. 4 and Ch. 8. The vast difference between these two measurements emphasizes the power of RF spectroscopy. As the two spectra are compared, models can be applied, physical quantities that describe the underlying processes can be extracted. Therefore novel and exotic systems, even in many-body physics, where theoretical predictions are sparse, can be investigated, described and eventually understood.

However, it is important to consider that in an experiment an RF pulse has a finite duration, hence, the Fourier transformed signal cannot be monochromatic, but rather shows a broad spectral feature as illustrated in Fig. 3.2. When applied to the atoms, the finite width leads to an averaged signal over the span  $\sigma_{\text{RF}}$ , as indicated by the green boxes in Fig. 3.4. Therefore, eventual smaller structures in the spectrum cannot be resolved. One could assume that applying a very long pulse with a corresponding small width would solve this problem. However, at longer time scales atom-loss processes can play an increasingly important role. Therefore, in ultracold-atom experiments, the adjusted pulse duration is a compromise between losses and spectral resolution. Furthermore, interacting systems can possess meta-stable states, which decay into the ground state after some time. Both scenarios, the excited-state and the ground state spectrum can be of interest, which is why spectroscopic methods can be divided into two principal approaches, called injection and ejection spectroscopy. The former, discussed in the text above, presents a possibility to probe fast-decaying metastable states. The atoms are prepared in a known reference state and get *injected* into the state of interest. If the RF pulse is short enough possible excited states can be detected. The other type of spectroscopy implies an initial preparation of the atomic sample in the state that is to be probed, following an *ejection* of the particles, via RF transfer, into the reference state. In this case, any excited states can decay into the corresponding ground states and an equilibrium state can be probed. Note that the topic of RF spectroscopy comprises many different methods which have a tremendous range of applications. So far, the rather simple case of a one-pulse spectroscopy, with  $\pi$ -pulse condition, was discussed. However many other methods, such as Rabi-oscillation measurements [Ket99, Ket08],

Ramsey spectroscopy (see e.g. Ch. 4), or spin-echo spectroscopy (see e.g. [Cet15]) are also popularly used in ultracold-atom experiments.

## 3.2 The polaron

In the 1940s, when Solomon I. Pekar and Lev D. Landau studied the motion of an electron in a crystal, they showed that an electron of the conduction band polarizes the surrounding crystal of atomic cores. They termed this dressed electron as *polaron* [Lan48]. In experiments that use ultracold atoms to simulate such condensed matter systems, the polaron is represented by an impurity atom that dresses itself with the fundamental excitations of the surrounding medium. In this Section, the properties of a polaron, its spectrum, and different types of polarons are discussed. The main focus of attention lies on the specific situation where a small dilute sample of K atoms is immersed in a large Li Fermi sea. In addition, a brief theoretical summary of the two commonly used methods for describing Fermi polarons is presented. Finally, other system configurations and the limitations of Fermi liquid theory are discussed.

### 3.2.1 Properties of a polaron

A polaron is a quasiparticle occurring in many-body systems in the presence of interactions between two (or more) different types of particles, differing in at least one quantum number. One further important ingredient is the strong population imbalance with the limiting case containing one impurity in an infinitely large environment (thermodynamic limit). Such a scenario is not achievable experimentally, but can be approximated by a few impurities to be considered non-interacting, and a relatively large environment. The low-energy excitations of the latter define the classification of the polaron. In the case where the majority species is represented by a BEC or a degenerate Fermi gas, the quasiparticle is called a Bose or Fermi polaron, respectively<sup>4</sup>. In either case, as inter-particle interactions are introduced to such a system, the minority species will still have its intrinsic properties, however, the single atoms will dress themselves with the low-energy excitations of the surrounding medium. Therefore physical quantities such as energy, mobility and mass of the particle are renormalized and the system can be described in terms of quasiparticles moving through the surrounding.

The spectrum of a strongly population-imbalanced system typically exhibits three main branches that correspond to the three states an impurity can occupy, the attractive (I) and repulsive (III) polaron as well as the molecule (II). Figure 3.5 illustrates the spectral response of a <sup>41</sup>K impurity<sup>5</sup> immersed in a <sup>6</sup>Li Fermi sea in the regime of strong inter-particle interactions  $-1 < X < 1$  (see Tab. 3.1). The solid and dashed lines depict

<sup>4</sup>Note that the collective excitations of a crystal lattice are described by phonons, which are bosons. In this case it does not matter whether the particles building the lattice are bosons or fermions. As an impurity is introduced to this scenario it is described by a Bose polaron.

<sup>5</sup>The quantum statistics of the impurity does not play a role in this picture, since the calculations are carried out for a single impurity. The difference w.r.t. the <sup>6</sup>Li-<sup>40</sup>K spectrum is simply given by the narrowness of the FR.

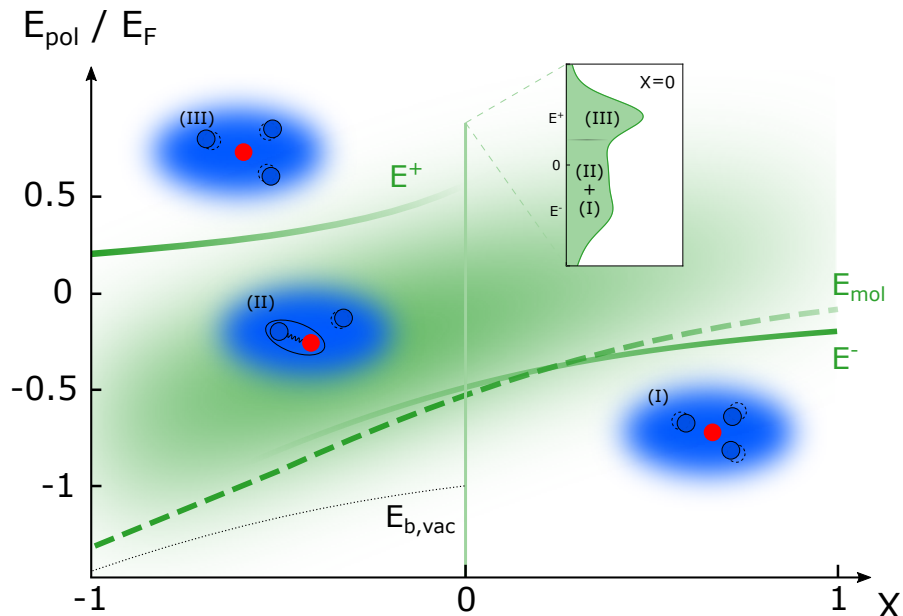


FIGURE 3.5: Illustration of the spectral response of a Fermi polaron following the example of  ${}^6\text{Li}^{41}\text{K}$  in the vicinity of a Feshbach resonance between  $\text{Li}|1\rangle$  and  $\text{K}|2\rangle$  around  $B_0 \approx 335\text{ G}$  (see Ch. 8). An impurity that is strongly interacting with the surrounding Fermi sea can occupy one of three states. The respective energy curves are depicted as two green solid lines and one dashed line. The repulsive and attractive polaron are represented by the energy curves  $E^+$  and  $E^-$ , respectively. The dashed green line depicts the binding energy of the dressed molecules, which presents the ground state of the system for  $X \lesssim 0.2$  and a lower bound for the molecule-hole continuum (shaded region). As an energy reference the binding energy for dimers in vacuum is inserted as the black dotted line. Due to the lack of the Fermi sea, it is shifted with respect to zero by the Fermi energy.

the dependence of the impurity energy on the interaction strength as it occupies one of the three states. The ground state of the system is given by the attractive polaron (I) with energy  $E_-$ , in the regime of attractive inter-particle interaction. Here, the particle of the minority species deforms the Fermi sea by attracting Li atoms. This process lowers the energy of the now dressed impurity with respect to the energy of the bare impurity. At an interaction strength of about  $X \approx 0.2$  the energetically lowest state of the system is represented by a molecular state (II). A Li and a K atom form a dimer by scattering off of a particle-hole excitation. The binding energy  $E_{\text{mol}}$  is increasing with decreasing  $X$ . The point in the spectrum at which the ground state changes from an attractive polaron to a dimer is dependent on the properties of the FR as mentioned in Sec. 3.1.1. In the case of very narrow resonances  $k_F R^* \ll 1$ , this state can persist to be energetically favourable with respect to the molecular state even in the presence of strong repulsive inter-particle interactions [Mas12]. However, in the region  $X < 0$  exists a meta-stable excited state, the repulsive polaron (III), from which the atoms can decay to the energetically lower-lying attractive, or molecular state. Atoms in state (III) repel the surrounding Li atoms and have an effectively higher energy. The shaded region in between the three previously defined states marks the molecule-hole continuum (MHC). It arises from the fact that a repulsive polaron can decay to the molecular state by exciting a particle hole excitation from energies between  $0 - E_F$  out of the Fermi sea.

Therefore the MHC exists in a region of energies between  $E_{\text{mol}}$  and  $E_{\text{mol}} + EF$ . The dotted black line represents the binding energy of a dimer in vacuum  $E_{\text{b,vac}}$ . The energy shift of  $-EF$  takes into account the missing Fermi sea. In this picture the shift of the resonance, due to the narrowness of the resonance and the mass imbalance of the two species, becomes apparent. For details on the resonance shift and the position of the molecule-polaron crossing I refer the reader to Ref. [Mas12].

The green vertical line in Fig. 3.5 at  $X = 0$  marks the interaction strength for which an example RF-injection spectrum is shown. This sketch shows a peak at  $E_{\text{pol}} = E^+$  on top of a broad background signal that is centered in the region of negative energies. At  $E_{\text{pol}} = E^-$  is another slight increase of the RF signal. The spectrum shows a repulsive polaron (III) and the MHC with a hint of the attractive polaron in (I)+(II). Note that the wave function of the molecular state has less overlap with the non-interacting wave function than any of the two polarons. For this reason, the atom transfer is more efficient for the latter and appear as the dominant peaks. This overlap is dependent on the interaction strength and commonly called the quasiparticle residue  $Z$ . The width of the repulsive polaron peak gives an indication of its decoherence rate (see [Sca17] and Ch. 8), which increases as the center of the FR is approached. The repulsive polaron is well-defined if its spectral width is much smaller than the inverse of its lifetime.

I have discussed the spectrum and properties of a Fermi polaron in the case of a mass imbalance of  $\sim 6/41$ . However, the spectrum can change drastically if slightly different systems are considered. If e.g. the impurity mass would be increased possible few-body effects could appear [Efi70, Chi10] and, in the case of  $m \rightarrow \infty$ , exotic states as e.g. the orthogonality catastrophe [And67, Kna12, Sch18] could be observed. A radical different system is described by the Bose polaron [Frö54, Hu16, Jør16], in which bosonic atoms form a Bose-Einstein condensate and represent the majority species. In such a system a fermion or another boson is inserted as an impurity, which dresses itself with the Bogoliubov excitations of the BEC. However, all these systems have one common conundrum: They are described by theories that make perturbative assumptions and, surprisingly, are valid even for very complex many-body domains such as strong interactions, high impurity densities, and increased impurity temperatures/momenta. The borders of these theoretical approaches are not yet exhausted and their breakdown is still under active experimental investigation.

### 3.2.2 Theoretical treatment

Quantum simulators, such as the one used to conduct the experiments presented in this thesis, were developed to simulate complex problems that cannot be solved by current state of the art technologies. This, however, also indicates that a theoretical description of the underlying problem is extremely challenging, if not impossible. For this reason, theoretical studies rely on good approximations, which help to simplify the system and enable physicists to find numerical or even analytical solutions for certain parts of a complex problem. The field of polaron physics started with the complex problem of charge transport of an electron in a crystal lattice. The electron was considered as a single impurity that is immersed in, and interacting with, a big fermionic environment

of atomic cores. Landau and Pekar [Lan33, Lan48] described this complex scenario such that the fermionic impurity dresses itself with basic excitations of a Fermi sea, which are described as particle-hole excitations [Pit16]. From this thought, the systems wave function was derived

$$|\Psi\rangle = (\Phi_0 a_{\mathbf{k}=0\downarrow}^\dagger + \sum_{\mathbf{q},\mathbf{k}} \Phi_{\mathbf{q},\mathbf{k}} a_{\mathbf{q}-\mathbf{k}\downarrow}^\dagger a_{\mathbf{k}\uparrow}^\dagger a_{\mathbf{q}\uparrow} + \dots) |\text{FS}\rangle, \quad (3.7)$$

$$+ \sum_{\mathbf{q},\mathbf{q}',\mathbf{k},\mathbf{k}'} \Phi_{\mathbf{q},\mathbf{q}',\mathbf{k},\mathbf{k}'} a_{\mathbf{q}'+\mathbf{q}-\mathbf{k}-\mathbf{k}'\downarrow}^\dagger a_{\mathbf{k}\uparrow}^\dagger a_{\mathbf{k}'\uparrow}^\dagger a_{\mathbf{q}\uparrow} a_{\mathbf{q}'\uparrow} + \dots) |\text{FS}\rangle, \quad (3.8)$$

where  $a_{\mathbf{p},\sigma}$  and  $a_{\mathbf{p},\sigma}^\dagger$  describe the annihilation and creation operators of a particle in state  $\sigma = \uparrow, \downarrow$  with momentum  $\mathbf{p}$ . Note that the states  $\uparrow, \downarrow$  represent the majority and minority species, respectively. The coefficients  $\Phi_\alpha$  are to be calculated. The first term in Eq.(3.7) shows an impurity with momentum  $\mathbf{k} = 0$  that is immersed in an unperturbed Fermi sea  $|\text{FS}\rangle$ . Note that the annihilation of a particle can also be viewed as the creation of a hole. Therefore, the second term can be interpreted as the creation of a particle and a hole with momentum  $\mathbf{k}$  and  $\mathbf{q}$ , respectively, that are scattering off an impurity with momentum  $\mathbf{q}-\mathbf{k}$ . The following terms in Eq.(3.7) describe processes where multiple particle-hole excitations are considered. Another characteristic quantity of polarons, originating from Landau's celebrated Fermi-liquid theory, is the quasi-particle residue  $Z$ , which describes the overlap between the initial wave function of the impurity and the perturbed wave function of the polaron. This value turns out to be related to the coefficient of (3.7) by  $\sqrt{Z} = \Phi_0$ . The initial state and the perturbed state possess the energies  $E = p^2/(2m)$  and  $E^* = p^2/(2m^*)$  with  $m^*$  being the effective mass arising from the renormalization of the bare particle [Lan48].

There exist two different commonly used approaches to calculate the ground state energy of such an interacting many-body system<sup>6</sup>. One of them is called the variational method, which in the context of polarons was introduced by F. Chevy [Che06] and the other one is called the T-matrix approximation [Com07] (or forward-scattering method, or diagrammatic approach). For the first, one has to guess a trial wave function, plug it into the Schrödinger equation and minimize the resulting Eigenvalues by varying certain parameters. If the wave function is approximated correctly, the resulting values present a good match with the real ground state of the system. Note that an excellent intuition is necessary in order to apply this method, where experimental findings represent an essential contribution to the finding of theoretical predictions. The drawback of this method is that obtaining excited state solutions, as e.g. the repulsive polaron, is intrinsically hard, because the method is developed to find the ground state of the system. However, it turned out that the T-matrix approach provides excellent agreement with the variational method and in contrast to the latter, it allows to predict the excited state and the decay rates of the system. Furthermore, it presents a possibility to include eventual finite impurity concentration and temperature.

<sup>6</sup>Note that in the limit of weak interactions the situation is well described by a mean-field calculation. In such a picture the many-body problem can be reduced to a single-body problem by considering the environment as an averaged global interaction.

The following calculations using the variational Ansatz, or Chevy Ansatz, is leaned on Ref. [Che06]. First, one establishes a trial wave function of the form

$$|\Psi\rangle = \Phi_0 a_{0\downarrow}^\dagger |\text{FS}\rangle + \sum_{q < k_F < k} \Phi_{\mathbf{q},\mathbf{k}} a_{\mathbf{q}-\mathbf{k}\downarrow}^\dagger a_{\mathbf{k}\uparrow}^\dagger a_{\mathbf{q}\uparrow} |\text{FS}\rangle, \quad (3.9)$$

in which only one particle-hole excitation is considered. The summation is executed for all momenta  $q < k_F$  and  $k > k_F$ , which assures that a hole is generated within the Fermi sea and the corresponding particle lies outside. The Hamiltonian of the system  $\hat{H} = \hat{H}_0 + \hat{V}$  consists of the non-perturbed energy of the impurity and the Fermi sea  $\hat{H}_0$  and an additional term that describes their interaction  $\hat{V}$ . In order to find the ground state of the system one can minimize the expectation value of the total energy with respect to the coefficients in Eq. (3.9) as

$$\frac{\delta \langle \Psi | \hat{H} - E | \Psi \rangle}{\delta \Phi_0^*} = 0, \quad (3.10)$$

$$\frac{\delta \langle \Psi | \hat{H} - E | \Psi \rangle}{\delta \Phi_{q,k}^*} = 0, \quad (3.11)$$

with  $E$  being the Lagrange multiplier, which in this case can be interpreted as the energy of the ground state. Eliminating the two coefficients  $\Phi_0$  and  $\Phi_{q,k}$  one can then obtain the final equation

$$E = \sum_{q < k_F} \frac{1}{\sum_{k > k_F} \left( \frac{1}{\epsilon_k + \epsilon_{q-k} - \epsilon_q - E} - \frac{1}{2\epsilon_k} \right) - \sum_{k < k_F} \frac{1}{2\epsilon_k}}, \quad (3.12)$$

in which the energies of the hole, the particle and the impurity are labeled  $\epsilon_q, \epsilon_k$ , and  $\epsilon_{q-k}$ , respectively and the term  $\sum_k 1/(2\epsilon_k)$  stems from the Lippman Schwinger equation. The solution of this self-consistent equation represents the ground state energy of the system. More detailed calculations of the Chevy Ansatz and Eq. (3.12) can be found in Ref. [Che06]. Note that these particular rather straight-forward calculations are valid only in the case of a broad resonance. It is presented here to illustrate the principal idea of the Ansatz. An extension to narrow resonances is given in Ref. [Tre12]. Since the variational Ansatz relies on the precise knowledge of the system in order to guess a right wave function, the calculated ground state energies represent an upper border for the real system. For completeness I want to mention that there exists also the dimeron Ansatz, which is used to calculate the energy of the dimer (see  $E_{\text{mol}}$  in Fig. 3.5) within the variational approach throughout various interaction strengths. The only difference with respect to the Chevy-Ansatz is the truncation of the wave function [Com07, Lan14].

In order to calculate the excited state energy and its lifetime, another approach, the  $\mathcal{T}$ -matrix approximation, is commonly utilized in the field of Fermi polarons. This method relies on the knowledge of the self-energy  $\Sigma(\mathbf{p}, E)$  of an impurity particle with momentum  $\mathbf{p}$  and energy  $E$ , which can be viewed as the change of the impurities energy, or effective mass, due to the effects of interaction with its surrounding. In other words, the self energy  $\Sigma$  describes a single-particle state that is renormalized by the surrounding many-body system, which corresponds here to the impurity, dressed by its fermionic

environment. The self-energy is a complex quantity whose real and imaginary parts, considered individually, contain information about the quasiparticle. Its derivation is described in detail in [Mas14] and Chapter 8 and relies on the knowledge of the Green's function, which itself gives rise to the spectral function of the system. In order to highlight the importance of the self-energy, the resulting dependencies of polaron properties shall be repeated here:

$$E_{\pm} = \text{Re}[\Sigma(0, E_{\pm})], \quad (3.13)$$

$$Z_{\pm} = [1 - \delta_{\omega}\Sigma(0, E) |_{E_{\pm}}]^{-1}, \quad (3.14)$$

$$m_{\pm}^* = \frac{m_{\downarrow}}{Z_{\pm}} \left[ 1 + \frac{\delta \text{Re}[\sigma(\mathbf{p}, E_{\pm})]}{\delta(\epsilon_{p,\downarrow})} \right]^{-1}, \quad (3.15)$$

$$\Gamma_{\text{pp}} = -2Z_+ \text{Im}[\Sigma(0, E_+)]. \quad (3.16)$$

In order to obtain the energies of the zero-momentum repulsive (+) and attractive (-) polaron, respectively, the self-consistent equation (3.13), which results from extracting the pole of the Green's function, must be solved. With the aid of these quantities the corresponding quasi-particle residues may be calculated in Eq. (3.14). Knowing the residue and the energy, the effective mass of the dressed impurity is given by Eq. (3.15). Finally, since the repulsive polaron is a metastable state and will therefore decay, its rate  $\Gamma_{\text{pp}}$  to decay into the attractive polaron is given in Eq. (3.16).

So it all boils down to the cumbersome calculation of self-energy, which is explained in many textbooks such as e.g. [Abr75] and shall not be further elaborated in this thesis. However, with the aid of Feynman diagrams one can truncate the Green's function (see e.g. Ref. [Mat92]) in a way that only single particle-hole excitations are considered. This approach was, in the context of Fermi polarons, introduced in Ref. [Com07] and is equivalent to the variational Ansatz explained above. Since the  $\mathcal{T}$ -matrix approximation relies on the summation of certain Feynman diagrams it is also called the diagrammatic method or, due to the fact that the diagrams are added step wise, the ladder (diagram) approximation.

One intriguing feature of both the variational Ansatz and the  $\mathcal{T}$ -matrix approximation is that despite the seemingly heavy truncation of the wave function and the propagator by only considering a single-particle hole excitation, the description is accurate even in the vicinity of strong inter-particle interactions. It agrees very well with experimental findings (see e.g. Ch.4 and 8). In the context of Fermi polarons, the two methods were compared to quantum Monte Carlo calculations [Lob06] and showed remarkable agreement.

### 3.2.3 Beyond Fermi-liquid theory

In the previous Sections, the basic description of a Fermi polaron is given, which hopefully answers many questions, but also raises a few. In order to not repeat the many excellent reviews about quasiparticles and their properties, in this subsection I state some questions that arise when working with Fermi polarons and I give rather intuitive

and hand-waving answers. For further reading I refer to the respective experimental and theoretical publications.

### What is the role of the impurity mass in the Fermi polaron picture?

If we consider a single impurity that is immersed in a degenerate gas of majority atoms, we intuitively know that as the impurity mass changes, the scattering properties of the system will change as well. It directly influences the polaron energy and therefore also all other properties. In a hand-waving picture one could argue that a light atom will feel more impact from a collision, compared to a heavy one, and therefore the influence on the energy and effective mass of the polaron will be bigger if the impurity mass is small. Furthermore, the ground state of the system is strongly dependent on the mass ratio between the majority and minority species. In the case of a light impurity atom, the ground state can take exotic forms. Besides the attractive polaron and a dressed molecule it could evolve to a dressed dimer or even to the long sought dimer with non-zero momentum (FFLO) [Mat11, Mas14]. Experimentally, it is difficult to achieve relatively low impurity masses, if the surrounding is represented by a Fermi sea. The reason lies in the possible choice of atomic species. The only stable fermionic isotopes in the alkali family are  $^6\text{Li}$  and  $^{40}\text{K}$ . The latter has a very low natural abundance and is therefore a more suitable candidate for the impurity in a two-species experiment. However, within the last years new experiments involving Er or Dy were proven to be operable. They would bring suitable masses for the environment, but at the same time introduce new complications. These species have a high magnetic dipole moment, and the question of how long-range interactions, which deform the Fermi surface [Aik14], alter the polaron picture has not yet been resolved [DO19, Bom19, Nis21, Kai14, Wen18].

A massive impurity, on the other hand, will be less perturbed by the Fermi sea and the ground state of the system will be the dressed dimer for most values of the interaction strengths [Mas12]. An example is presented in Fig. 3.5 for a mass ratio of  $m_{\text{Li}}/m_{\text{K}} = 6/41$ . However, the limiting case of infinite impurity mass holds exciting states. An impurity with infinite mass is not only a theoretical construct, but can be experimentally realized by pinning down one species with the aid of a species-selective potential. The fact that the atoms cannot move due to their tight optical confinement is equivalent to an infinite-mass scattering partner. If such a scenario is realized at zero temperature in the thermodynamic limit ( $N_{\uparrow} \rightarrow \infty$ ), the *orthogonality catastrophe* [And67, Kna12, Sch18] is predicted to occur. Then, in a finite amount of time, the system will become orthogonal, or in other words the wave-function overlap of the initial and the final state is zero. This puzzling phenomenon indicating a complete loss of memory of the system is not yet experimentally observed, due to the very challenging setup that is necessary. Two main ingredients are an infinite-mass impurity and a zero temperature sample, where the latter is the factor that prevented the FeLiKx-team from observing it.

### What is the role of quantum statistics of the majority and minority atoms?

As already briefly mentioned in Sec. 3.2.1 the polarons can be divided into two classes according to the fundamental nature of their surroundings, the Bose and the Fermi polaron. The latter is the main topic of this thesis and was therefore introduced, so let us consider the differences with respect to the former. The basic collective excitations in a

BEC are described by Bogoliubov excitations and represent the dressing of the impurity. Reference [Gru15] presents a wonderful overview of common theoretical approaches to describe the Bose polaron. From the point of view of an experimentalist, ultracold bosons are in general more difficult to generate than ultracold fermions due to three-body loss. Most bosonic species are operated at a certain magnetic field to keep the background-scattering length at a desired value with the aid of FRs. If this is achieved, a suitable FR between the minority and majority species must be found in order to tune the scattering length and observe a spectrum. Another important difference between the Fermi and Bose systems is that the latter, due to its two orders of magnitude higher density, is subject to the miscibility-immiscibility problem [Bie16]. For repulsive inter-particle interactions the BEC can undergo a phase separation with the second species (see Ch. 7 and 6) whereas for attractive interactions the collapse of the BEC [Osp06b, Zac06] can lead to additional fast particle loss. Despite these difficulties, the first experimental observations of the Bose polaron were presented in 2016 [Hu16, Jør16]. The Bose-polarons problem is far from being solved and many predictions are still to be experimentally verified, as the orthogonality catastrophe [Mis19], bi-polarons [Cam18b], or the famous Efimov resonances [Lev15b].

Since the minority species is theoretically considered as a single impurity, the question of its quantum statistics is rather superfluous. However, in experiments typical concentrations are on the order of  $\sim 20\%$  and temperatures are so low that even small numbers of bosons and fermions can lead to the occurrence of Bose-Einstein condensation and formation of a degenerate Fermi gas, respectively. In this case, impurity-impurity or mediated interactions will differ depending on the fundamental nature of the particles. Furthermore, the interaction between dimers and their environment changes. In principle one can generate Bose-Bose, Fermi-Fermi and Fermi-Bose mixtures. In the first two cases the dimer state is bosonic. The latter of the two may have suppressed collision rates because the constituents are still subject to the Pauli exclusion principle. The third possible mixture will contain less reactive fermionic dimers [Mar19, Zel19] and may even form a Fermi sea (see also Ch. 4). Note that these effects only occur at sufficiently high impurity concentrations.

### What is the role of the system dimension?

It is well known that one-, two- and three-dimensional systems cannot be treated in the same way and have different effects under similar conditions, see e.g. [Pit16]. One way to look at this fact is that the density of states decreases as the dimensionality of the system is reduced. It follows that quantum and thermal fluctuations will have an increasing effect in the physics involved, since they will destroy the long-range order in 1D and 2D systems at zero temperature. This affects the occurrence of phase transitions, which promotes the emergence of exotic states such as the fractional quantum Hall effect [Lau98] or superconducting nanowires [Sch00].

Considering Fermi polaron physics, its theoretical basis is given by Landau's Fermi liquid theory, which is a valid assumption only in three and two dimensions [Mas14, Sar21]. In one dimension the Fermi liquid picture breaks down and the situation is

described by a non-Fermi liquid, the Luttinger liquid [Lut63]<sup>7</sup>. The first experimental observation of the polaron in two dimensions is presented in Ref. [Kos12] and theoretical calculations in Refs. [Par11, Zöl11]. The one-dimensional case was treated theoretically in [Gir09, Les10]. A summary of calculations of the spectral function of polarons with finite temperature and concentration in 1D, 2D and 3D can be found in [Taj21]. Note that recently, the polaron with atoms from the lanthanide series has been experimentally studied in Ref. [DO19]. Corresponding theoretical predictions can be found in [Xu18, Den18, Che18].

### How does the polaron evolve in time?

In order to answer this question one has to view the timescales of the system. The fastest possible time scale of a zero temperature Fermi sea is given by the Fermi time  $\tau_F = \hbar/E_F$  since it originates from particles with the highest possible energy. Many processes like few-body physics, temperature and density induced effects, and dephasing, depend strongly on the considered system. However, in order to see such effects, the system must be probed accordingly fast. Typical Fermi times are on the order of a few  $\mu\text{s}$ , which implies that excitation schemes faster than this must be applied. One example of such a measurement is presented in Ch. 4, where the FeLiKx team was able to observe the birth and subsequent decay of the Fermi polaron, by measuring its contrast, using Ramsey-interferometric techniques. A time resolved measurement in addition to a spectrum, such as the one shown in Fig. 3.5, can give further information about the coherence of the system and is more suitable to resolve fast dynamics. For an excellent overview on the temporal evolution of heavy impurities in a Fermi sea, see Ref. [Sch18].

### What are the limits of the single particle-hole (SPH) description?

The temperature  $T$  and the concentration  $\mathcal{C} = n_1/n_2$ , defined here as the density ratio of the atoms occupying the states  $|1\rangle$  and  $|2\rangle$ , are currently under theoretical and experimental investigation. It is not fully understood how they influence the single particle-hole approximation, at what point it will break down, and how the system can be described in the transitional region. The lower limits of temperature and density ( $T, \mathcal{C} \rightarrow 0$ ) are well described by the SPH description. In the limit, in which the temperature exceeds the Fermi temperature  $T \gg T_F$  the majority species is rather described by a Boltzmann gas than a Fermi sea and will not form polarons. The connection between the two limits is an open question and is tackled by theorists and experimentalists. The influence of the temperature of the majority species was experimentally [Yan19, Nes20] and theoretically [Hu18, Taj19, Mul19, Fra10] investigated recently. Interestingly, for Bose polarons, theories predict three-body states even in the limit of high temperatures. Also in this scenario the transitional behavior around the critical temperature for the condensation of the Bose gas could be theoretically described [Sun17, Gue18, Fie20, Dzs20]. However, this was not verified experimentally up to now.

---

<sup>7</sup>An intuitive picture about the two models and their validity can be obtained from Ref. [Gia04] and references therein.

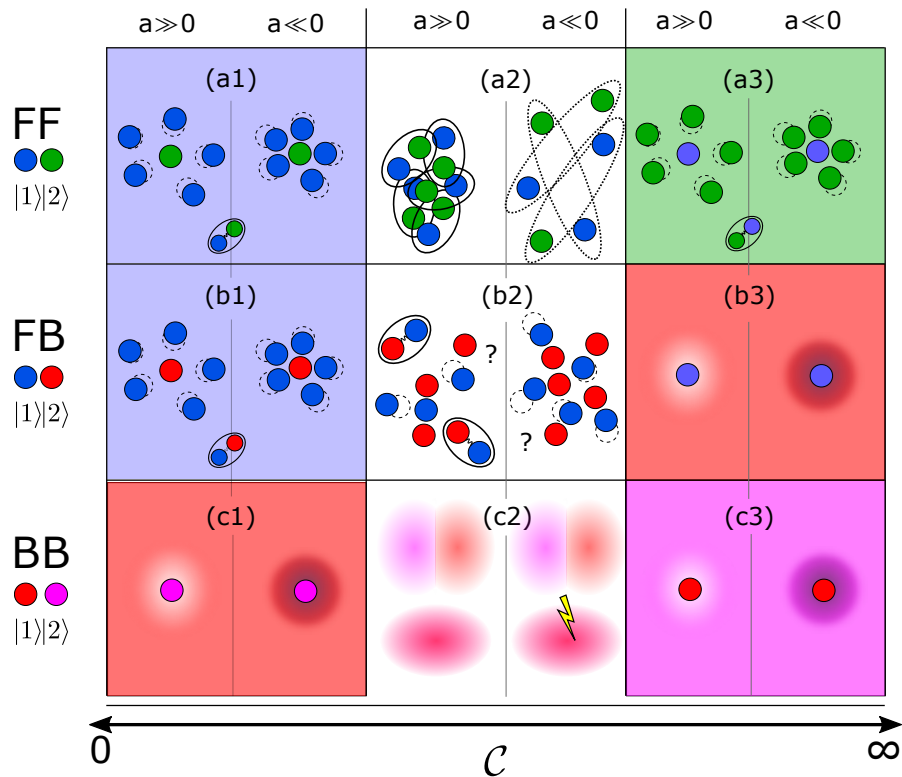


FIGURE 3.6: Illustration of a Fermi-Fermi, Fermi-Bose, and Bose-Bose mixture for three different concentration regimes and strong repulsive ( $a \gg 0$ ) and attractive ( $a \ll 0$ ) inter-particle interactions. Green and blue circles represent fermions, whereas red and purple circles represent bosons. From left to right the concentration is increased and from top to bottom the system changes from two fermionic, to a fermionic and a bosonic, and finally to two bosonic components. Colorful backgrounds indicate the degenerate majority component of the respective mixture. Panels (a1), (a3), (b1) picture the repulsive and attractive Fermi polarons, which are indicated by repelling and attracting the surrounding medium. A possible dimer state is indicated in the bottom of the panel. The illustration of the repulsive and attractive Bose polaron in panels (b3), (c1), (c3) is chosen differently in order to emphasize that the environment is a BEC, in contrast to a Fermi sea. The second column depicts the corresponding population balanced mixtures, in which the components have equal densities. In (a2) two fermions will form a molecular BEC and loosely bound halo-states for positive and negative scattering lengths, respectively. The panel (c2) illustrates two condensed Bose gases, which are either in a phase separated or miscible state. The central panel (b2) represents the strongly interacting, balanced Fermi-Bose mixture. It illustrates a thermal Bose gas, in which the interaction leads to the formation of Fermi polarons and eventual sequential decay into molecules. The question mark indicates further unexplored processes, as mentioned in the main text. First experimental observations for the different regimes in references [Sch09, Koh12] for (a1) and (a3), [Reg04, Bar04a, Zwi04] for (a2), Ch. 8 for (b1) and (b2), [Hu16] for (b3), [Jør16] for (c1) and (c3), and [Pap08] for (c2).

### What is the role of the impurities concentration in the polaron picture?

Just as high temperature, a finite impurity concentration will also provoke the breakdown of the single-particle hole approximation. However for different mixtures of atomic species the situation looks drastically different. In order to simplify this picture I shall discuss the case of a Fermi-Fermi (FF), a Bose-Bose (BB) and a Fermi-Bose (FB) mixture for the cases  $C \rightarrow 0$ ,  $C = 1$ ,  $C \rightarrow \infty$ , as depicted in the three columns of Fig. 3.6. Note

that I will not go into detail of the wealth of physical effects that can occur in each system, but rather follow an explanation from the point of the occurrence of polarons. The left and right columns of the respective panels illustrate the mixtures for strong repulsive and strong attractive interactions. In the first case of a single impurity in  $|1\rangle$  a repulsive and an attractive Fermi/Fermi/Bose polaron will form in the FF/FB/BB case, as depicted in (a1)/(b1)/(c1). The other limiting case where only one atom occupies state  $|2\rangle$  presents an inverted situation where the former minority, becomes the majority component of the system and a repulsive and an attractive Fermi/Bose/Bose polaron will form in the FF/FB/BB case, as shown in (a3)/(b3)/(c3). The intermediate cases  $\mathcal{C} = 1$  of the FF mixture (a2) shows the emergence a molecular BEC and Cooper pairs. The behavior of two-component Fermi mixtures at strong interactions is described by the famous BEC-BCS crossover as elaborated in the excellent review in Ref. [Ket08]. Note that in the case of repulsive interactions, effects such as itinerant ferromagnetism are predicted [Jo09, Mas11, Mas14], but not yet observed [San12, Vall17]. The equal mixture of bosons (c2), here assumed to be two condensed clouds, can lead to two different scenarios, depending on their intra-particle interaction strength [Pap08]. Either the system phase separates and the two spatially separated components show reduced three-body losses (see Ch. 6 and Ch. 7), or the system mixes. The same effects appear as well for attractive interactions. However, in this case the mean field collapse will lead to strongly enhanced loss (indicated by the yellow lightning symbol). The last scenario (b2) is until now largely unexplored. If the density of the bosons in a FB system is increased to be equal to the density of the fermions, the situation of a mixture of thermal bosons and degenerate fermions is realized. Since the densities are equal, we do not expect phase separation to happen. Furthermore, since dimer states are fermionic, we do not expect any BCS pairing or a molecular BEC to occur. Therefore we assume that Fermi polarons will form, since the bosons are not condensed. At this stage, however, mediated interactions can no longer be neglected.

As one approaches states of intermediate concentrations  $0 < \mathcal{C} < 1$ , induced interactions, one component mediates the interaction between particles of the second component, can evolve and change the behavior of the system dramatically. For increased boson density, with respect to the other component, exotic few-body states and interacting polarons that can even lead to a bound polaronic state, the bipolaron [Ran06], are predicted to occur. Furthermore, Ruderman–Kittel–Kasuya–Yosida (RKKY) interactions have been observed [Edr20]. In the FF case the early measurements presented in Ref. [Zwi06b] and later in [Sca17] show the influence of the minority concentration in a FF, w.r.t. the BEC-BCS crossover and w.r.t. the polaron energy. However, mediated interactions or polaron-polaron interactions in Fermi-Bose systems have not yet been observed, but first indications on the influence were seen in [Yan20b] where observations towards boson induced hydrodynamic behavior in single component Fermi gases were made and in Ch. 8 where observations towards the transition from a Fermi to a Bose polaron were made.

# 4

## Chapter 4

# Publication: Ultrafast many-body interferometry of impurities coupled to a Fermi sea

Journal: Science, Vol. **354**, Issue 6308, pp. 96-99

Published: 07. Oct 2016

DOI: [10.1126/science.aaf5134](https://doi.org/10.1126/science.aaf5134)

Marko Cetina<sup>1,2</sup>, Michael Jag<sup>1,2</sup>, Rianne S. Lous<sup>1,2</sup>, Isabella Fritsche<sup>1,2</sup>, Jook T. M. Walraven<sup>1,3</sup>, Rudolf Grimm<sup>1,2</sup>, Jesper Levinsen<sup>4</sup>, Meera M. Parish<sup>4</sup>, Richard Schmidt<sup>5,6</sup>, Michael Knap<sup>7</sup>, Eugene Demler<sup>6</sup>

<sup>1</sup> Institut für Quantenoptik und Quanteninformation, Österreichische Akademie der Wissenschaften, 6020 Innsbruck, Austria.

<sup>2</sup> Institut für Experimentalphysik, Universität Innsbruck, 6020 Innsbruck, Austria.

<sup>3</sup> Van der Waals–Zeeman Institute, Institute of Physics, University of Amsterdam, 1098 XH Amsterdam, Netherlands.

<sup>4</sup> School of Physics and Astronomy, Monash University, Victoria 3800, Australia.

<sup>5</sup> Institute for Theoretical Atomic, Molecular and Optical Physics (ITAMP), Harvard-Smithsonian Center for Astrophysics, Cambridge, MA 02138, USA.

<sup>6</sup> Department of Physics, Harvard University, Cambridge, MA 02138, USA.

<sup>7</sup> Department of Physics, Walter Schottky Institute and Institute for Advanced Study, Technical University of Munich, 85748 Garching, Germany.

Contribution to the publication: I joined the experiment while the measurements for this publication were taken. I contributed to discussions on the data and final measurements with M. Cetina, M. Jag and R. S. Lous. All authors of this publication contributed to discussing and writing the manuscript.

Note on the present version of the publication: This version can vary from the published version since final changes by the editor are not included. Typos have been corrected. The sections structure has been introduced for better readability and references have been updated.

## 4.1 Abstract

The fastest possible collective response of a quantum many-body system is related to its excitations at the highest possible energy. In condensed matter systems, the time scale for such “ultrafast” processes is typically set by the Fermi energy. Taking advantage of fast and precise control of interactions between ultracold atoms, we observed nonequilibrium dynamics of impurities coupled to an atomic Fermi sea. Our interferometric measurements track the nonperturbative quantum evolution of a fermionic many-body system, revealing in real time the formation dynamics of quasi-particles and the quantum interference between attractive and repulsive states throughout the full depth of the Fermi sea. Ultrafast time-domain methods applied to strongly interacting quantum gases enable the study of the dynamics of quantum matter under extreme nonequilibrium conditions.

## 4.2 Introduction

The nonequilibrium dynamics of fermionic systems is at the heart of many problems in science and technology. The wide range of energy scales, spanning the low energies of excitations near the Fermi surface up to high energies of excitations from deep within the Fermi sea, challenges our understanding of the quantum dynamics in such fundamental systems. The Fermi energy  $E_F$  sets the shortest response time for the collective response of a fermionic many-body system through the Fermi time  $\tau_F = \hbar/E_F$ , where  $\hbar$  is the Planck constant divided by  $2\pi$ . In a metal (i.e., a Fermi sea of electrons),  $E_F$  is in the range of a few electron volts, which corresponds to  $\tau_F$  on the order of 100 attoseconds. Dynamics in condensed matter systems on this time scale can be recorded by attosecond streaking techniques [Kra09], and the initial applications were demonstrated by probing photoelectron emission from a surface [Paz15]. However, despite these advances, the direct observation of the coherent evolution of a fermionic many-body system on the Fermi time scale has remained beyond reach.

In atomic quantum gases, the fermions are much heavier and the densities far lower, which brings  $\tau_F$  into the experimentally accessible range of typically a few microseconds. Furthermore, the powerful techniques of atom interferometry [Cro09] now offer an opportunity to probe and manipulate the real-time coherent evolution of a fermionic quantum many-body system. Such techniques have been successfully used to measure bosonic Hanbury-Brown-Twiss correlations [Sim11], to demonstrate topological bands [Ata13], to probe quantum and thermal fluctuations in low-dimensional condensates [Gri12, Had06], and to measure demagnetization dynamics of a fermionic gas [Kos13, Bar14]. Impurities coupled to a quantum gas provide a unique probe of the many-body state [Sch09, Nas09, Koh12, Kos12, Zha12, Mas14, Sid17]. Strikingly, they allow direct access to the system’s wave function when the internal states of the impurities are manipulated using a Ramsey atom-interferometric technique [Goo11, Kna12].

We used dilute  $^{40}\text{K}$  atoms in a  $^6\text{Li}$  Fermi sea to measure the response of the sea to a suddenly introduced impurity. For near-resonant interactions, we observed coherent quantum many-body dynamics involving the entire  $^6\text{Li}$  Fermi sea. We also observed in

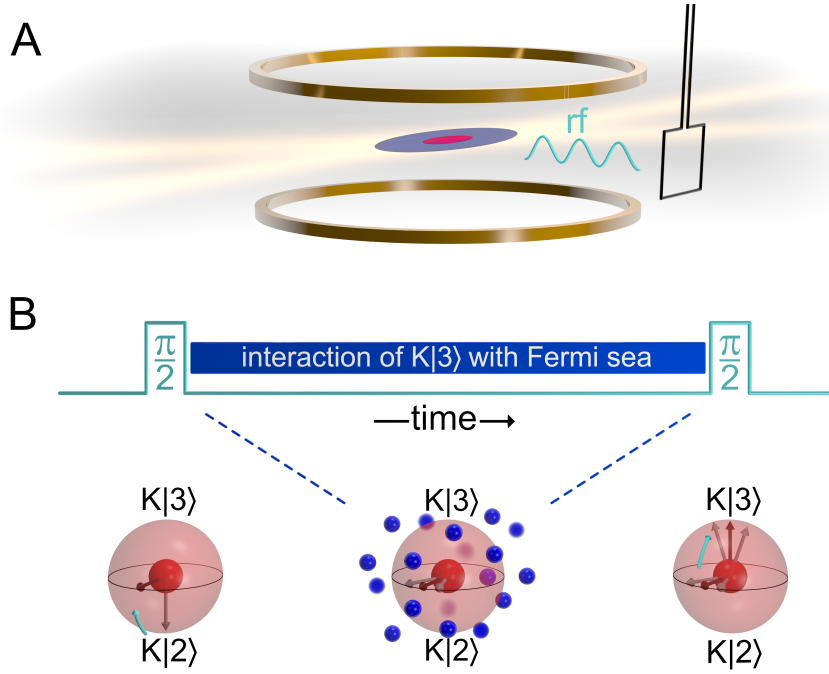


FIGURE 4.1: Illustration of the experimental setup and procedure. **(A)** Li (blue) and K (red) atoms are held in a crossed-beam optical dipole trap, forming the Fermi sea and the sample of impurity atoms, respectively. The magnetic field coils (gold) are used to tune interactions via a Feshbach resonance, and the rf coil (black) allows the manipulation of the spin state of the impurity atoms. **(B)** The Ramsey sequence starts with a first rf  $\pi/2$  pulse, which is applied in the presence of weak interactions between the impurity atoms and the Fermi sea. As illustrated on the Bloch sphere, this pulse drives an impurity atom (red dot) into a superposition of the spin states  $K|2\rangle$  and  $K|3\rangle$ . By optical resonance shifting (see text), the interaction of the  $K|3\rangle$  component with the atoms of the Fermi sea (blue dots) is abruptly turned on while the  $K|2\rangle$  component remains noninteracting. The impurity state then evolves for a variable interaction time, at the end of which its state is probed by a second  $\pi/2$  pulse and subsequent measurement of the spin-state populations.

real time the formation dynamics of the repulsive and attractive impurity quasiparticles. In the limit of low impurity concentration, our experiments confirm that an elementary Ramsey sequence is equivalent to linear-response frequency-domain spectroscopy. We demonstrate that our time-domain approaches allow us to prepare, control, and measure many-body interacting states.

### 4.3 Main results

Our system consists of a small sample of typically  $1.5 \times 10^4$   $^{40}\text{K}$  impurity atoms immersed in a Fermi sea of  $3 \times 10^5$   $^6\text{Li}$  atoms ([Cet15] and Sec. 4.6). The mixture is held in an optical dipole trap (Fig. 4.1A) at a temperature of  $T = 430$  nK after forced evaporative cooling. Because of the Li Fermi pressure, and because our optical potential for K has more than twice the strength of that for Li, the K impurities are concentrated in the central region of the large Li cloud. Here they experience a nearly homogeneous

environment with an effective Fermi energy of  $\epsilon_F = k_B \times 2.6 \mu\text{K}$  (Sec. 4.6), where  $k_B$  is the Boltzmann constant. The corresponding Fermi time,  $\tau_F = 2.9 \mu\text{s}$ , sets the natural time scale for our experiments. The degeneracy of the Fermi sea is characterized by  $k_B T / \epsilon_F \approx 0.17$ . The concentration of K in the Li sea remains low, with  $\bar{n}_K / \bar{n}_{\text{Li}} \approx 0.2$ , where  $\bar{n}_{\text{Li}}$  is the average Li number density and  $\bar{n}_K$  is the average K number density sampled by the K atoms (Sec. 4.6).

The interaction between the impurity atoms in the internal state  $\text{K}|3\rangle$  (third-to-lowest Zeeman sublevel) and the Li atoms (always kept in the lowest Zeeman sublevel) is controlled using a rather narrow (Sec. 4.6) interspecies Feshbach resonance near a magnetic field of 154.7 G [Nai11, Cet15]. We quantify the interaction with the Fermi sea by the dimensionless parameter  $X \equiv -1/\kappa_F a$ , where  $\kappa_F = \hbar^{-1} \sqrt{2m_{\text{Li}} \epsilon_F}$  is the Li Fermi wave number (with  $m_{\text{Li}}$  the Li mass) and  $a$  is the  $s$ -wave interspecies scattering length. Slow control of  $X$  is realized in a standard way by variations of the magnetic field, whereas fast control is achieved using an optical resonance shifting technique [Cet15]. The latter permits sudden changes of  $X$  by up to  $\pm 5$  within  $\tau_F/15 \approx 200$  ns.

Our interferometric probing method is based on a two-pulse Ramsey scheme (Fig. 4.1 (B)), following the suggestions of [Goo11, Kna12]. The sequence starts with the impurity atoms prepared in the spin state  $\text{K}|2\rangle$  (second-to-lowest Zeeman sublevel), for which the background interaction with the Fermi sea can be neglected. An initial radio-frequency (rf)  $\pi/2$  pulse, of duration  $10 \mu\text{s}$ , drives the K atoms into a coherent superposition between this noninteracting initial state and the state  $\text{K}|3\rangle$  under weakly interacting conditions (interaction parameter  $X_1$  with  $|X_1| \approx 5$ ). Using the optical resonance shifting technique [Cet15], the system is then rapidly quenched into the strongly interacting regime ( $|X| < 1$ ). After an evolution time  $t$ , the system is quenched back into the regime of weak interactions and a second  $\pi/2$  pulse is applied. The population difference  $N_3 - N_2$  in the two impurity states is measured as a function of the phase  $\varphi$  of the rf pulse. By fitting a sine curve to the resulting signal  $(N_3 - N_2)/(N_3 + N_2)$ , we obtain the contrast  $|S(t)|$  and the phase  $\varphi(t)$  (Sec. 4.6), which yields the complex-valued Ramsey signal  $S(t) = |S(t)| e^{-i\varphi(t)}$ . In the limit of low impurity concentration and rapid quenching,  $S(t) = \langle e^{i\hat{H}_0 t/\hbar} e^{-i\hat{H} t/\hbar} \rangle$  describes the sensitivity of the time evolution to perturbations of the system. Here, the angle brackets denote the quantum statistical average, the Hamiltonian  $\hat{H}_0$  describes the noninteracting Fermi gas, and the interacting Hamiltonian  $\hat{H}$  differs from  $\hat{H}_0$  by the additional scattering between the Fermi sea atoms and the impurity atoms. The function  $S(t)$ , which for pure initial states is often referred to as the Loschmidt amplitude [Los76], was introduced in the context of nuclear magnetic resonance experiments [Hah50] and was also applied in the analysis of the orthogonality catastrophe [Noz69] as well as in the study of quantum chaos [Jal01]. We first consider the interaction conditions for which earlier experiments have demonstrated that the spectral response is dominated by polaronic quasi-particles [Mas14]. Figure 4.2, A to D, shows the evolution of the contrast and the phase measured in the repulsive and the attractive polaron regimes, where  $X = -0.23(6)$  and  $X = +0.86(6)$ , respectively. For short evolution times up to  $\sim 4\tau_F$ , we observed that both contrast signals exhibit a similar initial parabolic transient, which is typical of a Loschmidt echo [Jal01]. For longer times, this connects to an exponential decay of the contrast and a linear evolution of the phase. In [Cet15], we showed that the exponential decay of the contrast in this regime can be interpreted in terms of quasiparticle scattering. Here, the linear phase

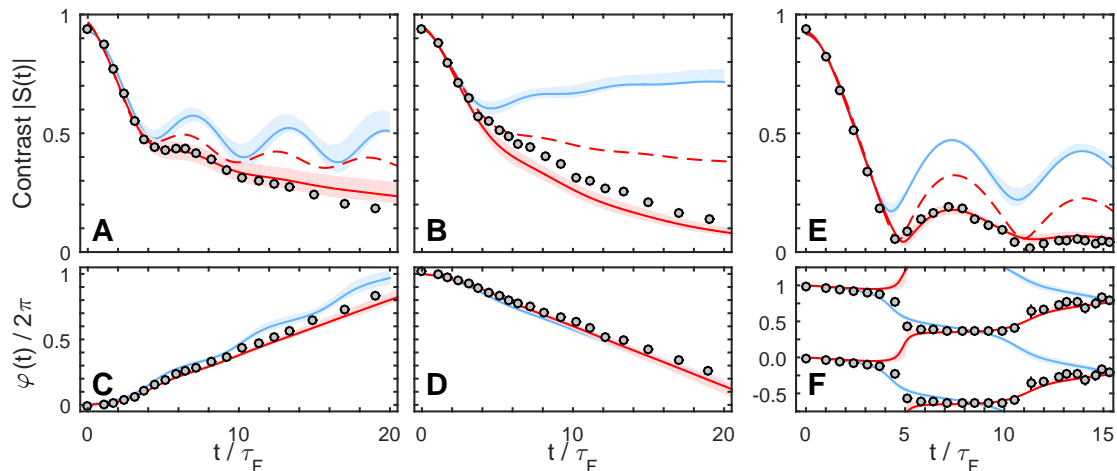


FIGURE 4.2: Impurity dynamics in the Fermi sea. (A and C) Contrast  $|S(t)|$  and phase  $\varphi(t)$  of the interference signal depending on the interaction time  $t$  in the repulsive polaron regime for  $X = -0.23(6)$ , with the rf pulse applied at  $X_1 = -3.9$ . (B and D) Same quantities in the attractive polaron regime for  $X = 0.86(6)$  and  $X_1 = 5.8$ . (E and F) Same quantities for resonant interactions ( $X = 0.08(5)$ ,  $X_1 = 4.8$ ). The solid blue lines show the results of the TBM calculations. The solid red lines show the results of the FDA calculations at the measured temperature; the dashed red lines show the calculated results at zero temperature. The shaded regions indicate the uncertainty range resulting from the combined experimental errors in  $X$ ,  $k_B T$  and  $\epsilon_F$ . The errors in the experimental data are typically smaller than the symbol size. The multiple representation of  $\varphi(t)$  in (F) accounts for the ambiguity of a phase modulo  $2\pi$ .

evolution corresponds to the energy shift of the quasiparticle state, for which we obtain  $+0.29(1)\epsilon_F$  for the repulsive case in Fig. 4.2C and  $-0.27(1)\epsilon_F$  for the attractive case in Fig. 4.2D. The longer-time behavior reflects the quasiparticle properties, whereas the observed initial parabolic transient reveals the ultrafast real-time dynamics of the quasiparticle formation.

On resonance, for the strongest possible interactions, a description of the dynamics in terms of a single dominant quasiparticle excitation breaks down. In this regime, our measurements—displayed in Fig. 4.2, E and F, for  $X = 0.08 \pm 0.05$ —reveal the striking quantum dynamics of an interacting fermionic system forced into a state far out of equilibrium. The contrast  $|S(t)|$  shows pronounced oscillations reaching almost zero, which indicates that the time-evolved state can become almost orthogonal to the initial state. Meanwhile, the phase  $\varphi(t)$  exhibits plateaus with jumps of  $\pi$  near the contrast minima. To further interpret our measurements, we used two different theoretical approaches: the truncated basis method (TBM) (Sec. 4.6) and the functional determinant approach (FDA) [Kna12]. The TBM models our full experimental procedure assuming zero temperature and considering only single particle-hole excitations. This approximation, first introduced in [Che06] to model the attractive polaron, was later applied to predict repulsive quasi-particles in cold gases [Cui10]. The predictions of the TBM are represented by the blue lines in Fig. 4.2. This method accurately describes the initial transient as well as the period of the oscillations of  $S(t)$  on resonance. Although the zero-temperature TBM calculation naturally overestimates the contrast in the thermally dominated regime ( $t > 6\tau_F$ ), it accurately reproduces the observed linear phase evolution and thus the quasiparticle energy. The FDA is an exact solution for a fixed impurity

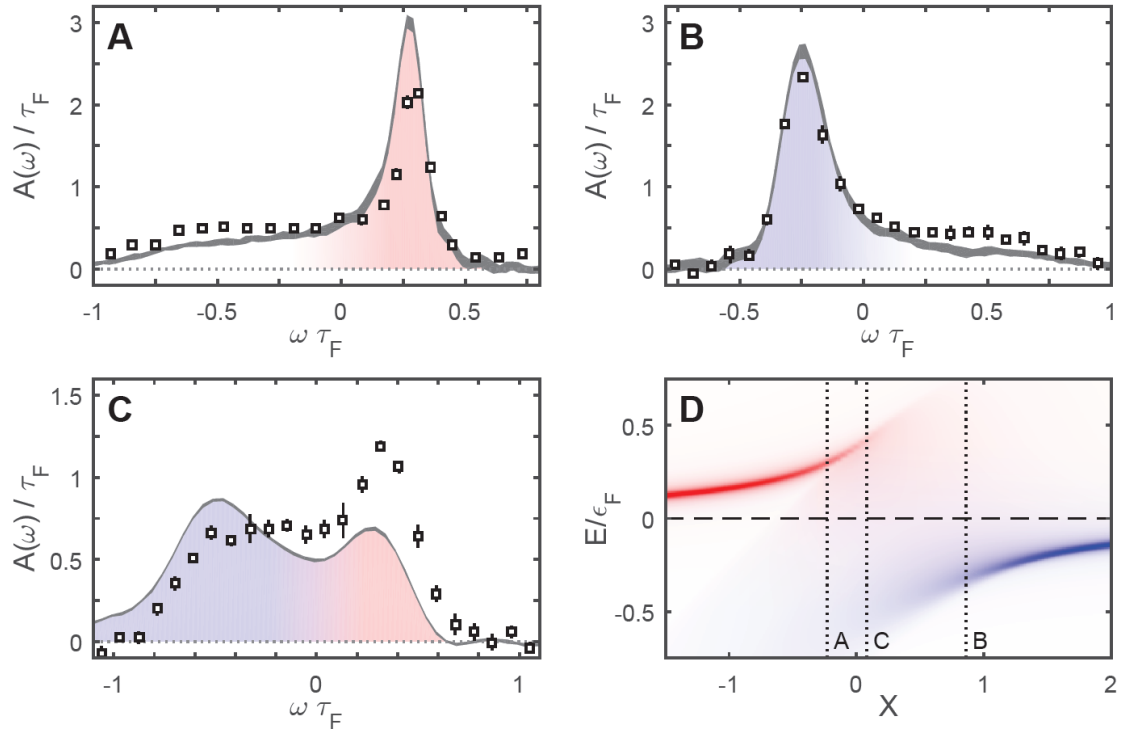


FIGURE 4.3: Frequency-domain rf spectroscopy versus time-domain Ramsey spectroscopy. (A to C) The data points show the rf spectra for the repulsive ( $X = -0.23 \pm 0.06$ ), attractive ( $X = 0.86 \pm 0.06$ ), and resonant ( $X = 0.08 \pm 0.05$ ) cases, all normalized to unit integral. Here,  $\omega$  corresponds to the detuning of the rf frequency from the unperturbed transition frequency. The gray lines correspond to the Fourier transform of the  $S(t)$  data from Fig. 4.2, with their widths indicating the standard error resulting from the combined experimental uncertainties in the  $S(t)$  data. The red and blue shading indicates the repulsive and attractive parts of the excitation spectrum, respectively. (D) Diagram of the excitation energy versus the interaction parameter, showing the repulsive (red) and the attractive (blue) quasiparticle branches. For illustrative purposes, we model the spectrum by a calculation of the spectral function together with additional broadening simulating the effects of finite rf pulse duration and finite temperatures. The three vertical dotted lines indicate the interaction conditions of (A) to (C).

at arbitrary temperatures, taking into account the nonperturbative creation of infinitely many particle-hole pairs. The FDA calculation is represented by the solid red lines in Fig. 4.2. We see excellent agreement with our experimental results, which indicates that the effects of impurity motion remain small in our system. This observation can be explained by the fact that our impurity is sufficiently heavy so that the effects of its recoil with energies of  $\sim 0.25 \epsilon_F$  are masked by thermal fluctuations. To identify the effect of temperature, we performed a corresponding FDA calculation for  $T = 0$ ; the results are shown as dashed lines in Fig. 4.2. Here, we see a slower decay of  $|S(t)|$ , which follows a power law at long times (Sec. 4.6) under the idealizing assumption of infinitely heavy impurities.

Time-domain and frequency-domain methods are closely related, as is well known in spectroscopy. In the limit of low impurity density, where the interactions between the impurities can be neglected,  $S(t)$  is predicted to be proportional to the inverse Fourier

transform of the linear excitation spectrum  $A(\omega)$  of the impurity [Noz69]. To benchmark our interferometric method, we measured  $A(\omega)$  using rf spectroscopy, similar to our earlier work [Koh12] but with great care taken to ensure a linear response (Sec. 4.6). The measured excitation spectra are shown in Fig. 4.3, **A** to **C**, together with a schematic energy diagram of the quasiparticle branches (Fig. 4.3 **D**). In the repulsive and attractive polaron regimes, we observed the characteristic structure of a peak on top of a broad pedestal [Mas14]. The peak corresponds to the long-time evolution of the quasiparticle, whereas the pedestal is associated with the rapid dynamics related to the emergence of many-body correlations. For resonant interactions, the rf response is broad and nearly symmetric. The latter implies that the imaginary part of  $S(t)$  remains small. Consequently, as seen in Fig. 4.2, **E** and **F**, the phase  $\varphi(t)$  essentially takes values near 0 and  $\pi$ , and each phase jump is accompanied by a pronounced minimum of  $|S(t)|$ . The apparent double-hump structure of the spectral response in the resonance regime suggests an interpretation of the observed oscillations of  $S(t)$  (Fig. 4.2 **E**) in terms of a quantum beat between the repulsive and attractive branches of our many-body system. The two branches are strongly broadened and overlap (Fig. 4.3 **D**), which results in a strong damping of the oscillations.

A detailed comparison of our time- and frequency-domain measurements reveals the potential of our approach to prepare and control many-body states. This is illustrated in Fig. 4.3, where we show the Fourier transform of the  $S(t)$  data from Fig. 4.2 as gray curves. We observed that time-domain measurements where the rf pulses are applied in the presence of weakly repulsive interactions (Fig. 4.3 **D**) emphasize the upper branch of the many-body system, whereas in the attractive case (Fig. 4.3 **B** and **C**), the lower branch is emphasized relative to the rf spectra. We interpret this as a consequence of the fact that the residual interactions during the rf pulse already bring the system into a weakly interacting polaron state before it is quenched to resonance (Sec. 4.6). Relative to the noninteracting initial state used in frequency-domain spectroscopy, these polarons have an increased wave function overlap with the corresponding strongly interacting repulsive and attractive branches, leading to the observed shift in the spectral weight. Our measurements show that the control over the initial state of many particles can be used to manipulate quantum dynamics in the strongly interacting regime. This unique capability of time-domain techniques can potentially be exploited in a wide range of applications, including the study of the dynamical behavior near the phase transition from a polaronic to a molecular system [Mas14] and the creation of specific excitations of a Fermi sea down to individual atoms [Dub13].

Our interpretation of the results in Figs. 4.2 and 4.3 relies on the assumption that our fermionic impurities are sufficiently dilute so that any interactions between them can be neglected. By increasing the impurity concentration, we can extend our experiments into a complex many-body regime where the impurities interact both with the Fermi sea and with each other (Sec. 4.6). Figure 4.4 shows the time-dependent contrast measured for  $k_B T = 0.24 \pm 0.02 \epsilon_F$  and  $\bar{n}_K/\bar{n}_{Li} = 0.20, 0.33, \text{ and } 0.53$ . An extrapolation of the  $S(t)$  data to zero concentration (open red circles) lies close to the data points for  $\bar{n}_K/\bar{n}_{Li} = 0.20$ , which is the typical concentration in our measurements and agrees with the FDA calculation. This confirms that the physics that we access in the measurements with a small sample of fermionic impurities is close to that of a single impurity, which we posit to be a consequence of the fermionic nature of the impurities. When the impurity

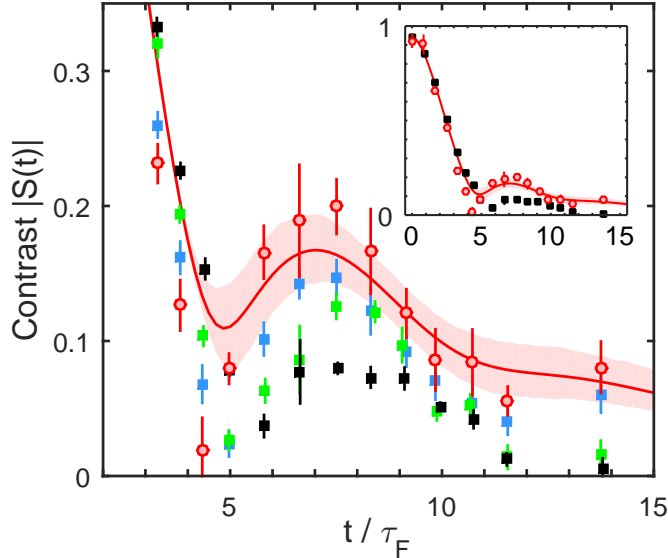


FIGURE 4.4: Observation of induced impurity-impurity interactions. Resonant dynamics of the contrast is shown for  $X = -0.01 \pm 0.05$ ,  $X_1 = 5.2$ ,  $\epsilon_F = k_B \times 2.1 \pm 0.1 \mu\text{K}$ ,  $k_B T / \epsilon_F = 0.24 \pm 0.02$ , and different impurity concentrations  $\bar{n}_K / \bar{n}_{Li}$ . The black, green, and blue squares correspond to  $\bar{n}_K / \bar{n}_{Li} = 0.53$ ,  $0.33$ , and  $0.20$ , respectively. The red circles correspond to the linear extrapolation of the complex  $S(t)$  data to the limit of a single impurity, taking into account the errors in the data. The inset reproduces this extrapolation together with the highest-concentration data points. The red line shows the result of the FDA calculation, and the shaded region indicates the corresponding uncertainty range resulting from the combined experimental errors in  $X$ ,  $k_B T$  and  $\epsilon_F$ .

concentration is increased, we find that the contrast for  $t > 5\tau_F$  is decreased and the period of the revivals of  $|S(t)|$  is prolonged. We interpret this as arising from effective interactions between the impurities induced by the Fermi sea [Mor10, Yu10]. Such interactions between fermionic impurities are predicted to lead to interesting quantum phases [Zwe12].

## 4.4 Conclusion

Our results demonstrate the power of many-body interferometry to study ultrafast processes in strongly interacting Fermi gases in real time, including the formation dynamics of quasi-particles and the nonequilibrium dynamics arising from quantum interference between different many-body branches. Of particular interest is the prospect of observing Anderson's orthogonality catastrophe (see [Kna12] and Sec. 4.6) by further cooling the Li Fermi sea [Har15] while pinning the K atoms in a deep species-selective optical lattice [LeB07]

## 4.5 Acknowledgments

Acknowledgments: We thank M. Baranov, F. Schreck, G. Bruun, N. Davidson, and R. Folman for stimulating discussions. Supported by NSF through a grant for ITAMP at Harvard University and the Smithsonian Astrophysical Observatory (R.S.); the Technical University of Munich-Institute for Advanced Study, funded by the German Excellence Initiative and the European Union FP7 under grant agreement 291763 (M.K.); the Harvard-MIT Center for Ultracold Atoms, NSF grant DMR-1308435, the Air Force Office of Scientific Research Quantum Simulation Multidisciplinary University Research Initiative (MURI), the Army Research Office MURI on Atomtronics, M. Rössler, the Walter Haefner Foundation, the ETH Foundation, and the Simons Foundation (E.D.); and the Austrian Science Fund (FWF) within the SFB FoQuS (F4004-N23) and within the DK ALM (W1259-N27).

## 4.6 Supplemental Material

# MATERIALS AND METHODS

### 4.6.1 Theoretical Description

In this section, we summarize the approaches that we developed to theoretically model the results of our interferometric Ramsey experiments. We first discuss the microscopic model that we use to describe the narrow Feshbach resonance of the Li-K mixture, and then we outline how we calculate the time evolution of the system within two approaches: the Truncated Basis Method (TBM) and the Functional Determinant Approach (FDA). In this section, we assume that a ‘perfect quench’ is performed, where the impurity is initially non-interacting with the Fermi sea and there are no interactions during the radio-frequency (rf) pulses. A discussion of the role played by interactions during the rf pulses is deferred to Section 4.6.5.

#### 4.6.1.1 Narrow Feshbach resonance model for Li-K mixtures

In our experiment, the K impurities are concentrated in the central region of the Li Fermi gas where they experience a nearly uniform Li environment (see Section 4.6.5.1). Hence we consider in our model K impurities that are immersed in a Li Fermi gas of uniform density. The Li-K mixture is prepared at magnetic fields near a closed-channel dominated Feshbach resonance between the  $Li|1\rangle$  and  $K|3\rangle$  states that occurs near 155 G. The narrow character of this resonance is a consequence of the limited strength of the coupling of atoms in the open channel to a closed-channel molecular state. To describe

this system we use the two-channel Hamiltonian, valid for a dilute ultracold gas,

$$\begin{aligned} \hat{H} = & \sum_{\mathbf{k}} \epsilon_{\mathbf{k},\text{Li}} \hat{c}_{\mathbf{k}}^\dagger \hat{c}_{\mathbf{k}} + \sum_{\mathbf{k}} \epsilon_{\mathbf{k},\text{K}} \hat{d}_{\mathbf{k}}^\dagger \hat{d}_{\mathbf{k}} + \sum_{\mathbf{k}} [\epsilon_{\mathbf{k},M} + \epsilon_M(B)] \hat{b}_{\mathbf{k}}^\dagger \hat{b}_{\mathbf{k}} \\ & + \frac{g}{\sqrt{V}} \sum_{\mathbf{k},\mathbf{q}} \chi(\mathbf{k}_{\text{rel}}) \left( \hat{b}_{\mathbf{q}}^\dagger \hat{c}_{\mathbf{q}/2+\mathbf{k}} \hat{d}_{\mathbf{q}/2-\mathbf{k}} + \hat{d}_{\mathbf{q}/2-\mathbf{k}}^\dagger \hat{c}_{\mathbf{q}/2+\mathbf{k}} \hat{b}_{\mathbf{q}} \right), \end{aligned} \quad (4.1)$$

where the first line defines the non-interacting Hamiltonian  $\hat{H}_0$ . Here,  $V$  is the total system volume,  $\hat{c}_{\mathbf{k}}^\dagger$  ( $\hat{c}_{\mathbf{k}}$ ) creates (annihilates) a Li fermion with momentum  $\hbar\mathbf{k}$  and single-particle energy  $\epsilon_{\mathbf{k},\text{Li}} = \frac{\hbar^2 k^2}{2m_{\text{Li}}}$ , and  $\hat{d}_{\mathbf{k}}^\dagger$  ( $\hat{d}_{\mathbf{k}}$ ) creates (annihilates) a K impurity atom in the  $\text{K}|3\rangle$  state with dispersion  $\epsilon_{\mathbf{k},\text{K}} = \frac{\hbar^2 k^2}{2m_{\text{K}}}$ , where we define  $k \equiv |\mathbf{k}|$ . The closed-channel molecule is created (annihilated) by  $\hat{b}_{\mathbf{k}}^\dagger$  ( $\hat{b}_{\mathbf{k}}$ ). It has the dispersion  $\epsilon_{\mathbf{k},M} = \frac{\hbar^2 k^2}{2(m_{\text{K}}+m_{\text{Li}})}$ , and a bare energy relative to the scattering threshold,  $\epsilon_M(B) = \delta\mu(B - B_c)$ . Here  $\delta\mu$  is the differential magnetic moment between the open and closed channels, and  $B_c$  denotes the threshold crossing of the bare molecular state [Chi10].

Close to the Feshbach resonance, the scattering length  $a$  diverges and the interaction between the K impurities and the Li atoms is predominantly mediated by exchange of the closed-channel molecule. We therefore neglect the background scattering potential in the open channel [Nai11]. The strength of the coupling between the open and closed channels is given by  $g$ , and we take a form factor  $\chi(\mathbf{k}_{\text{rel}}) = 1/[1 + (r_0 k_{\text{rel}})^2]$ , which accounts for the finite extent  $r_0$  of the closed-channel wave function  $\sim e^{-r/r_0}/r$ . Here,  $k_{\text{rel}} = |\mathbf{k}_{\text{rel}}|$  is the magnitude of the relative momentum in the two-atom scattering [Mor11].

The parameters of the model  $\delta\mu$ ,  $B_c$ ,  $g$ , and  $r_0$  are fully determined by known experimental parameters. First, the differential magnetic moment has recently been measured to be  $\delta\mu = h \times 2.35(2)$  MHz/G [Cet15]. Second, close to resonance, the scattering length may be parametrized as

$$a = a_{\text{bg}} \left( 1 + \frac{\Delta B}{B_0 - B} \right) \approx a_{\text{bg}} \frac{\Delta B}{B_0 - B}, \quad (4.2)$$

where  $B_0$  is the center of the Feshbach resonance with width  $\Delta B = 0.880$  G and background scattering length  $a_{\text{bg}} = 63.0 a_0$  [Nai11]. To connect with our model, we consider the on-shell two-body scattering amplitude  $f(k)$ , which for the Hamiltonian (4.1) is given by [Sch12a]

$$f(k) = \frac{\mu_{\text{red}}}{2\pi\hbar^2} g^2 \chi(\mathbf{k})^2 \left[ -\frac{\hbar^2 k^2}{2\mu_{\text{red}}} + \epsilon_M(B) - \frac{g^2 \mu_{\text{red}}}{4\pi\hbar^2 r_0 [1 - ikr_0]^2} \right]^{-1}, \quad (4.3)$$

where  $\mu_{\text{red}} = m_{\text{Li}} m_{\text{K}} / (m_{\text{Li}} + m_{\text{K}})$  is the reduced mass and  $\mathbf{k}$  is the relative scattering wave vector. Since the gas is ultracold and dilute, scattering of atoms is well described within the low energy expansion  $f^{-1}(k) \approx -a^{-1} + \frac{1}{2} r_{\text{eff}} k^2 - ik$ , with  $r_{\text{eff}}$  the effective range, and we thus identify

$$a = \frac{1}{\frac{1}{2r_0} + 2R^* \mu_{\text{red}} \delta\mu (B - B_c) / \hbar^2}, \quad (4.4)$$

$$r_{\text{eff}} = -2R^* + 3r_0 - 4r_0^2/a, \quad (4.5)$$

where  $R^* \equiv \hbar^4 \pi / (\mu_{\text{red}}^2 g^2)$  is the range parameter of the Feshbach resonance [Bru04, Pet04]. Comparing Eqs. (4.2) and (4.4) yields

$$R^* = \frac{\hbar^2}{2\mu_{\text{red}} a_{\text{bg}} \delta \mu \Delta B}, \quad (4.6)$$

$$B_0 - B_c = \frac{1}{2} \Delta B a_{\text{bg}} / r_0. \quad (4.7)$$

Equation (4.6) relates  $R^*$ , and thus the coupling constant  $g$ , to the known experimental parameters. The extent of the closed-channel wave function  $r_0$  in turn follows by comparing Eq. (4.7) to the theoretical prediction from quantum defect theory [Gor04, Szy05],  $B_0 - B_c = a_{\text{bg}} \Delta B / \bar{a}$ , where  $\bar{a} = 0.955 l_{\text{vdw}}$  and  $l_{\text{vdw}} = 40.8 a_0$  is the van der Waals length [Nai11]. Thus we obtain  $r_0 = \bar{a} / 2$ . Finally,  $B_0$  was obtained in Ref. [Cet15], allowing the determination of  $B_c$ .

In our experiment, the range parameter  $R^*$  takes the value  $R^* = 2650(25) a_0$  [Cet15]. Furthermore, the K impurities effectively experience a homogeneous Li environment. Thus, in the theory calculations we use the value  $k_F R^* = 1.1$ , with  $k_F$  the effective Li Fermi momentum.

#### 4.6.1.2 Truncated Basis Method

To model a mobile impurity as in the experiment, we consider an approximate wave function for the zero-momentum impurity that incorporates the scattering of a single particle out of the Fermi sea:

$$|\psi_\alpha\rangle = \alpha_0 \hat{d}_0^\dagger |\text{FS}\rangle + \sum_{\mathbf{q}} \alpha_{\mathbf{q}} \hat{b}_{\mathbf{q}}^\dagger \hat{c}_{\mathbf{q}} |\text{FS}\rangle + \sum_{\mathbf{k}, \mathbf{q}} \alpha_{\mathbf{k}, \mathbf{q}} \hat{d}_{\mathbf{q}-\mathbf{k}}^\dagger \hat{c}_{\mathbf{k}} \hat{c}_{\mathbf{q}} |\text{FS}\rangle. \quad (4.8)$$

Here, the first term on the right hand side describes the product state of the impurity K atom at zero momentum and the ground state of the non-interacting Li Fermi sea  $|\text{FS}\rangle = \prod_{|\mathbf{k}| < k_F} \hat{c}_{\mathbf{k}}^\dagger |0\rangle$ , where the Fermi momentum  $k_F$  is related to the Fermi energy by  $\epsilon_F = \hbar^2 k_F^2 / (2m_{\text{Li}})$ . The last two terms correspond, respectively, to the impurity binding a Li atom to form a closed-channel molecule, and the impurity exciting a particle out of the Fermi sea, in both cases leaving a hole behind. When using the TBM, we focus on zero temperature in order to capture the purely quantum evolution of the impurity. For convenience, within this model we also take  $r_0 \rightarrow 0$ , which formally requires taking the bare crossing  $B_c \rightarrow \infty$  to keep  $a$  finite. This approximation is justified, as  $R^*$  exceeds  $r_0$  by about two orders of magnitude.

Truncated wave functions of the form (4.8) have been used extensively in the study of Fermi polarons in ultracold atomic gases, starting with the work of Chevy [Che06]. While most of the previous work has focused on equilibrium properties, recently it has been proposed that these wave functions may be extended to dynamical problems using a variational approach to obtain the equations of motion [Par13], for instance to calculate the decay rate of excited states.

Here, we adapt the use of truncated wave functions for the Fermi polaron to the calculation of the dynamical response of the impurity to an interaction quench. For a perfect quench and at zero temperature, the quantity measured in experiment corresponds to

the overlap between the interacting and non-interacting states of the system, i.e., we have [Goo11, Kna12]

$$S(t) = \langle \psi_0(t) | \psi_{\text{int}}(t) \rangle = \langle \psi_0 | e^{i\hat{H}_0 t/\hbar} e^{-i\hat{H} t/\hbar} | \psi_0 \rangle. \quad (4.9)$$

Here  $|\psi_0\rangle \equiv \hat{d}_0^\dagger |\text{FS}\rangle$  is the initial non-interacting state of energy  $E_0$ , and  $\psi_{\text{int}}(t)$  is the state after a quench at time  $t = 0$  from zero to finite impurity interactions with the Fermi sea. Formally expanding in a complete set of states for the single impurity problem, the Ramsey signal (4.9) then becomes

$$S(t) = \sum_j |\langle \psi_0 | \phi_j \rangle|^2 e^{-i(E_j - E_0)t/\hbar}, \quad (4.10)$$

where  $|\phi_j\rangle$  is an eigenstate of the interacting Hamiltonian with energy  $E_j$ . However, this requires one to solve the entire problem which is generally not possible for a mobile impurity. Thus, within the Truncated Basis Method (TBM), we restrict the Hilbert space to wave functions of the form (4.8) and diagonalize the Hamiltonian within this truncated basis. As we shall see, this truncation permits an extremely accurate description of the initial quantum dynamics of the impurity.

For small  $t$ , we expand  $e^{-i\hat{H}t/\hbar}$  up to second order and obtain<sup>1</sup>

$$S(t) \approx 1 - (t/\tau_F)^2 \frac{(1 + m_{\text{Li}}/m_{\text{K}})^2}{3\pi k_F R^*}, \quad (4.11)$$

with  $\tau_F$  the Fermi time. This reveals that the short-time dephasing dynamics of  $S(t)$  is completely determined by the two-body properties, which are captured exactly by the TBM. In particular, we find that  $S(t)$  at short times is *independent* of the scattering length, while it depends on  $k_F R^*$ . As we will see below, the TBM describes the impurity behavior also beyond the two-body timescale since higher order correlations and multiple particle-hole excitations take longer to build up. Indeed, for a mobile impurity and for sufficiently weak attraction  $X \equiv -1/k_F a \gtrsim 0.6$  [Koh12] where the attractive polaron, and not a molecular state, is the ground state, the TBM correctly describes the long-time behavior  $S(t) \rightarrow |\alpha_0|^2 e^{-i\varepsilon_p t/\hbar}$ . Here,  $|\alpha_0|^2$  is the polaron residue (squared overlap with the non-interacting state) and  $\varepsilon_p$  is the polaron energy, which are both accurately determined using a wave function of the form (4.8) [Vli13].

With the TBM we consider zero temperature in order to isolate the quantum dynamics of the impurity. To better model the experiment, in principle one can extend the TBM to finite temperature by taking the initial state to be a statistical thermal distribution involving multiple impurity momenta. However, a more convenient approach at finite temperature is described in the next section.

#### 4.6.1.3 Functional Determinant Approach

At times  $t$  substantially exceeding  $\tau_F$ , the full description of the impurity dynamics requires the inclusion of multiple particle-hole pair excitations as well as the effect of

<sup>1</sup>In Preparation, M.M. Parish and J. Levinsen (2016)

finite temperature, both of which present a theoretical challenge. In order to study and describe both effects, we employ the Functional Determinant Approach (FDA) [Lev96, Lev93, Kli03, Kna12].

In the FDA the impurity is treated as an infinitely heavy object. In this limit, the FDA provides an exact solution of the dynamical many-body problem at arbitrary temperatures and times. The justification of the infinite mass approximation, which will be discussed in more detail in Section 4.6.4, is rooted in two observations. First, in our experiment, the mass of the K impurities is much larger than that of the Li atoms (mass ratio  $m_K/m_{\text{Li}} \approx 6.7$ ) which constitute the surrounding Fermi gas. Therefore, the recoil energy gained by the K impurities due to the scattering with a Li atom is small. We estimate the typical recoil momentum  $k_R$  by averaging over all possible scattering processes on the Fermi surface, yielding  $k_R = 4k_F/3$ . From that we obtain an estimate for the typical recoil energy  $E_R = \frac{16}{9} \frac{m_{\text{Li}}}{m_K} \epsilon_F \approx 0.25\epsilon_F$ , which determines a typical time scale  $\tau_R = \hbar/E_R \approx 4\tau_F$ , up to which one expects recoil to have a minimal effect on the many-body quantum dynamics, cf. Section 4.6.4.2. Second, at times exceeding the thermal time scale  $\tau_T = \hbar/(k_B T)$ , which in our experiment is given by  $\tau_T \approx 6\tau_F$ , thermal effects due to the averaging over various statistical realizations become relevant. The resulting thermal fluctuations disrupt the coherent quantum propagation of the impurity, and hence, for times  $t > \tau_T$ , mask the effect of recoil [Ros99].

To a good approximation, we may thus take the limit of infinite impurity mass, which admits the mapping of Eq. (4.1) onto the bilinear Hamiltonian

$$\hat{H} = \epsilon_M(B)\hat{m}^\dagger\hat{m} + \sum_{\mathbf{k}} \epsilon_{\mathbf{k}}\hat{c}_{\mathbf{k}}^\dagger\hat{c}_{\mathbf{k}} + g \sum_{\mathbf{k}} \chi(\mathbf{k})[\hat{m}^\dagger\hat{c}_{\mathbf{k}} + \hat{m}\hat{c}_{\mathbf{k}}^\dagger]. \quad (4.12)$$

Here,  $\hat{m}^\dagger$  is the creation operator of the localized closed channel molecule and the interaction is described by the annihilation of a Li atom converting the empty impurity molecular state into an occupied one. By taking the limit  $m_K \rightarrow \infty$  we obtain a modified reduced mass  $\mu'_{\text{red}} = m_{\text{Li}}$ , which differs by a factor of 40/46 from the experimental one. This needs to be taken into account when identifying the microscopic parameters. To ensure, in particular, that the off-diagonal coupling  $g$  in Eq. (4.12) remains of the same strength as in the experiment, a reduced resonance parameter  $R'^* = (40/46)^2 R^*$  has been used, which we do for all data shown in the main text. Using these identifications, the model Eq. (4.12) also accurately describes the short-time dynamics as given by Eq. (4.11), cf. Fig. 4.2 in the main text.

The calculation of time-resolved, many-body expectation values such as Eq. (4.9) at arbitrary temperature presents a theoretical challenge. However, for the model (4.12), we are able to calculate the time-resolved Ramsey response in an exact way using the FDA [Kli03, Kna12]. This is based on the observation that for bilinear Hamiltonians thermal expectation values in the many-body Fock space can be reduced to determinants in the single-particle space by virtue of the identity

$$\text{tr}[\hat{\rho} e^{\hat{Y}_1} e^{\hat{Y}_2} \dots] = \det[1 - \hat{n} + \hat{n} e^{\hat{Y}_1} e^{\hat{Y}_2} \dots]. \quad (4.13)$$

Here  $\hat{Y}_1, \hat{Y}_2, \dots$  are many-body operators,  $\hat{Y}_1, \hat{Y}_2, \dots$  are their single-particle counterparts,  $\hat{\rho}$  is the many-body density matrix describing the state of the system, and  $\hat{n} = 1/[e^{\beta(\hat{H}_0 - \mu)} + 1]$  is the occupation operator defined in the single-particle space,

with  $\mu$  the fermion chemical potential. A specific example for Eq. (4.13) is the perfect quench Ramsey response, which at finite temperature is given by [Kna12]

$$S(t) = \text{tr}[\hat{\rho} e^{i\hat{H}_0 t} e^{-i\hat{H} t}] = \det[1 - \hat{n} + \hat{n} e^{i\hat{H}_0 t} e^{-i\hat{H} t}]. \quad (4.14)$$

Here,  $\hat{H}_0 = \sum_{\mathbf{k}} \epsilon_{\mathbf{k}} \hat{c}_{\mathbf{k}}^\dagger \hat{c}_{\mathbf{k}}$  is the free Hamiltonian of the Li Fermi gas and  $\hat{H}$  is the Hamiltonian in the presence of impurity scattering given in Eq. (4.12), while  $\hat{H}_0$  and  $\hat{H}$  are their single-particle counterparts. A numerical evaluation of Eq. (4.14) then only requires a calculation of the single particle orbitals and energies in order to obtain the single-particle determinant.

## 4.6.2 Experimental and Data Analysis Procedure

In this section we discuss the procedures used to record and analyze the data presented in this work. We detail the cooling and preparation of our atomic samples, the details of the rf pulses used in our Ramsey sequences, the methods used to analyze the data and the method that we use to vary the concentration of the K atoms.

### 4.6.2.1 Sample Preparation

The atomic samples are prepared by forced evaporation of Li atoms from a Li-K mixture held in an optical trap, where the K atoms are sympathetically cooled by the Li environment. This preparation procedure is described in detail in Refs. [Tre11, Spi10]. At the end of the forced evaporation, the Li and K atoms are transferred into an optical trap composed of two crossed 1064-nm laser beams, as described in Ref. [Cet15]. The measured radial and axial trap frequencies of the Li atoms are  $f_{r,\text{Li}} = 941(5)$  Hz and  $f_{z,\text{Li}} = 134(1)$  Hz, respectively. The measured radial and axial trap frequencies of the K atoms are  $f_{r,\text{K}} = 585(3)$  Hz and  $f_{z,\text{K}} = 81(1)$  Hz, respectively.

At the end of the preparation procedure, the Li and the K atoms are in their lowest Zeeman states  $\text{Li}|1\rangle$  and  $\text{K}|1\rangle$ . Before the Ramsey sequence, the K atoms are transferred to the  $\text{K}|2\rangle$  state using an rf pulse. Following this rf transfer, the Li and K atoms are thermalized by holding them for 750 ms in the crossed-beam optical trap. While the interaction between the  $\text{Li}|1\rangle$  and  $\text{K}|2\rangle$  atoms, characterized by the scattering length  $a_{12} = 63a_0$  [Nai11], is sufficient to ensure thermalization during this hold time, it can be neglected during the Ramsey experiments. The temperature of the atoms is determined by releasing the atoms from the trap and observing the free expansion of the K cloud. Due to the Li Fermi pressure and the more than two times stronger optical potential for K, the K cloud is much smaller than the Li cloud [Tre11], and therefore samples a nearly homogeneous Li environment. Because of the small variation of the Li environment sampled by the K atoms, we introduce the effective Li Fermi energy  $\epsilon_F$  as

$$\epsilon_F = \frac{1}{N_K} \int E_F(\mathbf{r}) n_K(\mathbf{r}) d^3\mathbf{r}. \quad (4.15)$$

Figure(s)	$N_{\text{Li}}$ ( $10^5$ )	$N_{\text{K}}$ ( $10^4$ )	$T$ (nK)	$\epsilon_F/h$ (kHz)	$\frac{\sigma(E_F)}{\epsilon_F}$ %	$\bar{n}_{\text{Li}}$ $10^{12}\text{cm}^{-3}$	$\bar{n}_{\text{K}}$ $10^{12}\text{cm}^{-3}$
4.2A, 4.2C, 4.3A	3.5(4)	0.95(10)	435(25)	54.6(2.7)	7.4	8.9(7)	1.8(3)
4.2B, 4.2D, 4.3B	3.3(4)	1.0(1)	410(25)	53.9(2.4)	7.1	8.7(6)	2.0(3)
4.2E, 4.2F, 4.3C	3.5(4)	1.0(1)	460(30)	54.1(2.4)	7.7	8.8(6)	1.7(3)
4.14A	3.1(4)	1.0(1)	430(30)	52.0(2.9)	7.7	8.2(7)	1.8(3)
4.14B	2.9(3)	1.05(10)	425(35)	50.8(2.1)	7.7	8.0(6)	2.0(3)
4.4	2.35(30)	2.5(1)	520(25)	44.2(2.3)	10.4	6.5(5)	3.4(3)

TABLE 4.1: The total number of the Li atoms  $N_{\text{Li}}$ , the total number of the K atoms  $N_{\text{K}}$ , the sample temperature  $T$ , the effective Li Fermi energy  $\epsilon_F$ , the standard deviation  $\sigma(E_F)$  of the local Li Fermi energy across the trap, the trap-averaged Li and K number densities  $\bar{n}_{\text{Li}}$  and  $\bar{n}_{\text{K}}$  in our measurements.

Here,  $n_{\text{K}}(\mathbf{r})$  is the local K number density at position  $\mathbf{r}$  in the trap, and

$$E_F(\mathbf{r}) = \frac{\hbar^2 (6\pi^2 n_{\text{Li}}(\mathbf{r}))^{2/3}}{2m_{\text{Li}}} \quad (4.16)$$

is the local Li Fermi energy as determined by the local Li number density  $n_{\text{Li}}(\mathbf{r})$ . We quantify the small inhomogeneity of the Li environment experienced by the K atoms by the standard deviation of the local Li Fermi energy

$$\sigma(E_F) = \left( \frac{1}{N_{\text{K}}} \int (E_F(\mathbf{r}) - \epsilon_F)^2 n_{\text{K}}(\mathbf{r}) d^3\mathbf{r} \right)^{1/2}. \quad (4.17)$$

We also introduce the average Li and K number densities  $\bar{n}_{\text{Li}}$  and  $\bar{n}_{\text{K}}$  sampled by the K atoms as

$$\bar{n}_{\text{Li,K}} = \frac{1}{N_{\text{K}}} \int n_{\text{Li,K}}(\mathbf{r}) n_{\text{K}}(\mathbf{r}) d^3\mathbf{r}. \quad (4.18)$$

In contrast to the Li atoms, the K atoms in our measurements remain non-degenerate, with  $k_B T / E_F^{\text{K}}(0) > 1.2$ , where  $E_F^{\text{K}}(0)$  is the local potassium Fermi energy in the center of the trap when all K atoms are in the same internal state. For all measurement presented in this work, Table 4.1 lists the total numbers of the Li and K atoms, their temperatures and trap-averaged densities, as well as the effective Li Fermi energies and their standard deviations. Throughout our measurements, these parameters remain nearly constant, with the exception of the measurements shown in Fig. 4.4. Here, in order to investigate the effect of the K concentration, the total number of the K atoms is increased from about  $1 \times 10^4$  to  $2.5 \times 10^4$ . The attendant increase in the thermal load during the Li evaporation results in a decrease of the Li atom number and an increase in the temperature of the final atomic sample.

Note that, in contrast to our previous work [Cet15], our present experiments have been optimized for large optically induced interaction shifts ( $|X - X_1| \approx 5$ ). These shifts are produced by switching one of the crossed trapping beams from a beam with a low peak intensity and small size to a beam with a large intensity and large size propagating in the same direction. In our previous work [Cet15], as well as in the measurements shown in Fig. 4.14, the waists, positions and intensities of the two beams are adjusted so as

to yield mode-matched trapping potentials, preventing excitations of the center-of-mass and breathing collective modes of the atomic clouds. In the measurements presented in Figs. 2, 3 and 4, a larger beam intensity was used in order to produce a larger optical shift, resulting in some excitation of the breathing modes.

The maximal interaction time in our Ramsey measurements of 60  $\mu\text{s}$  is much smaller than the shortest period of a collective oscillation (about 500  $\mu\text{s}$ ). We calculate that, during our short interaction time, the oscillations of the breathing modes cause at most a 6% variation of  $\epsilon_F$  around its initial value specified in Table 4.1, without any significant effect on the measurements presented here.

#### 4.6.2.2 RF pulses

We apply rf pulses in the Ramsey procedures by discretely gating a continuously running rf source. To record the atomic populations  $N_3$  and  $N_2$  as a function of the phase of the second rf pulse, we change the phase of the rf source by a variable amount  $\phi_{\text{rf}}$  before applying this pulse.

The weak interactions between the K atoms in the  $\text{K}|3\rangle$  state and the Li atoms corresponding to the interaction parameter  $X_1$  cause the transition frequency between the  $\text{K}|2\rangle$  and the  $\text{K}|3\rangle$  states to differ from the transition frequency  $\omega_0$  in the absence of the Li atoms. We compensate for this effect by adjusting the frequency  $\omega_{\text{rf}}$  of the rf source to be resonant with the  $\text{K}|2\rangle$ - $\text{K}|3\rangle$  transition at the time when the rf pulses are applied. For the data in Figs. 2A, 2B, 2C,  $(\omega_{\text{rf}} - \omega_0)\tau_F$  is equal to +0.06, -0.07, -0.05, respectively. For the data in Fig. 4.14C and 4.14D where the interaction of the K atoms during the rf pulses is stronger,  $(\omega_{\text{rf}} - \omega_0)\tau_F$  is equal to +0.11 and -0.16.

The shift in the frequency of the rf source from  $\omega_0$  to  $\omega_{\text{rf}}$  causes the signal  $S(t)$  to accumulate an additional phase  $(\omega_{\text{rf}} - \omega_0)t$  during the interaction time  $t$ . To account for this added phase, we introduce the phase  $\phi = \phi_{\text{rf}} + (\omega_{\text{rf}} - \omega_0)t$ .

#### 4.6.2.3 Analysis Methods

We determine the contrast  $|S(t)|$  and the phase  $\varphi(t)$  by fitting the Ramsey signal  $(N_3 - N_2)/(N_3 + N_2)$  as a function of the phase  $\phi$  to a sine wave with an offset i.e.  $F(t) + |S(t)| \cos(\phi - \varphi(t))$ . Decoherence during the rf pulses, as well as imperfections of the rf pulses and the atom detection, cause the contrast for  $t = 0$  to be slightly smaller than unity. When comparing theoretical results from Figs. 4.12 and 4.13 to the experimental data in Fig. 2, we account for this effect by scaling the theoretical predictions for  $|S(t)|$  by an overall factor  $\eta$ . For each calculation, this factor is determined by fitting the prediction for  $|S(t)|$  to the three data points with the the shortest interaction times. We obtain  $0.92 < \eta < 1$ , which corresponds to an additional loss of contrast that is of the same order as the decoherence during the rf pulses predicted by the FDA (see Fig. 4.13).

To compute the Fourier transform of the experimental  $S(t)$  data, we use piecewise linear interpolations of  $\log S(t)$  and  $\varphi(t)$  between the individual data points. Outside of the range of the data, we set  $S(t) = 0$ . To determine the error of the Fourier transform,

we sample the values of  $S(t)$  and  $\varphi(t)$  at each data point from Gaussian distributions whose means and standard deviations correspond to the measured values and errors, respectively. We use the standard deviation of the computed values of the Fourier transform for each value of  $\omega$  as an estimate of the error indicated by the shaded areas in Figs. 3 and 4.14.

#### 4.6.2.4 Varying the K concentration

We study the effects of the impurity concentration by varying the number of the strongly interacting K atoms. If this were done by changing the total number of the K atoms in the experiment, the change in the thermal load on the Li atoms during forced evaporation would result in a correlated variation in the number of Li atoms and the sample temperature (compare the settings for Fig. 2 and Fig. 4 in Table 4.1). To avoid these systematic effects, in the measurements presented in Fig. 4, we keep the total number of the K atoms constant and vary the fraction of the K atoms that participate in the Ramsey sequence. We accomplish this by changing the intensity of the rf pulse that transfers the K atoms from the  $|1\rangle$  state to the  $|2\rangle$  state before the Ramsey procedure. During the subsequent 750 ms preceding the Ramsey sequence, the K atoms collisionally thermalize with the much larger Li cloud, resulting in an incoherent mixture of  $K|1\rangle$  and  $K|2\rangle$  atoms at a constant temperature. When referring to these measurements, we use  $\bar{n}_K$  not for the average density of all K atoms, but for the density of those K atoms that participate in the Ramsey sequence.

We minimized the small effects of long-time drifts in the temperature, the atom numbers and the trapping potential by varying the experimental parameters in a specific order. For each K concentration and interaction time, we recorded data for 4 different phases of the second rf pulse in order to obtain  $S(t)$ . For each interaction time, the data with different K concentrations were recorded in immediate succession. The data sets for different interaction times were then recorded in a random order.

#### 4.6.3 Linearity of RF response

The response of atoms to an applied rf field is linear if the fraction of the atoms transferred from one state to another is proportional to the intensity of the field. Linearity can be ensured by using a sufficiently weak rf pulse that is also much longer than the inverse width of the relevant spectral features. The narrowest spectral features in the present work are the polaron peaks in Figs. 3A and 3B with rms widths  $0.06 \hbar/\tau_F$  and  $0.09 \hbar/\tau_F$ , respectively. To record these polaron spectra, we used Blackman-shaped rf pulses [Kas92] whose duration  $t_{\text{rf}} = 300 \mu\text{s} \approx 100 \tau_F$  is much longer than the inverse widths of the polaron peaks. We checked the linearity of the response by varying the intensity  $I_{\text{rf}}$  of the applied rf field. Fig. 4.5A shows the fraction of the K atoms transferred from the  $K|2\rangle$  to the  $K|3\rangle$  state in the repulsive polaron regime, under conditions similar to those in the measurements shown in Fig. 3A. The frequency of the rf pulse is adjusted so that  $(\omega_{\text{rf}} - \omega_0)\tau_F = 0.3$ , corresponding to peak response and resonant

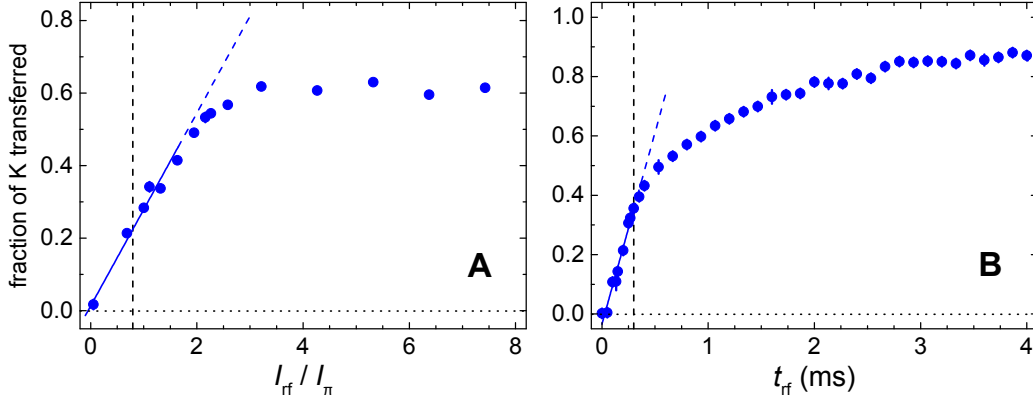


FIGURE 4.5: **Linearity of the rf response in the repulsive polaron regime.** (A) Fraction of the K atoms transferred from state  $K|2\rangle$  to the state  $K|3\rangle$  for  $X = -0.13(6)$  as a function of the intensity  $I_{\text{rf}}$  of an rf pulse with duration  $t_{\text{rf}} = 300 \mu\text{s}$ . (B) Fraction of the K atoms transferred for  $X = -0.23(6)$  as a function of the duration  $t_{\text{rf}}$  of the rf pulse for the rf pulse intensity  $I_{\text{rf}} = 0.79 I_{\pi}$ . Vertical dashed lines correspond to  $I_{\text{rf}} = 0.79 I_{\pi}$  and  $t_{\text{rf}} = 300 \mu\text{s}$ , respectively. The pulse frequencies are adjusted to resonantly excite the repulsive polaron. The blue solid lines indicate linear fits to the data in the ranges indicated by the same lines. The blue dashed lines show extrapolations of these fits.

excitation of the repulsive polaron. The rf intensity is measured in units of the intensity  $I_{\pi}$  that results in a  $\pi$ -pulse for noninteracting K atoms. For intensities up to the intensity  $I_{\text{rf}} = 0.79 I_{\pi}$ , which is used in the measurements shown in Figs. 3A and 3B, we observe that the transferred fraction of the K atoms stays essentially proportional to the intensity of the pulse.

In the linear-response regime, the atomic response is predicted to be proportional to the duration of the rf pulse. Fig. 4.5B shows the fraction of the K atoms transferred in the repulsive polaron regime by rf pulses with  $I_{\text{rf}} = 0.79 I_{\pi}$ , as a function of the pulse duration. The frequency of the rf pulse is adjusted so that  $(\omega_{\text{rf}} - \omega_0)\tau_F = 0.3$ , in order to obtain the peak response, as in Fig 4.5A. For pulses with duration up to  $300 \mu\text{s}$  (indicated by the dashed line), we observe that the transferred fraction of the K atoms stays essentially proportional to the duration of the pulse.

Note that the maximal transferred fraction exceeds 0.5. We explain this observation by the coupling of the initial non-interacting K state to multiple interacting K states by the rf pulse, which manifest themselves as the polaron peak and the broad pedestal in our spectra.

The spectra for resonant Li-K interactions shown in Figs. 3B, 4.14A, 4.14B were recorded using Blackman-shaped rf pulses with duration of  $t_{\text{rf}} = 100 \mu\text{s}$  (approximately  $35 \tau_F$ ). The intensity of these pulses was adjusted to 50% of that needed to produce  $\pi$  pulses for noninteracting K atoms. We verified the linearity of the rf response by comparing the spectra recorded using this rf intensity to those recorded using the intensity needed to produce full  $\pi$  pulses for noninteracting K atoms (Fig. 4.6). Our observations are in good agreement with linear response.

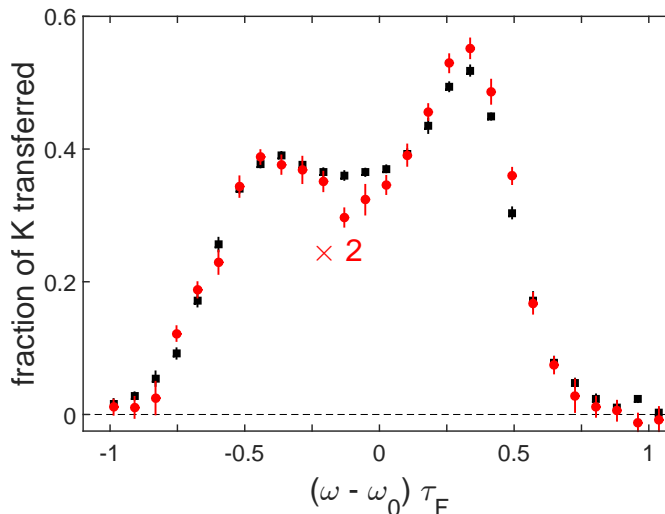


FIGURE 4.6: **Linearity of the rf response for resonant interactions.** Fraction of the K atoms transferred from state  $K|2\rangle$  to the state  $K|3\rangle$  by an rf pulse with duration  $t_{\text{rf}} = 100 \mu\text{s}$  for  $X = +0.02(6)$ . For the black data points, the intensity of the rf pulse is adjusted to obtain a  $\pi$ -pulse in the absence of Li atoms. The red data points correspond to a 50% lower intensity of the rf field.

## SUPPLEMENTARY TEXT

### 4.6.4 Role of Physical Processes on Different Timescales

The combination of both our theoretical approaches allows us to accurately model the physics at various time scales in our experiment. Making use of the fact that the FDA and the TBM differ distinctly in their treatment of multiple particle-hole excitations, the impurity mass, and finite temperature, we can use a comparison of their predictions to determine the role of these processes and effects in the many-body non-equilibrium dynamics of our experiment. We also discuss the role of two-body physics in the initial time evolution. To keep the analysis transparent, in this section we still assume that a perfect quench is performed.

#### 4.6.4.1 Multiple Particle-Hole Excitations

In order to analyze the role of multiple particle-hole excitations, we first consider the limit of a fixed (infinitely heavy) impurity at zero temperature. In this scenario, the FDA yields the exact solution of the impurity problem. Since, in this case, the TBM only differs from the FDA by its neglect of multiple particle-hole excitations, a comparison of the predictions of the two methods allows us to isolate the effect of these excitations. In Fig. 4.7 we display the predictions for the Ramsey response using the two theoretical approaches. We find that both theoretical predictions agree extremely well at short times. In particular, for both the amplitude and phase of  $S(t)$ , our results imply that multiple particle-hole excitations start to influence our observables at a time scale of around  $6\tau_F$ , and only become prominent beyond  $10\tau_F$ . Thus, at shorter time scales,

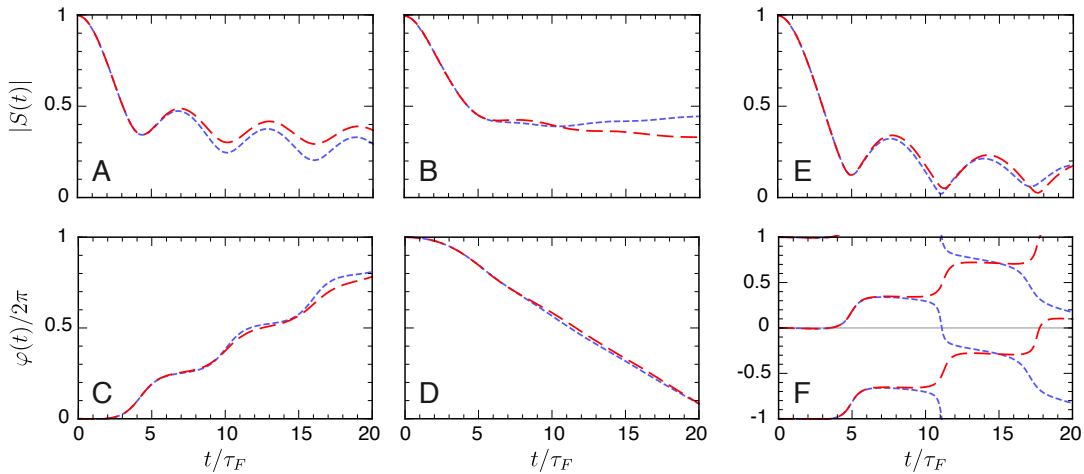


FIGURE 4.7: **Effect of multiple particle-hole fluctuations.** Taking the idealizing limit of zero temperature and infinite impurity mass, we compare the Ramsey response for a perfect quench (top: amplitude, bottom: phase) obtained exactly with the FDA (red, long dashed) to the one obtained with TBM (blue, short dashed) for (A, C)  $X = -0.23$ , (B, D)  $X = 0.86$ , and (E, F)  $X = 0.08$ . For this comparison, we take  $r_0 = 0$  and  $k_F R^* = 1.1(40/46)^2$ .

multiple particle-hole excitations can be neglected when predicting the results of the Ramsey measurements.

We note that the fixed impurity scenario is a worst-case scenario for the TBM: At  $T = 0$ , the infinitely heavy impurity is subject to the orthogonality catastrophe with an associated power-law decay of the Ramsey contrast at long times [And67]. This decay, which arises due to an infinite number of particle-hole fluctuations and which leads to a vanishing quasiparticle weight, is exactly incorporated in the FDA. By contrast, in the long-time limit, the TBM predicts the saturation of  $|S(t)|$  to a constant value (see Fig. 4.7), corresponding to a spurious finite residue. However, for a *mobile* impurity at zero temperature, recoil becomes relevant. These recoil effects lead to the absence of the orthogonality catastrophe [Ros99], and thus to an increased accuracy of the TBM in the case of finite impurity mass.

Generally, one expects that the relevant time scale for multiple particle-hole excitations is closely related to the Fermi time  $\tau_F$ . As discussed above, we find that such excitations become relevant for a description of  $S(t)$  only at around  $6\tau_F$  or beyond. This observation can be understood in a twofold way. First, in the equilibrium case it was found that contact interactions in the Fermi polaron problem lead to an approximate cancellation of terms involving identical fermions, thus suppressing the emergence of multiple particle-hole fluctuations [Com08]. Our observation may hence be interpreted as a generalization of these findings to the non-equilibrium case. Second, the spectrum of the Fermi polaron problem features a dominant contribution involving the excitation of fermions from the bottom of the Fermi sea to the Fermi surface [Kna12]. As discussed in Ref. [Kna12], these excitations manifest themselves as oscillations with period  $2\pi\tau_F$  in the Ramsey contrast  $|S(t)|$ . Such a bottom of the band excitation is also present in the truncated wavefunction (4.8), and indeed the remarkable agreement of the TBM with the exact

solution from the FDA up to the time  $2\pi\tau_F$  suggests that this effect can be captured by single-particle hole excitations.

#### 4.6.4.2 Impurity Mass

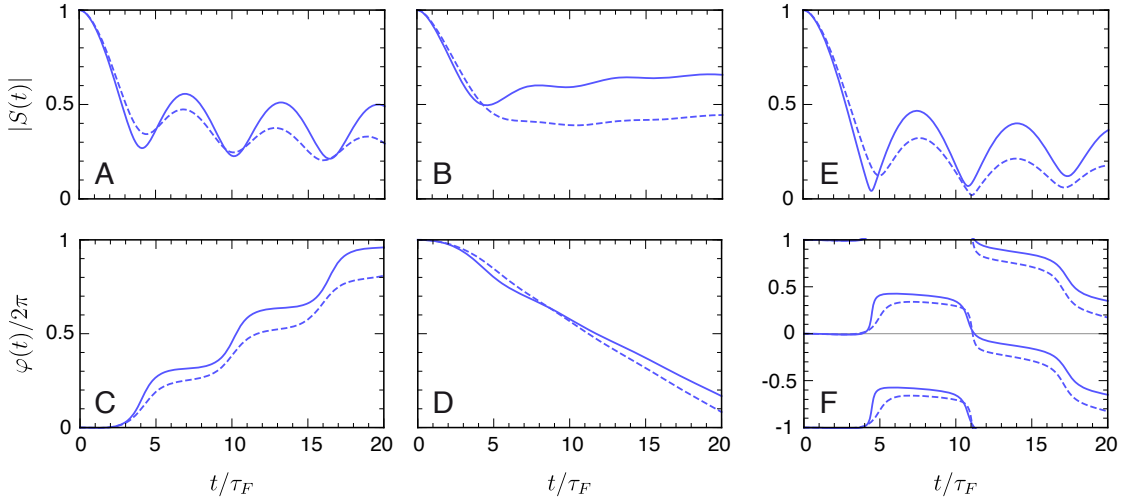


FIGURE 4.8: **Effect of the impurity motion on the short-time dynamics.** Amplitude (top) and phase (bottom) of the perfect quench zero temperature Ramsey response  $S(t)$  as a function of time for (A, C)  $X = -0.23$ , (B, D)  $X = 0.86$ , and (E, F)  $X = 0.08$ . We compare the results of the TBM obtained for  $m_K = (40/6)m_{\text{Li}}$  and  $k_F R^* = 1.1$  (solid) with the TBM results for fixed impurities  $m_K \rightarrow \infty$  and  $k_F R^* = 1.1(40/46)^2$  (dashed).

As discussed in the main text, our experimental findings are well described by the static impurity approximation, although the impurity has finite mass. To quantify the effect of the finite impurity mass, we study here the case of zero temperature. This allows us to isolate the effect of finite impurity recoil from the influence of thermal fluctuations, which will become dominant beyond times  $\tau_T \approx 6\tau_F$ , as discussed in the section below. In order to estimate at which time scale recoil becomes important, we make use of the capability of the TBM to describe impurities of arbitrary mass. Furthermore, our analysis in Sec. 4.6.4.1 shows that the TBM yields highly accurate results for the short-time dynamics of  $S(t)$ . Accordingly, in Fig. 4.8 we display the Ramsey response for a static impurity and for the experimentally relevant impurity mass, both calculated within the TBM. We see that for both amplitude and phase, the impurity motion only results in a small difference in the Ramsey signal at times  $t \lesssim 4\tau_F$ . Physically, this time scale corresponds to the effective recoil time  $\tau_R$  associated with Li collisions on K atoms, which we estimated in Sec. 4.6.1.3 to be  $\tau_R \approx 4\tau_F$ , in agreement with our findings here. At times exceeding  $\tau_R$ , we find that the dynamics is indeed affected by the finite impurity mass. However, at such times, thermal fluctuations dominate the behavior in experiment, as we now discuss.

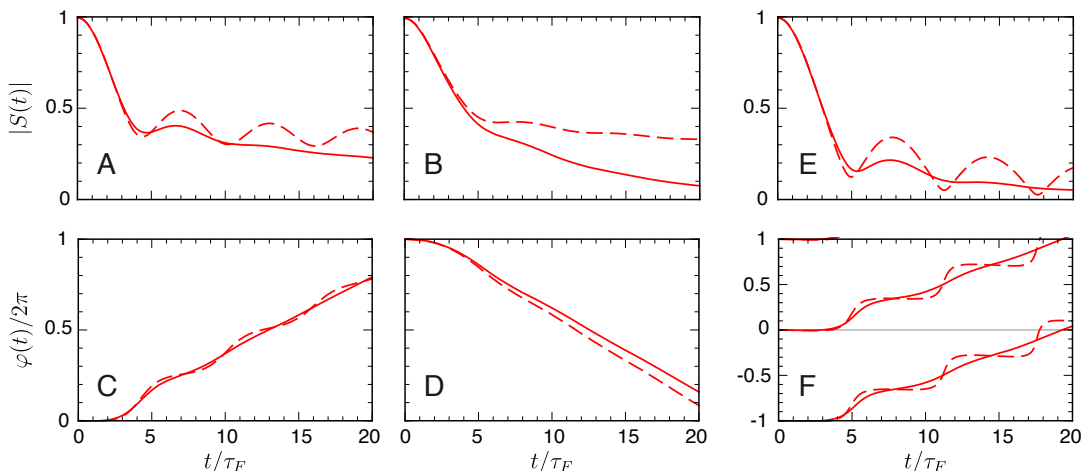


FIGURE 4.9: **Effect of finite temperature on the impurity dynamics.** We compare the Ramsey signal (upper panels: amplitude, lower panels: phase) for an infinitely heavy impurity obtained from an exact FDA calculation at zero (long dashed) and finite temperature (solid curves). The ordering of the graphs is as in the main text: (A, C)  $X = -0.23$ ,  $T/T_F = 0.17$ , (B, D)  $X = 0.86$ ,  $T/T_F = 0.16$ , and (E, F)  $X = 0.08$ ,  $T/T_F = 0.18$ . We assume a perfect quench and choose  $r_0 = 0$  as well as  $k_F R^* = 1.1$ , i.e.,  $k_F R'^* = 1.1(40/46)^2$ .

#### 4.6.4.3 Temperature

At long times, the time evolution reduces to a simple exponential decoherence of  $S(t)$ . The time scale at which this crossover to exponential decay takes place is given by the thermal time scale  $\tau_T$ . In our experiment, where  $T/T_F \approx 0.15$ , this corresponds to  $\tau_T \approx 6\tau_F$  and, hence, we observe both regimes within the dynamical range probed in our experiment.

In this section, we use finite-temperature FDA calculations to gauge the role of temperature in the impurity dynamics. To this end we compare the results for the Ramsey signal at zero and finite temperature for the experimentally realized parameters. The results are shown in Fig. 4.9. We indeed find that at times  $\sim 6\tau_F$  the time evolution at finite temperature starts to deviate from the purely quantum behavior. Finite temperature leads to an exponential decoherence of the Ramsey signal and has the consequence that thermal fluctuations dominate over the impurity motion at times  $t \gtrsim 6\tau_F$  [Ros99]. Hence they mask the effect of impurity recoil as discussed in Sec. 4.6.1.3.

Overall, the conditions in our experiment give rise to three competing time scales. Multiple particle hole excitations become relevant for our measurement of  $S(t)$  at around  $6\tau_F$ , the recoil time is  $\tau_R \approx 4\tau_F$ , and the thermal scale is set by  $\tau_T \approx 6\tau_F$ . A comparison of these scales reveals the reason for the remarkable agreement between the FDA and experiment: Recoil is only weakly probed at short times  $t < \tau_R$ , while its effect is washed out by the thermal fluctuations at long times  $t > \tau_T \approx \tau_R$ .

#### 4.6.4.4 Two-Body Physics in the Initial Time Evolution

At short times  $t \ll \tau_F$ , the response is dominated by two-body scattering processes, while the fast collective many-body dynamics, which is the focus of this work, only sets in for  $t \gtrsim \tau_F$ . As discussed in Sec. 4.6.1.1, two-body scattering in the current experiment is well described by the low energy expansion of the scattering amplitude, i.e.,  $1/f(k) \approx -a^{-1} + \frac{1}{2}r_{\text{eff}}k^2 - ik$ . Hence, our system is universally governed by the two parameters, scattering length  $a$  and effective range  $r_{\text{eff}}$ .

The effective range is a function of the van der Waals length  $l_{\text{vdw}}$  and the range parameter  $R^*$ , which characterizes the strength of the Feshbach resonance, cf. Eq. (4.5) [Chi10]. For our system, the van der Waals length is given by  $l_{\text{vdw}} = 40.8 a_0$ . This corresponds to time scales short compared to the ones we study in this work, and hence  $l_{\text{vdw}}$  is irrelevant for our considerations here. However, the range parameter  $R^*$  requires a more careful consideration. Our experiment is performed in the vicinity of a closed-channel dominated resonance which is characterized by  $R^*/l_{\text{vdw}} \gg 1$ . Therefore, the effective range is dominated by the parameter  $R^*$ .

In the previous section, we have shown that at times  $t \ll \tau_F$ ,  $1 - S(t) \propto t^2$  with a prefactor which depends on  $R^*$ , but is *independent* of the scattering length<sup>2</sup>, see Eq. (4.11). Here we demonstrate this fact in more detail by studying numerically the short-time evolution of our system. At  $t \ll \tau_F$ , neither temperature nor multiple particle hole excitations play a role. Hence TBM becomes an essentially exact theory. In Fig. 4.10, we display  $\sqrt{1 - |S(t)|}$  evaluated within the TBM for different values of  $k_F R^*$  and scattering lengths  $a$ . We see that at short times the prediction, Eq. (4.11), is indeed satisfied with  $S(t)$  being independent of the scattering length and being solely dependent on  $R^*$ . This clearly demonstrates that the initial Ramsey response depends solely on the short-distance behavior, determined by the scale  $k_F R^*$ .

However, once  $t \gtrsim \tau_F$ , the response is governed by many-body physics. The predicted short-time evolution is challenging to probe in experiment since it requires a high density of data for  $t < \tau_F$  and no interactions in the initial state. Furthermore, in practice, the applied rf pulses introduce weak interactions into the system, and thus modify the response, as we discuss in the following section.

#### 4.6.5 Role of Interaction During Finite-Length RF Pulse

In this section, we analyze the role of the ‘imperfect’ interaction quench in our experiments, where residual interactions are present during the rf pulses. Furthermore, we discuss how our findings pave the way towards the use of our experimental techniques to exert control over many-body states in real time.

<sup>2</sup>In Preparation, M.M. Parish and J. Levinsen (2016)

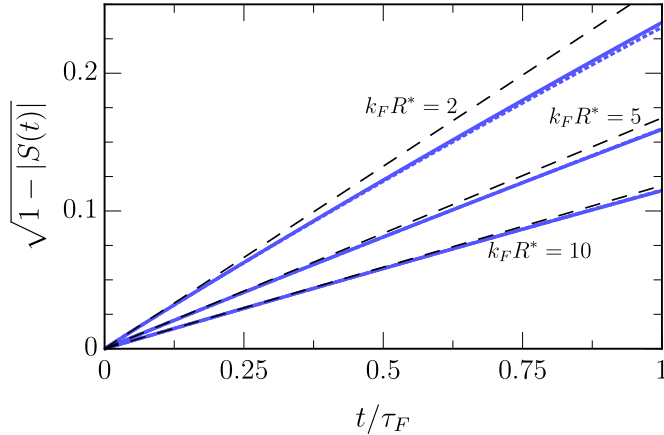


FIGURE 4.10: **Short time evolution of  $S(t)$ .** We show the results obtained using the TBM at  $T = 0$  at scattering length  $X = 0.86$  (thick dotted),  $X = 0.08$  (thick dashed), and  $X = -0.23$  (thick solid) for different choices of  $k_F R^*$ . Note, the results for the various interaction strength  $X$  are almost identical, since at short times they are independent of  $X$ , as predicted by Eq. (4.11) (thin dashed black line). For all results shown we assume a perfect Ramsey sequence.

#### 4.6.5.1 Idealized Versus Realized Ramsey Scenario

Thus far, we have assumed the idealized scenario of a perfect two-pulse Ramsey scheme. In this case, the initial spin state of the impurity ( $|K|2\rangle$  in the experiment) is non-interacting with the Li Fermi sea and there are no interactions during the applied rf  $\pi/2$  pulses. Each pulse then yields a perfect rotation on the Bloch sphere, e.g., the initial state  $|K|2\rangle$  is transformed into the spin-state superposition  $(|K|2\rangle + |K|3\rangle)/\sqrt{2}$ . For such a perfect Ramsey sequence, the measured Ramsey signal  $S(t)$  gives the overlap between the time-evolved interacting and non-interacting states of the system [Goo11, Kna12], yielding Eqs. (4.9) and (4.14) for zero and finite temperature, respectively. In this idealized scenario, the Fourier transform of  $S(t)$  corresponds to the excitation spectrum of the system in linear response [Mah90],

$$A(\omega) = \text{Re} \int_0^\infty \frac{dt}{\pi} e^{i\omega t} S(t), \quad (4.19)$$

where  $\omega$  is the detuning of the frequency of the applied rf field from the unperturbed transition frequency.

In our experiments, however, residual interactions are present during the  $\pi/2$  pulses, which take a finite time to be completed. As shown in the illustration of our experimental sequence in Fig. 4.11, the state  $|K|3\rangle$  can already interact with the Li cloud during the  $\pi/2$  rotation, which potentially affects the observed dynamics of the system. Specifically, this stage of the experiment is performed at a detuning from the Feshbach resonance which corresponds to a weak interaction strength  $X_1$  between the impurities and the Fermi sea (cf. Section 4.6.5.2 and Fig. 4.11). After preparing the superposition state of the impurity spin, we quench the system to strong interactions (interaction parameter  $X$ ) by optically shifting the Feshbach resonance [Cet15]. We previously focussed on the complex non-equilibrium dynamics resulting from the strong interactions  $X$  during the time  $t$ . In the following, we analyze the effect of the residual interaction  $X_1$  during the

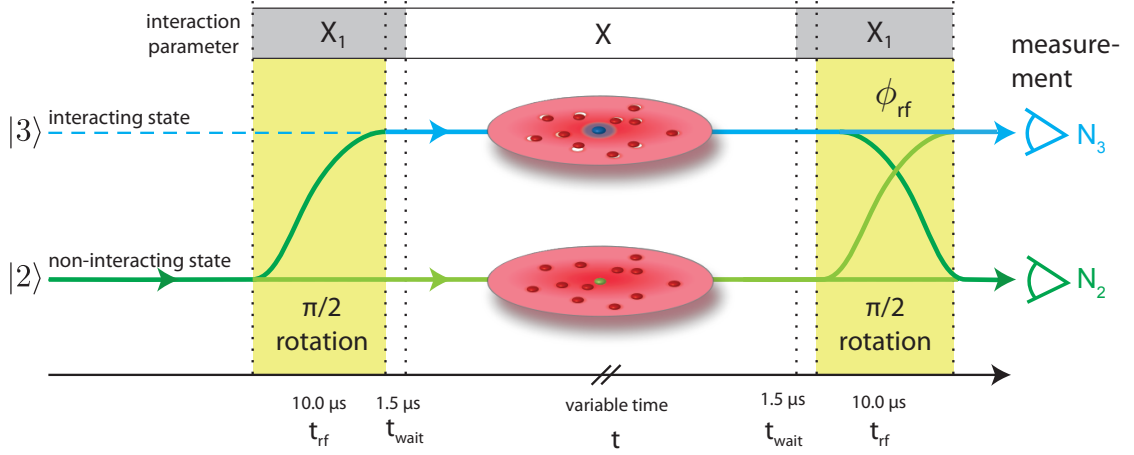


FIGURE 4.11: **Schematic of the experimental Ramsey procedure.** The K atoms start out in the hyperfine state  $K|2\rangle$ , which is effectively non-interacting with the Fermi sea. A  $10\ \mu\text{s}$  ( $3.4\ \tau_F$ ) long square  $\pi/2$  pulse is applied in the presence of weak interactions between the  $K|3\rangle$  atoms and the Li atoms, quantified by the interaction parameter  $X_1$ . We then use optical control of our Feshbach resonance to rapidly (in less than 200 ns ( $0.08\ \tau_F$ )) quench the system into the strongly interacting regime (interaction parameter  $X$ ). After a variable interaction time  $t$  we optically shift the interaction strength back to  $X_1$ , and then close the Ramsey sequence by a second  $\pi/2$  pulse. We vary the phase of this pulse by shifting the phase of the rf source by  $\phi_{\text{rf}}$  before the second pulse is applied.

finite-duration  $\pi/2$  spin rotations. In particular, we investigate the impact of these weak interactions during the rf pulses on the Ramsey response  $S(t)$  and the spectrum  $A(\omega)$  as obtained from the Fourier transform Eq. (4.19).

#### 4.6.5.2 Modelling of RF Pulses within TBM

In this section, we extend our modelling of the zero-temperature impurity dynamics within the TBM to directly simulate the entire experimental procedure, as illustrated in Fig. 4.11. In order to model the rf pulses, we explicitly include both  $K|2\rangle$  and  $K|3\rangle$  spin states, as well as the rf field. This modifies the Hamiltonian, Eq. (4.1), to  $\hat{\mathcal{H}} = \hat{H} + \hat{H}_{\text{rf}}$  with the additional term

$$\hat{H}_{\text{rf}} = \frac{\Omega}{2i} \sum_{\mathbf{k}} \left( e^{i\phi_{\text{rf}}} \hat{d}_{\mathbf{k},2}^\dagger \hat{d}_{\mathbf{k},3} - e^{-i\phi_{\text{rf}}} \hat{d}_{\mathbf{k},3}^\dagger \hat{d}_{\mathbf{k},2} \right) + \sum_{\mathbf{k}} (\epsilon_{\mathbf{k},K} + \hbar(\omega_{\text{rf}} - \omega_0)) \hat{d}_{\mathbf{k},2}^\dagger \hat{d}_{\mathbf{k},2}. \quad (4.20)$$

Here, we have used the rotating wave approximation.  $\Omega$  corresponds to the strength of the rf field,  $\phi_{\text{rf}}$  is the variable phase of the second rf pulse, and  $\hat{d}_{\mathbf{k},\sigma}^\dagger$  creates a particle in the state  $K|\sigma\rangle$  with momentum  $\hbar\mathbf{k}$ . Note that  $\hat{d}_{\mathbf{k}}^\dagger \equiv \hat{d}_{\mathbf{k},3}^\dagger$  in the original two-channel Hamiltonian (4.1). The interactions during the rf pulses cause a shift in the transition frequency between the  $K|2\rangle$  and  $K|3\rangle$  states from the bare transition frequency  $\omega_0$  to  $\omega_0 + \varepsilon_1/\hbar$ , where  $\varepsilon_1$  is the polaron energy at interaction parameter  $X_1$ . As described in Sec. S5.B, we account for this shift by adjusting the frequency of our rf pulses to  $\omega_{\text{rf}} = \omega_0 + \varepsilon_1/\hbar$ .

According to the last term in Eq. (4.20), the shift in the frequency of the rf source

from  $\omega_0$  to  $\omega_{\text{rf}}$  causes the observed signal to accumulate an additional phase  $(\omega_{\text{rf}} - \omega_0)t$  during the interaction time  $t$ . To account for this, we introduce the phase  $\phi = \phi_{\text{rf}} + (\omega_{\text{rf}} - \omega_0)t$ . We then determine  $|S(t)|$  and the phase  $\varphi(t)$  by noting that the Ramsey signal  $(N_3 - N_2)/(N_3 + N_2)$  corresponds to a sine-wave function of  $\phi$  plus an offset, i.e., it takes the form  $F(t) + |S(t)| \cos(\phi - \varphi(t))$  with  $F(t)$  a real,  $\phi$ -independent function. This mirrors the experimental procedure, where  $F(t)$ ,  $|S(t)|$ , and  $\varphi(t)$  appear as fit-parameters for the Ramsey signal, see Sec. S5.B. Within the TBM, we determine the

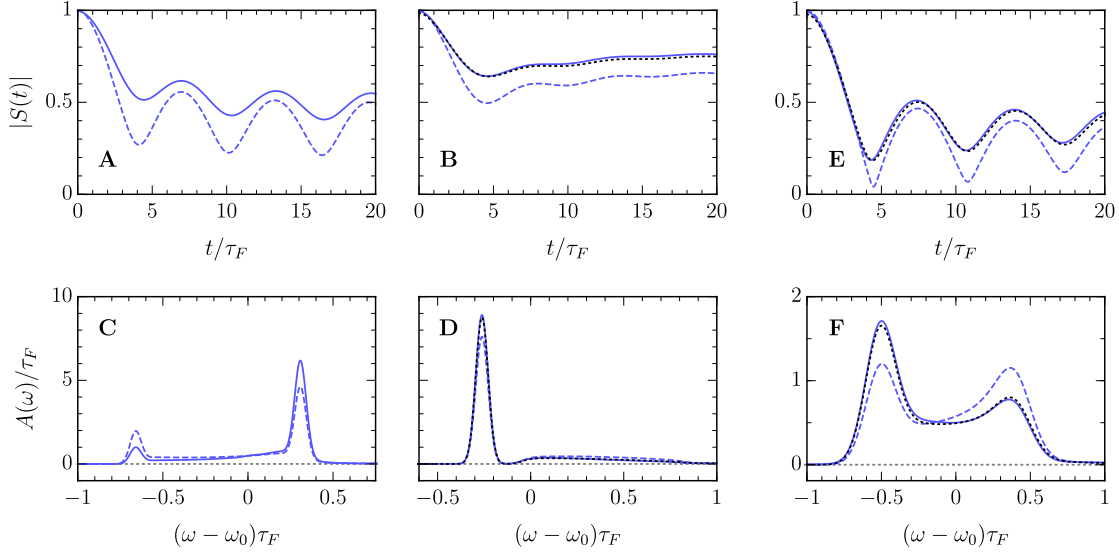


FIGURE 4.12: **Role of the residual interactions within TBM.** We present the zero-temperature response  $S(t)$  and the corresponding spectrum  $A(\omega)$  for the perfect quench (dashed blue) and the actual experimental sequence shown in Fig. 4.11 (solid blue). As in the main text, we take  $k_F R^* = 1.1$  and the interaction parameters: (**A**, **C**)  $X = -0.23$ ,  $X_1 = -3.9$ , (**B**, **D**)  $X = 0.86$ ,  $X_1 = 5.8$ , and (**E**, **F**)  $X = 0.08$ ,  $X_1 = 4.8$ . For comparison, in (**B**, **D**, **E**, **F**), we represent by black dotted lines the scenario where the initial state before the quench is approximated as a weakly attractive polaron — see Sec. 4.6.5.2 for details. The spectra have been convolved with the experimental Fourier-limited rf spectral lineshapes, which are Gaussian-shaped with width  $\sigma$ , where  $\sigma\tau_F = 0.03$  for  $X = 0.86$ ,  $-0.23$ , and  $\sigma\tau_F = 0.1$  for  $X = 0.08$ .

approximate eigenstates and eigenvalues of  $\hat{\mathcal{H}}$  within the more general class of truncated wavefunctions:

$$|\psi_{\text{rf}}\rangle = \left( \alpha_{0,3} \hat{d}_{0,3}^\dagger + \alpha_{0,2} \hat{d}_{0,2}^\dagger \right) |\text{FS}\rangle + \sum_{\mathbf{q}} \alpha_{\mathbf{q}} \hat{b}_{\mathbf{q}}^\dagger \hat{c}_{\mathbf{q}} |\text{FS}\rangle + \sum_{\mathbf{k}\mathbf{q}} \left( \alpha_{\mathbf{k}\mathbf{q},3} \hat{d}_{\mathbf{q}-\mathbf{k},3}^\dagger \hat{c}_{\mathbf{k}}^\dagger \hat{c}_{\mathbf{q}} + \alpha_{\mathbf{k}\mathbf{q},2} \hat{d}_{\mathbf{q}-\mathbf{k},2}^\dagger \hat{c}_{\mathbf{k}}^\dagger \hat{c}_{\mathbf{q}} \right) |\text{FS}\rangle.$$

To model the experimental quench sequence illustrated in Fig. 4.11, we apply a series of time evolution operators to the initial state consisting of a  $\text{K}|2\rangle$  atom and the Li Fermi sea. At the end of the sequence we then extract the number of  $\text{K}$  atoms in states  $\text{K}|2\rangle$  and  $\text{K}|3\rangle$ , respectively. We include explicitly the rf pulses, the wait times, and the interaction time  $t$  during which the system is strongly interacting. The results of this procedure are displayed in Fig. 2 of the main text. Here, we account for slight additional experimental decoherence by scaling the prediction for  $|S(t)|$  as described in Section S.5C.

In the upper panels of Fig. 4.12 we compare the Ramsey response obtained by simulating the actual experimental sequence (solid line) with that of the perfect quench scenario (dashed line). We see that the residual interactions  $X_1$  in experiment can indeed influence the quantum evolution of the impurity. The difference in the responses can be straightforwardly explained by assuming that the main effect of  $X_1$  is to produce a weakly interacting initial state. Specifically, for weak attractive interactions  $X_1 > 0$ , the Ramsey response can be approximated as

$$S(t) \simeq \langle \psi_{X_1} | e^{-i\hat{H}t/\hbar} | \psi_{X_1} \rangle, \quad (4.21)$$

where  $|\psi_{X_1}\rangle$  is the ground state of the Hamiltonian (4.1) at interaction parameter  $X_1$ . Note that we cannot formally construct a similar expression for the repulsive case  $X_1 < 0$ , since the repulsive polaron is a metastable state, involving multiple eigenstates of the Hamiltonian.

Referring to Fig. 4.12, the excellent agreement between the approximation (4.21) and the full Ramsey signal provides strong evidence that the residual interactions  $X_1$  produce a weakly attractive initial state. This is further supported by the spectrum  $A(\omega)$  shown in the bottom panels, where we see that the residual interactions enhance the attractive polaron peaks for  $X = 0.08$  and  $0.86$ . A similar enhancement of the repulsive polaron peak is observed for  $X = -0.23$ . Hence we conclude that the explicit modelling of the impurity dynamics using the full Hamiltonian  $\hat{\mathcal{H}} = \hat{H} + \hat{H}_{\text{rf}}$  is not essential for the description of the dynamics during the initial  $\pi/2$  spin rotation and instead one can fully describe the time evolution using the Hamiltonian (4.1).

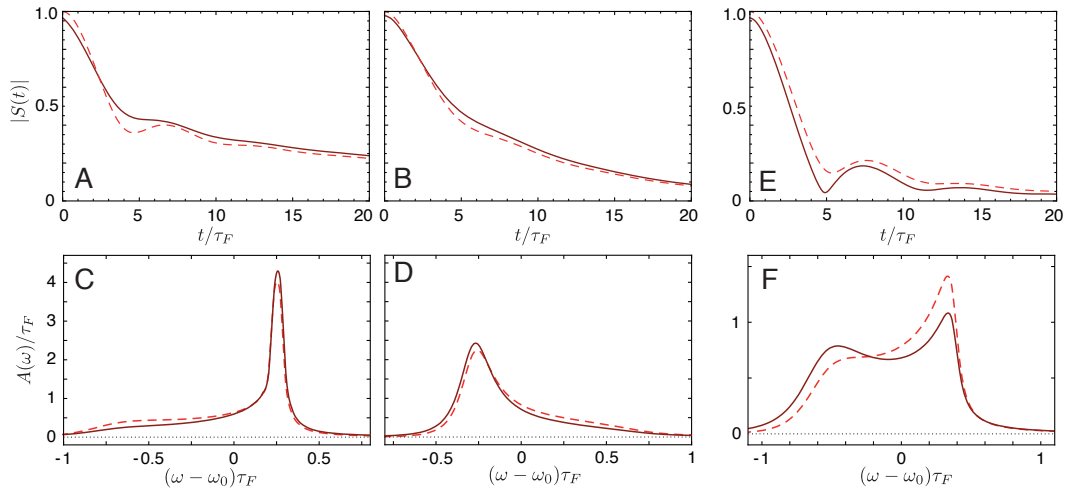


FIGURE 4.13: **Role of the residual interactions in the Ramsey sequence at finite temperature.** Upper panels: we compare the perfect quench Ramsey response (dashed) with a simulation of the experimental sequence (solid). Lower panels: we compare the linear-response excitation spectrum (dashed) with the Fourier transform of the signal obtained using the experimental sequence (solid). As in the main text, we take  $k_F R^* = 1.1$  and the interaction parameters: (A, C)  $X = -0.23$ ,  $X_1 = -3.9$ , (B, D)  $X = 0.86$ ,  $X_1 = 5.8$ , and (E, F)  $X = 0.08$ ,  $X_1 = 4.8$ . The temperatures are  $T/T_F = 0.166, 0.158, 0.177$ , respectively.

### 4.6.5.3 Modelling of Experimental Procedure at Finite Temperature within FDA

The interplay between the residual interactions and finite temperature presents a further theoretical challenge. In the following, we use the FDA to simulate the experimental protocol (Fig. 4.11) at finite temperature. To achieve this, we exploit the finding from Sec. 4.6.5.2 that the detailed dynamics of the rf-driven oscillations between the  $K|2\rangle$  and  $K|3\rangle$  states can be ignored when calculating  $S(t)$ . Thus, we assume that the initial  $\pi/2$  rotation effectively produces a spin superposition  $(K|2\rangle + K|3\rangle)/\sqrt{2}$ , independently of the residual interaction  $X_1$  of the impurity in the state  $K|3\rangle$  with the Fermi sea. To account for the dynamics due to the weak interaction  $X_1$ , we then let the system evolve under this interaction for a hold time  $t_h = t_{\text{rf}}/2 + t_{\text{wait}}$ , which models the dynamics at weak interaction  $X_1$  as the result of a sudden switch-on of this interaction at the midpoint of the  $\pi/2$  pulses. After the hold time  $t_h$ , the final quench to the strong interactions  $X$  is performed. For the measurement of the Ramsey contrast, this sequence is reversed. Theoretically, this yields the modified time-dependent overlap

$$S(t) = \text{tr} \left[ \hat{\rho} e^{i\hat{H}_0(2t_h+t)} e^{-i\hat{H}_1 t_h} e^{-i\hat{H}_X t} e^{-i\hat{H}_1 t_h} \right], \quad (4.22)$$

where  $\hat{H}_1$  and  $\hat{H}_X$  denote the Hamiltonian (4.1) at interaction strength  $X_1$  and  $X$ , respectively. Using the FDA, the expression Eq. (4.22) is evaluated exactly according to Eq. (4.13) at the experimental temperature. As can be inferred from Eq. (4.22), this simplified model of the experimental protocol corresponds to a sequence of interaction quenches.

In the upper panel of Fig. 4.13 we compare the result for  $|S(t)|$  at the experimental temperatures obtained for the experimental sequence (solid lines) to the result for an idealized, i.e., perfect quench, Ramsey sequence (dashed lines). Similarly to the case of zero temperature, we see that the time evolution at  $X_1$  has an experimentally observable effect on the dynamics. In particular, it generates an additional decoherence of the Ramsey signal already at  $t = 0$ , as well as an enhancement of the oscillations in  $|S(t)|$  for resonant interactions – see Fig. 4.13E.

For the calculation of the FDA results shown in Fig. 2 of the main text we use the same procedure as described above. We account for slight additional experimental decoherence by scaling the prediction for  $|S(t)|$  as described in Section S.5C. We also note that the phase  $\varphi_{\text{FDA}}(t)$  of the Ramsey signal  $S(t) = |S(t)|e^{-i\varphi_{\text{FDA}}(t)}$ , as determined from Eq. (4.22), differs from the experimentally measured phase  $\varphi(t)$  due to the detuning of the rf frequency from  $\omega_0$ . They are related by  $\varphi(t) = \varphi_{\text{FDA}}(t) - (\omega_{\text{rf}} - \omega_0)(2t_{\text{wait}} + t_{\text{rf}})$ . Similar to the previous section and to the experiment, we take  $\omega_{\text{rf}} - \omega_0 = \varepsilon_1/\hbar$ .

As outlined in Section 4.6.5.1, in the idealized Ramsey scenario the Fourier transform  $A(\omega)$  of  $S(t)$  is equivalent to the rf absorption in linear response, cf. (4.19) [Kna12]. Similarly to our  $T = 0$  analysis in Sec. 4.6.5.2, we now study the effect of the residual interactions  $X_1$  on the spectral decomposition of  $S(t)$ . To this end we compare the two signals  $A(\omega)$  for the perfect quench with the result obtained for the experimental sequence as modelled by Eq. (4.22). We show the comparison of the spectra obtained in the idealized (dashed) and experimentally realized scenario (solid) in the lower panel of Fig. 4.13. As for our  $T = 0$  results discussed above, we find only a small difference

between the two finite-temperature spectra. Therefore, in agreement with the experimental observation, cf. Fig. 3 in the main paper, under the condition of  $|X_1| \approx 5$  we see that the weak interactions during the rf pulses have an observable but small effect on the predicted spectra.

In accordance with the results from the TBM shown in Fig. 4.12, we find from the evaluation of Eq. (4.22) that weak interactions  $X_1$  lead to a small shift of spectral weight into the corresponding dominant polaron branches. This shift of spectral weight is also observed experimentally, see Fig. 3 of the main text.

#### 4.6.5.4 Stronger Interactions During RF Pulses: Illustration of Quantum State Preparation

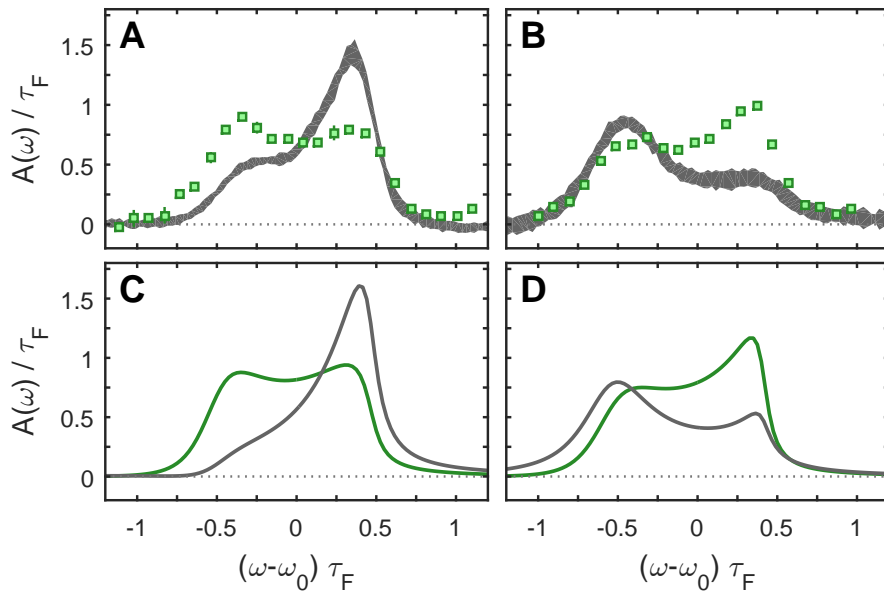


FIGURE 4.14: **Control of the spectral decomposition of many-body quantum states.** Upper panel: We compare the experimentally measured rf spectrum at the interaction parameter  $X$  (green squares) to the Fourier transform of  $S(t)$  obtained using the measurement procedure illustrated in Fig. 4.11 with initial interaction parameter  $X_1$  (gray shading). Lower panel: we compare the theoretical prediction from the FDA for the linear-response excitation spectrum (green) to the Fourier transform of the signal obtained by simulating the experimental sequence according to Eq. (4.22). (A, C)  $X = 0.14$ ,  $X_1 = -2.2$ ,  $k_F R^* = 1.09$ ,  $T/T_F = 0.174$ . (B, D)  $X = -0.25$ ,  $X_1 = 1.7$ ,  $k_F R^* = 1.1$ ,  $T/T_F = 0.17$ .

The shift of spectral weight towards the attractive or repulsive branches of the spectrum, cf. Figs. 4.12 and 4.13, may be interpreted as follows: The residual interactions present during the initial  $\pi/2$  impurity spin rotation serve to produce an interacting many-body quantum state. As such, this procedure can be viewed as an adiabatic preparation of an attractive or repulsive polaron. Compared to the noninteracting state, this polaron has an increased wavefunction overlap with the corresponding branch of the strongly interacting system. When the system is then quenched into the regime of strong interactions, the increased overlap results in the corresponding shift of the spectral weight. An intriguing question is then whether such an approach can provide a novel way to experimentally control the spectral decomposition of quantum states.

To investigate this possibility, we increase the interaction during the  $\pi/2$  rotations, corresponding to decreasing  $|X_1|$ , and determine the effect on  $A(\omega)$ . In the upper panel of Fig. 4.14 we show the spectra obtained by linear-response rf spectroscopy (green squares). Similar to Fig. 3 of the main paper, we compare this result to the Fourier transform of the Ramsey signal  $S(t)$  (gray shading), as obtained from the experimental sequence described in Fig. 4.11. We also compare our experimental result to the prediction from the FDA, where the dynamics has been modelled as described by Eq. (4.22). As in the main text, we find excellent agreement between experiment and theory. Indeed, both feature a strong shift of spectral weight to regions of the spectrum that are adiabatically connected to the dominant polaron branches at interaction  $X_1$ . Furthermore, when comparing  $A(\omega)$  in Fig. 4.14, with the spectrum for  $|X_1| \approx 5$  in Figs. 4.12 and 4.13, it is clear that the amount by which the spectrum is shifted can be controlled by the strength of the interaction during the rf pulses. This strongly supports the assertion that the initial interactions can be used to precisely control the many-body dynamics. Our experimental techniques thus allow for a precise, dynamic control of the spectral decomposition of quantum states in future experiments.

The excellent agreement between theory and experiment also demonstrates that our theoretical approaches can be used to explore experimental ramps in combination with interferometric protocols in order to find, for instance, optimized spin and interaction trajectories.

#### 4.6.6 Universal Features of Impurity and Relation to Orthogonality Catastrophe

For impurities localized in space, which, for instance, can be achieved by species-selective three dimensional optical lattices, our experimental setup allows one to study universal features exhibited by the Anderson orthogonality catastrophe [And67]. The orthogonality catastrophe was originally studied in the context of x-ray absorption spectra in metals, where high-energy x-ray photons create atomic core holes by photoemission of inner-shell electrons [Mah90]. These core holes produce a scattering potential for the electrons in the conduction band, leading to characteristic power-law edges in the absorption spectra with an exponent that is universally determined by the scattering phase shift at the Fermi surface [And67]. However, impurities, phonons, residual interactions between the electrons, and a lack of knowledge of microscopic parameters makes it difficult to unambiguously determine the universal features of the orthogonality catastrophe in typical solid state materials [Oht90]. In contrast, the Hamiltonian in our experiment is well characterized on all relevant energy scales, and therefore the full dynamic response of the system can be reliably calculated by theory and probed by the ultrafast experimental techniques demonstrated in this work. This enables one to obtain fundamental insights into universal features of the orthogonality catastrophe, which are difficult to access in other systems. To illustrate how the orthogonality catastrophe would manifest itself in an ultracold atomic gas experiment, the response of infinite mass impurities calculated using the FDA for the perfect quench scenario is shown in Fig. 4.15. First, at short times and for a range parameter of the Feshbach resonance  $R^* > 0$ , we see that the Ramsey contrast decays quadratically for all scattering parameters and temperatures

considered, in accordance with Eq. (4.11). The main universal feature associated with the orthogonality catastrophe is expected in the long-time dynamics at  $T = 0$ : Here, the Ramsey response is predicted to exhibit power law tails, which depend only on the scattering phase shift at the Fermi surface [And67, Kna12]. This is explicitly verified in Fig. 4.15A where we fix the scattering phase shift at the Fermi surface but change the scattering parameters. While the response at intermediate times depends on the scattering parameters, we see that the long-time evolution approaches a universal power law that only depends on the phase shift at the Fermi surface. We note that the long-time dynamics is universal: It is the same for a system with a broad resonance where  $R^* = 0$  (solid line in Fig. 4.15A), as it is for our system with a finite range parameter (dashed and dotted lines).

When the temperature is non-zero, as in the experiment, thermal fluctuations alter the power law dephasing dynamics at sufficiently long times. Instead, exponential tails due to thermal decoherence appear as another universal feature of the dynamics [Kor50, And67, Yuv70, Kna12]. The exponential tails are illustrated in Fig. 4.15B. The effects of thermal decoherence could be countered by employing the recently developed cooling methods [Har15], opening the door to observing the orthogonality catastrophe in a cold-atom system.

Finally, we note that in our experiment temperature becomes relevant at a time scale similar to those associated with recoil and multiple particle-hole excitations. It is a challenge for theoretical approaches to exactly account for both recoil and higher order particle-hole excitations [Ros99]. However, experiments at lower temperatures which take advantage of the tunability of the impurity mass using optical lattices would be ideally suited to probe the competition between these effects. Such ultracold-atom experiments would hence provide important insight into this longstanding theoretical question.

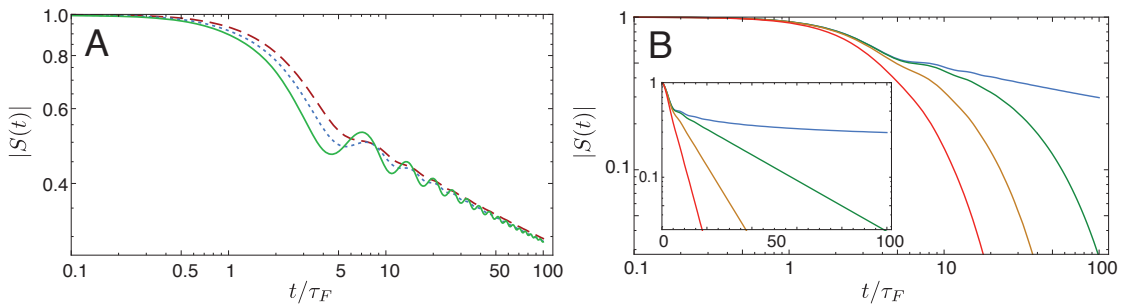


FIGURE 4.15: **Universal features of the dynamical orthogonality catastrophe.**

We show the Ramsey contrast for an infinitely heavy impurity obtained within the FDA. (A) The zero-temperature Ramsey contrast exhibits a power law decay, shown on a double logarithmic scale. We change the Feshbach resonance range  $k_F R^*$  and interaction parameter  $X$  in such a way that the scattering phase shift at the Fermi surface is constant leading to a constant exponent of the power law tail. The data corresponds to a fixed phase shift  $\delta_{k_F} = 1.4$  with the choices  $(X, k_F R^*) = (1, 1.12)$  (dashed red),  $(X, k_F R^*) = (0.58, 0.56)$  (dotted blue), and  $(X, k_F R^*) = (0.15, 0)$  (solid green). (B) Ramsey contrast at various temperatures on a double logarithmic scale. We choose temperatures  $T/T_F = 0$  (blue), 0.05 (green), 0.15 (orange), 0.4 (red) at fixed values  $X = 1$  and  $k_F R^* = 1.12$ . The inset shows the same data on a logarithmic-linear scale to emphasize the appearance of exponential tails at finite temperature.



# 5

## Chapter 5

### Publication: Thermometry of a deeply degenerate Fermi gas with a Bose-Einstein condensate

Journal: Physical Review A, Vol. **95**, Issue 5

Published: 23. May 2017

DOI: [10.1103/PhysRevA.95.053627](https://doi.org/10.1103/PhysRevA.95.053627)

Rianne S. Lous<sup>1,2</sup>, Isabella Fritsche<sup>1,2</sup>, Michael Jag<sup>1,2</sup>, Bo Huang<sup>1</sup>, and Rudolf Grimm<sup>1,2</sup>

<sup>1</sup> Institut für Quantenoptik und Quanteninformation, Österreichische Akademie der Wissenschaften, 6020 Innsbruck, Austria.

<sup>2</sup> Institut für Experimentalphysik, Universität Innsbruck, 6020 Innsbruck, Austria.

Contribution to the publication: I took, together with the leading author R. S. Lous, a significant part in the measurements and lab operation of this publication. Furthermore, I contributed to the preparation of the manuscript.

Note on the present version of the publication: This version can vary from the published version since final changes by the editor are not included. Typos have been corrected. The sections structure has been introduced for better readability and references have been updated.

## 5.1 Abstract

We measure the temperature of a deeply degenerate Fermi gas, by using a weakly interacting sample of heavier bosonic atoms as a probe. This thermometry method relies on the thermalization between the two species and on the determination of the condensate fraction of the bosons. In our experimental implementation, a small sample of  $^{41}\text{K}$  atoms serves as the thermometer for a  $^6\text{Li}$  Fermi sea. We investigate the evaporative cooling of a  $^6\text{Li}$  spin mixture in a single-beam optical dipole trap and observe how the condensate fraction of the thermometry atoms depends on the final trap depth. From the condensate fraction, the temperature can be readily extracted. We show that the lowest temperature of 5.9(5)% of the Fermi temperature is obtained, when the decreasing trap depth closely approaches the Fermi energy. To understand the systematic effects that may influence the results, we carefully investigate the role of the number of bosons and the thermalization dynamics between the two species. Our thermometry approach provides a conceptually simple, accurate, and general way to measure the temperature of deeply degenerate Fermi gases. Since the method is independent of the specific interaction conditions within the Fermi gas, it applies to both weakly and strongly interacting Fermi gases.

## 5.2 Introduction

Since the first demonstration of Fermi degeneracy in an ultracold gas [DeM99], experimental progress has provided unprecedented access to a great wealth of exciting phenomena, as highlighted by the prominent example of a crossover superfluid [Zwe12]. The great interest in fermionic quantum gases results from the fact that fermions constitute the elementary building blocks of matter and provide the possibility to investigate various phenomena of strong interactions. The experimental availability of degenerate Fermi gases has led to new insights into intriguing few- and many-body behavior, the many facets of which are studied in a great variety of current experiments.

The lowest achievable temperature is crucial for the experimental observation of many phenomena. While fermionic superfluidity [Pit16] is now routinely achieved in many experiments worldwide, other phenomena like antiferromagnetic ordering [Har15] require much lower temperatures, which are still very hard to obtain experimentally. In the range of very low temperatures, well below one tenth of the Fermi temperature  $T_F$ , thermometry becomes increasingly difficult. In deeply degenerate Fermi systems, one faces the general problem that only a small fraction of atoms near the Fermi surface carry the temperature information, which reduces the detection sensitivity for common imaging methods. For strongly interacting systems, the interpretation of density profiles is not straightforward and requires detailed knowledge of the equation of state [Luo07, Nas10, Ku12] to extract temperature information from thermodynamic observables. For the specific case of a unitary Fermi gas with resonant interactions, where thermodynamics follows universal behavior [Ho04], thermometry is now well established, but not for the general situation of Fermi gases in strongly interacting regimes.

The conceptually most simple way of thermometry is to use a probe in thermal equilibrium with the object under investigation and to rely on a phenomenon with an easily detectable and well-understood temperature dependence. This is the working principle of thermometers in our daily life, where the underlying phenomenon is thermal expansion or temperature-dependent resistivity. We apply the same basic idea to a deeply degenerate Fermi sea, using a small sample of weakly interacting bosonic atoms as a probe, and we rely on the sensitive detection of the condensate fraction.

Our Fermi gas is a spin mixture of deeply degenerate  ${}^6\text{Li}$  atoms with resonantly tuned interactions, as it is used in many current experiments worldwide. For such a system, temperatures around 10% of the Fermi temperature  $T_F$  or even below have been reported by various groups (see [Yef13, Lin14, Bur14, Del15, Rev16] for a few recent examples). Our thermometer is a small sample of bosonic  ${}^{41}\text{K}$  atoms immersed in the Fermi sea. In addition to the condensate formation serving as the main observable, our system takes advantage of the large mass ratio and the much smaller number of bosons as compared to the fermions. Related thermometry approaches that rely on coupling to a weakly interacting probe component, have been implemented in other Bose-Fermi systems [Roa02, Fer14, Del15, Ono16], in population-imbalanced spin mixtures [Zwi06a], and in a Fermi-Fermi mixture [Spi09], but without combining all these three advantages. For our system, the critical temperature for Bose-Einstein condensation (BEC) corresponds to about  $0.1T_F$ , which makes the condensate fraction a sensitive and accurate probe right in the temperature range of main interest for deep cooling.

In this paper, we present a thorough experimental investigation of Fermi gas thermometry using a bosonic species. In Sec. 5.3, we discuss the basic principle of thermometry for a Fermi-Bose system in general and for the particular case of our mixture of  ${}^6\text{Li}$  and  ${}^{41}\text{K}$ . We then, in Sec. 5.4, describe the experimental procedures of preparation, cooling, trapping, and detection. In Sec. 5.5, we present the main experimental results on deep cooling of the  ${}^6\text{Li}$  spin mixture, as probed by the  ${}^{41}\text{K}$  BEC.

### 5.3 Bosons as a Fermi gas thermometer

Here, we first discuss the basic idea of our thermometry approach in general terms, before we turn our attention to the specific case of  ${}^{41}\text{K}$  bosons in a  ${}^6\text{Li}$  Fermi sea.

#### 5.3.1 Basic idea

The basic idea of our thermometry approach is illustrated in Fig. 5.1. We assume that both harmonically trapped species are in sufficient thermal contact with each other to establish a thermal equilibrium with a common temperature  $T$ . The main observable is the condensate fraction  $\beta$  of the bosonic cloud, from which  $T$  can be derived.

To obtain the temperature  $T$  of the two-component system in relation to the Fermi temperature  $T_F$ , we start with the identity  $T/T_F = (T/T_c) \times (T_c/T_F)$ , where  $T_c$  is the critical temperature for BEC. The first factor,  $T/T_c$ , can readily be obtained from the

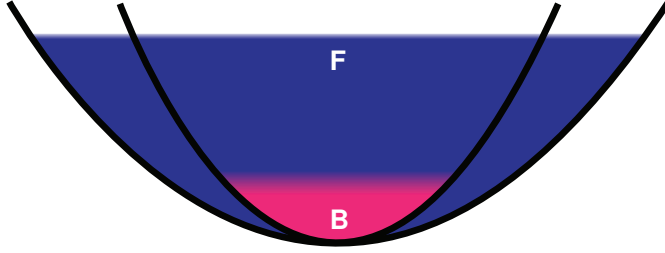


FIGURE 5.1: (Color online) Basic idea of the thermometry. A small sample of bosonic atoms (B) is immersed in a large, deeply degenerate sea of fermions (F) under thermal equilibrium conditions. The harmonic trapping potentials (solid lines) are different for both species, depending on the particular trapping configurations used. The temperature is derived from the condensate fraction.

condensate fraction of the bosonic component through the well-known relation

$$\frac{T}{T_c} = (1 - \beta)^{1/3}. \quad (5.1)$$

For calculating  $T_c/T_F$  we use the textbook formulas

$$k_B T_c = 0.940 \hbar \omega_B N_B^{1/3}, \quad (5.2)$$

$$k_B T_F = 1.817 \hbar \omega_F N_F^{1/3}, \quad (5.3)$$

where  $N_B$  and  $N_F$  represent the number of trapped bosons and fermions, and  $\omega_B$  and  $\omega_F$  are the respective geometrically averaged trap frequencies. Note that Eqs. (5.1) and (5.2) are strictly valid only for non-interacting systems in the thermodynamic limit. In practice, the finite sample size and interaction effects may lead to corrections [Gio96]. By combining Eqs. (5.1)-(5.3) we arrive at the central equation that underlies our thermometry approach,

$$\frac{T}{T_F} = 0.518 (1 - \beta)^{1/3} \frac{\omega_B}{\omega_F} \left( \frac{N_B}{N_F} \right)^{1/3}. \quad (5.4)$$

In an experiment, the ratio of the trap frequencies,  $\omega_B/\omega_F$ , will be determined by the specific properties of the two different components and the particular trap configuration used for the experimental realization.

Equation (5.4) highlights the conditions for optimized thermometry in the deeply degenerate regime. A small ratio of the trap frequencies,  $\omega_B/\omega_F$ , is highly desirable. This favors heavy bosons in combination with light fermions. The number ratio  $N_B/N_F$  enters with its third root, which shows that a very large number imbalance ( $N_B \ll N_F$ ) is required to take real advantage of this factor. In this case, the bosons can be considered as impurities in the large Fermi sea.

### 5.3.2 Case of the ${}^6\text{Li}$ - ${}^{41}\text{K}$ mixture

We now turn our attention to the specific situation of bosonic  ${}^{41}\text{K}$  atoms in a Fermi sea of  ${}^6\text{Li}$  atoms. The mixture [Wu11, Yao16] exhibits favorable properties for our purpose. The interspecies interaction is moderate, with a background scattering length of about

$+60 a_0^1$ , where  $a_0$  is Bohr's radius. This is large enough to provide a sufficient cross section for thermalization on a realistic experimental time scale, but weak enough to avoid effects of strong interactions, such as a mutual repulsion or attraction or fast three-body decay.

We consider a hybrid trapping scheme, as realized in our experiment, where the atoms are confined radially by an infrared laser beam and axially by a curved magnetic field (see Sec. 5.4.2), under conditions ensuring that the trap frequency ratio for the two species is not changed by the gravitational sag (see Appendix 5.8). For such a trap, in a harmonic approximation, the frequency ratio in Eq. (5.4) can be expressed as

$$\frac{\omega_B}{\omega_F} = \left( \frac{m_K}{m_{Li}} \right)^{-1/2} \left( \frac{\alpha_K}{\alpha_{Li}} \right)^{1/3} \left( \frac{\mu_K}{\mu_{Li}} \right)^{1/6}, \quad (5.5)$$

For our experimental situation (Sec. 5.4.2), the mass ratio is  $m_K/m_{Li} = 6.810$ , the ratio of optical polarizabilities is  $\alpha_K/\alpha_{Li} = 2.209$  [Tan10, Saf13], and the ratio of magnetic moments is  $\mu_K/\mu_{Li} = 0.999$ . With these accurately known numbers, Eqs. (5.4) and (5.5) yield

$$\frac{T}{T_F} = 0.258 (1 - \beta)^{1/3} \left( \frac{N_B}{N_F} \right)^{1/3}, \quad (5.6)$$

which we will use for extracting  $T/T_F$  from our experimental data, as described in the following sections.

The dynamical range of our thermometry approach as applied to the  $^{41}\text{K}$ - $^6\text{Li}$  mixture can now be illustrated by a numerical example, based on typical experimental conditions. We assume  $N_B/N_F = 1/30$  and possible measurements of the condensate fraction in the range  $0 \leq \beta \lesssim 0.95$ . According to Eq. (5.6), this corresponds to a temperature range of  $0.03 \lesssim T/T_F \lesssim 0.08$ , right in the interesting regime for state-of-the-art experiments in the deeply degenerate Fermi gases.

## 5.4 Experimental procedures

In this section, we present our general experimental procedures applied to a Fermi-Bose mixture of  $^6\text{Li}$  and  $^{41}\text{K}$ . In Sec. 5.4.1, we give an overview of the main preparation steps. In Sec. 5.4.2, we present in detail the optical dipole trap used in the final stage of deep evaporative cooling. In Sec. 5.4.3, we discuss the main detection schemes.

### 5.4.1 Preparation of the $^6\text{Li}$ - $^{41}\text{K}$ mixture

The mixture is prepared in an all-optical cooling and hybrid trapping approach, very similar to the one described in detail in Ref. [Spi10] and applied in various previous experiments on the mixture of  $^6\text{Li}$  and  $^{40}\text{K}$  atoms (see, e.g., Refs. [Spi09, Tre11, Koh12, Jag14, Cet16]). A spin mixture of  $^6\text{Li}$  atoms in the lowest two sublevels of the electronic ground state is evaporatively cooled close to a Feshbach resonance [O'H02, Bou03, Joc03]

<sup>1</sup>T. Hanna and E. Tiesinga. (private communication)

and serves as the agent to sympathetically cool a K minority component. For the whole cooling process, we found that it makes no difference whether the fermionic  $^{40}\text{K}$  or the bosonic  $^{41}\text{K}$  isotope is present, if we avoid any interspecies scattering resonances and rely on the background interaction with the  $^6\text{Li}$  cooling agent, being about the same for both K isotopes.

The preparation process involves a spin relaxation stage, which we employ to prepare a single K spin state. Here, the parameters differ from our previous work on  $^{40}\text{K}$  [Spi10]. For  $^{41}\text{K}$ , the initial laser cooling stage provides an unpolarized sample in the three magnetic sublevels ( $m_F = -1, 0, 1$ ) of the lowest hyperfine level ( $F = 1$ ). We found [Lou18a] that spin-exchange collisions with  $^6\text{Li}$  atoms in the second-lowest sublevel can efficiently produce a polarized  $^{41}\text{K}$  sample in the  $m_F = -1$  state, which is the third-lowest Zeeman sublevel. The spin relaxation is performed near a magnetic field of 200 G, where the process appears to be resonantly enhanced. This stage has a duration of about 500 ms and is implemented right after loading the optical dipole trap, when the temperature is still rather high (few 100  $\mu\text{K}$ ). To remove a residual population of K in the  $m_F = 0$  state (typically 15%), we apply a resonant laser pulse right before the final evaporation stage to push those atoms out of the trap. It is interesting to note that, without applying the spin cleaning, the evaporation process leads to a spinor condensate [Sta13] with clear signatures of immiscibility [Liu16]. The  $s$ -wave background interaction between the bosons is relatively weak (intraspecies scattering length of  $+60 a_0$  [D'E07, Pat14]), which makes the condensate very stable against three-body decay.

#### 5.4.2 Trap for deep evaporative cooling

The whole evaporation process takes place in several stages [Spi10] within a total time of 12 s. Here, we focus on the final stage, where the power of a single laser beam is ramped down exponentially within 5 s, from an initial value of 440 mW to a final value in the range between 110 and 45 mW. Then, a hold time of 10 s is introduced to ensure full thermalization, before the two species are finally detected; see Sec. 5.4.3. As in our previous work [Spi09, Tre11, Koh12, Jag14, Cet16], the magnetic bias field of 1180 G is applied for standard Feshbach tuning of the interaction between the two  $^6\text{Li}$  spin components. This leads to a large negative  $s$ -wave scattering length of  $a = -2900 a_0$  [Zür13], and thus facilitates highly efficient evaporative cooling with very low inelastic losses. We note that, because of the absence of any significant losses, the number of K atoms stays essentially the same during the whole evaporative cooling process.

We hold the spin mixture of  $^6\text{Li}$  together with the single spin state of  $^{41}\text{K}$  in a hybrid trap [Joc03] as illustrated in Fig. 5.2(a). Here, the radial confinement ( $y, z$  directions) is provided by a single 1064-nm laser beam and the axial confinement ( $x$  direction) results from the curvature of the applied magnetic field. In the vertical direction, gravity also comes into play and decreases the trap depth, which influences both species differently. We apply an additional magnetic levitation field to compensate for the latter effect. The levitation potential is given by

$$U_{\text{lev}}(z) = -\mu_B B' z, \quad (5.7)$$

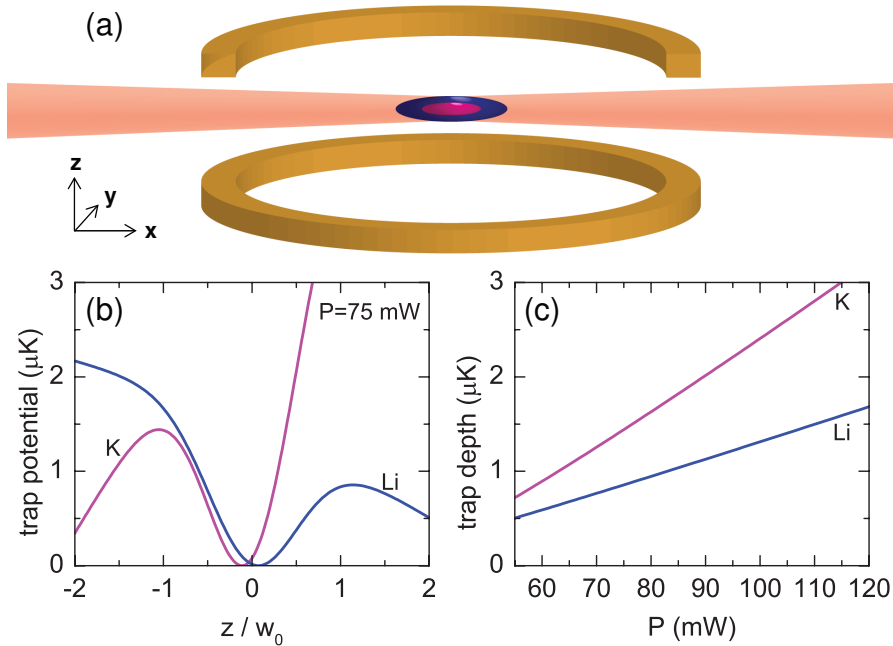


FIGURE 5.2: (Color online) Trapping scheme in the final stage of evaporative cooling. (a) A single infrared laser beam for radial trapping ( $y, z$  directions) is used in combination with a magnetic field (coil setup schematically shown). The magnetic field serves multiple purposes, providing the bias field for Feshbach tuning, a curvature for axial trapping ( $x$  direction), and a vertical levitation gradient. (b) The vertical potentials  $U_{tot}^i(z)$  resulting from Eq. (5.8) for both Li (blue) and K (magenta) are shown for a typical laser power of  $P = 75\text{ mW}$ . For illustrative purposes, we have introduced species-dependent offsets to shift the potential minima to zero. (c) The trap depths  $U_{trap}^i$  depend on the laser power  $P$ , with the K trap being always deeper than the Li trap.

where  $\mu_B$  is Bohr's magneton and  $B'$  represents the vertical gradient of the magnetic field. Note that for our high bias magnetic field of 1180 G the levitation potential is essentially the same for both species, since the magnetic moments of both species are within 0.1% close to  $\mu_B$ . We use a gradient of 2.5(2) G/cm, for which we obtain  $\mu_B B' / m_K g = 0.34(3)$ , i.e., we realize a partial levitation of the K atoms by compensating one-third of the effect of gravity (gravitational acceleration  $g$ ). For Li, we obtain  $\mu_B B' / m_{Li} g = 2.36(20)$ , which means a strong overlevitation. These conditions are close to a "magic" levitation condition, where the combined tilt effect of gravity and levitation on the trap depth is the same for both species; see Appendix 5.8 for a detailed description.

For both species ( $i = \text{Li, K}$ ), the total potential along the vertical direction in the trap center can be written as

$$U_{tot}^i(z) = -U_{opt}^i \exp(-2z^2/w^2) + (m_i g - \mu_B B')z - \frac{1}{2} \mu_B B'' z^2, \quad (5.8)$$

where  $U_{opt}^i$  is the optical potential depth and  $w$  is the waist of the single optical beam. The combined effect of gravity and magnetic levitation is represented by the term linear in  $z$ . The quadratic term describes a weak magnetic antitrapping effect, resulting from

the negative curvature of the magnetic field. In the saddle-potential of our configuration [Fig. 5.2(a)], the curvature along the  $z$  axis is two times larger and of opposite sign as compared to the curvature along the  $x$  axis, the latter determining the axial magnetic confinement. Therefore, the curvature  $B''$  is related to the axial trapping frequency  $\omega_x^i$  by the formula  $\mu_B B'' = 2m_i(\omega_x^i)^2$ .

The vertical trap potentials are shown in Fig. 5.2(b) for both Li and K atoms under typical conditions of our experiment ( $P = 75$  mW). This clearly illustrates the different optical potentials and the effect of the opposite tilt on both Li and K. The tilt and the curvature substantially reduces the total trap depths  $U_{trap}^i$  to values below the respective depths of the optical potentials ( $U_{trap}^i < U_{opt}^i$ ).

Figure 5.2(c) illustrates the dependence of the trap depths  $U_{trap}^i$  on the laser power in the range relevant for our final evaporative cooling stage. It is important to note that  $U_{trap}^K > U_{trap}^{Li}$  is always fulfilled. The effect of the magnetic levitation ensures that evaporative cooling removes Li atoms, but leaves all K atoms in the trap. This is essential for our interpretation of the cooling process, where Li acts as the cooling agent and K is cooled sympathetically via collisions with Li and not directly.

We characterize the trap by measuring the frequencies of radial and axial sloshing oscillations of both the confined species. For the radial trap frequencies of Li and K, we find

$$\omega_r^{Li} = 2\pi \times 37.6(5)\text{Hz} \times \sqrt{P/\text{mW}}, \quad (5.9a)$$

$$\omega_r^K = 2\pi \times 21.0(6)\text{Hz} \times \sqrt{P/\text{mW}}, \quad (5.9b)$$

where  $P$  is the power of the trapping beam. The measured frequency ratio  $\omega_r^{Li}/\omega_r^K = 1.79(6)$  is consistent with the more accurate value of 1.756 as calculated from the dynamic polarizabilities [Tan10, Saf13] and the mass ratio. For the single-beam optical dipole trap, assuming a Gaussian laser beam profile, we then obtain [Gri00] the waist  $w = 44.3 \mu\text{m}$  and the optical potential depths

$$U_{opt}^{Li}/(k_B \times \text{nK}) = 19.8(3) P/\text{mW}, \quad (5.10a)$$

$$U_{opt}^K/(k_B \times \text{nK}) = 43.7(6) P/\text{mW}. \quad (5.10b)$$

For the axial frequencies, characterizing the magnetic confinement, we obtain

$$\omega_x^{Li} = 2.61 \omega_x^K = 2\pi \times 25.6(1) \text{Hz}. \quad (5.11)$$

We note that, for the trap frequencies, the optical contribution to the axial trapping and magnetic effects on the radial confinement remain negligibly small. Furthermore, the levitation field that counteracts gravity leaves the oscillation frequencies at the bottom of the trap essentially the same [Hum08], in spite of its substantial effect on the trap depths. This ensures that the frequencies according to Eqs. (5.9a) and (5.9b) remain a very good approximation for all our experimental conditions.

### 5.4.3 Detection

For detection of the two species we apply standard time-of-flight absorption imaging, realized with probe beams propagating along the  $z$  axis. From images of the  ${}^6\text{Li}$  cloud, we selectively determine the number  $N_F$  of fermionic atoms in each of the two lowest spin states with relative uncertainties of about 15% [Cet15]. For  ${}^{41}\text{K}$ , we detect the number  $N_B$  of bosonic atoms in the third-to-lowest spin state with an estimated relative uncertainty of 15%. From the images of the bosons, we also extract the condensate fraction  $\beta$ , which is the quantity of main interest for our thermometry approach.

Time-of-flight absorption imaging of the expanding  ${}^{41}\text{K}$  component can, in principle, be implemented by turning off the trapping laser beam and letting the cloud expand in the same magnetic field configuration as it is used for evaporative cooling. However, in such a simple scheme, the magnetic field curvature causes a focusing effect [Don01] in the  $x, y$  plane (oscillation frequency  $\sim 10$  Hz), which occurs right in the time interval of main interest for the imaging. For analyzing the ballistic expansion of the thermal cloud, it is rather straightforward to take the focusing effect into account [Ket08], so that the temperature can be readily extracted. For the condensed part, however, the focusing effect leads to an increase of the density and the optical depth of the cloud, which makes a determination of the condensate fraction problematic.

We employ a modified scheme for time-of-flight absorption imaging, where we adiabatically transform our hybrid trap into a purely optical one, before the cloud is released into free space. To prevent any effect of interspecies interaction in the transfer stage, we remove the Li atoms before the transfer into the crossed-beam trap by smoothly applying a short stage with a magnetic gradient of about 8 G/cm, which levitates the K cloud and spills all Li atoms out of trap. Then we slowly ramp up a second trapping beam, which has a fixed final power of  $P' = 70$  mW, and a waist of  $\sim 50 \mu\text{m}$  and crosses the first beam under an angle of  $16^\circ$  [Cet15]. The magnetic field is simultaneously changed to a homogenous configuration without curvature, but with the same bias field. The potential of the resulting crossed-beam dipole trap is similar to the hybrid trap of the evaporation stage and the transfer is realized over a rather long time of 4 s, which ensures adiabaticity of the process. The transfer into the detection trap, being somewhat tighter than the cooling trap, implies a moderate adiabatic compression. This increases the temperature by a factor of roughly 1.5, as easily obtained from the ratio of the trap frequencies <sup>2</sup>. This factor is taken into account when we determine the temperature of the thermal component from the temperature of the expanding cloud. To image the expanding cloud after time of flight, we apply a levitation field that counteracts gravity and facilitates long observation times up to 45 ms.

We have performed several tests on the performance of our detection scheme. We have carefully checked that the adiabatic transfer stage does not lead to any detectable loss of K atoms and that its influence on the condensate fraction remains negligibly small.

---

<sup>2</sup>At an intermediate power of  $P = 75$  mW, the geometrically averaged trap frequency increases from 69 to 109 Hz. The frequency ratio depends on the value of  $P$ , but quite weakly. We have carried out measurements on the trap frequencies in the crossed-beam detection trap, from which we determine the change in trap frequencies with an accuracy of about a few percent.

## 5.5 Cooling and thermometry results

In this section, we present our experimental results. We focus on the final stage of the deep evaporative cooling process, where the lowest temperatures are achieved. In Sec. 5.5.1, we consider the fermionic  ${}^6\text{Li}$  component only and identify the conditions where cooling crosses over into spilling of the Fermi sea. In Sec. 5.5.2, we turn our attention to the bosonic  ${}^{41}\text{K}$  component and present measurements of the condensate fraction and the temperature, which allows us to determine  $T/T_F$  for the Fermi gas. In Sec. 5.5.3, we investigate the interspecies thermalization process, justifying the assumption of interspecies thermalization. In Sec. 5.5.4, we finally discuss the performance of our thermometry scheme in terms of measurement uncertainties and systematical effects.

### 5.5.1 Crossover from evaporation to spilling

In the final stage of evaporative cooling, when the laser power is reduced to very low values, a crossover between two regimes takes place [Joc03]. Above a certain threshold, the continuous reduction of the trap power removes thermal atoms with some excess energy above the Fermi energy level, which efficiently cools down the sample. Then a threshold is reached where the Fermi energy level in the shallow trap reaches the trap depth. Below that threshold, the atoms are spilled out of the trap. We identify this crossover by measuring the number of  ${}^6\text{Li}$  atoms remaining in the trap as a function of the final trap power at the end of the evaporation ramp.

Figure 5.3 shows our observations for a final trap power  $P$  between 45 and 110 mW. The crossover between the two different regimes can be clearly seen in the behavior of both the atom numbers (a) and the resulting Fermi energies (b). The results reveal a change between 70 and 80 mW, which marks the crossover into the spilling regime. This interpretation is further confirmed by the behavior of the trap depth, as calculated from Eq. (5.8). Below a power of about 70 mW, the corresponding solid line in (b) gets very close to the data points and shows essentially the same slope<sup>3</sup>. It is also interesting to note that the spilling effect removes a small initial imbalance in the population of both spin states.

As we will see in Sec. 5.5.2, the deepest cooling takes place in the discussed crossover regime. We therefore summarize the relevant experimental parameters at  $P = 75$  mW, where we have  $N_F = 2.0 \times 10^5$  atoms per spin state in a trap with an average frequency  $\omega_F = 2\pi \times 140$  Hz. This results in a Fermi energy of  $E_F = k_B \times 710$  nK, corresponding to a peak number density of  $n_F = 1.3 \times 10^{12}$  cm<sup>-3</sup> per spin state and a Fermi wavenumber of  $k_F = 1/(4500 a_0)$ .

The interaction in the spin mixture [Zwe12] is characterized by the parameter  $1/(k_F a) \approx -1.6$ , which shows that our gas is not in the strongly interacting regime as defined by  $|1/(k_F a)| < 1$ , but also not far away from it. The attraction in the gas can be estimated [Nav10] to have  $\sim 10\%$  effect on the chemical potential and the number density as compared to the interaction-free values. We point out that this does not play any role

<sup>3</sup>The Fermi energy is calculated in the harmonic approximation. We estimate that the anharmonicity of the trap leads to an error on the order of 5%.

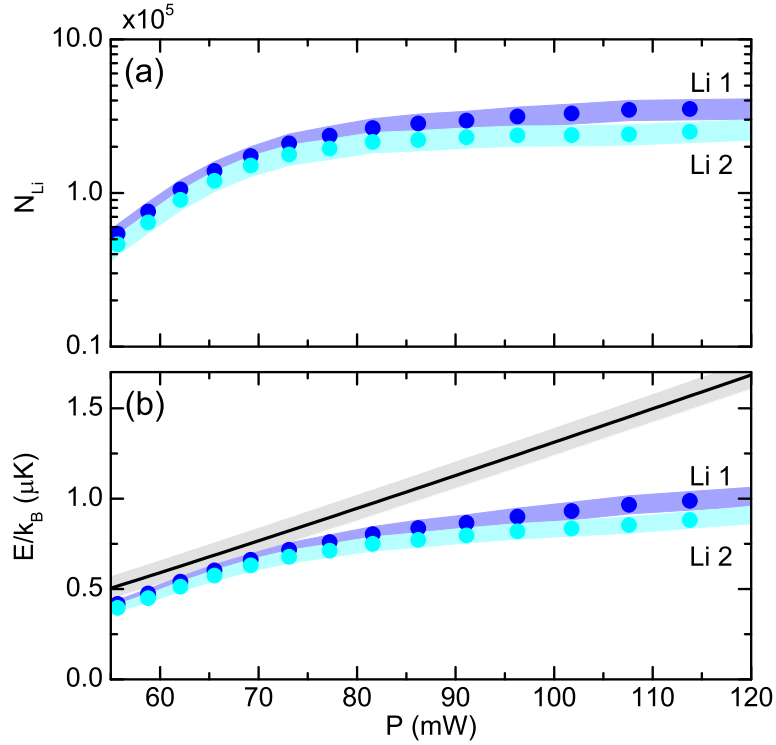


FIGURE 5.3: (Color online) Crossover from the cooling to the spilling regime in deep evaporative cooling of  ${}^6\text{Li}$ . In (a), we show the measured dependence of the atom number in both spin states as a function of the laser power  $P$ , which decreases during the evaporation ramp. Here the labels Li 1 and Li 2 refer to the lowest and second-to-lowest spin state of Li, respectively. The systematic calibration uncertainty in the number determination ( $\pm 15\%$ ) is indicated by the shaded error band. In (b), we plot the corresponding behavior of the Fermi energy  $E_F$  and compare it with the decreasing trap depth  $U_{\text{trap}}^{\text{Li}}$  (solid line). The shaded region indicates a systematic uncertainty in the trap depth resulting from the determination of the levitation gradient, which we consider as the dominant error source for  $E_F$ .

for our thermometry approach, because we probe the temperature with another species. This is in contrast to temperature measurements that are based on the size and shape of the trapped cloud. The latter require knowledge of the temperature-dependent equation of state [Ku12] for the particular interaction conditions.

### 5.5.2 Condensate fraction and equilibrium temperatures

Here, we first present our measurements of the condensate fraction, from which we derive the relative temperature  $T/T_F$ . Then we compare these results with direct temperature measurements of the thermal fraction of the bosons, and we finally investigate how the number of bosonic atoms affects our results.

Figure 5.4(a) shows the BEC fraction  $\beta$ , measured as a function of the final power  $P$  of the evaporation ramp. Each data point is the mean derived from images taken at seven different times of flight (12 to 24 ms), with the corresponding standard error of the mean. The total number of bosonic  ${}^{41}\text{K}$  atoms is  $N_B \approx 1.3 \times 10^4$ , independent of  $P$ . We locate the condensation threshold somewhere near 125 mW and, with decreasing power,

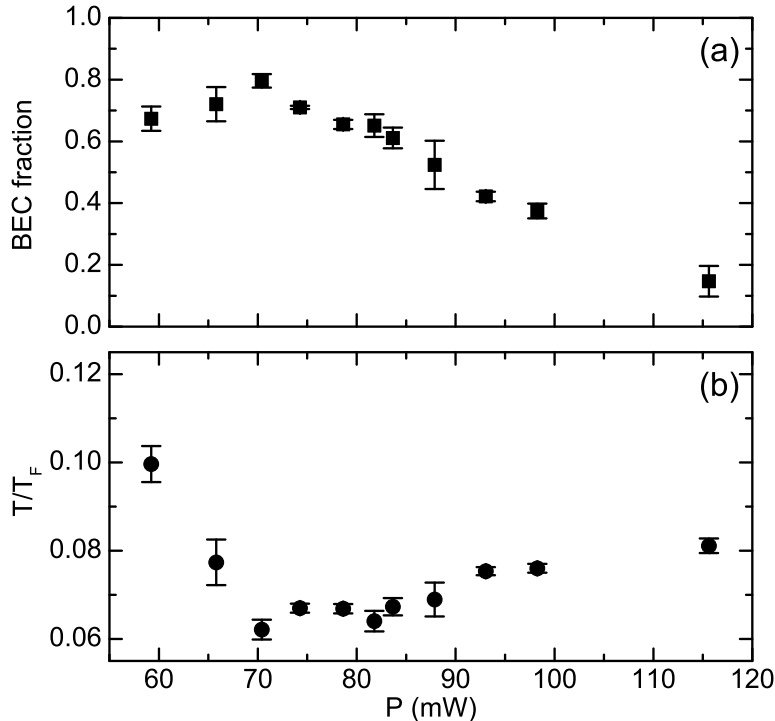


FIGURE 5.4: Fermi gas thermometry based on partially condensed bosons. (a) The measured condensate fraction  $\beta$  is shown as a function of the final power  $P$  of the evaporation ramp. Here the small error bars (most of them smaller than the symbol size) reflect the uncertainties of bimodal fits to time-of-flight images. In (b), we show the corresponding results for the relative temperature  $T/T_F$ . Here the error bars reflect the total statistical uncertainties from fitting the condensate fraction and the atom numbers, but not the calibration uncertainties in the atom numbers. The latter result in an additional systematic scaling uncertainty of  $\pm 7\%$ .

we observe a steady increase of the condensate fraction until a maximum of  $\beta \approx 0.8$  is reached near 75 mW. The conditions of the Fermi sea of  ${}^6\text{Li}$  atoms are exactly the ones already described in the preceding section.

Using Eq. (5.6) and applying small finite-size and interaction corrections to the critical temperature [Gio96], we derive the relative temperature  $T/T_F$  for the degenerate Fermi gas<sup>4</sup>. The results are shown in Fig. 5.4(b). We observe lowest values of  $T/T_F \approx 0.07$  for  $P$  between 70 and 85 mW. This power range corresponds to what we have identified before as the crossover regime between evaporative cooling and spilling. In the spilling regime, we see an increase in the relative temperature, due to a fast spilling of the Li atoms. We conclude that the deepest degeneracy of the Fermi gas is achieved when the evaporation is stopped just before the onset of spilling.

Figure 5.5 displays the absolute temperature  $T$  derived according to Eqs. (5.1) and (5.2) from the BEC fraction data already presented in Fig. 5.4(a). We compare these results with the temperature of the thermal component, which we extract from the same time-of-flight images by fitting the expansion dynamics. The comparison shows that both

<sup>4</sup>Finite-size effects and interaction effects lead to small downshifts of  $T_c$ . To derive the temperature from the condensate fraction, for the sake of simplicity, we use Eq. (5.1) with corrections to  $T_c$  from [Gio96]. Even at our smallest atom numbers, the temperature corrections stay well below 10%. Interaction corrections in our largest clouds stay below 2%.

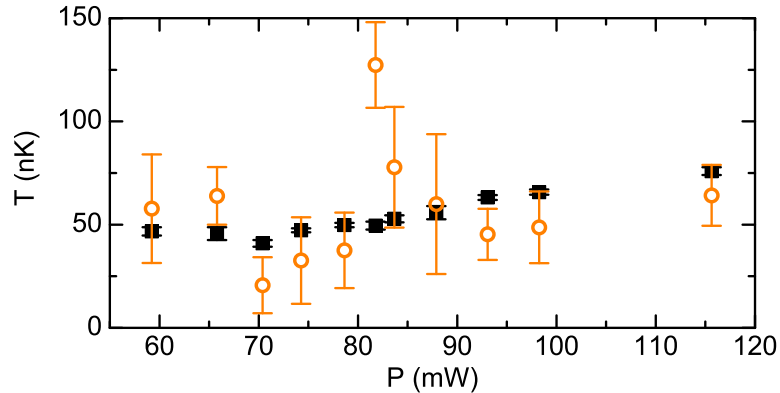


FIGURE 5.5: Comparison of two methods to obtain the temperature from time-of-flight images. The filled symbols represent the temperatures determined from the condensate fraction [see data in Fig. 5.4(a)] together with the total number of bosons and the separately measured trap frequency. The open symbols represent the temperatures that result from the expansion of the thermal component of the bosonic cloud. For the closed symbols, most of the errors derived are smaller than the symbol size. These errors represent the statistical uncertainties as derived from measurements at seven different expansion times. For the open symbols, the error bars are the uncertainties from fits to the expansion dynamics.

methods provide consistent results, but it also reveals much smaller statistical uncertainties (see error bars) for the first method. This observation highlights an important advantage for accurate thermometry of our method that is based on the determination of the condensate fraction.

In an additional set of experiments, we have addressed the question of whether the presence of the  $^{41}\text{K}$  bosons has an influence on the cooling of the Fermi gas. We therefore reduced the number of K atoms from about 15,000 (similar to Fig. 5.4) down to about 7500. Here, for the sake of shorter data acquisition time, we applied a simpler, but somewhat less accurate detection scheme than before<sup>5</sup>. In Fig. 5.6, we show the results for four different values of the K atom number. The BEC fraction in (a) decreases for a reduced number of bosons, but this can be fully attributed to the reduced critical temperature. The relative temperature in (b) shows a significant decrease for the lowest number of bosons.

Our results show that a reduction of the number of K atoms slightly improves the cooling performance of the Li Fermi gas. We interpret this observation as a consequence of the weak additional heat load associated with the bosons, which has to be removed by the evaporative cooling process. However, we do not observe any significant effect on the temperature of the Fermi sea if the number of K atoms stays below 12,000, which corresponds to about 3.0% of the total number of  $^6\text{Li}$  atoms. The lowest temperature that we have observed in these measurements corresponds to  $T/T_F \approx 0.06$ .

<sup>5</sup>In Fig. 5.6, we have used a single time of flight of 22 ms to reduce the total measurement time. This method may be somewhat less accurate, but produces results fully consistent with the method used in Fig. 5.4.

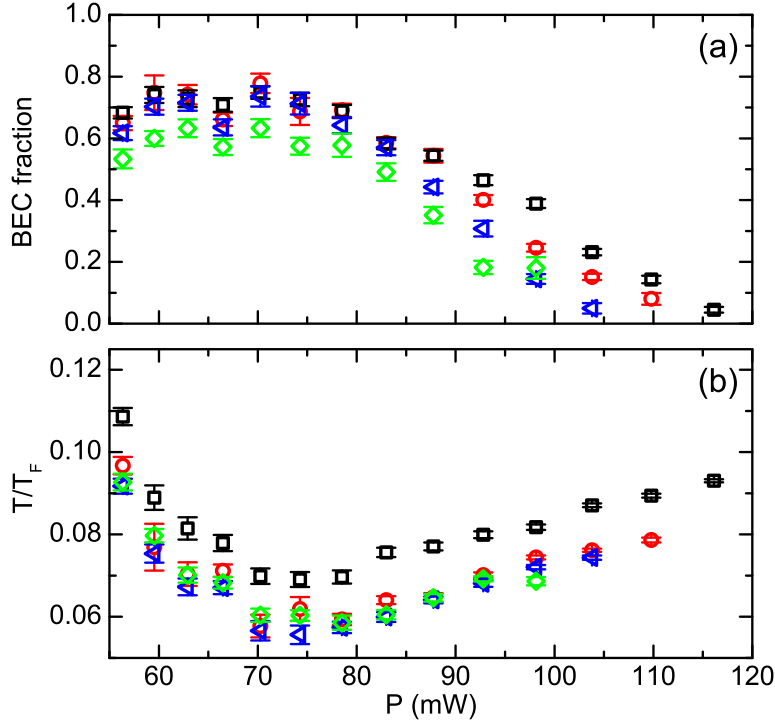


FIGURE 5.6: Influence of the number of bosons on (a) the condensate fraction  $\beta$  and (b) the resulting relative temperature  $T/T_F$ . Four different data sets are shown, with different numbers of bosonic K atoms: black squares,  $N_B = 1.5(1) \times 10^4$ ; red circles,  $1.2(1) \times 10^4$ ; blue triangles,  $0.9(1) \times 10^4$ ; green diamonds,  $0.76(6) \times 10^4$ . The error bars represent the statistical uncertainties as derived from the fit errors of the condensate fraction.

### 5.5.3 Thermalization and heating dynamics

A central assumption underlying our paper is thermal equilibrium between the boson “thermometer” and the Fermi sea. In order to test the validity of this assumption we have investigated the thermalization dynamics and residual heating effects that may affect our results. In all experiments discussed before, a hold time of 10 s was introduced between the end of the evaporation ramp and the temperature measurement. We now present measurements on the temperature evolution during this hold time at a constant trap power of  $P = 75$  mW, again based on the detection of the condensate fraction. Figure 5.7(a) shows how the temperature drops from about 78 nK right after the evaporation ramp to its equilibrium value of 53 nK. An exponential fit yields a thermalization time scale of 2.5(5) s, which is short compared with the total hold time of 10 s. This ensures that the K cloud reaches its equilibrium temperature with negligible deviations well below 1 nK.

The thermalization time can be estimated from our experimental parameters, using the approximation

$$\frac{1}{\tau} = 2 \cdot \frac{3T}{2T_F} \cdot \frac{\xi}{3} \cdot n_F \sigma v_F, \quad (5.12)$$

which is a product of four factors. The prefactor of 2 accounts for the two different spin states in the Fermi sea. The factor  $3T/(2T_F) \approx 0.1$  results from the Pauli blocking of

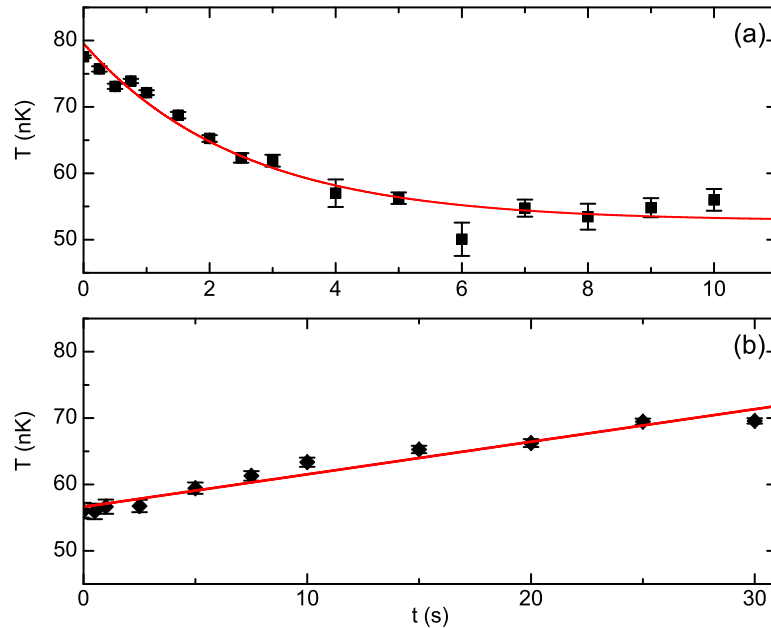


FIGURE 5.7: Thermalization and heating dynamics with and without the Fermi sea. (a) The data points show the measured temperature evolution of the bosonic  $^{41}\text{K}$  cloud [ $N_B = 1.6(2) \times 10^4$ ] after evaporative cooling of the  $^6\text{Li}$  Fermi sea. The solid curve is an exponential fit, yielding a relaxation-time constant of 2.5(5)s. (b) The data points display the measured temperature increase of the  $^{41}\text{K}$  cloud after full removal of the  $^6\text{Li}$  coolant. The linear fit (solid line) yields a heating rate of 0.49(4) nK/s. The error bars represent the temperature uncertainties as derived from the fit errors of the condensate fraction.

collisions<sup>6</sup>. The third factor  $3/\xi$  estimates the number of elastic collisions needed for thermalization, with  $\xi = 4m_K m_{\text{Li}} / (m_K + m_{\text{Li}})^2 \approx 0.45$  for the specific mass ratio of our mixture [Mud02]. The last factor represents the elastic collision rate in the limit of relative velocities dominated by the light atoms at the top of the Fermi sea, with the corresponding Fermi velocity  $v_F = \sqrt{2E_F/m} \approx 44$  mm/s. The cross section for elastic collisions between  $^6\text{Li}$  and  $^{41}\text{K}$  atoms is  $\sigma \approx 1.3 \times 10^{-16} \text{ m}^2$ <sup>7</sup>. This results in a relaxation time of  $\tau \approx 4.5$  s, which is larger than the observed value, but still within the errors of the simple estimation used.

We have also checked the influence of a possible effect of residual heating of the K cloud, which may be induced by trap light fluctuations. This heat would have to be removed by thermal contact with the coolant, i.e., the Fermi sea of  $^6\text{Li}$  atoms, and the corresponding heat flow would require a temperature difference between the two components. We have experimentally investigated the heating of the K cloud after removing the Li atoms from the trap, by application of a magnetic gradient, and observed the temperature evolution over 30 s. Figure 5.7(b) reveals a very weak temperature increase, with a slope corresponding to a heating rate of  $\gamma_{\text{heat}} \approx 0.5$  nK/s. Here, for simplicity, we assume a linear heating model. With the relaxation time  $\tau \approx 2.5$  s discussed before, we obtain

<sup>6</sup>We approximate this effect by assuming that only the fraction of Li atoms with energies in an interval between  $k_B(T_F - T/2)$  and  $k_B(T_F + T/2)$  is thermally active. The factor 3/2 results from the number of states, which increases  $\propto E^{3/2}$  for the approximately homogeneous environment sampled by the bosons in the trap center.

<sup>7</sup>T. Hanna and E. Tiesinga. (private communication)

a temperature difference of  $\gamma_{\text{heat}}\tau \approx 1.2 \text{ nK}$ , which is negligibly small. In additional experiments, we have investigated heating in our detection trap, see Sec. 5.4.3, and found an effect of less than 2 nK/s within the 4 s when the atoms are kept in this trap.

#### 5.5.4 Uncertainties

Our thermometry approach is based on Eq. (5.6) to determine the relative temperature  $T/T_F$ . The underlying model relies on the harmonic approximation of the trap potential, and we estimate that anharmonicity effects on  $T_F$  do not exceed a few percent.

The model also assumes the bosonic probe to be a weakly interacting gas, which is well fulfilled. We have checked that we are not near any intraspecies or interspecies Feshbach resonances. Furthermore, the intraspecies background scattering length of  $^{41}\text{K}$  is about  $+60 a_0$  [D'E07, Pat14] and the background scattering length between  $^6\text{Li}$  and  $^{41}\text{K}$  is also about  $+60 a_0$ <sup>8</sup>. This means that for the reference power ( $P = 75 \text{ mW}$ ) and  $N_B \approx 1.2 \times 10^4$ , the chemical potential of the bosons corresponds to  $\sim 16 \text{ nK}$ . The peak number density of the fermions is about 26 times smaller than the one of the bosons. The mean field of the fermions as seen by the bosons is very small, only  $\sim 2.3 \text{ nK}$ . The correction to the boson trap frequencies caused by the fermion mean field, is on the order of  $10^{-3}$ , which is negligibly small. The mean field of the bosons on the fermions corresponds to  $\sim 64 \text{ nK}$ , which is much smaller than the Fermi energy of about 710 nK. In addition to these model assumptions, the experimental determination of the temperature is subject to four main error sources. First of all, there are the statistical measurement uncertainties. These come from the analysis of the time-of-flight images and give uncertainties of a few percent in both the atom number and the determination of the condensate fraction.

A second source that influences the measured values of  $T/T_F$  are calibration errors. For the atom number determination, we estimate calibration uncertainties of 15% for both species. This results in a systematic scaling uncertainty in  $T/T_F$  of  $\pm 7\%$ . Another systematic error source is the trap frequency ratio, which slightly changes if the trap does not exactly fulfill the magic levitation condition. However, the effect on  $T/T_F$  for the range of powers used in our experiments is negligibly small.

Third, the thermalization between the two species may be imperfect, owing to heating in combination with weak thermal coupling. We estimate that the corresponding temperature difference stays below 2 nK, which results in an effect below 3% on the relative temperature.

Furthermore, as a fourth error source, we observed a slight heating effect during the transfer into the detection trap, which may also affect the temperature by a few percent at most. We are confident that other heating sources are very weak and can be safely neglected. All these residual heating effects may somewhat increase the temperature of the bosonic probe atoms, and may thus lead to an overestimation of the temperature, but not by more than 10%.

Taking all statistical and systematic uncertainties into account, we can report a lowest

---

<sup>8</sup>T. Hanna and E. Tiesinga. (private communication)

observed temperature of  $T/T_F = 0.059(5)$ <sup>9</sup>. The true temperature of the Fermi gas may even be slightly below this value (about 5%) because of residual heating directly affecting the thermometry atoms.

## 5.6 Conclusion

We have thoroughly investigated a conceptually simple and accurate method for determining the temperature of a deeply degenerate Fermi gas. Our method essentially relies on detecting the condensate fraction of a second, weakly interacting bosonic species that is thermalized with the Fermi sea. High accuracy of the temperature measurements can be achieved, since the relevant trap frequency ratio can be very well determined and uncertainties in the atom number only weakly influence the results.

We have employed the method in experiments on a spin mixture of  ${}^6\text{Li}$ , where we have used a small sample of  ${}^{41}\text{K}$  bosons as the probe. The large mass ratio and a large number ratio have enabled us to measure the temperature in the range of 0.03 to  $0.1 T_F$ , which is right in the regime of state-of-the-art cooling experiments. We have investigated the final stage of deep evaporative cooling and we have observed that the deepest degeneracy of the Fermi gas, with  $T/T_F = 0.059(5)$ , is achieved when the evaporation is stopped just before the onset of spilling. We found the temperature not to be affected by the presence of the probe atoms if the number of K atoms stays below 3.0% of the number of Li atoms. The K atoms then represent impurities in a Fermi sea.

Our thermometry method provides us with a powerful tool to further optimize the cooling. For optimization, we can improve the starting conditions for evaporation by implementing a sub-Doppler cooling stage [Bur14, Sie15] and we can optimize the evaporation sequence by variation of the magnetic field, the trap configuration and the details of the ramp. With sensitive and accurate thermometry, it will be very interesting to investigate the practical and fundamental limitations of the cooling process. Under our present conditions, we may be limited by residual trap light fluctuations [Sav97] or other sources of noise in the experiment or by inelastic losses in combination with the hole heating effect [Tim01].

For the interaction parameter of  $1/(k_F a) \approx -1.6$ , as chosen in our experiments, the predicted critical temperature for superfluidity is  $\sim 0.03 T_F$  [Blo08, Hau07]. Thus, even for our lowest temperatures, the Li spin mixture is not superfluid. However, the system is stable enough at resonant interaction conditions [Spi09], so that the realization of a mass-imbalanced Bose-Fermi double superfluid, as already demonstrated in Ref. [Yao16], would be straightforward. Thermometry on the bosons could be performed in a wide range of the BEC-BCS crossover, as long as the thermalization time stays much shorter than the timescale of inelastic losses<sup>10</sup>. While the BEC side may be problematic [Spi09], the method would work well in the unitary case and on the BCS side.

The implementation of the presented thermometry method should be straightforward for other Bose-Fermi mixtures. Extreme mass ratios [Pir14, Tun14, Roy17, Kon16] are

<sup>9</sup>The reported temperature is the mean value of the red circles, blue triangles, and green diamonds in Fig. 5.6, in the range of 68 – 80 mW.

<sup>10</sup>Inelastic decay of  ${}^{41}\text{K}$  is observed predominantly on the BEC side of the  ${}^6\text{Li}$  Feshbach resonance, similar to what was observed on a strongly interacting  ${}^{40}\text{K}$ - ${}^6\text{Li}$  mixture [Spi09]

of particular interest for pushing the accessible regime further down to temperatures on the order of  $0.01 T_F$ . However, at such ultralow temperatures, the larger number of collisions required for thermalization and the increasing Pauli blocking effect will increase the thermalization time, which will make it more difficult to reach thermal equilibrium on a realistic experimental time scale. This may be compensated for by larger interspecies collision cross sections or higher number densities. Our paper shows how the conditions can be optimized for specific mixtures, including the role of optical polarizabilities, magnetic moments, magnetic levitation for trapping, and the effect of interspecies collisions. In our future work, we are particularly interested in the deep cooling of the Fermi sea. This reduces thermal decoherence effects as observed in studies of impurities coupled to the Fermi sea [Cet15] and opens up the possibility of observing new phenomena [Cet16], such as multiple particle-hole excitations and the onset of the orthogonality catastrophe [Kna12]. Moreover, we are interested in the collective zero-temperature dynamics of bosonic impurities in the Fermi sea close to an interspecies Feshbach resonance [Lou18b, Hua19].

## 5.7 Acknowledgments

We thank J. Walraven for stimulating discussions, Y. Colombe for fiber fusing, L. Reichsöllner for support regarding the atomic-beam characterization, the Dy-K team for general discussions, and M. Cetina for contributions in the early stage of the  $^{41}\text{K}$  implementation. We also thank F. Lehmann, E. Kirilov and R. Onofrio for comments on the paper. We acknowledge support by the Austrian Science Fund FWF within the Spezialforschungsbereich FoQuS (F4004-N23) and within the Doktoratskolleg ALM (W1259-N27).

## 5.8 Appendix: ‘Magic’ levitation trap

We refer to a ‘magic’ levitation trap as an optical dipole trap for two different species, in which the corresponding potential depths and trap frequencies maintain a constant ratio at any optical power applied. In optical dipole trapping experiments, one often has to deal with the effect of gravity. Two species in the same trap are in general affected differently, in particular in the case of largely different masses or different optical polarizabilities. The tilted potentials usually give a different reduction of the effective trap depth as compared to the depth of the optical potentials. During evaporative cooling this often leads to a much faster reduction of the potential depth for the heavier species than for the lighter one, which may pose a severe limitation to the whole cooling process. Magnetic levitation [And95, Han01, Web03a] offers a solution to this problem and allows one to realize conditions, where the combined effect of gravity and levitation results in the same effect on the total shape of the potential.

The magic gradient can be derived from the condition that the combined magnetic and gravitational force is the same for both traps, if considered relative to the optical

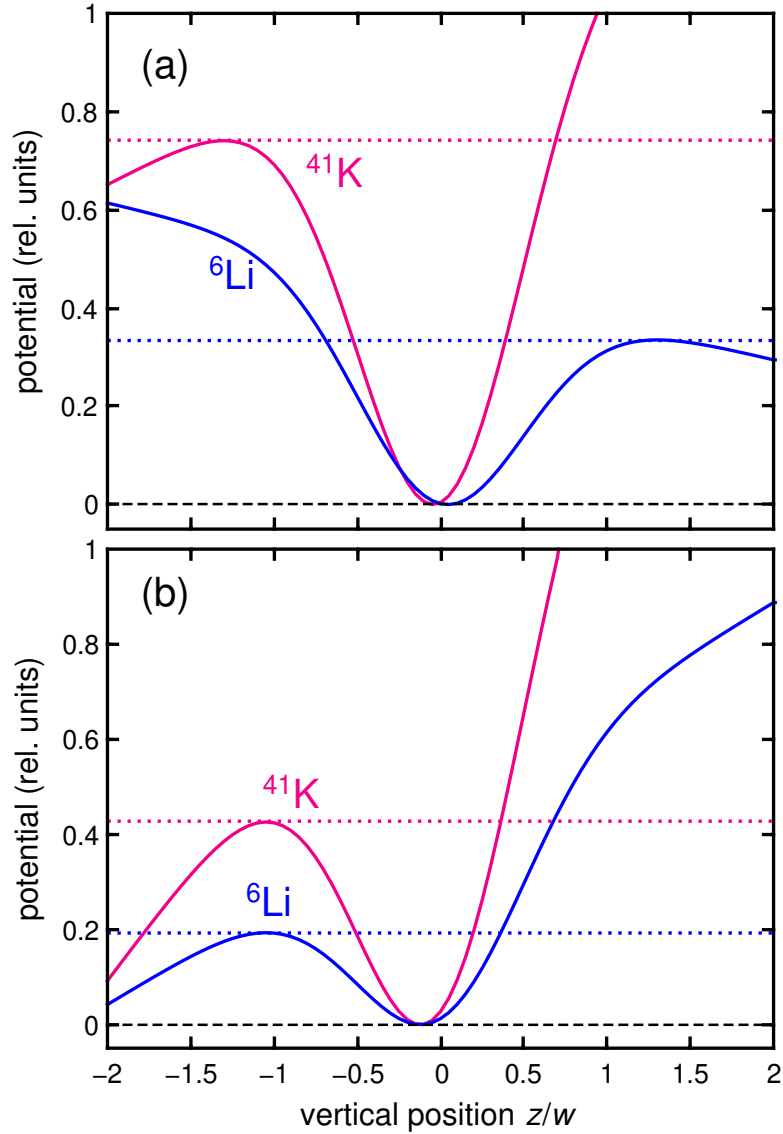


FIGURE 5.8: (Color online) Illustration of magic levitation for  $^6\text{Li}$  and  $^{41}\text{K}$ . All potentials are normalized to the optical potential depth of K, and zero potential refers to the trapping potential minima. The combined magnetic and gravitational forces cause a trap depth reduction, as indicated by the horizontal dotted lines. For two distinct values of the magnetic gradient, see Eq. (5.14), the ratio of the resulting trap depths for K and Li remains constant and corresponds to the ratio of optical polarizabilities ( $\alpha_{\text{K}}/\alpha_{\text{Li}} \approx 2.2$ ). (a) With the magnetic gradient set to  $B'_-$ , K is partially levitated, while Li is overlevitated. The relative tilt has the same magnitude, but opposite sign. (b) With the gradient set to  $B'_+$ , the magnetic force effectively increases the effect of gravity for both species, resulting in a tilt in the same direction.

potential, the depth of which in turn is proportional to the optical polarizabilities. The condition reads

$$\frac{\mu_1 B'_\pm - m_1 g}{\alpha_1} = \pm \frac{\mu_2 B'_\pm - m_2 g}{\alpha_2}, \quad (5.13)$$

where  $m_i$ ,  $\mu_i$ , and  $\alpha_i$  represent the different masses, magnetic moments, and optical polarizabilities of the two species, respectively. The lower sign refers to the situation illustrated in Fig. 5.8(a), where the trapping potentials are tilted in the opposite direction. The upper sign corresponds to the situation, where both potentials are tilted in the same direction. Solving Eq. (5.13) yields the two corresponding magnetic gradients

$$B'_\pm = \frac{\alpha_2 m_1 \mp \alpha_1 m_2}{\alpha_2 \mu_1 \mp \alpha_1 \mu_2} g. \quad (5.14)$$

The solution  $B'_-$  means partial levitation for one species and overlevitation for the other one, so that the tilts have opposite signs. The other solution ( $B'_+$ ) corresponds to the same direction of the tilt for both species. The application of  $B'_-$  causes a separation of the trap centers, similar to the gravitational sag effect. In contrast,  $B'_+$  does not cause such a spatial shift, but it may imply much stronger tilts. The optimum solution for an experiment depends on the specific situation.

For our situation of optically trapped  ${}^6\text{Li}$  and  ${}^{41}\text{K}$  at high magnetic bias fields ( $\mu_1 = \mu_2 \approx \mu_B$ ), we obtain a magic levitation gradient of  $B'_- = 2.97 \text{ G/cm}$ , corresponding to a partial levitation of 41.3% for K and an overlevitation of 281% for Li. The small spatial separation of the trap centers is irrelevant for our application. For the experimental power range we use, the separation between the trapcenters of the two species lies between 12 and 28 % of the optical beam waist. Note that the other solution ( $B'_+ = -4.02 \text{ G/cm}$ ) does not correspond to levitation, but to an effective increase of the gravitational effect for both species. As described in Sec. 5.4.2, we realize a situation close to the magic levitation gradient  $B'_-$ .

# 6

## Chapter 6

# Publication: Probing the Interface of a Phase-Separated State in a Repulsive Bose-Fermi Mixture

Journal: Physical Review Letters, Vol. **120**, Issue 24

Published: 13. June 2018

DOI: [10.1103/PhysRevLett.120.243403](https://doi.org/10.1103/PhysRevLett.120.243403)

Rianne S. Lous<sup>1,2</sup>, Isabella Fritsche<sup>1,2</sup>, Michael Jag<sup>1,2</sup>, Fabian Lehmann<sup>1,2</sup>, Emil Kirilov<sup>2</sup>, Bo Huang<sup>1</sup>, and Rudolf Grimm<sup>1,2</sup>

<sup>1</sup> Institut für Quantenoptik und Quanteninformation, Österreichische Akademie der Wissenschaften, 6020 Innsbruck, Austria.

<sup>2</sup> Institut für Experimentalphysik, Universität Innsbruck, 6020 Innsbruck, Austria.

Contribution to the publication: I contributed to this publication by taking calibration and preparation measurements as well as assisting in taking the main measurements. All authors contributed on writing the manuscript.

Note on the present version of the publication: This version can vary from the published version since final changes by the editor are not included. Typos have been corrected. The sections structure has been introduced for better readability and references have been updated.

## 6.1 Abstract

We probe the interface between a phase-separated Bose-Fermi mixture consisting of a small Bose-Einstein condensate of  $^{41}\text{K}$  residing in a large Fermi sea of  $^6\text{Li}$ . We quantify the residual spatial overlap between the two components by measuring three-body recombination losses for variable strength of the interspecies repulsion. A comparison with a numerical mean-field model highlights the importance of the kinetic energy term for the condensed bosons in maintaining the thin interface far into the phase-separated regime. Our results demonstrate a corresponding smoothing of the phase transition in a system of finite size.

## 6.2 Introduction

Multicomponent systems and materials are ubiquitous in nature and technology. The interactions between the different constituents and the ways in which they coexist are essential for understanding the general properties of such systems. Repulsive interactions between different components can induce phase transitions to spatially separated states. The effects of phase separation appear in a wide range of different systems such as alloys, combinations of different liquids, colloids, polymers, glasses and biological systems. In a phase-separated state, the interaction between the components no longer takes place in the bulk but is restricted to the thin interface where the constituents still maintain some residual overlap. The physics of this interface has therefore attracted a great deal of attention in many different fields, e.g. in liquid-liquid systems [Dav96, Han13]. However, since the interaction takes place in a very small volume, it is generally much more difficult to obtain experimental information from these systems as compared to systems in which the components are mixed.

Quantum fluids exhibit a great wealth of phenomena related to phase separation. Early experiments with cryogenically cooled liquid helium have shown phase separation in mixtures of the bosonic isotope  $^4\text{He}$  and the fermionic  $^3\text{He}$  [Ebn71]. This effect has found an important technological application in the working principle of dilution refrigerators [Das65, Pob07]. Ultracold gases, in particular, mixed-species systems have opened up many intriguing experimental possibilities to study phases of multicomponent quantum matter [Blo08]. The large experimental toolbox includes a variety of available bosonic and fermionic constituents, a superb level of control of confinement, and a wide tunability of interactions [Chi10]. Phase separation has been studied extensively in degenerate Bose-Bose mixtures [Pap08, Toj10, McC11, Sta13, Wac15, Wan15, Lee16], where interactions are dominated by mean-field potential energies. The situation becomes more complicated when fermionic constituents are involved, as strong repulsion on the scale of the Fermi energy is required to observe phase separation. Superfluid fermionic mixtures [Shi08] and repulsive atomic Fermi gases [Val17] are examples of intriguing phase-separation effects. In a broad sense, mixtures involving fermionic constituents are promising candidates for realizing new phases, e.g., in Fermi-Fermi systems [Liu03a, Isk06, Par07, Bar08b, Baa10, Wan17] and in Bose-Fermi systems [Pow05, Suz08, Mar08, Lud11, Ber13, Kin15].

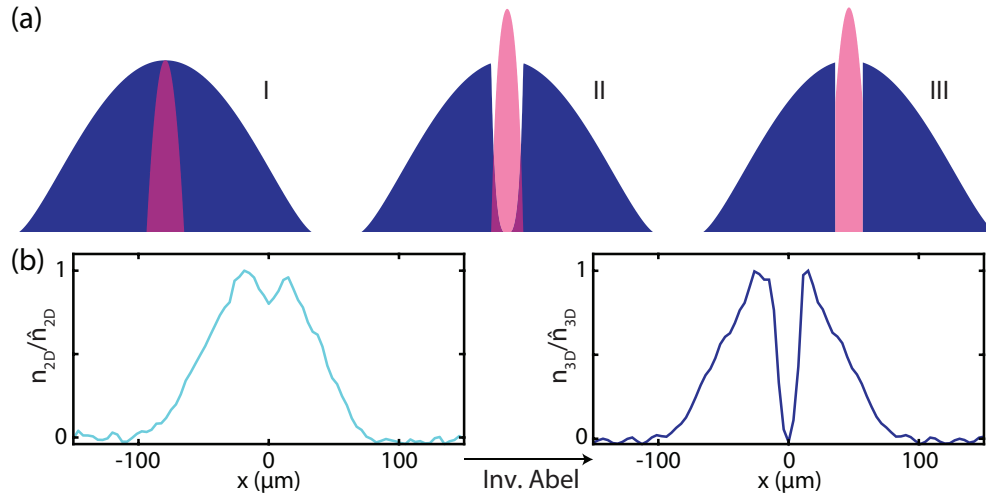


FIGURE 6.1: Emergence of phase separation. (a) Schematic density profiles for bosons (magenta) and fermions (blue) for an increasing repulsive interaction. The densities are normalized to the corresponding peak value without an interaction. Note that in reality the boson peak density is a factor of 40 larger than the fermion peak density. (b) Experimentally observed normalized column density of a cut through the fermionic cloud and normalized reconstruction of the corresponding radial density profile using the inverse Abel transformation.

In this Letter, we consider a Bose-Fermi model system that undergoes phase separation and study the interface between the constituents. We produce a Bose-Einstein condensate (BEC) of  $^{41}\text{K}$  atoms in a large Fermi sea of  $^6\text{Li}$ , and we use an interspecies Feshbach resonance for controlling the repulsive interaction. We characterize the overlap between the species by measuring three-body recombination losses and thus probe the thin interface between both components. By comparing the experimental results with theoretical model calculations, we demonstrate the importance of the kinetic energy of the condensed bosons at the thin interface.

### 6.3 General idea

Figure 6.1(a) illustrates the onset of phase separation with an increasing interspecies repulsion, showing the density profiles of a small-sized BEC coexisting with a large Fermi sea in a harmonic trap. The main conditions and criteria for phase separation in such Bose-Fermi mixtures have been theoretically introduced in Refs. [Møl98, Viv00, Rot02]. For a vanishing interspecies interaction, the independent spatial profiles of the clouds show maximum overlap [I in Fig. 6.1(a)]. With an increasing repulsion, the density of the lithium atoms in the center of the trap decreases, the BEC is compressed, and the spatial overlap between the clouds is reduced (II). For strong repulsive interactions, the two clouds undergo phase separation (III), and the bosons reside at the center of the trap, forming a hole in the Fermi sea.

We can observe the depletion in the center of the Fermi sea by imaging the  $^6\text{Li}$  cloud. As Fig. 6.1(b) shows, we observe a small dip in the radial column density profile taken from a thin slice of the fermion cloud. These data were taken under similar conditions

as our main data presented later <sup>1</sup>. The hole in the fermion density becomes more visible when reconstructing the fermionic radial density profile using the inverse Abel transformation [Fig. 6.1(b)]. We see an essentially complete depletion of the fermionic density in the center, which indicates a significant reduction of the overlap with the BEC. A quantitative analysis of the physics at the interface is obstructed by the limited signal-to-noise ratio of the image, the small size of the overlap region compared to our imaging resolution, and the high optical density of the trapped cloud. Note that strong indications of phase separation in a Bose-Fermi mixture have been observed in earlier experiments on mixtures of <sup>87</sup>Rb and <sup>40</sup>K [Osp06b, Zac06], but these experiments did not provide quantitative information on the overlap reduction.

Here, we introduce an alternative approach to study the spatial overlap between the two species. Our observable is the boson-boson-fermion three-body recombination loss from the trap. We assume that all losses can be attributed to three-body processes, since two-body losses are energetically suppressed when both atomic species are in their lowest internal substates. In our system, decay processes of three <sup>41</sup>K atoms (three identical bosons) occur at a very low rate, since the intraspecies scattering length  $a_{bb} = 60.9a_0$  <sup>2</sup>, with  $a_0$  being the Bohr radius, is small compared with the interspecies scattering length  $a_{bf}$  in the range of interest. On the other hand, recombination processes involving one <sup>41</sup>K atom and two <sup>6</sup>Li atoms (one boson and two identical fermions) are Pauli suppressed [Esr01]. At a large interspecies scattering length, this leaves the recombination events of two <sup>41</sup>K atoms with one <sup>6</sup>Li atom as the dominant three-body decay mechanism.

A favorable property of our system is the fact that the BEC is much smaller than the fermion cloud and occupies a very small volume within the Fermi sea. Thus, the BEC can cause only a local perturbation of the Fermi sea with a negligible effect on the global scale. This scenario enables a description in terms of a *fermionic reservoir approximation* (FRA), which assumes a homogeneous environment characterized by a constant Fermi energy  $E_F$  and considerably simplifies our study of the overlap.

In the zero-temperature limit, where a pure BEC is formed, the bosonic atom loss can be related to the overlap integral as

$$\dot{N} = -\frac{1}{2} L_3 \int n_f n_b^2 dV, \quad (6.1)$$

where  $N$  is the total number of bosons and  $n_b$  and  $n_f$  represent the position-dependent number densities of the bosons and fermions, respectively. The parameter  $L_3$  is the three-body loss coefficient, and the symmetry factor  $1/2$  results from the suppression of thermal bunching in a BEC [Kag85, Bur97, Söd99, Hal11] for a process involving two identical bosons. The  $L_3$  coefficient can be determined as a function of  $a_{bf}$  in a standard way [Web03b, Ulm16] using a noncondensed cloud instead of a BEC. In this case, the interspecies repulsion can be neglected, and the density profiles of the bosons and the fermions are well known.

In order to characterize the effect of the boson-fermion interaction on the spatial overlap

<sup>1</sup>The thin slice is taken from a typical absorption image of the Li cloud with a time of flight of 2 ms and at  $a_{bf} \approx 1480a_0$

<sup>2</sup>Eberhard Tiemann. (private communication)

between the BEC and the Fermi sea, we define the overlap factor

$$\Omega \equiv \frac{\int n_f n_b^2 dV}{\int \tilde{n}_f \tilde{n}_b^2 dV} \quad (6.2)$$

as the three-body density integral normalized to the case of vanishing interspecies interaction ( $a_{bf} = 0$ ), where  $\tilde{n}_f$  ( $\tilde{n}_b$ ) is the fermionic (bosonic) noninteracting density.

The overlap integral for the case of a vanishing interspecies interaction,  $\int \tilde{n}_f \tilde{n}_b^2 dV$ , can be calculated analytically based on two approximations. First, we apply the FRA and replace  $\tilde{n}_f$  by its peak value  $\hat{n}_f$ , which as a constant factor can be taken out of the integral. Second, for a not too small BEC, we can apply the Thomas-Fermi approximation and solve  $\int \tilde{n}_b^2 dV$  as  $\frac{4}{7} N_b \hat{n}_b$ , with  $\hat{n}_b$  the peak density of the BEC. Finally, with the overlap integral for the interacting case given by Eq. (6.1), the overlap factor can be experimentally obtained as

$$\Omega = \frac{7}{2 \hat{n}_f \hat{n}_b} \frac{\gamma}{L_3}, \quad (6.3)$$

where we introduce the normalized loss rate  $\gamma = -\dot{N}/N$  as the experimental observable extracted from measuring the atom loss in a BEC.

## 6.4 Main results

For our experiments, we prepare an ultracold Bose-Fermi mixture of typically  $10^4$  K and  $10^5$  Li atoms in a cigar-shaped, crossed-beam optical dipole trap with a wavelength of 1064 nm and an aspect ratio of 1:7. The preparation procedures are similar to those described in Ref. [Lou17] and earlier work on  ${}^6\text{Li}$ - ${}^{40}\text{K}$  mixtures [Spi09, Tre11, Koh12, Jag14, Cet16]. In addition, we employ a laser cooling scheme for lithium using the  $D1$  line [Gri13, Bur14, Fri15], which provides improved starting conditions, and we take advantage of an alternative evaporative cooling approach [Bur14] (see also Sup.Mat. in Sec. 6.7).

A key ingredient of our experiment is the Feshbach resonance (FR) near  $335 \text{ G}^3$  [Wu11, Lou18a] (see also Sup.Mat. 6.7), between the lowest spin states of the two species. The scattering length can be varied by magnetic field tuning according to

$a_{bf} = a_{bg} [1 - \Delta/(B - B_0)]$  [Chi10], where  $\Delta = 0.949 \text{ G}$ ,  $a_{bg} = 60.9a_0$  and  $B_0 = 335.057(1) \text{ G}$ . The FR center  $B_0$  somewhat depends on the optical trap intensity because of a light shift effect (see Sup.Mat. in Sec. 6.7) and can be experimentally determined by radio-frequency spectroscopy. The other parameters are obtained from scattering models<sup>4</sup> (see also Sup.Mat. in Sec. 6.7).

To obtain the critical interspecies scattering length for the onset of phase separation, we employ the FRA together with the results of Ref. [Viv00]. This yields the condition

$$a_{bf} > 1.15 \sqrt{a_{bb}/k_F}, \quad (6.4)$$

<sup>3</sup>E. Tiemann and T.M. Hanna and E. Tiesinga and P.S. Julienne. (Private Communication)

<sup>4</sup>E. Tiemann and T.M. Hanna and E. Tiesinga and P.S. Julienne. (Private Communication)

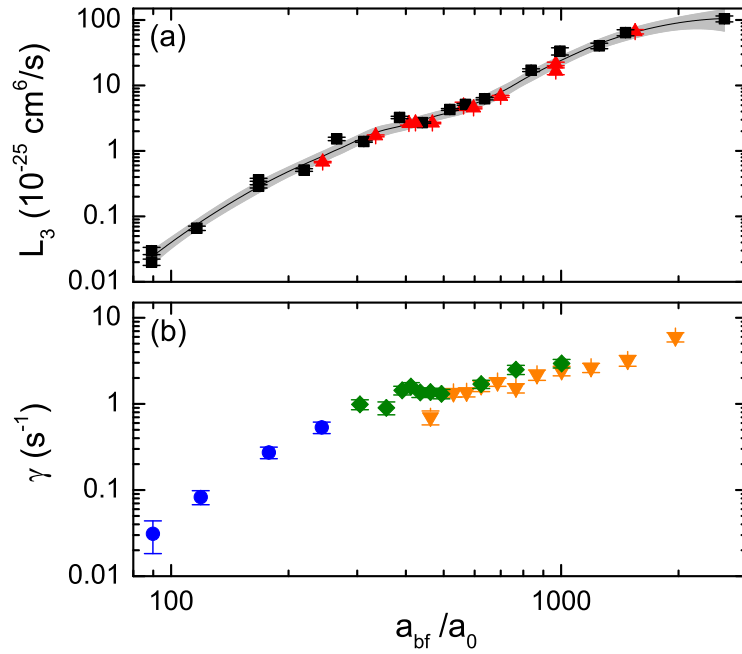


FIGURE 6.2: Loss measurements on noncondensed and condensed bosonic  $^{41}\text{K}$  clouds in a  $^6\text{Li}$  Fermi sea. The error bars represent  $1\sigma$  fit uncertainties. (a) Three-body loss coefficient  $L_3$  for  $T = 440$  (set A1: squares) and 240 nK (set A2: triangles). The solid curve is an interpolation from applying a smoothing method (see Sup.Mat. in Sec. 6.7), with the gray-shaded area representing the corresponding 95% confidence band. (b) Normalized loss rate  $\gamma$  of the total atom number of a partially condensed bosonic cloud for data sets B1-B3 (inverse triangles, diamonds, and circles, respectively).

where  $k_{\text{F}} = (6\pi^2\hat{n}_{\text{f}})^{1/3}$  is the Fermi wave number, corresponding to  $E_{\text{F}} = \hbar^2 k_{\text{F}}^2 / (2m_{\text{f}})$  with  $m_{\text{f}}$  the mass of the fermions. For our typical experimental conditions ( $\hat{n}_{\text{f}} \approx 1.2 \times 10^{12} \text{ cm}^{-3}$ ), it gives a moderate value for the critical scattering length of about  $600a_0$ . This is well within our tuning range and allows us to explore the entire scenario from weak to strong repulsion, reaching far into the phase-separated regime.

We first present our measurements of  $L_3$ , which were obtained with noncondensed samples of  $^{41}\text{K}$  in a degenerate Fermi sea of  $^6\text{Li}$  at about  $0.2T_{\text{F}}$ , with  $T_{\text{F}}$  the Fermi temperature. From the measured decay curves we obtain the  $L_3$  values that are shown in Fig. 6.2(a). The K samples are prepared close to degeneracy at two different temperatures with a typical fermion peak density of  $\hat{n}_{\text{f}} \approx 4.5 \times 10^{12} \text{ cm}^{-3}$ . In one set of measurements (set A1, see Sup.Mat. in Sec. 6.7), we have  $T = 440$  nK, corresponding to  $T/T_{\text{c}} = 1.7$  with  $T_{\text{c}}$  the critical temperature for condensation. In the other set (A2), we have  $T = 240$  nK, corresponding to  $T/T_{\text{c}} \approx 1$ . By applying a smoothing method (see Sup.Mat. in Sec. 6.7), we interpolate between the data points and obtain  $L_3$  for any  $a_{\text{bf}}$  between 80 and  $2100a_0$ . Our results on  $L_3$  show the expected strong increase with  $a_{\text{bf}}$ , while the broad dent around  $600a_0$  may point to an Efimov-related feature [Kra06, Joh17].

Second, we present the boson loss rate  $\gamma$  in a degenerate Bose-Fermi mixture at various interaction strengths. Typically, we have  $2.9 \times 10^4$  K atoms with a 50% condensate fraction in a Fermi sea of  $1.4 \times 10^5$  Li atoms with a peak density of  $\hat{n}_{\text{f}} = 1.2 \times 10^{12} \text{ cm}^{-3}$  and a temperature of  $\sim 0.13T_{\text{F}}$ . The sample is first prepared at 200 mG below  $B_0$ , and

then the magnetic field is changed in a near-adiabatic ramp of 2 ms to the specific field on the repulsive side of the FR, where we observe the loss of the K atoms for various hold times. We fit the initial decay of the total atom number with a linear curve and determine the normalized loss rate  $\gamma$  (see Sup.Mat. in Sec. 6.7). Figure 6.2(b) shows the corresponding data points, which were recorded in three sets (B1-B3, see Sup.Mat. in Sec. 6.7) with slightly varying parameters.

With the normalized loss rate  $\gamma$  and the three-body recombination coefficient  $L_3$ , we can now quantify the spatial overlap. In a real experiment, two complications arise that require an extension of our model beyond Eq. (6.3). First, at a finite temperature, we have only a partial BEC and the presence of the thermal component plays a significant role in the observed loss. Second, there is the possibility of observing secondary loss, where a short-lived LiK dimer, produced in a first recombination, recollides with another K atom, and therefore this leads to additional loss (see Sup.Mat. in Sec. 6.7). This process is likely to happen for the dense BEC but negligible for the thermal K cloud. To take both effects into account, we extend Eq. (6.1) and include all loss contributions:

$$\dot{N} = -L_3 \int n_f \left( \frac{1}{2} \alpha n_b^2 + \alpha n_b n_t + n_t^2 \right) dV, \quad (6.5)$$

where  $n_t$  represents the thermal bosonic density and  $\alpha$  is a factor that takes into account secondary loss. In our case, we assume  $\alpha = 3/2$  (see Sup.Mat. in Sec. 6.7). The density integral consists of three terms, which describe the loss caused by one fermion and two bosons. The bosons can either be two atoms from the BEC, one from the BEC and one from the noncondensed component, or two from the noncondensed bosonic cloud. Within the FRA and the Thomas-Fermi approximation, these integrals can be calculated, and an effective overlap factor results from an extension of Eq. (6.3) as

$$\Omega_{\text{eff}} = \frac{1}{\hat{n}_f \left[ \frac{2}{7} \alpha \hat{n}_b \beta + \alpha \hat{n}_t \beta + \frac{1}{\sqrt{8}} \hat{n}_t (1 - \beta) \right]} \frac{\gamma}{L_3}, \quad (6.6)$$

where  $\beta$  is the BEC fraction and  $\hat{n}_t$  the peak density of a thermal Bose gas, as given by  $\hat{n}_t = [m_b \bar{\omega}_b^2 / (2\pi k_B T)]^{3/2} (1 - \beta) N$ , with  $\bar{\omega}_b$  being the geometrically averaged trap frequency of the bosons,  $m_b$  their mass, and  $T = T_c (1 - \beta)^{1/3}$  [Lou17] (see also Sup.Mat. in Sec. 6.7).

Figure 6.3 shows the values of  $\Omega_{\text{eff}}$  that result from the data in Fig. 6.2. We qualitatively distinguish three regions. Below  $a_{\text{bf}} \approx 250a_0$ , the values are close to one, and there seems to be a downward trend for  $\Omega_{\text{eff}}$  with increasing  $a_{\text{bf}}$ . Then, as  $a_{\text{bf}}$  further increases to about  $1000a_0$ , the spatial overlap drastically decreases to a small value of about 0.04. For larger scattering lengths,  $\Omega_{\text{eff}}$  tends to remain at this small value. According to Eq. (6.4), phase separation is expected to happen at  $\sim 600a_0$  (vertical dotted line). In contrast, we observe that beyond this point a considerable spatial overlap remains, which then smoothly decreases with a further increasing scattering length. The observed behavior does not reveal any discontinuity related to a phase transition.

To interpret the observed behavior of  $\Omega_{\text{eff}}$ , we construct a numerical mean-field model [Hua20] (see also Sup.Mat. in Sec. 6.7) which allows us to calculate the density distributions for an interacting Bose-Fermi mixture at a zero temperature for our typical

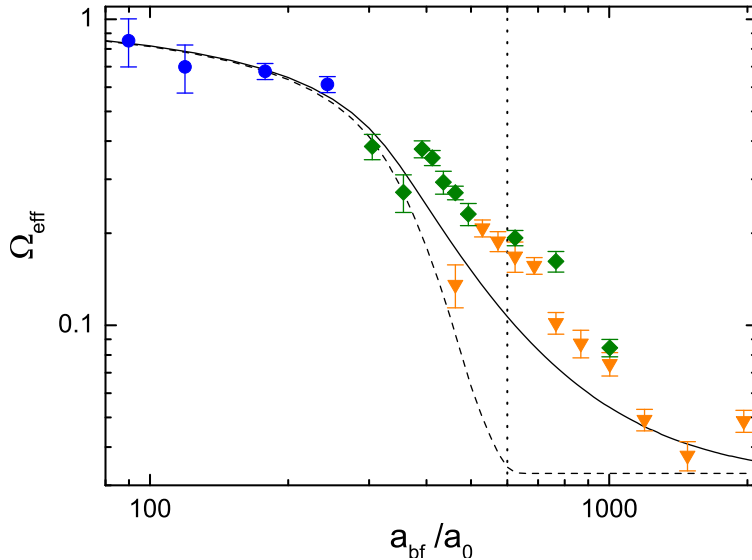


FIGURE 6.3: Effective overlap factor versus Bose-Fermi scattering length for data sets *B1-B3* (inverse triangles, diamonds, and circles, respectively). The error bars reflect the statistical uncertainties of  $\gamma$ . The vertical dotted line shows the phase-separation point as predicted by Eq. (6.4). The solid line shows the results of our full numerical calculation (see the text) and the dashed line our results obtained within the Thomas-Fermi approximation.

experimental parameters<sup>5</sup>. Our model starts from the energy functional of the mixture as given by Refs. [Ima06, Tra16], and we use imaginary time evolution to vary the BEC and the fermionic densities and to minimize the energy functional. At the end, the evolution gives the static solution of  $n_f$  and  $n_b$  at a zero temperature. Since we have a partial BEC, we additionally take into account the thermal bosonic density  $n_t$  including bosonic enhancement effects (see Sup.Mat. in Sec. 6.7). With these density distributions, we numerically calculate the overlap integrals and the effective overlap factor  $\Omega_{\text{eff}}$ .

The results of our numerical model are represented in Fig. 6.3 by the dashed and solid curves. For the dashed curve, the densities are obtained within the Thomas-Fermi approximation. The results indeed show a rapid decrease of  $\Omega_{\text{eff}}$  until the onset of phase separation at about  $600a_0$ , as given by Eq. (6.4). Then, in a fully phase-separated regime, a plateau is reached where only the thermal bosonic component can lead to loss. Evidently, this theoretical behavior is not consistent with the experimental data points. A notably smoother decrease of  $\Omega_{\text{eff}}$  results from our numerical model (solid line in Fig. 6.3), when we consider the full energy functional which includes the kinetic energy of the BEC as well as the much weaker density gradient correction from the Fermi gas [Ima06]. Within the residual uncertainties of our method (see Sup.Mat. in Sec. 6.7), this model reproduces the observed behavior very well.

Our results show that the kinetic energy term prevents the BEC density from changing abruptly. This plays an essential role in smoothing the density profiles of the separated components near the interface and, thus, in maintaining the residual spatial overlap. Accordingly, the relevant length scale that determines the thickness of the interface layer

<sup>5</sup>In our model, we consider an atom-atom mixture, neglecting any molecular component as the LiK Feshbach molecules are short-lived and decay rapidly.

corresponds to the BEC healing length [Dal99], which for our present conditions can be estimated to  $\xi = (8\pi \hat{n}_b a_{bb})^{-1/2} \approx 0.50 \mu\text{m}$ . This length scale can be compared with the shortest macroscopic length scale of the system, which in our case is the radial size of the BEC of a few micrometers. The measured overlap factor can be understood as the volume ratio of the interface layer and the whole BEC, and the smoothing of the phase transition can thus be interpreted as a consequence of the finite size of the system [Bin84, Br685].

## 6.5 Conclusion and Outlook

The basic idea of our method to probe the interface between spatially separated components may be generalized to many other situations of interest. The working principle just relies on a mechanism that selectively addresses the region where the different components mix. While in our case three-body recombination served this purpose, one may also apply photoassociative or radio-frequency-induced processes to stimulate loss or state-transfer processes.

The interface between two quantum fluids is a topic of broad interest yet largely unexplored in quantum gases. We speculate that future studies could focus on the role of quantum fluctuations, the two-dimensional character of the thin interface layer, and testing the validity of the mean-field approach. Unwinding the microscopic nature underlying the interface may give access to new phenomena such as Andreev bound states [Löf01, Sat17], familiar in superconductor physics. Concerning the phase-separated Bose-Fermi mixture, it would be natural to go beyond the static properties and to investigate the dynamics of the mixture. We expect a strong impact of phase separation on collective oscillation modes [VS09, Mar13] and on the behavior of the system after a quench [Wil15].

## 6.6 Acknowledgments

We acknowledge valuable discussions with M. Baranov and D. Yang on the theoretical model, with E. Tiemann and P. S. Julienne on the scattering properties, and with A. Turlapov on general topics. We thank J. T. M. Walraven for fruitful insights and our new team members C. Baroni, A. Bergschneider, T. W. Grogan and T. Öttl for comments on the manuscript. We acknowledge support by the Austrian Science Fund FWF within the Spezialforschungsbereich FoQuS (F4004-N23) and within the Doktoratskolleg ALM (W1259-N27).

## 6.7 Supplemental Material

### 6.7.1 Preparation of the ${}^6\text{Li}$ - ${}^{41}\text{K}$ mixture

In this Section, we describe the procedure applied for preparing an optically trapped mixture of K and Li atoms in their lowest Zeeman states near 335 G, where an inter-species Feshbach resonance (FR) is located<sup>6</sup> [Wu11, Lou18a].

Initially, the  ${}^6\text{Li}$  and  ${}^{41}\text{K}$  atoms are collected in a dual-species magneto-optical trap (MOT) and loaded consecutively into a single-beam optical dipole trap (ODT) with a wavelength of 1070 nm, power of 150 W and waist of  $38\ \mu\text{m}$ . The loading scheme of the ODT is optimized for a large number of Li atoms, since we evaporate with a Li spin mixture and cool K sympathetically. First, the K atoms are loaded by ramping up the magnetic field gradient and thus compressing the K MOT, while decompressing the Li MOT by increasing its detuning. With the K atoms transferred to the ODT, the K light is turned off and the Li MOT is recompressed to facilitate loading into the ODT. Up to this point, the details of the procedure are similar to those described in our earlier work on the  ${}^6\text{Li}$  and  ${}^{40}\text{K}$  mixture [Spi10].

Next, we apply a gray-molasses cooling on the D1 line of lithium [Fri15, Gri13, Bur14], to further improve the starting conditions for the evaporative cooling with Li. This gives an increase of the phase-space density of the lithium cloud by a factor of fifteen and a factor of five decrease in the initial temperature, while capturing the same amount of lithium as before in the ODT [Fri15]. With these improved starting conditions, after evaporative cooling, we reach a significant lower  $T/T_F$  and higher lithium atom number. After the D1 cooling stage, we remove the hottest atoms, by linearly ramping down the ODT to 50% of its initial power and we create a Li spin mixture for evaporative cooling. Nearly all the lithium atoms captured in the ODT are found in the lowest Zeeman state  $\text{Li}|1\rangle$  ( $F = 1/2, m_F = 1/2$ ). To obtain a 50/50 Li spin mixture in the lowest  $|1\rangle$  and second-lowest  $|2\rangle$  spin state ( $F = 1/2, m_F = -1/2$ ), we ramp the magnetic field, turned off during the D1 cooling stage, to 90 G and apply a radio-frequency (rf)  $\pi/2$ -pulse. This creates a superposition state which has enough time to decohere during the following stages and forms an incoherent Li spin mixture.

Then we exploit a spin relaxation stage to create a polarized sample of K. The K atoms in the ODT are a mixture of the three lowest Zeeman states. Thus, we ramp to a magnetic field of 200 G, where we previously observed the occurrence of spin relaxation [Lou17], and wait for 500 ms. We end up with an almost fully polarized  ${}^{41}\text{K}$  sample in the third-lowest Zeeman state  $\text{K}|3\rangle$  ( $F = 1, m_F = -1$ ) and a very small amount of  $\text{K}|2\rangle$ , the second-lowest spin state ( $F = 1, m_F = 0$ ). After ramping to 335 G we observe complete polarization of the K sample and we speculate that the small amount of  $\text{K}|2\rangle$  is lost by recombination with lithium during the magnetic field ramps we apply to reach 335 G. We note that the presence of the  $\text{K}|2\rangle$  during evaporation does not lead to any observable immiscibility phenomena [Liu16], in contrast to what we observed with another evaporation scheme in Ref. [Lou17]. After the spin relaxation stage, we further decrease the power of the ODT linearly to 15 W in 3 s. Besides the single beam ODT, the atoms also experience a trapping force from the magnetic curvature.

<sup>6</sup>E. Tiemann and T.M. Hanna and E. Tiesinga and P.S. Julienne. (Private Communication)

Subsequently we prepare a  $\text{Li}|1\rangle\text{-Li}|3\rangle$  spin mixture to evaporatively cool at low magnetic fields [Bur14], where  $\text{Li}|3\rangle$  is the third-lowest Zeeman state ( $F = 3/2, m_F = 3/2$ ). After the spin relaxation stage, we ramp to 580 G, where we use a rf  $\pi$ -pulse to transfer all  $\text{Li}|2\rangle$  atoms to  $\text{Li}|3\rangle$ . At this magnetic field the interaction with  $\text{Li}|1\rangle$  has the same strength for both  $\text{Li}|2\rangle$  and  $|3\rangle$  [Zür13]. Additionally the scattering length between  $\text{Li}|2\rangle$  and  $|3\rangle$  is negligible. The  $\text{Li}|1\rangle\text{-Li}|3\rangle$  spin mixture is then used for evaporative cooling at about 483 G, where the scattering length is about  $-635 a_0$ . This magnetic field is chosen to avoid the region between 350-450 G where multiple Feshbach resonances occur and ramping over this with the  $\text{Li}|2\rangle, \text{Li}|3\rangle$  and  $\text{K}|3\rangle$  mixture leads to significant loss.

The evaporation sequence at 483 G contains several stages. First, we evaporate in the single beam ODT by exponentially ramping down its power and simultaneously load the atoms into another single beam ODT (1064 nm, 2.4 W,  $44 \mu\text{m}$ ). Then, we continue evaporation in this new trap and ramp up the power of a second beam (1064 nm, 0.22 W,  $60 \mu\text{m}$ ) to form a cigar-shaped (1:7) crossed-beam optical dipole trap (CDT). The two beams intersect at an angle of  $17^\circ$ . In a third cooling step, we further exponentially ramp down the power of the CDT to the desired final trap depth. Depending on the final trap depth, we end up with a condensed or non-condensed bosonic cloud in a Fermi sea of lithium. Note that  $\text{K}|3\rangle$  is sympathetically cooled along the evaporation route and we do not observe any evaporative loss of K. The fact that the trap depth for potassium is about twice as deep as that of lithium and the thermalization rate is high enough, enables the sympathetic cooling.

In the final stage of the sequence, we ramp to a magnetic field slightly below 335 G avoiding inter- and intraspecies resonances. However, we first switch to a different set of magnetic field coils, which removes the magnetic curvature and allows a high-precision control of the magnetic field. Then we ramp to 565 G, where we remove the  $\text{Li}|3\rangle$  component by a resonant light pulse. At this magnetic field the zero crossing between  $\text{Li}|1\rangle$  and  $\text{Li}|3\rangle$  can be found and removing the  $\text{Li}|3\rangle$  does not significantly heat up the remaining  $\text{Li}|1\rangle$  atoms. Then we transfer  $\text{K}|3\rangle$  to  $\text{K}|2\rangle$  with a rf  $\pi$ -pulse. This is followed by a series of magnetic field ramps, where the final field of 335 G is reached with a pure mixture of  $\text{Li}|1\rangle$  and  $\text{K}|2\rangle$ . Using a rf  $\pi$ -pulse we transfer  $\text{K}|2\rangle$  to  $\text{K}|1\rangle$  ( $F = 1, m_F = 1$ ) and we can start with our measurements.

For the loss measurements we use the following sequence. At a magnetic field detuning ( $\delta_B = B - B_0$ ) of  $-200 \text{ mG}$ , we transfer  $\text{K}|2\rangle$  to  $\text{K}|1\rangle$  with a rf  $\pi$ -pulse of 0.056 ms and directly afterwards ramp adiabatically in 2 ms to a given  $\delta_B$ . Since we stay on the repulsive side of the FR, no Feshbach molecules are associated and they can only be formed in three-body recombination processes. For various hold times at the given  $\delta_B$ , we take spin-specific absorption images of Li and K after respectively, 2 and 8 ms time-of-flight.

### 6.7.2 Feshbach resonance parameters

The scattering length between the lowest Zeeman spin states of  ${}^6\text{Li}$  and  ${}^{41}\text{K}$  is tuned by a FR near  $335 \text{ G}$ <sup>7</sup> [Wu11, Lou18a]. We first discuss the available theoretical predictions (Sec. 6.7.2.1) for the background scattering length  $a_{\text{bg}}$  and the resonance width  $\Delta$ . Then, in Sec. 6.7.2.2, we show how we experimentally determine the differential magnetic

<sup>7</sup>E. Tiemann and T.M. Hanna and E. Tiesinga and P.S. Julienne. (Private Communication)

moment  $\delta\mu$  and the resonance position  $B_0$ . In Sec. 6.7.2.3, we discuss how  $B_0$  changes for different trap settings as a result of a light shift, and in Sec. 6.7.2.4 we discuss the measurements which verify the theoretical value for  $\Delta$ .

### 6.7.2.1 Theory predictions

Coupled-channel calculations by T. Hanna, E. Tiesinga and P. Julienne<sup>8</sup> and independently by E. Tiemann<sup>9</sup> predict the magnetic-field dependent scattering length between  $\text{Li}|1\rangle$  and  $\text{K}|1\rangle$  around 335 G. These calculations are based on the potentials from Ref. [Tie09]. Two FRs show up, a broader one around 335 G and a narrower one at 341 G. Experimentally, the 335 G FR was observed in Ref [Wu11] by detecting the loss of K atoms. The loss maximum, corresponding to  $B_0$ , was found at  $B=335.8$  G and the width determined by a Gaussian curve fit gave a value of  $\Delta B_{\text{exp}} = 1.1$  G. For the FR center  $B_0$ , the experimental value (335.8 G [Wu11]) and the two theoretical values (335.1 G<sup>10</sup> and 335.9 G<sup>11</sup>) are only consistent within a Gauss. For a more accurate determination of  $B_0$ , we measure the binding energy of the dimers on the repulsive side of the FR (see Sec. 6.7.2.2).

We find that both coupled-channel calculations agree very well on the value of the scattering length if compared as a function of the magnetic detuning  $\delta_B = B - B_0$ , and we use these calculations to extract theoretical values for  $a_{\text{bg}}$  and  $\Delta$ . The predicted scattering length can be fitted with the simple formula

$$a_{\text{bf}}(\delta_B) = a_{\text{bg}} \left( 1 - \frac{\Delta}{\delta_B} - \frac{\Delta_1}{\delta_B - \delta_1} \right), \quad (6.7)$$

where  $a_{\text{bg}} = 60.865 a_0$ , with  $a_0$  being the Bohr radius, and  $\Delta = 0.9487$  G is the width of the FR at 335 G. The width of the narrow FR is  $\Delta_1 = 0.0566$  G and the detuning of this resonance with respect to the 335 G FR center is  $\delta_1=6.1577$  G. The free parameters are obtained by fitting the scattering length calculations for a detuning of  $-5$  to  $+7$  G and the expression is plotted in Fig. 6.4. The agreement between the calculations and the fit is excellent, with deviations of about 1 permille. Note that because of the narrow FR at 341 G the position of the zero crossing no longer corresponds to the width of the 335 G FR but instead is shifted down by 10 mG.

In our analysis of the data, we neglect the influence of the FR at 341 G and apply the common formula  $a_{\text{bf}} = a_{\text{bg}} (1 - \Delta/\delta_B)$  to describe the scattering length. Here, we use the values of  $a_{\text{bg}} = 60.865 a_0$  and  $\Delta = 0.9487$  G from the fit to the theoretical predictions. The Feshbach resonance center  $B_0$  is determined experimentally. On the repulsive side of the FR, the difference between this approach and Eq. 6.7 is very small.

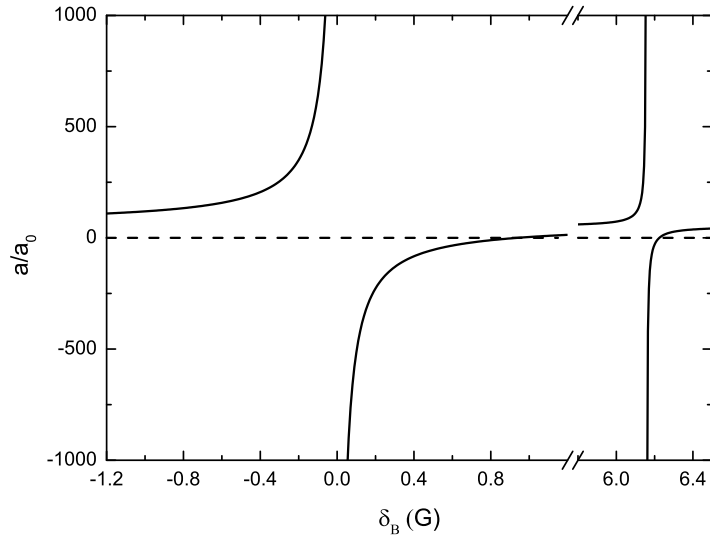


FIGURE 6.4: Scattering length between  $\text{Li}|1\rangle$  and  $\text{K}|1\rangle$  around 335 G versus magnetic field detuning as described by Eq. (6.7).

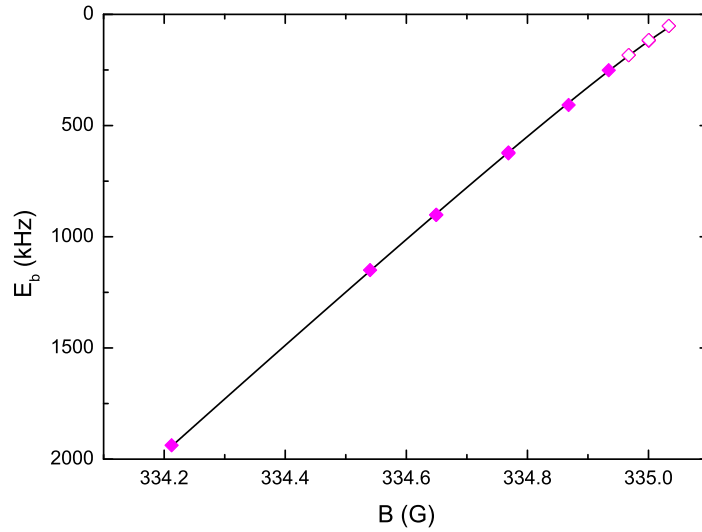


FIGURE 6.5: Binding energy versus magnetic field. The binding energy is determined either by magnetic modulation (filled diamonds) or rf (open diamonds) spectroscopy. The solid line represents the fit of Eq. (6.12) to the data, with  $B_0 = 335.0795(9)$  G and  $R^* = 2241(7) a_0$ .

### 6.7.2.2 Obtaining the Feshbach resonance center $B_0$ by binding energy measurements

To experimentally determine  $B_0$ , we measure the binding energy of the Li-K dimer by magnetic modulation (“wobble”) spectroscopy and/or radio-frequency spectroscopy [Chi10]. Fig. 6.5 shows the result of measuring the binding energy by applying both methods for a CDT with a power of 92 mW and 127 mW in the two beams. Magnetic modulation spectroscopy enables us to measure binding energies in the range of 0-2 MHz, while rf spectroscopy is typically performed up to a 100 kHz. This provides us with a wide range of binding energies which we can measure and fit with a known binding energy formula. The magnetic modulation spectroscopy data is obtained by modulating the magnetic field and measuring which frequency is required to drive the transition between the free atom state and the molecular state at a various magnetic fields. At each magnetic field the duration and amplitude of the modulation are adjusted such that the transfer is measurable, without driving the transition too strongly. We observe the loss of  $K|1\rangle$  atoms as a function of the modulation frequency. The center between the low-frequency onset of the loss of K atoms and the maximum loss is used as the modulation frequency that corresponds to the binding energy. We estimate the error as half of this range. The measurements are shown by the filled symbols in Fig. 6.5.

To measure the binding energy with rf spectroscopy we prepare a non-interacting mixture of  $Li|1\rangle$  and  $K|2\rangle$  at several tens of mG below the expected  $B_0$  and measure the frequency needed for a strong 800- $\mu$ s rf-pulse to associate  $Li|1\rangle$ - $K|1\rangle$  dimers [Jag14]. After the rf pulse, we ramp in 50  $\mu$ s to roughly 100 mG above the resonance position. This dissociates the created dimers into  $Li|1\rangle$  and  $K|1\rangle$  atoms. By plotting the atom number in the  $K|1\rangle$  state as a function of the rf frequency, we get the molecule association spectrum. From the spectrum we determine the lowest frequency  $\nu$ , where the atom number is at roughly 20% of its peak height. We found that for a typical maximum transfer of 4000 K atoms, this gives a good estimate of the onset frequency for association. We estimate the error in  $\nu$  as half of the range between  $\nu$  and the peak frequency, which is 2 to 5 kHz. We obtain the rf detuning  $\nu - \nu_0$  by subtracting the unperturbed  $K|2\rangle \rightarrow K|1\rangle$  transition frequency  $\nu_0$ , which corresponds to the Zeeman splitting of the two states as calculated from the Breit-Rabi formula. The rf detuning gives a direct measurement of the binding energy and the results are shown by the open symbols in Fig. 6.5.

To fit the data we use the binding energy formula derived in Refs. [Pet04, Lev11] for a weakly bound molecule near a narrow resonance. Near the dissociation threshold,  $E_b$  can be written as

$$E_b = \frac{\hbar^2 \kappa^2}{2 m_r}, \quad (6.8)$$

where  $m_r$  is the reduced mass

$$m_r = \frac{m_f m_b}{m_f + m_b}, \quad (6.9)$$

---

<sup>8</sup>private communication

<sup>9</sup>private communication

<sup>10</sup>T.M. Hanna and E. Tiesinga and P.S. Julienne. (Private Communication)

<sup>11</sup>E. Tiemann. (Private Communication)

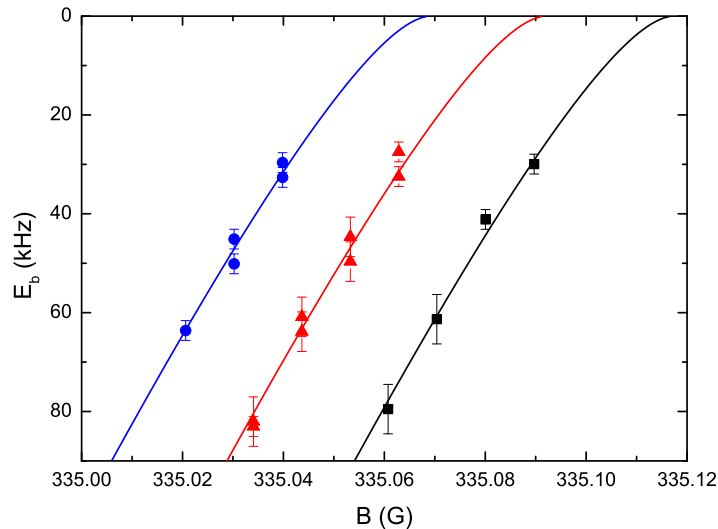


FIGURE 6.6: Binding energy versus magnetic field for the three trap settings of the main text. The solid lines are the fits of Eq. (6.12), with  $B_0$  as the only free parameter. The blue circles show the rf spectroscopy measurements with the trap settings of data set B1-B3, red triangles those of data set A2 and the black squares those of data set A1. The error bars represent the estimated error (see text) in determining the onset frequency.

with  $m_{f(b)}$  the mass of Li (K). The wavenumber  $\kappa$  can be expressed in a second-order Taylor expansion as

$$-\kappa = -\frac{1}{a} + R^* \kappa^2, \quad (6.10)$$

where  $a = -a_{bg} \Delta / \delta_B$  and the usual background scattering term is neglected. The length parameter  $R^*$  is related to the narrowness of the resonance [Pet04]

$$R^* = \frac{\hbar^2}{2 m_r \delta \mu a_{bg} \Delta}, \quad (6.11)$$

with  $\delta \mu$  the differential magnetic moment of the closed and open channel. All together this gives the formula

$$E_b = \frac{\hbar^2}{8 (R^*)^2 m_r} \left( \sqrt{1 - \frac{4 R^* \delta_B}{a_{bg} \Delta}} - 1 \right)^2. \quad (6.12)$$

We fit the measured binding energies with Eq. (6.12), leaving both  $B_0$  and  $R^*$  as free parameters, as depicted in Fig. 6.5. For  $a_{bg}$  and  $\Delta$  the values from the fit to the coupled-channel calculations of Sec. 6.7.2.1 are used and assumed to be free of any relevant uncertainties. The fit results give  $B_0 = 335.0795(9)$  G,  $R^* = 2241(7) a_0$  and thus  $\delta \mu = h \times 2.660(8)$  MHz/G.

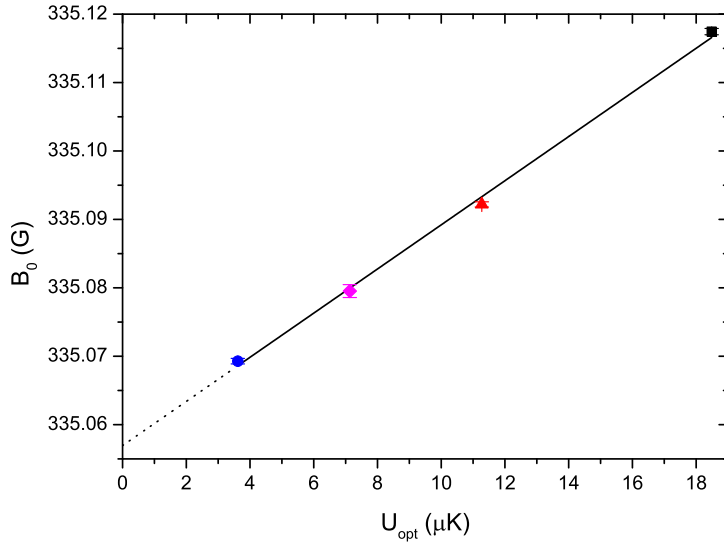


FIGURE 6.7: Feshbach resonance position as a function of the trap depth for potassium. The symbols correspond to the same trap settings as in Fig. 6.6 and the additional diamond corresponds to those of Fig. 6.5. Error bars represent fit errors in the determination of  $B_0$ . The solid line represents a weighted linear fit of  $B_0 = A + D U_{\text{opt}}$ , with  $A=335.057(1)$  G and  $D = 3.2(1) \times 10^{-3} \text{ G}/\mu\text{K}$ . The dashed line shows the extrapolation of the linear fit to zero trap depth.

### 6.7.2.3 Light shift of the Feshbach resonance center $B_0$

As already pointed out in Refs. [Koh12, Jag14, Cet16], for a similar FR in the  ${}^6\text{Li}$ - ${}^{40}\text{K}$  mixture, the trap light of 1064 nm causes a differential light shift between the atom pair state and the molecular state. This leads to a light-induced shift of the Feshbach resonance position  $B_0$ . Thus, for every trap we use, we need to measure the trap-specific  $B_0$ . We do this by performing rf spectroscopy of the Feshbach molecules. For the trap of Sec. 6.7.2.2 we have checked that the fit to rf spectroscopy data only, with fixed  $\delta\mu$ , agrees with the  $B_0$  obtain from the two-parameter fit to both modulation and rf spectroscopy data. For each trap and at various magnetic fields we thus determine the rf detuning  $\nu - \nu_0$  via rf spectroscopy. This is a direct measurement of the binding energy  $E_b$  and Fig. 6.6 shows the measurements for the three trap settings discussed in the main text. The resulting values for  $B_0$  are given in Table 6.1 and plotted depending on the optical trap depth  $U_{\text{opt}}$  for potassium in Fig. 6.7. The trap depth of the crossed dipole trap is calculated from the power and widths of the two intersecting laser beams, under the assumption that the beams are Gaussian. Here, we do not consider the reduction of the trap depth by gravity. Extrapolating a linear fit to the  $B_0$  data as a function of trap depth, shows that the Feshbach resonance center in the absence of a trap is  $335.057(1)$  G, where the error represents the fit uncertainty.

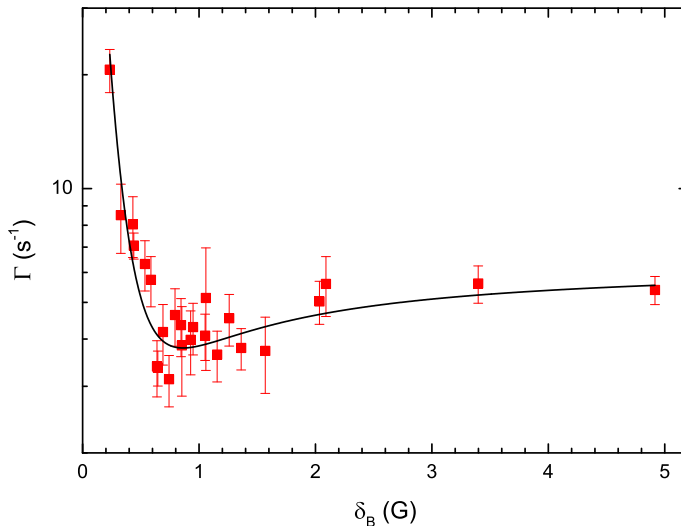


FIGURE 6.8: Damping rate of the axial COM mode versus magnetic field detuning. The solid line represents a fit by Eq. (6.13) with  $B = 3.8(2) \text{ s}^{-1}$ ,  $A = 2.6(5) \text{ s}^{-1}$  and  $C = 0.86(5) \text{ G}$ .

#### 6.7.2.4 Verification of the Feshbach resonance width $\Delta$

The width of the FR is given by the theoretical predictions to be 0.949 G. We verified this value by measuring the damping of the axial center-of-mass (COM) oscillations at different magnetic field detunings  $\delta_B$  for the trap settings of data set A2 (see Table 6.1). We excite both the COM oscillations of K and Li, which oscillate at a different frequency, but measure only the oscillations in K. The interaction between Li and K leads to friction and this damps the COM oscillations. At the point where the interspecies scattering length is zero, the least amount of damping is expected. Note that other types of damping will still be present. This method, as presented in Ref. [Nai11], enables us to determine the zero crossing of the Feshbach Resonance.

To excite the COM oscillations of the clouds (both Li and K) we use the following scheme. At a fixed magnetic field detuning we excite a non-interacting  $\text{Li}|1\rangle\text{-K}|2\rangle$  sample by ramping up a strong additional trapping beam in 100 ms. This beam is slightly misaligned with one of the beams of the CDT and thus displaces the COM of the clouds. We hold the sample in this trap configuration for 100 ms and then release it in 1 ms into the original trap configuration by switching off the additional beam. With a rf  $\pi$ -pulse we transfer  $\text{K}|2\rangle$  to  $\text{K}|1\rangle$  in  $56 \mu\text{s}$  and obtain a mixture of  $\text{Li}|1\rangle\text{-K}|1\rangle$ . Then we quickly ramp in 2 ms to the final  $\delta_B$ . The final detuning determines the strength of the interaction between  $\text{Li}|1\rangle$  and  $\text{K}|1\rangle$ . For different hold times, we observe the center position of the K cloud and obtain the K COM oscillations. We fit these oscillations with a damped sinusoidal curve to extract the damping rate  $\Gamma$ . This is repeated for several positive values of  $\delta_B$  around the expected zero crossing of the scattering length, as is shown in Fig. 6.8.

The damping rate around the zero crossing can be fitted with

$$\Gamma = B + A \left(1 - \frac{C}{\delta_B}\right)^2 \quad (6.13)$$

where  $A, B$  and  $C$  are free parameters. Here,  $B$  represents the background damping, which is not caused by the interspecies scattering length, and  $A$  is a constant which is proportional to  $(a_{bg})^2$ . The fit gives  $C = 0.86(5)$  G for the zero crossing and this is equivalent to the width of the Feshbach resonance if no other Feshbach resonances were close by. In our case the zero crossing is influenced by the close presence of the other rather narrower FR at 341 G and Eq. (6.7) shows that this shifts the zero crossing by about 10 mG. The width of the FR should therefore be 0.87(5) G.

From our measurements we obtain a value of 0.87(5) G for  $\Delta$ , which deviates from the theoretical value by less than  $2\sigma$ . This deviation may be of statistical nature or may be explained by an oversimplification of the model [Eq.(6.13)] we use to fit to our data. The result can be considered to be consistent with the theoretical value for  $\Delta$ , the latter being used in our calculations and analysis. Note that using the experimental value for  $\Delta$  would not significantly affect the  $B_0$  determination, however it would give an about 10% lower scattering length  $a_{bf}$  near resonance, where  $a_{bg}$  can be neglected.

### 6.7.3 Measurement procedures and data analysis

In this Section, we discuss the measurements and analysis behind the data points displayed in the figures of the main text. We summarize the experimental parameters for the data sets A1, A2 and B1-B3 in Sec. 6.7.3.1. The measurements and analysis of the three-body loss coefficient  $L_3$  and the normalized loss rate  $\gamma$  are then described in Sec. 6.7.3.2 and Sec. 6.7.3.3. In Sec. 6.7.3.4 we show the experimental determination of the effective overlap factor  $\Omega_{\text{eff}}$ , and in Sec. 6.7.3.5 we explain how we take into account secondary loss.

#### 6.7.3.1 Experimental parameters

Table 6.1 shows the experimental parameters for the data sets A1, A2 and B1-B3. We first show the parameters that are independent of the atom number for lithium  $N_f$  and potassium  $N$  in the given data set and the quantities derived thereof. The errors in the atom number represent the statistical errors due to fluctuations in the data points of the data sets. Additionally there is a systematic calibration error of about 10% for both Li and K. As described in Sec. 6.7.2.3, we measure  $B_0$  for each trap by rf spectroscopy. For each trap setting we measured the radial and axial trap frequencies for the bosons ( $\omega_b^r, \omega_b^z$ ) by exciting the COM modes in axial and radial direction. The trap frequencies for the fermions can be calculated accurately by  $\omega_f^i = 1.756 \omega_b^i$ , where the factor is derived from the ratio of the masses and the dynamical polarizabilities of the two species [Lou17]. The estimated effective trap depth  $U_b(U_f)$  for the bosons (fermions) in the  $z$ -direction is also shown. This trap depth is calculated from the power and waist of the CDT beams under the assumption that the beams are Gaussian and we took into account the effect

of gravity, which lowers the trap depth. For a non-condensed K cloud (data set A1, A2), the temperature is determined from the time-of-flight expansion of the K atoms. For the BEC cloud (B1-B3 data sets), the temperature is derived from the measured BEC fraction  $\beta$  [Lou17]. When comparing the temperature with the trap depth of the bosons, we can see that the potassium atoms are trapped in a deep trap and loss can only happen due to recombination with lithium.

The peak density of lithium  $\hat{n}_f$  and the Fermi temperature  $T_F$  are derived from the atom number by the textbook equation (for  $T = 0$ )

$$\hat{n}_f = \left( 2 \frac{k_B T_F m_f}{\hbar^2} \right)^{3/2} \frac{1}{6\pi^2} = \frac{2\sqrt{N_f}}{\sqrt{3}\pi^2} \left( \frac{\bar{\omega}_f m_f}{\hbar} \right)^{3/2}, \quad (6.14)$$

where  $k_B$  is the Boltzmann constant and  $\hbar$  is the Planck constant. The geometrical average of the trap frequency as seen by lithium,  $\bar{\omega}_f$ , can be calculated as  $\bar{\omega}_f = (\omega_f^x \omega_f^y \omega_f^z)^{1/3}$ . When we compare  $T_F$  to the effective trap depth  $U_f$ , we see that the final trap settings are deep enough for lithium. We also give the relative temperature  $T/T_F$ , which shows that we are indeed very cold and justifies the use of Eq. (6.14), which is valid for  $T=0$ . The BEC fraction is obtained from a bimodal fit to the absorption images after time-of-flight and we quote the average BEC fraction and its standard error for the given data sets. The peak density of the BEC  $\hat{n}_b$  and the thermal peak density  $\hat{n}_t$  are given by

$$\begin{aligned} \hat{n}_b &= \frac{15^{2/5}}{8\pi} \left( \frac{\bar{\omega}_b m_b}{\hbar\sqrt{a_{bb}}} \right)^{6/5} (\beta N)^{2/5}, \\ \hat{n}_t &= \left( \frac{\bar{\omega}_b^2 m_b}{2\pi k_B T} \right)^{3/2} (1 - \beta) N, \end{aligned} \quad (6.15)$$

where  $a_{bb} = 60.9 a_0^{12}$ , and we assume the thermal density to follow the Boltzmann distribution. When calculating the critical temperature  $T_c$  we correct for finite-size and interaction effects [Gio96], which leads to a down shift of the critical temperature of less than 10%, when compared to the common expression  $k_B T_c = 0.940 \hbar \bar{\omega}_b N^{1/3}$ .

### 6.7.3.2 Measurements of the three-body loss coefficient $L_3$

For the two data sets (A1, A2) with non-condensed K atoms, we measure the loss of K atoms for various hold times  $t$  at different repulsive Bose-Fermi scattering lengths  $a_{bf}$  in order to determine  $L_3$ . The atom loss can be quantified as

$$\dot{N} = -L_3 \int n_f n_t^2 dV = -L_3 \hat{n}_f \frac{\hat{n}_t}{\sqrt{8}} N. \quad (6.16)$$

Within the *fermionic reservoir approximation (FRA)*, we can assume that the fermion density as seen by the potassium atoms is constant and replace  $\tilde{n}_f$  by the peak density  $\hat{n}_f$  at zero temperature and take it out of the integral. The remaining integral is solved, assuming that the thermal density of the bosons follows the Boltzmann distribution.

The measured evolution of the atom number follows an effective two-body loss equation

<sup>12</sup>Eberhard Tiemann. (private communication)

TABLE 6.1: Summary of the data sets and their experimental parameters.

data set symbol	A1 black squares	A2 red triangles	B1 orange inv. triangles	B2 green diamonds	B3 blue circles
$B_0$ (G)	335.1175(5)	335.0922(4)		335.0693(4)	
$\omega_b^1/2\pi$ (Hz)	376(1)	300(1)		171.1(6)	
$\omega_b^2/2\pi$ (Hz)	54.8(4)	42.2(1)		23.58(6)	
$\omega_f^1/2\pi$ (Hz)	660(2)	527(2)		300(1)	
$\omega_f^2/2\pi$ (Hz)	96.2(7)	74.1(2)		41.4(1)	
$U_b$ ( $\mu\text{K}$ )	14.5	7.60		0.856	
$U_f$ ( $\mu\text{K}$ )	7.68	4.46		1.10	
$T$ (nK)	438(18)	238(7)	88(2)	93(2)	97(5)
$N_f$	$1.8(2) \times 10^5$	$3.3(4) \times 10^5$	$1.33(8) \times 10^5$	$1.5(1) \times 10^5$	$1.1(1) \times 10^5$
$\hat{n}_f$ ( $\text{cm}^{-3}$ )	$4.7(2) \times 10^{12}$	$4.4(3) \times 10^{12}$	$1.20(4) \times 10^{12}$	$1.27(4) \times 10^{12}$	$1.11(6) \times 10^{12}$
$T_F$ (nK)	$1.72(6) \times 10^3$	$1.64(7) \times 10^3$	690(13)	718(16)	656 (24)
$T/T_F$	0.25(1)	0.145(7)	0.128(4)	0.130(4)	0.148(9)
$N$	$2.6(6) \times 10^4$	$4.3(2) \times 10^4$	$2.60(7) \times 10^4$	$2.96(5) \times 10^4$	$3.0(3) \times 10^4$
$\beta$	-	-	0.54(3)	0.50(2)	0.46(5)
$\hat{n}_b$ ( $\text{cm}^{-3}$ )	-	-	$4.8(2) \times 10^{13}$	$5.0(1) \times 10^{13}$	$4.9(3) \times 10^{13}$
$\hat{n}_t$ ( $\text{cm}^{-3}$ )	$0.38(8) \times 10^{13}$	$0.77(5) \times 10^{13}$	$0.18(2) \times 10^{13}$	$0.20(1) \times 10^{13}$	$0.21(3) \times 10^{13}$
$T/T_c$	1.7(1)	1.01(3)	0.78(2)	0.79(1)	0.82(5)

with  $\dot{N} \propto -N^2$  and we fit the data with

$$N(t) = N_0 (1 + N_0 C t)^{-1}, \quad (6.17)$$

where the free parameters  $N_0$  and  $C$  represent the initial atom number and the constant we extract. An example curve is displayed in Fig. 6.9(a) for  $a_{\text{bf}} \approx 850 a_0$ . The  $L_3$  coefficient is then calculated as

$$L_3 = C \frac{\sqrt{8}}{\hat{n}_f \bar{\omega}_b^3} \left( \frac{2\pi k_B T}{m_b} \right)^{3/2}. \quad (6.18)$$

The error in  $L_3$  is propagated from the fit error in  $C$ . Additionally, there is about a 12% systematic error in the conversion from  $C$  to  $L_3$ , coming from the Li and K atom number calibration, the temperature, and the trap frequency determination.

There are two additional corrections to Eq. (6.18), both taken into account for the data points displayed in Fig. 2(a) of the main text. First of all, for temperatures close to the critical temperature for condensation, the bosonic system deviates from the classical Boltzmann distribution and Eq. (6.18) overestimates the value of  $L_3$ . The Bose enhancement of the density gives a correction factor to Eq. (6.18) of 0.97 for set A1 and 0.78 for set A2.

Second, for  $a_{\text{bf}}$  below  $150 a_0$ , the three-boson loss becomes significant. This adds a second term to the equation for the atom loss

$$\dot{N} = -L_3 \hat{n}_f \int n_t^2 dV - K_3 \int n_t^3 dV. \quad (6.19)$$

We use this equation instead of Eq. (6.16) to correct for the influence of the additional loss term. Measurement of  $K_3$  in the trap of A1, with a pure bosonic sample and  $T = 536(20)$  nK, gives a rate constant of  $K_3 = 0.012(3) \times 10^{-25}$  cm<sup>6</sup>/s. Here, we fitted the atom loss data with the solution to the differential equation  $\dot{N}/N^3 = -A$ , with  $A$  the free parameter. Solving the integral for the three-boson loss,  $K_3$  can then be extracted as

$$K_3 = \frac{A\sqrt{27}}{\left(\frac{m_b}{2\pi k_B T}\right)^3 \bar{\omega}_b^6} \quad (6.20)$$

This leads to a 4-12% correction of  $L_3$  for the three points with the lowest  $a_{\text{bf}}$ . For the other  $L_3$  data the effect of the three-boson loss compared to the boson-boson-fermion three-body recombination loss is two orders of magnitude smaller.

The value of  $L_3$  for any  $a_{\text{bf}}$  between 80 and  $2100 a_0$  is approximated by applying the LOESS smoothing method [NIS18] to the data. LOESS is a locally weighted polynomial least squares regression method, based on the idea that any function can be well approximated in a small local region by a low-order polynomial. More weight is given to the data points close to the local region than to those farther away. The great advantage of this method is the fact that it does not require a specific model to fit the data. We use a LOESS smoothing with a degree of 2 and  $q = 0.5$  to fit the data of  $L_3$ , using the fitting program R [Ven17] and calculate the  $2\sigma$  confidence interval of the smoothing as displayed in Fig. 2(a) of the main text. The degree of 2 means that we locally fit with a simple parabola. The smoothness parameter  $q$  determines how much of the data is being used for each local fit. The typical  $1\sigma$  uncertainty in the smoothed data is about 10%.

### 6.7.3.3 Measurements of the normalized loss rate $\gamma$

We observe the loss of the atom number of a partial BEC for various hold times and for different values of the scattering length. A typical loss measurement is shown in Fig. 6.9(b) for  $a_{\text{bf}} \approx 850 a_0$ . To fit the data, we approximate the initial loss as a linear decay given by  $\dot{N}/N = -C$ . In practice this means that we fit the data with

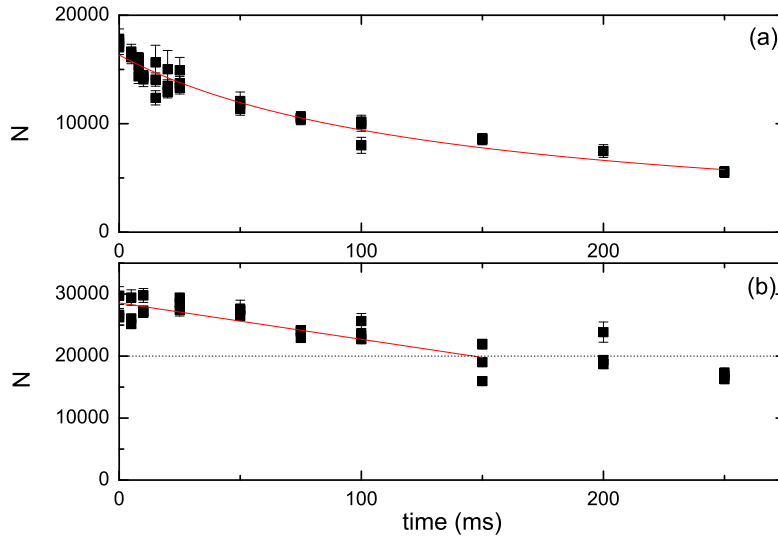


FIGURE 6.9: Decay curves of a thermal (a) and partial BEC (b) cloud of  $^{41}\text{K}$  for  $a_{\text{bf}}$  of about  $850 a_0$ . The red curves are the fitting curves used in the analysis and the vertical dashed line in (b) shows the cut-off criterion for the linear fit. The error bars represent the statistical uncertainties corresponding to the fit errors of the atom number obtained from the absorption images.

$N(t) = N_0 - Ct$ , where  $N_0$  and  $C$  are free parameters. We limit the fit to 30% of the initial atom number. Fig. 6.9(b) shows a typical fit and the cut-off criterion. We obtain the normalized loss rate as  $\gamma = C/(0.85 N_0)$ . The thus obtained values of  $\gamma$  are displayed in Fig. 2(b) of the main text, where the error represents the fit error in  $C$ . Three data sets (B1-B3) are taken in this way and Table 6.1 shows their parameters, where  $N = 0.85 N_0$ . During the time in which the K atom number decreases by 30%, we observe that the BEC fraction only changes within 10% and heating due to the loss of K atoms does not lead to a substantial change in  $\beta$ . We assume this is because of sympathetic evaporation of lithium [Mos01].

Additional three-boson loss mostly affects the two data points taken below  $150 a_0$ . For the other points the measured loss rate is an order of magnitude higher than the measured decay of a K partial BEC without lithium. We measured the decay of a pure K sample with a 39(4)% BEC fraction and  $N_K = 2.7(2) \times 10^4$  and we found a normalized loss rate of the total atom number of  $\gamma_{3b} = 0.01(1)/\text{s}$ . We correct for this additional form of loss by subtracting  $\gamma_{3b}$  from the measured  $\gamma$ . This significantly affects only the two points below  $150 a_0$  in Fig. 2(b) of the main text and the uncertainty in the measured three-boson decay is reflected in the error bar for  $\gamma$ . Moreover, these two data points show a very slow decay and therefore we fit their loss curves only up to 3 s instead of 30% of the initial atom number.

### 6.7.3.4 Experimental determination of the effective overlap factor $\Omega_{\text{eff}}$

As an extension of Eq. (2) in the main text, we define the effective overlap factor  $\Omega_{\text{eff}}$  for a partial BEC as

$$\Omega_{\text{eff}} \equiv \frac{\int \left( \frac{1}{2} \alpha n_f n_b^2 + \alpha n_f n_b n_t + n_f n_t^2 \right) dV}{\int \left( \frac{1}{2} \alpha \tilde{n}_f \tilde{n}_b^2 + \alpha \tilde{n}_f \tilde{n}_b \tilde{n}_t + \tilde{n}_f \tilde{n}_t^2 \right) dV}, \quad (6.21)$$

which is the total three-body density integral including all loss contributions normalized to the corresponding non-interacting ( $a_{\text{bf}} = 0$ ) integral. It takes into account the additional loss because of the thermal bosonic density and the effect of secondary loss through the factor  $\alpha$  (see Sec. 6.7.3.5).

With this definition, the atom loss equation [Eq. (5) in the main text] can be rewritten

$$\dot{N} = -L_3 \Omega_{\text{eff}} \int \tilde{n}_f \left( \frac{1}{2} \alpha \tilde{n}_b^2 + \alpha \tilde{n}_b \tilde{n}_t + \tilde{n}_t^2 \right) dV = -L_3 \Omega_{\text{eff}} I_0, \quad (6.22)$$

where we have introduced  $I_0$  as the overlap integral for the non-interacting mixture. This integral can be simplified by replacing  $\tilde{n}_f$  with the peak density  $\hat{n}_f$  at zero temperature and taking  $\hat{n}_f$  out of the integral, as justified by the FRA. The three integrals left to solve are then

$$\int \tilde{n}_b^2 dV = \frac{4}{7} \hat{n}_b \beta N, \quad (6.23)$$

$$\int \tilde{n}_b \tilde{n}_t dV = \hat{n}_t \beta N, \quad (6.24)$$

$$\int \tilde{n}_t^2 dV = \frac{1}{\sqrt{8}} \hat{n}_t (1 - \beta) N. \quad (6.25)$$

Here we treat the BEC within the Thomas-Fermi approximation and we use the Boltzmann distribution to describe the thermal bosonic density. For solving the second integral we assume that the BEC samples the peak density of the thermal cloud. With these three solutions,  $I_0$  becomes

$$I_0 = \hat{n}_f \left( \frac{2}{7} \alpha \hat{n}_b \beta N + \alpha \hat{n}_t \beta N + \frac{1}{\sqrt{8}} \hat{n}_t (1 - \beta) N \right). \quad (6.26)$$

We finally arrive at the central equation for our data analysis [Eq. (6) in the main text], which allows us to calculate  $\Omega_{\text{eff}}$  from the measured values of  $\gamma$  and  $L_3$  and the experimental parameters,

$$\Omega_{\text{eff}} = \frac{1}{\hat{n}_f \left( \frac{2}{7} \alpha \hat{n}_b \beta + \alpha \hat{n}_t \beta + \frac{1}{\sqrt{8}} \hat{n}_t (1 - \beta) \right)} \frac{\gamma}{L_3}. \quad (6.27)$$

For the atom number of lithium and potassium, and the BEC fraction we take the average value in the time frame set by the cut-off criterion of 30% K atom loss. The average values of the peak densities, atom numbers and the BEC fraction for each data set are listed in Table 6.1.

### 6.7.3.5 Secondary loss

In our definition of  $\Omega_{\text{eff}}$  in Eq. (6.6) we implemented a factor  $\alpha$ , which gives an estimate on the importance of secondary loss. When  $\alpha = 1$ , there is no secondary loss and a three-body loss event leads to the loss of two K atoms and one Li atom. However, in a dense sample it may happen that further atoms are lost by collisions with the products of a previous recombination [Sch01b, Zac09].

A possible scenario for secondary loss is the following. In a first collision event of two bosons (b) and one fermion (f), a weakly bound dimer ( $\text{bf}^*$ ) is formed according to  $\text{b} + \text{b} + \text{f} \rightarrow \text{bf}^* + \text{b} + E_{\text{b}}$ . In this recombination event the binding energy ( $E_{\text{b}}$ ) of the dimer is released and distributed almost evenly into the motion of the K atom and Li-K dimer, where the K atom takes 47/88 and the dimer 41/88. The K atom and the Li-K dimer may quickly escape from the trap if their obtained kinetic energy is higher than the trap depth. The Li-K dimer can recollide with another K atom as  $\text{bf}^* + \text{b} \rightarrow \text{bf} + \text{b} + E_{\text{kin}}$ , whereby the dimer relaxes to a energetically lower internal state (bf) and releases the energy  $E_{\text{kin}}$ . Since  $E_{\text{kin}}$  is very large as compared to the trap depth, all products will be lost immediately. This inelastic atom-dimer decay is more likely to take place when the K sample is dense enough such that the Li-K dimer can find a collision partner in a reasonable amount of time.

Important in the discussion of secondary loss is also the comparison between the binding energy of the formed dimer and the trap depth. If there is not enough energy released for the dimer to leave the trap, there will be enough time for it to recollide with the other K atoms in the trap. The effective trap depth for K for the data sets B1-B3 is  $0.856 \mu\text{K}$ , where the effect of gravity is taken into account. Thus, for scattering lengths below about  $1500 a_0$  (almost our entire measurement range), the recombination products will obtain enough energy to escape the trap. For higher scattering lengths, we expect the collisional products to remain trapped and the released energy will be redistributed among the other atoms in the trap, leading to additional heating and loss.

A typical rate constant for inelastic atom-dimer decay is  $\beta_{\text{AD}} \approx 1.4 \times 10^{-10} \text{cm}^3/\text{s}$  [Jag16]. Together with the peak density of our BEC of  $5 \times 10^{13} \text{cm}^{-3}$ , this gives a time scale for inelastic collisions of  $\tau \approx (\beta_{\text{AD}} \hat{n})^{-1} \approx 140 \mu\text{s}$ , which is about one order of magnitude shorter than the oscillation period of the particles in the trap. After the three-body recombination event the dimer has an estimated kinetic energy of  $\sim 5 \mu\text{K}$ , which gives a typical velocity for the dimer of  $v_{\text{AD}} = 42 \text{mm/s}$  and thus it can travel a distance of  $\sim 6 \mu\text{m}$  before undergoing an inelastic collision event. Given the size of the BEC (see Fig. 6.11) there is a high probability that the dimer encounters a K atom from the BEC before leaving the trap, and undergoes a transition to a deeply bound molecular level with a large release of kinetic energy. For the thermal potassium density, the time scale for the inelastic collision is more than an order of magnitude higher and it is therefore less likely that the Li-K dimer will recollide with a thermal K atom. Thus, the secondary collisions mostly happens with K atoms from the BEC and we add the factor alpha only to the overlap integrals in Eq. (6.6) which contains the BEC density.

Since the inelastic rate coefficient is not exactly known, the influence of secondary loss on  $\Omega_{\text{eff}}$  cannot be *a priori* calculated, but we rather rely on estimates. We know that the factor  $\alpha$  should be at least 1 (two K atoms lost per recombination event) and it is reasonable to assume that  $\alpha$  does not exceed 3/2 (one additional K atom lost). In

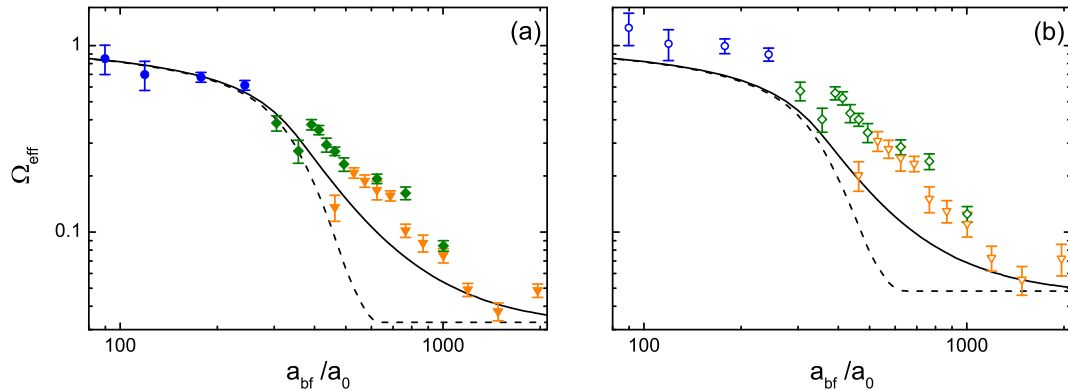


FIGURE 6.10: Effective overlap factor as a function of the Bose-Fermi scattering length for (a)  $\alpha = 3/2$  (Fig. 3 in the main text) and (b)  $\alpha = 1$ .

Fig. 6.10 we show a plot of  $\Omega_{\text{eff}}$  versus  $a_{\text{bf}}$  for  $\alpha = 3/2$  (same as in Fig. 3 of the main text) in comparison with the corresponding result for  $\alpha = 1$ . Note that  $\alpha$  has also been adjusted for the theory curves. As is clearly visible, the plot with  $\alpha = 3/2$  gives a better agreement between the data and the calculations. This indicates that the presence of secondary loss processes is very likely.

Additionally K atoms can be lost because of a boson-boson secondary collision. The typical mean free path for the identical bosons is  $\ell \approx (8\pi a_{\text{bb}}^2 n)^{-1}$  and this gives for our typical peak densities a mean free path of about  $78 \mu\text{m}$  (BEC) and  $1.4 \text{mm}$  (thermal). Thus, it is reasonable to assume that the K atom does not recollide and we can rule out that elastic collisions between the condensate atoms lead to an avalanche effect [Sch01b].

#### 6.7.4 Theoretical model and numerical solution

In this Section, we start with a zero temperature mean-field model for the boson-fermion mixture, and then extend it by introducing a thermal cloud to include finite temperature effects of the bosons. Finally, we calculate the effective overlap factor  $\Omega_{\text{eff}}$  from the density of the different components.

##### 6.7.4.1 Zero-temperature approach

In order to study quantitatively our observations on the overlap factor  $\Omega_{\text{eff}}$ , we construct a numerical mean-field model to calculate the density distributions of the BEC ( $n_{\text{b}}$ ) and the fermions ( $n_{\text{f}}$ ) for an interacting Bose-Fermi mixture at zero temperature. Our model starts from the energy functional of the mixture as [Ima06, Tra16]

$$\begin{aligned}
 E = \int d^3r \left[ \frac{\hbar^2}{2m_{\text{b}}} (\nabla \sqrt{n_{\text{b}}})^2 + U_{\text{b}} n_{\text{b}} + \frac{1}{2} g_{\text{bb}} n_{\text{b}}^2 \right. \\
 + \frac{1}{9} \frac{\hbar^2}{2m_{\text{f}}} (\nabla \sqrt{n_{\text{f}}})^2 + U_{\text{f}} n_{\text{f}} + \frac{\hbar^2}{2m_{\text{f}}} \frac{3}{5} (6\pi^2)^{2/3} n_{\text{f}}^{5/3} \\
 \left. + g_{\text{bf}} n_{\text{b}} n_{\text{f}} \right], \tag{6.28}
 \end{aligned}$$

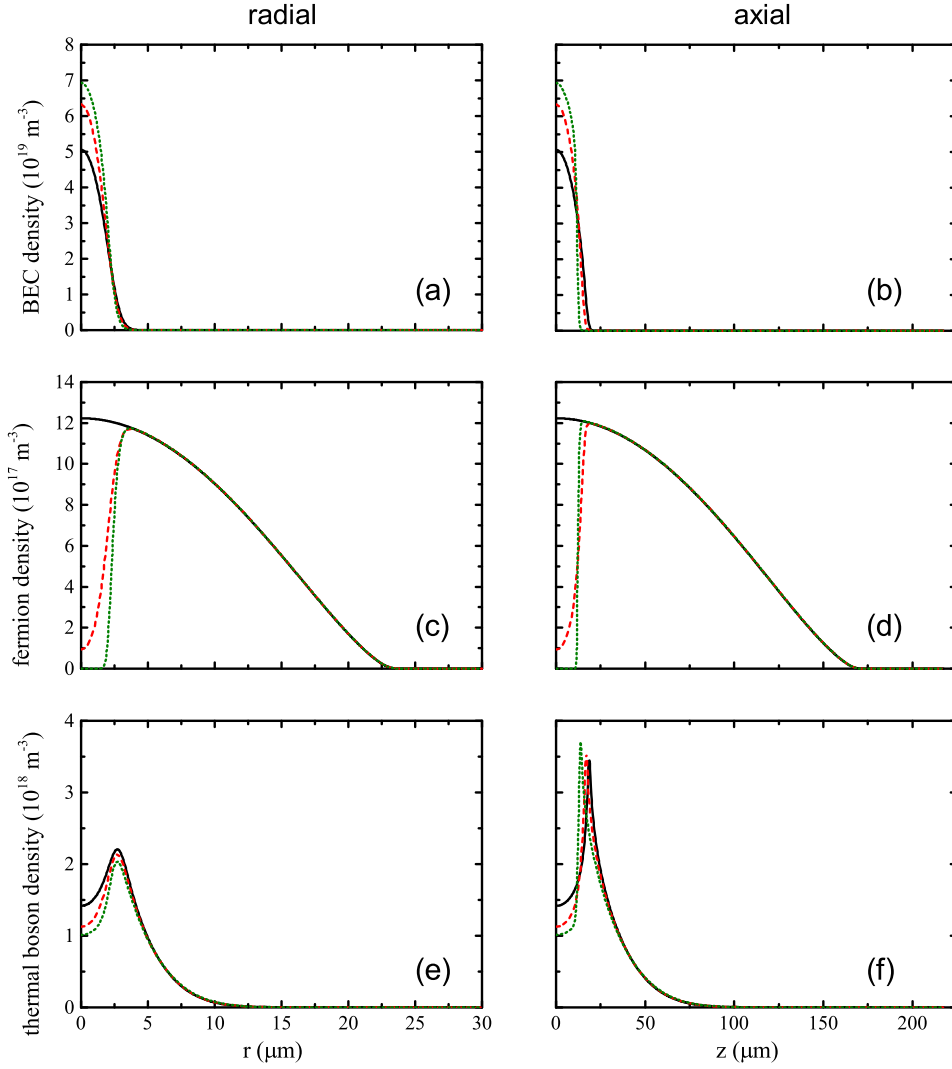


FIGURE 6.11: Number density profiles of the different components of the Bose-Fermi mixture at various values of the boson-fermion scattering length, i.e.  $a_{bf}$  is  $0 a_0$  for the curves in solid black,  $300 a_0$  for dashed red, and  $600 a_0$  for dotted green. Panel (a) and (b) show the radial and the axial density of the BEC. Panel (c) and (d) show the fermion densities and (e) and (f) the thermal boson densities. Note that different density scales are used for the three components. The densities are calculated by considering all terms in Eq. (6.28).

where  $U_b(\vec{r})$  and  $U_f(\vec{r})$  are the bosonic and fermionic harmonic trapping potentials, and  $g_{bb} = 4\pi\hbar^2 a_{bb}/m_b$  and  $g_{bf} = 2\pi\hbar^2 a_{bf}/m_f$  are the boson-boson and boson-fermion coupling constants.

To obtain the densities within the Thomas-Fermi approximation, the term  $(\nabla\sqrt{n_b})^2$ , which arises from the kinetic energy of the BEC, is ignored. Additionally the  $(\nabla\sqrt{n_f})^2$  term of the fermions is ignored as well. This term is the leading term for the density-gradient correction [Kir57], which is much smaller than the other terms under our typical experimental conditions.

To solve Eq. (6.28) numerically, we set up a numerical grid of  $1024 \times 1024$  points in real

space for  $n_b$  and  $n_f$  as our system has cylindrical symmetry. Then for each value of  $a_{bf}$  we minimize this energy functional by varying the densities with imaginary time evolution (also known as the steepest descent method [Ima06]), which is constrained by a fixed total atom number for each species ( $N_b$  and  $N_f$ ) and finally gives the static solution for  $n_b$  and  $n_f$ .

Our typical experimental system has a total boson number of  $N = 2.9 \times 10^4$ , a BEC fraction of  $\beta = 50\%$  and consequently  $N_b = 1.45 \times 10^4$ , and a total fermion number of  $N_f = 1.4 \times 10^5$  (see sets B1-B2 in Table 6.1). Our elongated optical dipole trap has an aspect ratio of 7.3 and the radial trap frequency is 171.1 Hz for the bosons and 300.3 Hz for the fermions. The scattering length for the bosons is  $a_{bb} = 60.9 a_0$ <sup>13</sup>. With these parameters, we obtain the zero- $T$  densities and the results of the full calculation, including both  $\nabla$  terms, are plotted in the upper four panels of Fig. 6.11. Panel (a) and (b) show  $n_b$  in the radial and the axial direction, and panel (c) and (d) show  $n_f$ . Different colors correspond to different values of  $a_{bf}$  (black for  $0 a_0$ , red for  $300 a_0$  and green for  $600 a_0$ ). Note that the effect of the kinetic energy terms, which tends to smooth out the density distributions especially when  $n_b$  is near zero, is more visible in the radial plots (panels (a) and (c)) because of the different scales (aspect ratio) between the radial and axial direction.

#### 6.7.4.2 BEC at a finite temperature: Thermal boson cloud

Because of the finite temperature of the experiment, we only obtain a partial BEC and we have to take the non-degenerate component ( $\sim 50\%$  of  $N$ ) into account. Thus we calculate the thermal boson density  $n_t$ , which is about two orders of magnitude smaller than  $n_b$ . It gives a small extra overlap between the bosons and fermions. In the main text and as outlined in Sec. 6.7.3.4, we approximate the thermal boson density  $n_t$  with a Boltzmann distribution and we obtain an analytical formula for the overlap integrals. For the theoretical model, we include boson statistics, which enhances the boson density in the trap center, as well as the mean-field interaction between the BEC and the thermal cloud, and we calculate  $n_t$  and the corresponding overlap integrals numerically. We assume  $n_t$  to be the density of a trapped saturated thermal Bose gas influenced by the mean-field potential formed by the BEC. Other mean-field effects, e.g. the interaction between fermions and thermal bosons and the influence of the thermal gas on the BEC, are considered to be weaker and ignored. Finally, different from the Boltzmann distribution, the thermal boson density for the numerical model is given by the polylogarithm function  $g$  as

$$n_t = \lambda^{-3} g_{3/2} \left( e^{-\frac{\mu - U_t}{k_B T}} \right), \quad (6.29)$$

where the thermal de Broglie wavelength is  $\lambda = \sqrt{2\pi\hbar^2/(mk_B T)}$ , the total potential for thermal bosons is  $U_t = U_{\text{opt}} + 2g_{bb}n_b$ , the chemical potential  $\mu$  for bosons is taken to be the minimum of  $U_t(r, z)$  so that the thermal gas is saturated in phase space, and  $T$  is the temperature which is obtained as a normalization factor for the total thermal

<sup>13</sup>Eberhard Tiemann. (private communication)

boson number, i.e.  $N_t = \int n_t(T) d^3r$ . Using the zero- $T$  densities of the BEC and the fermions, obtained in the previous Section, we calculate the thermal bosonic density with Eq. (6.29) and we get the radial and axial density profiles displayed in panel (e) and (f) of Fig. 6.11.

It is interesting to note that the bosonic enhancement effect in the thermal cloud substantially increases the peak density by a factor of  $\sim 2.4$ . However, the repulsion by the BEC has the opposite effect, and for the overlap with the Fermi gas, both effects approximately cancel each other. Therefore, we find that the approximation used for the thermal gas in our analysis and the derivation of Eq. (6.27) turns out to be a good one.

### 6.7.4.3 Effective overlap factor $\Omega_{\text{eff}}$

With the numerically calculated densities the effective overlap factor  $\Omega_{\text{eff}}$  at finite temperature can be calculated by numerically solving the overlap integrals in the interacting and non-interacting cases and using Eq. (6.6), where  $\alpha = 3/2$  (see Sec. 6.7.3.5). The results are plotted in Fig. 3 of the main text (here Fig. 6.10a). In Fig 6.10b, the results for  $\alpha = 1$  are shown.

We emphasize that this numerical model does not use the Boltzmann distribution for thermal bosons, and it does not rely on the peak density approximations used in Sec. 6.7.3.5, and it includes effects beyond the Thomas-Fermi limit. The value of the denominator in Eq. (6.6) from the analytical model is only about 9% higher than the numerical result in the non-interacting case and the remaining difference mostly comes from the TF approximation in the analytical model [Eq. (6.27)]. This agreement indicates the validity of the analytical model for the thermal bosons and  $\Omega_{\text{eff}}$ .

## 6.7.5 Systematic errors in theory and experiment

As Fig. 3 of the main text shows, the measured overlap is slightly higher than the calculated values and there can be several reasons for this discrepancy. In this Section, we discuss the possible systematic effects we have in the theoretical calculations as well as in the experimental procedures and data analysis .

### 6.7.5.1 The fermion density: Finite temperature effects and the FRA

In our analysis of the experimental data we use the FRA and the peak density at zero temperature. Both assumptions lead to a systematic error. When using the FRA, we assume the bosons to sample a fixed local fermion density. This assumption leads to an underestimation of the overlap between the fermions and the thermal bosons by about two percent. However, for the overlap with the BEC atoms the deviation from the FRA is negligible because of their small spatial extend.

Furthermore, we assume that the fixed fermion density as sampled by the bosons is given by the fermion peak density at zero temperature (See Eq. (6.18) and Eq. (6.18)). However, finite temperature effects and the gravitational sag on the bosonic cloud challenge

this assumption. For the  $L_3$  measurements, ignoring the finite temperature leads to an underestimation of  $L_3$  of about 20% for the highest temperatures (data set A1). For the peak density used in Eq. (6.27), the finite-T effect is about 7% percent.

The gravitational sag on the bosonic cloud leads to a shift of the center of the cloud by about  $8 \mu\text{m}$ , which, as can be seen in Fig. 6.11, leads to the bosons sampling a 20% lower fermion density than the peak density. Thus, using the lithium peak density in Eq. (6.27) leads to an underestimation of  $\Omega_{\text{eff}}$  by 20%. The effect for the  $L_3$  measurements is less drastic because of the spatial extend of the thermal cloud.

For the final values of  $\Omega_{\text{eff}}$  the effects of finite-temperature on the  $L_3$  measurements and the gravitational sag on the lithium peak density in Eq. (6.27) cancel each other out. We estimate that when taking all the above mentioned corrections into account, we have an underestimation of  $\Omega_{\text{eff}}$  by about 5%.

### 6.7.5.2 Systematic errors in the effective overlap factor $\Omega_{\text{eff}}$

In Fig. 3 of the main text (see Fig. 6.10a), the uncertainty in the  $\Omega_{\text{eff}}$  data points reflects the statistical uncertainties of  $\gamma$ . Additionally, there are systematic errors in determining  $\Omega_{\text{eff}}$  via Eq. (6.27), which come from the determination of the atom number, BEC fraction, temperature and trap frequencies. The systematic calibration error in the determination of the Li and K atom number is about 8%, and we estimate the BEC fraction determination from the bimodal fit to have a 10% error. The systematic error in  $\gamma$  is thereforw11% and for the fermion and BEC peak density it is about 10%. The thermal peak density is estimated to have an error of 17%. The systematic error in  $L_3$  is about 15% and has two main sources. First, the typical  $1\sigma$  uncertainty in the smoothing of  $L_3$  is about 10% and second there is a systematic error in all  $L_3$  data points of about 12% which comes from the uncertainty in the atom numbers, temperature and trap frequencies. All together this leads to a systematic uncertainty in  $\Omega_{\text{eff}}$  of about 26%.

### 6.7.5.3 Other processes

When we prepare the samples, we assume that we ramp adiabatically to the final field, since we did not observe any noticeable excitation. However an unnoticeable yet weak excitation of the mixture can lead to additional overlap and losses. This would both affect the  $\gamma$  and  $L_3$  measurements, and thus only have a weak influence on  $\Omega_{\text{eff}}$ .

Moreover, we speculate that recombination in a degenerate sample may not be exclusively attributed to three-body recombination. Higher-order processes such as four-body recombination may contribute. If at all important, such processes may be present at the high phase-space densities of a BEC, but they will be suppressed for thermal clouds. Such processes would lead to increased values for  $\Omega_{\text{eff}}$ .

The high density of the boson cloud may lead to another effect causing a spatial separation between the two species, as observed in Ref. [Bau11]. If the mean free path of a Li atom in the dense cloud of K is much smaller than the spatial extend of the boson cloud, then the motion is diffusive and it takes a long time for a Li atom to reach the center of the K cloud. If three-body processes happen at a shorter time scale than this

diffusive motion, the result will be an effective reduction of the spatial overlap of both species. The mean free path for a Li atom moving in a thermal cloud of K is about  $20 \mu\text{m}$  ( $a_{\text{bf}} \approx 600 a_0$ ), so for our  $L_3$  measurements, the motion of the Li atom stays essentially ballistic and the effect described in Ref. [Bau11] can be safely neglected. In the case of the K-BEC, the mean free path of the Li atom is an order of magnitude lower and the collision time is on the order of  $20 \mu\text{s}$ . Comparing this to the typical time for three-body loss  $\tau = 2(L_3 n^2)^{-1} \approx 1.5 \text{ms}$ , shows that also for our  $\gamma$  measurements the effect observed in Ref. [Bau11] cannot play a significant role.

# 7 Chapter 7

## Publication: Breathing mode of a Bose-Einstein condensate repulsively interacting with a fermionic reservoir

Journal: Physical Review A, Vol. **99**, Issue 4

Published: 3. April 2019

DOI: [10.1103/PhysRevA.99.041602](https://doi.org/10.1103/PhysRevA.99.041602)

Bo Huang<sup>1</sup>, Isabella Fritsche<sup>1,2</sup>, Rianne S. Lous<sup>1,2</sup>, Cosetta Baroni<sup>1,2</sup>, Jook T. M. Walraven<sup>1,3</sup>, Emil Kirilov<sup>2</sup>, and Rudolf Grimm<sup>1,2</sup>

<sup>1</sup> Institut für Quantenoptik und Quanteninformation, Österreichische Akademie der Wissenschaften, 6020 Innsbruck, Austria.

<sup>2</sup> Institut für Experimentalphysik, Universität Innsbruck, 6020 Innsbruck, Austria.

<sup>3</sup> Van der Waals–Zeeman Institute, Institute of Physics, University of Amsterdam, 1098 XH Amsterdam, Netherlands.

Contribution to the publication: In this publication, I performed preparatory and calibration measurements, implemented and tested the excitation scheme, performed the main part of the measurements and analyzed them. I assisted in preparing the manuscript and wrote a part of the Appendix.

Note on the present version of the publication: This version can vary from the published version since final changes by the editor are not included. Typos have been corrected. The sections structure has been introduced for better readability and references have been updated.

## 7.1 Abstract

We investigate the fundamental breathing mode of a small-sized elongated Bose-Einstein condensate coupled to a large Fermi sea, which consists of fully spin-polarized atoms in the collisionless regime. Our observations show a dramatic shift of the breathing frequency when the mixture undergoes phase separation at strong interspecies repulsion. We find that the maximum frequency shift in the full phase-separation limit depends essentially on the atom number ratio of the components. We interpret the experimental observations by modelling the complex dynamics of the collisionless fermions within two complementary approaches. One model assumes an adiabatic response of the Fermi sea, while the other one considers single fermion trajectories for a fully phase-separated mixture. Our models capture the observed features over the full range of interest.

## 7.2 Introduction

Mixtures of quantum fluids play a fascinating role in our understanding of multi-component many-body quantum systems. For decades, the study of such mixtures focused on the phases of the helium isotopes  $^3\text{He}$  and  $^4\text{He}$  and their properties in mixed states, under phase-separated conditions, or at the interface between two phases [Ebn71]. Ultracold atomic gases have opened up many new opportunities, and various weakly and strongly interacting Bose-Bose, Fermi-Fermi and Bose-Fermi mixtures have been investigated [Pit16, Pet02]. A unique feature of ultracold quantum gases is the possibility to tune the interparticle interactions over a wide range by magnetically controlled Feshbach resonances (FRs) [Chi10].

Right from the early experiments on harmonically trapped quantum gases [Jin96, Mew96], collective modes have served as powerful probes for interparticle interactions. Depending on their particular character [Pit03], collective modes can be sensitive to different effects. If the trapped sample changes its position, angle, or form without undergoing significant volume changes, the mode can be classified as a surface mode. Excitations of this kind have been used to study the transition from hydrodynamic to collisionless behavior in both bosonic [Sta98, Bug05] and fermionic [Alt07b, Wri07] quantum gases. If, in contrast, the oscillation involves significant changes of the volume and thus of the density of the sample, then the mode can be classified as a compression or breathing mode. Modes with predominant compression character can serve as sensitive probes for the equation of state. As an example, the radial breathing mode in an elongated trap [Str96, Che02] has served as a tool to probe strongly interacting Fermi gases [Kin04, Bar04b, Alt07a].

In ultracold atomic mixtures, the motional coupling generally leads to rich behavior in the collective modes, see e.g. Refs. [Bus97, Esr98, Ho98, Bij00, Yip01, Cap01, Pu02, Liu03b, Rod04] for early theoretical considerations. As a basic example, the center-of-mass (COM) oscillations of different components (their so-called dipole modes), which can experience frequency shifts and damping [Vic99, Mad00, Gen01], have been utilized in recent experiments to study coupling effects in mixed superfluids [Fer14, Del15,

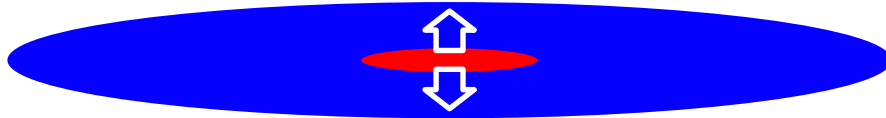


FIGURE 7.1: Radial breathing mode of a small BEC (red) residing in a large Fermi sea (blue). The atomic quantum-gas mixture is kept in a highly elongated optical trap.

Roy17, Wu18]. The dipole modes have also been used to investigate mediated interactions [DeS19] of a BEC interacting with a Fermi sea, where the collisionless fermions have no order parameter. In general, excitations in mixtures involving collisionless motion become rather complex.

In the case of strong interspecies interactions, instabilities (collapse [Mod02, Osp06a] or phase separation [Zac06, Osp06b, Pap08, Shi08, Val17, Lou18b]) render the collective dynamics even more complex. Although the understanding of collective behavior near instabilities is essential in view of proposed fermionic superfluids based on mediated pairing [Bij00, Hei00, Efr02, Suz08, Ens09, Car17, Kin18b], corresponding experimental information is rather scarce.

### 7.3 Experimental procedure and results

In this Rapid Communication, we consider the fundamental breathing mode of a Bose-Einstein condensate (BEC) repulsively coupled to a large fermionic reservoir of atoms. Our system, realized with optically trapped  $^{41}\text{K}$  bosons and  $^6\text{Li}$  fermions (see Fig. 7.1), offers tunable interspecies interaction and allows us to explore the regime of strong repulsion, where the BEC phase separates from the surrounding fermions [Lou18b]. As a dynamic phenomenon resulting from phase separation, we demonstrate the emergence of a drastic up-shift of the BEC's breathing mode frequency. We show how this effect depends on the interaction strength and on the atom number ratio of bosons and fermions. We interpret the complex dynamical many-body physics of our system in terms of two complementary models, which capture the observed features over the full range of interest.

The frequency shift can be understood qualitatively by considering the interface that emerges from phase separation of the Bose-Fermi mixture. In the presence of the interface, the BEC becomes hydrostatically compressed by the Fermi pressure. Exciting a collective mode of the BEC leads to a motion of this interface. If the mode is a breathing mode, the oscillation inflates and deflates the interface, like modulating a bubble in the Fermi sea. Intuitively, the volume change of the BEC leads to a significant reversible work against the Fermi pressure. Because of the existence of this strong restoring mechanism the oscillation frequency substantially increases. This stands in contrast to surface modes of BECs immersed in Fermi gases, which have been observed in experiments [Fer14, Dell5, Roy17, DeS19, Wu18]. There, the frequency shifts are rather small, since surface modes do not change the volume and thus do no work against the Fermi pressure.

The transition into the phase-separated regime is characterized by two distinct values of the interspecies scattering length  $a_{bf}$ . We define a depletion scattering length  $a_d$  as

the value at which the fermion density drops to zero in the center of the trap, where one finds the highest boson density. The value of  $a_d$  is trap specific and depends on the densities of the components, so we obtain it numerically [Lou18b]. We also define a critical scattering length

$$a_c = \frac{\sqrt{15\pi}}{4} r_m \sqrt{\frac{a_{bb}}{k_F}} \quad (7.1)$$

as the value where the mixture fully phase separates in the Thomas-Fermi limit [Viv00]. Here  $r_m = 2\sqrt{m_b m_f}/(m_b + m_f)$ ,  $m_b$  and  $m_f$  are the boson and the fermion masses respectively,  $k_F = \sqrt{2m_f E_F/\hbar^2}$  is the Fermi wave number, and  $a_{bb}$  is the boson-boson scattering length. We note that, under the realistic experimental conditions of a system of finite size, the phase transition is smoothed by the kinetic energy of the BEC [Lou18b]. Our  $^{41}\text{K}$ - $^6\text{Li}$  mixture is produced via laser and evaporative cooling following a procedure described in Ref. [Lou18b] and kept in an elongated optical dipole trap, which is formed by two crossed infrared laser beams and has an aspect ratio of 7.6<sup>1</sup>. The radial trap frequency is  $\omega_b = 2\pi \times 171$  Hz for K and  $\omega_f = 2\pi \times 300$  Hz for Li. Typically, we have a sample of  $10^5$  Li atoms in the lowest spin state Li|1> ( $F = 1/2$ ,  $m_F = 1/2$ ) and  $4 \times 10^4$  K atoms prepared in the second-to-lowest spin state K|2> ( $F = 1$ ,  $m_F = 0$ ). The mixture is thermalized at a temperature of  $T/T_F \approx 0.13$ , where  $T_F \approx 700$  nK is the Fermi temperature of the Li cloud. With a condensate fraction of about 1/3, the K BEC has an atom number of  $\sim 2 \times 10^4$ .

We vary the interspecies interaction strength by a combination of spin-state manipulation and Feshbach tuning. First, we control the particular spin state of the K atoms by application of radio-frequency (rf)  $\pi$ -pulses. In the case of the Zeeman sublevel K|1> ( $F = 1$ ,  $m_F = 1$ ), a Feshbach resonance near 335G facilitates tuning of the interspecies scattering length according to  $a_{bf} = a_{bg}[1 - \Delta/(B - B_0)]$ , where  $a_{bg} = 60.9a_0$  ( $a_0$  is Bohr's radius),  $\Delta = 0.949$  G and  $B_0 = 335.057(1)$  G<sup>2</sup>. In the case of K|2>, only the weak background interaction is present ( $a_{bf} \approx 60a_0$ ), which provides enough thermalization for sympathetic cooling between the two species, but is too weak to induce significant changes to the density profiles [Lou18b]. The boson-boson scattering length stays constant as  $a_{bb} = 60.9a_0$ <sup>3</sup>.

To excite the breathing mode of the K condensate we modulate the interspecies interaction by periodically changing the scattering length [Mat98, Pol10]. As illustrated in Fig. 7.2, this is achieved by alternating the state of the K atoms between K|2> ( $a_{bf} \approx 60a_0$ ) and K|1> ( $a_{bf} \approx 700a_0$ ) using a short burst of rf-pulses at  $B - B_0 = -100$  mG. The  $\pi$ -pulse duration is 100  $\mu\text{s}$ , which is much shorter than the pulse spacing of 1.4 ms. The latter is roughly matched to half the period of the radial breathing mode (full period  $\tau \approx \pi/\omega_b$ ) in order to resonantly drive the oscillation. Starting in K|2>, a burst of three rf pulses enables us to excite the fundamental breathing mode of the K|1> condensate (which is mostly radial) with a  $\pm 25\%$  modulation of the radial size, accompanied by a much slower oscillation in the axial size (see Sup. Mat. in Sec.7.5). The

<sup>1</sup>The two trapping laser beams have a wavelength of 1064 nm and are crossed at an angle of 16 degrees. The waist of the lasers are 44 and 60  $\mu\text{m}$ , respectively.

<sup>2</sup>The light-induced shift of the Feshbach resonance center  $B_0$  has been taken into account. For our typical experimental conditions, it is about ten mG. See the Supplemental Material in Ref. [Lou18b] for details.

<sup>3</sup>The values for  $a_{bb}$  and  $a_{bg}$  are accidentally the same within three digits.

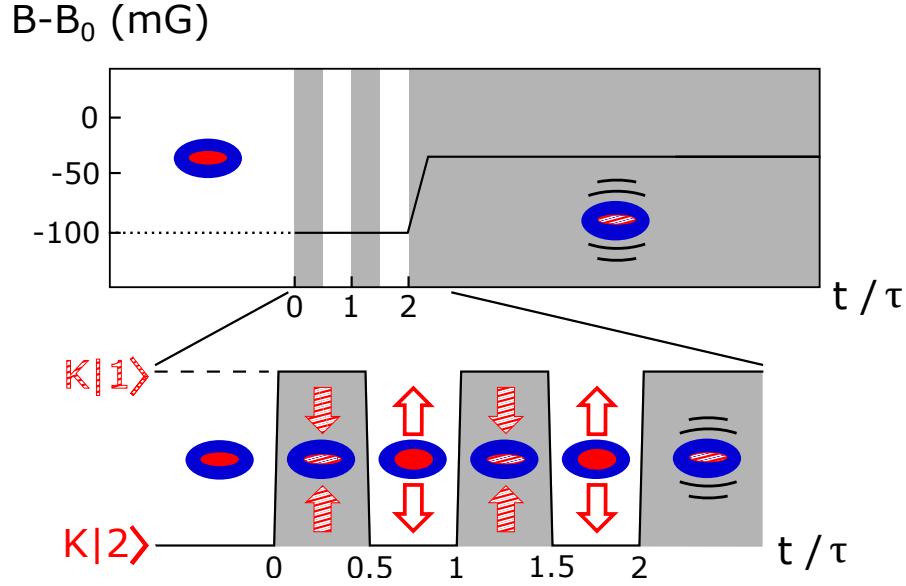


FIGURE 7.2: Excitation procedure for the breathing oscillation of the BEC with a series of interaction quenches. The magnetic field is first set to a value where  $a_{bf} \approx 700a_0$  in the K|1)-Li|1) mixture, but we start in the K|2)-Li|1) mixture, where the interaction is weak ( $a_{bf} \approx 60a_0$ ). Then we apply several radio-frequency  $\pi$ -pulses where the time between consecutive flips is  $\tau/2$ , which corresponds to half of the radial breathing mode period of the BEC in the absence of fermions. After this multiple-pulse excitation we ramp the  $B$ -field to the target value and let the oscillation continue there.

duration of the burst affects the oscillation amplitude but has no noticeable influence on the measured breathing mode frequency  $\omega$ . Within our detection limits, we do not observe oscillations in the thermal cloud of K atoms or in the Li cloud.

Immediately after the excitation stage, the  $B$ -field is ramped within 1 ms to the target value of  $a_{bf}$ . We hold the excited mixture for a variable time and then we switch off the trap and take time-of-flight images of the expanding atomic clouds. To obtain the frequency  $\omega$  of the breathing mode, we fit the recorded time evolution of the width of the BEC with a damped harmonic oscillation with a slowly varying background, the latter being caused by the small residual excitation of the axial mode (see Sup. Mat. in Sec.7.5). Typically we record about six breathing mode periods for each measurement, as a longer hold time can only marginally improve the precision of the measurement (see Sup. Mat. in Sec.7.5). Moreover, we can safely ignore the influence of atom number decay on  $\omega$  within this short period, since the recombination loss from the BEC is below 20% at most of the values of  $a_{bf}$  and still smaller than 50% for the few points taken very close to the FR center ( $a_{bf} > 2000a_0$ ).

In order to normalize  $\omega$  we measure corresponding value  $\omega_0$  in the limit of small  $a_{bf}$ . This is accomplished by adding an additional  $\pi$ -pulse to the above excitation sequence to prepares a K|2) BEC, which provides a good approximation of the non-interaction case. We verified the expected relation to the trap frequency  $\omega_0 = 2\omega_b$  for the radial breathing mode of an elongated BEC [Str96, Che02] within a  $1\sigma$  uncertainty of 2%.

In Fig. 7.3(a) we present our measurements of  $\omega/\omega_0$  as a function of the dimensionless interaction parameter  $a_c/a_{bf}$  with  $a_c$  according to Eq. (7.1). The first set of measurements (filled black circles) was taken with the boson number  $N_b = 1.6 \times 10^4$  and the

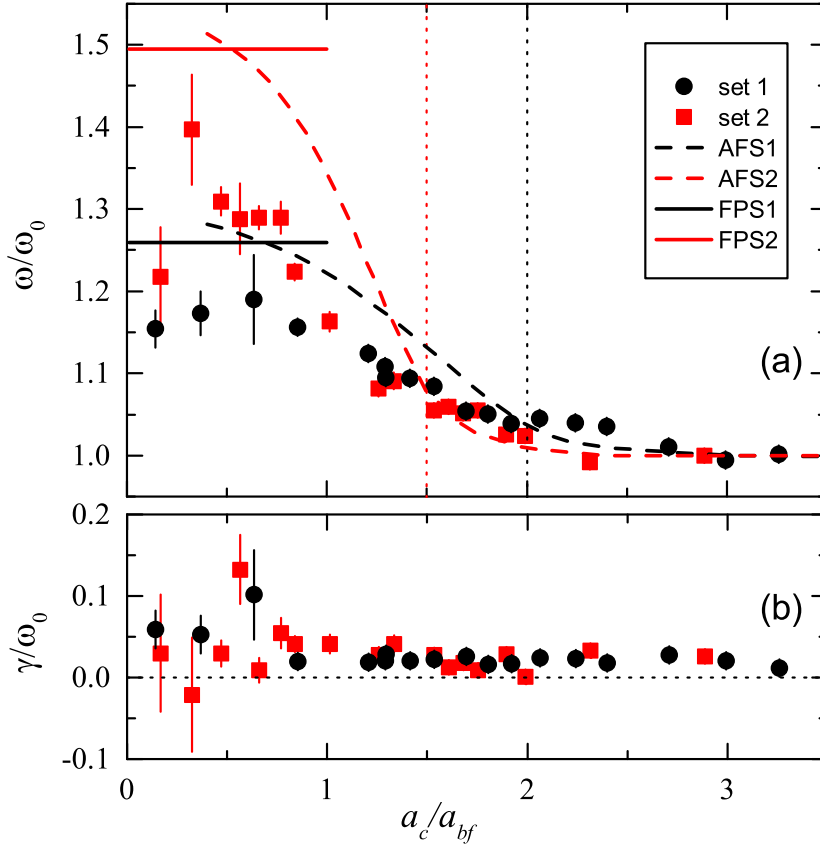


FIGURE 7.3: BEC breathing mode frequency  $\omega$  and damping rate  $\gamma$  as a function of the dimensionless interaction parameter  $a_c/a_{bf}$ . The two sets of measurements (filled black circles and red squares) correspond to different atom number ratios (see text). Both observables are normalized to  $\omega_0$ . The vertical dotted lines indicate the corresponding  $a_d/a_{bf}$ . The theoretical results from the AFS and FPS model are plotted as dashed and solid curves with corresponding color for the two sets of measurements. The error bars indicate the  $1\sigma$  fitting uncertainty.

fermion number  $N_f = 1.0 \times 10^5$  ( $N_b/N_f = 0.16$ ), for which we calculate the two characteristic values of the scattering length as  $a_c = 619a_0$  and  $a_d = 308a_0$  ( $a_c/a_d = 2.0$ ). For increasing repulsive strength, i.e. decreasing  $a_c/a_{bf}$ , we first observe a slow increase of  $\omega/\omega_0$  until  $a_c/a_{bf} \approx 2$  is reached. Here the fermion cloud becomes fully depleted in the center of the BEC [Lou18b]. Then, in the intermediate range of  $a_c/a_{bf}$  between 2 and 1,  $\omega/\omega_0$  rapidly rises until a plateau value of about 1.2 is reached. For even stronger repulsion in the phase-separated regime, no further frequency change is observed. These results show that the frequency up-shift emerges exactly where the transition to the phase-separated regime occurs and finally levels off at the plateau value when full phase separation is reached.

We conducted a second set of measurements with a different atom number ratio ( $N_b = 8.0 \times 10^3$ ,  $N_f = 1.7 \times 10^5$  and thus  $N_b/N_f = 0.05$ , see Sup. Mat. in Sec.7.5), for which  $a_c = 595a_0$  and  $a_d = 400a_0$  ( $a_c/a_d = 1.5$ ). The corresponding results (set 2) are presented as filled red squares in Fig. 7.3. In comparison with set 1, the breathing mode frequency in set 2 starts to increase at a slightly smaller value of  $a_c/a_{bf}$ . But the increase of  $\omega/\omega_0$  is steeper, and a higher plateau value around 1.3 is reached. This is

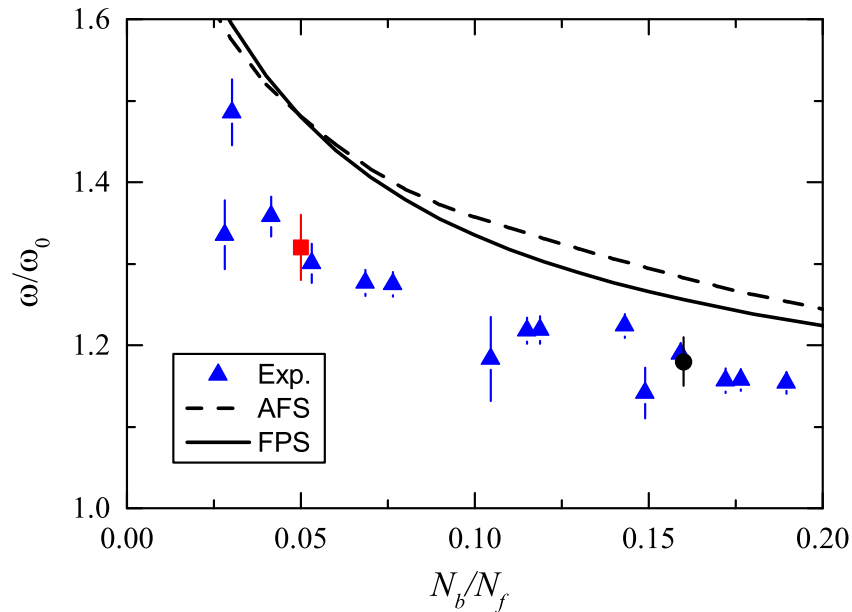


FIGURE 7.4: Breathing mode frequency in the phase-separation limit as a function of  $N_b/N_f$ . The blue triangles show the measurements performed at a fixed  $a_{bf} = 1330a_0$  ( $a_c/a_{bf} \approx 0.45$ ). The error bars show the  $1\sigma$  fitting error. The black circle and the red square show the frequency shift at  $a_{bf} \approx 1330a_0$  as extracted from sets 1 and 2 in Fig. 7.3. The numerical curves from the AFS (dashed) and FPS (solid) model are calculated for a total atom number of  $1.5 \times 10^5$  (see Sup. Mat. in Sec.7.5).

qualitatively expected since a smaller value of  $N_b/N_f$  corresponds to a more strongly compressed BEC and thus a larger frequency change.

For completeness we also show the normalized damping rate  $\gamma/\omega_0$  as a function of the interaction parameter  $a_c/a_{bf}$  in Fig. 7.3(b). In the region of  $a_c/a_{bf} > 1$  we observe a nearly constant value of  $\gamma/\omega_0 \approx 0.02$ , and we attribute this weak damping to the anharmonicity of the crossed optical dipole trap and the interaction between the BEC and the non-condensate bosons [Jin96].<sup>4</sup> In the phase-separated regime where  $a_c/a_{bf} < 1$ , the damping rate shows a trend towards higher values with larger uncertainties, which may be due to a residual excitation of higher-order radial modes.

Motivated by the observed different plateau values of  $\omega/\omega_0$  in the phase-separated regime, we further study the role of the number ratio  $N_b/N_f$ . We carried out a series of measurements at a fixed scattering length of  $a_{bf} = 1330a_0$  ( $a_c/a_{bf} \approx 0.45$ )<sup>5</sup>. As shown in Fig. 7.4, the largest frequency shift observed amounts to about 40% for the smallest  $N_b/N_f$ , and it decreases to  $\sim 10\%$  when  $N_b/N_f$  increases from 0.03 to 0.19 (see Sup. Mat. in Sec.7.5).

A theoretical description of the many-body dynamics of our Bose-Fermi system turns out to be rather challenging, because of the kinetics of the Fermi sea being essentially determined by the collisionless motion of the trapped fermions. The most simple model that captures the elementary features is an adiabatic Fermi sea (AFS) model, which assumes

<sup>4</sup>The observed damping rate  $\gamma/\omega_0$  of the BEC breathing mode remains near 0.02 in the absence of the fermions. We attribute this to the properties of the trap and the bosons.

<sup>5</sup>The ratio  $a_c/a_{bf}$  varies between 0.43 and 0.47, because of small changes in  $a_c$  with variations of  $E_F$  (see Sup. Mat. in Sec.7.5)

that the whole Fermi sea adapts adiabatically to the time-dependent mean-field formed by the BEC. This can be justified if at any position the local Fermi velocity is much larger than the speed of sound of the BEC [Yip01, Hua20]. In addition we take advantage of the fermionic reservoir approximation [Lou18b], which assumes a constant global chemical potential for the fermions. This leads to a time-dependent Gross-Pitaevskii equation for the BEC with a mean-field term from the fermions calculated in a quasi-stationary way. We solve the resulting differential equation numerically (see Sup. Mat. in Sec.7.5) and show the results for the BEC breathing mode frequency by the dashed lines in Figs. 7.3 and 7.4 for  $a_c/a_{bf} > 0.4$ . For stronger repulsion strengths ( $a_c/a_{bf} < 0.4$ ), the extremely thin interface leads to numerical instabilities and challenges the basic assumption of an adiabatic fermion response.

Regarding the dependence on the strength of the repulsive effect (Fig. 7.3), the AFS model predictions agree with the measured points if the Fermi sea is not completely depleted in the trap center ( $a_{bf} < a_d$ ). Beyond that, in the intermediate regime ( $a_d \lesssim a_{bf} \lesssim a_c$ ) the model reproduces the emergence of a strong frequency up-shift, and it finally also shows the tendency of leveling-off in the limit of full phase separation (FPS), where  $a_c/a_{bf} \rightarrow 0$ . Qualitative agreement is also found in the dependence of the up-shift value on the number ratio (the dashed curve in Fig. 7.4) in the FPS regime. Quantitatively, however, the frequency change calculated at  $a_c/a_{bf} \approx 0.45$  is about 1.5 times larger than observed experimentally.

For the case of full phase separation, we develop another approach, named the FPS model, to calculate the frequency shift [VS09, Hua20] (see also Sup. Mat. in Sec.7.5). Instead of assuming a quasi-static behavior of the Fermi sea, the FPS model describes the full dynamic response of a trapped Fermi sea. Intuitively, it embodies the trajectories of individual fermions, which repeatedly bounce off the interface and fall back to it at time intervals up to half of the fermion oscillation period  $\pi/\omega_f$ . Based on the collisionless Boltzmann transport equation, we calculate the dynamic response of the Fermi pressure at the oscillating Bose-Fermi interface. Then the frequency is obtained by matching the pressure and the radial speed at the interface. We find that the FPS model (solid curves in Fig. 7.3 and 7.4) gives a frequency shift very similar to the AFS results in the regime of full phase separation for all  $N_b/N_f$  values that we have studied. Therefore we conclude that the dynamic character of the response does not provide an explanation for the deviation from the experiment [Hua20] (see also Sup. Mat. in Sec.7.5).

A possible reason for the deviation may be due to the excitation scheme, which involves rapid switching of the interaction and thus creates additional fermion excitations [Nas09], which remain unresolved in the oscillation signal (see Sup. Mat. in Sec.7.5) and contaminate our signal. Another reason may be a finite-temperature effect. The thermal bosonic component overlaps with the fermions and, at large interspecies scattering lengths, this forms a hydrodynamic shell around the BEC, which may affect the whole oscillation spectrum. Further investigations will be necessary to fully account for all mechanisms contributing to the large breathing mode frequency shift. Essentially, we encounter the situation where a superfluid is interacting with another quantum fluid without long-range order. The collective and single-particle excitations of the two components are coupled to each other, and hence the excitation spectrum of the mixture becomes more intricate than that of mixtures of two superfluids.

In general terms, our work shows how a small-sized BEC serves as a probe in a quantum fluid and provides information on both the interaction regime and the local properties of the environment. The latter can be described in terms of a decomposition into moments, which couple differently to various collective modes. The local pressure couples to the monopole (breathing) mode, the pressure gradient to dipole modes, and more complex anisotropies to higher-order modes. In our specific situation, the dominant effect results from the Fermi pressure acting on the breathing mode, whereas many scenarios can be envisioned where higher moments will strongly affect the collective mode spectrum. This can be the case in inhomogeneous systems, in more complex trapping potentials, in anisotropic environments realized in dipolar quantum fluids [Bar08a, Lah09, Bur16, Kad16, Tra18], or in spin-orbit coupled systems [Gal13, Zha15].

Bose-Fermi mixtures with tunable interactions represent promising systems for the realization of novel fermionic superfluids based on boson-mediated pairing effects [Bij00, Hei00, Efr02, Suz08, Ens09, Car17, Kin18b], for both strongly attractive and repulsive interspecies interactions. The current experimental possibilities are enhanced by the increasing number of mixtures available in the laboratory; see e.g. Refs. [Tra18, Rav18] for recent examples. In all candidate systems for boson-mediated fermion pairing, an issue of crucial importance is the competition between the formation of pairing phases and the onset of instabilities. Our current studies unveil the elementary dynamics in a strongly repulsive Bose-Fermi mixture and point to more general ways to extract information from the collective dynamics in regimes of particular interest.

## 7.4 Acknowledgment

We acknowledge valuable discussions with M. Baranov, D. Yang, R. van Bijnen, B. van Schaeybroeck, A. Lazarides and T. Maruyama on the theoretical models. We also thank A. Bergschneider and T. W. Grogan for comments on the manuscript. We acknowledge support by the Austrian Science Fund FWF within the Spezialforschungsbereich FoQuS (F4004-N23) and within the Doktoratskolleg ALM (W1259-N27).

## 7.5 Supplemental Material

### 7.5.1 Analysis of the oscillation data

Here, we explain the fitting procedure for our data by which we extract the results presented in the main text. We obtain the data by taking absorption pictures of the partial BECs. We fit the images with a bimodal distribution (assuming a simple Thomas-Fermi distribution for the BEC) and extract the width of the condensed part of the atomic cloud in both the radial and the axial ( $z$ ) direction. By varying the time after the excitation (see Fig. 2 in the main text), we typically record six oscillation periods of the radial width. In Fig. 7.5(a) we show an extended time evolution of the radial width  $R$ , which shows the dynamics on a longer time scale. We observe an oscillation at a frequency  $\omega$ , which corresponds to the radial breathing mode of the BEC. Its

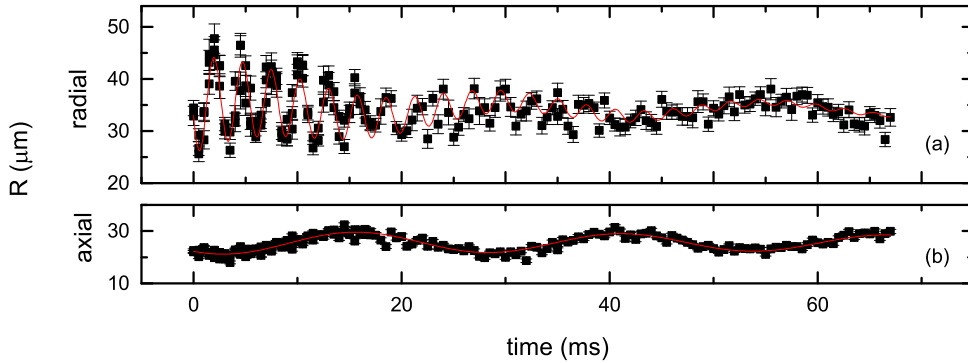


FIGURE 7.5: Long-term time evolution of the BEC size  $R$  in the radial and the axial directions at  $a_{bf} = 362a_0$  ( $a_c/a_{bf} \approx 1.66$ ) and  $N_b/N_f = 0.18$ . The error bars show the  $1\sigma$  error of the bimodal fit. Panel (a) shows the fast radial mode on the background of a slow oscillation induced by the axial mode and panel (b) the slow axial mode. The results of the fits are presented as solid red curves.

frequency is twice the trap frequency of the bosons. In addition to that, we notice a slow background oscillation. This corresponds to an axial mode, which is known as the quadrupole mode for BECs in elongated traps [Mew96]. The excitation of this mode is visible in the time evolution of the axial width  $R_z$  depicted in Fig. 7.5(b). It takes place on a much longer time scale than the radial breathing mode, because of the large aspect ratio (7.6) in our elongated trap.

We obtain the radial breathing mode frequency, by fitting  $R(t)$  by a damped harmonic oscillation with a slowly oscillating background,

$$R(t) = R_0 + Ae^{-\gamma t} \sin(\omega t - \phi) + A_z e^{-\gamma_z t} \sin(\omega_z t - \phi_z), \quad (7.2)$$

where the free parameters of interest are the frequency  $\omega$  and the damping rate  $\gamma$ . Other free parameters of this fitting function are the offset  $R_0$ , the amplitudes  $A$  and  $A_z$  and the phases  $\phi$  and  $\phi_z$ . We determine the axial frequency  $\omega_z$  and damping rate  $\gamma_z$  independently by fitting a damped sinusoidal function to the time evolution of the axial width  $R_z$ , as depicted in Fig. 7.5(b). For most of the data presented in the main text we record about six breathing mode periods. This means that each set of oscillations only shows a part of a period of the axial mode. Therefore the obtained values of  $\omega$  and  $\gamma$  are largely insensitive to the exact values of the axial parameters  $\omega_z$  and  $\gamma_z$ . For this reason we take only one data set for the axial mode and then fix  $\omega_z$  and  $\gamma_z$  in Eq. (7.2) for the analysis of all measurements of the radial breathing mode.

### 7.5.2 theoretical models

Here we briefly summarize the two models, the adiabatic Fermi sea (AFS) and full phase-separation (FPS), which we used in the main text to describe our experimental observations. Both models approximate the elongated mixture as a cylindrical system, where the density distribution in radial direction over the whole  $z$ -axis (axial direction) corresponds to the radial density at the center of the original system. Detailed

studies on these models as well as another numerical model applying the test-particle method [Bra97] for fermions will be discussed separately [Hua20].

### 7.5.2.1 Adiabatic Fermi sea (AFS) model

For each given set of parameters, e.g.  $\{a_{bf}, N_b, N_f\}$ , we obtain the equilibrium state of the Bose-Fermi mixture via a numerical procedure as described in Ref. [Lou18b]. Then we approximate our elongated mixture with a cylindrical system, of which the radial density profiles take the numerical values in the plane at the trap center ( $z = 0$ ). Particularly, the order parameter of the BEC at equilibrium is given by the BEC density as  $\psi_0 = \sqrt{n_{b0}}$ . In order to simulate the oscillations, we start with a perturbed order parameter  $\psi = \psi_0 + \delta\psi$ , e.g. the  $\psi_0$  for a slightly different  $a_{bf}$ . Then we let  $\psi$  evolve in time following

$$i\hbar \frac{\partial \psi}{\partial t} = -\frac{\hbar^2}{2m_b} \nabla^2 \psi + g_{bb} \psi^* \psi^2 + (U_b + g_{bf} n_f) \psi, \quad (7.3)$$

where  $g_{bb} = 4\pi\hbar^2 a_{bb}/m_b$  and  $g_{bf} = 2\pi\hbar^2 a_{bf}(m_b + m_f)/m_b m_f$  are coupling constants, and  $U_b$  is the external trapping potential for bosons. The fermion density is

$$n_f = C(\mu_f - U_f - g_{bf} n_b)^{3/2} H(\mu_f - U_f - g_{bf} n_b), \quad (7.4)$$

where  $C = (2m_f/\hbar^2)^{3/2}/2\pi^2$ ,  $\mu_f$  is the global chemical potential of fermions,  $U_f$  the trapping potential for fermions,  $n_b = \psi^* \psi$  the BEC density, and  $H$  the Heaviside step function. Furthermore we apply the fermionic reservoir approximation [Lou18b], which assumes a constant global chemical potential  $\mu_f$ .

The weighted averaged width of the cylindrical BEC,  $R = \int r^2 n_b(r) dr / \int r n_b(r) dr$ , is recorded as a function of time up to the typical duration of observations and fitted with a cosine function to extract the oscillation frequency  $\omega$  for the current set of parameters.

### 7.5.2.2 Full phase separation (FPS) model

At the limit of large  $a_{bf}$  when the full phase separation occurs, we first study the dynamics of the two components separately within the Thomas-Fermi approximation. Then the frequency of the collective mode is determined by matching the boundary conditions, i.e. velocity and pressure, at the interface. Following a procedure introduced in Ref. [VS09] for a spherical case, we investigate the oscillation for a cylindrical mixture, which is more relevant to our experiment. We note that the currently ignored finite kinetic energy of the BEC at the interface can be included as a surface tension effect [VS08]. However, to adhere to a simple and transparent picture here, we neglect the contribution of the surface tension term, which involves several further assumptions and tends to give a slightly higher frequency shift.

In the cylindrical case, the perturbation of the BEC density is described by

$$\delta n_b(r) \propto F \left( \frac{1 + \sqrt{1 + 2\omega^2/\omega_b^2}}{2}, \frac{1 - \sqrt{1 + 2\omega^2/\omega_b^2}}{2}, 1, \frac{r^2}{R^2} \right), \quad (7.5)$$

where  $F$  is the hypergeometric function  ${}_2F_1$ ,  $\omega$  the frequency of the collective mode,  $\omega_b$  the trapping frequency of bosons, and  $R$  the Thomas-Fermi radius of the BEC. For a phase-separated mixture in a harmonic trap, the value of  $R$  is determined by the chemical potential  $\mu_b$  of the compressed BEC via  $\mu_b = m_b \omega_b^2 R^2 / 2$ .

The ansatz describing the deformation of the Fermi surface in a cylindrical system is  $f = f_0 + \delta(|\mathbf{p}| - p_f)u(r, \alpha, \beta)e^{-i\omega t}$ , where  $\alpha = \cos \phi$  as  $\phi$  is the angle between the momentum  $\mathbf{p}$  and the position  $\mathbf{r}$  in the radial plane,  $\beta = \cos \theta$  as  $\theta$  is the angle between  $\mathbf{p}$  and the  $z$ -axis (axial direction), and  $p_f(r) = \sqrt{2m_f[\mu_f - U_f(r)]}$  is the local Fermi momentum. Then the fermion perturbation has a solution as

$$u(r, \alpha, \beta) = \mathcal{F}_1[L^2]\mathcal{F}_2[v_z^2]e^{-i\omega\tau/2} \quad (7.6)$$

where

$$L^2 = \omega_f^2 r^2 (R_f^2 - r^2)(1 - \alpha^2)(1 - \beta^2), \quad (7.7)$$

$$v_z^2 = \omega_f^2 (R_f^2 - r^2)\beta^2, \quad (7.8)$$

$\mathcal{F}_1[x]$  and  $\mathcal{F}_2[x]$  are arbitrary differentiable functions of  $x$ , the angular momentum  $L$  and velocity  $v_z$  in the axial ( $z$ ) direction are constants of motion.  $R_f$  is the Thomas-Fermi radius. The single fermion trajectory period  $\tau$  is

$$\tau(r, \alpha, \beta) = \frac{\psi_0 - \arctan[2\alpha/g(r, \beta)]}{\omega_f}, \quad (7.9)$$

where  $\psi_0 = \pi H[g(r, \beta)]$ ,  $g(r, \beta) = \sqrt{(1 - \beta^2)(R_f^2 - r^2)}/r - r/\sqrt{(1 - \beta^2)(R_f^2 - r^2)}$  and the domain of  $\alpha$  and  $\beta$  is  $[0, 1]$ . For other values of  $\alpha$  and  $\beta$ , we have  $\tau(r, -\alpha, \beta) = -\tau(r, \alpha, \beta)$  and  $\tau(r, \alpha, -\beta) = \tau(r, \alpha, \beta)$ . In an intuitive picture, fermions repeatedly bounce off ( $\alpha > 0$ ) the Bose-Fermi interface and fall back (with  $\alpha' = -\alpha$ ) to it, because of the trapping potential, at a time interval of  $\tau$ .

We obtain the collective motion frequency  $\omega$  by matching the boundary conditions at the interface  $r = \zeta$ . In the first place, the pressures of the BEC and the fermions should be equal when the surface tension is ignored [VS08]. The pressure of the excited Fermi sea is given by the momentum flux  $\Pi(r) = (1/m_f h^3) \int d^3\mathbf{p} \alpha^2 (1 - \beta^2) p^2 f(\mathbf{p}, r)$  in the radial direction. Moreover, assuming a perfect phase-separation without exchange of particles, the radial speeds of the two components are equal at the interface. We now arrive at the equation for  $\omega$  as

$$\frac{\partial_r F}{F} = \frac{\omega^2 m_b n_b}{\frac{p_f^4 C_\Pi}{(2\pi\hbar)^3} - \partial_r (P_b - P_f)}, \quad (7.10)$$

where  $C_\Pi = 8\omega \int_0^{\pi/2} d\phi \int_0^1 d\beta (1 - \beta^2)^{3/2} \cos^3 \phi \cot(\omega\tau/2)$ . Finally we apply the parameters at the interface into Eq. (7.10) and solve it to get  $\omega$ .

### 7.5.3 role of the atom number ratio

Here we clarify the dependence of  $\omega$  in the full phase-separation regime on the atom number ratio  $N_f/N_b$ , as this dependence is shown in Fig. 4 of the main text. In view of our theoretical models, the dependence can be understood by considering the FPS model and apply further approximations to Eq. (7.10). First we ignore the fluctuation of the Fermi momentum flux, i.e. the term with  $C_{\text{II}}$ , and arrive at an AFS model in the Thomas-Fermi limit. Secondly, we assume  $\zeta \ll R_f$  and drop  $\partial_r P_f$ . Finally, we consider the limit of  $N_f/N_b \gg 1$ , where the BEC is tightly squeezed ( $\zeta \ll R$ ) and  $n_b$  becomes a constant. In this condition, Eq. (7.10) reduces to  $\omega^2/\omega_b^2 = (r\partial F/\partial r)/F$ , the pressure balance condition requires  $R^4 \propto R_f^5$ , and the atom number conservation corresponds to  $N_b \propto R^2\zeta^3$  and  $N_f \propto R_f^6$ . By solving the simplified equation, we find  $\omega/\omega_b \propto (N_b/N_f^{25/24})^{1/3} \sim (N_b/N_f)^{1/3}$ . Consequently, it is valid to approximate  $\omega/\omega_b$  (and  $\omega/\omega_0$  in the main text) as a function of  $N_b/N_f$ .

In the numerical calculations, we use a total atom number of  $1.0 \times 10^5$  and change the atom number ratio  $N_f/N_b$  to study the corresponding variation of  $\omega$ . To justify that any change of the total atom number has only minor influences on our results, we test the dependence of  $\omega$  on the total atom number. We verify that if we increase the total atom number by a factor of two while keeping  $N_f/N_b$  constant, the breathing mode frequency increases by less than 1% (4%) in the FPS (AFS) model.

In the experiment we change the atom number ratio by varying the duration of loading atoms into the magneto-optical trap. In our system we consecutively load Li and K. While loading the latter, the Li atom number decays. Therefore to increase the atom number ratio  $N_b/N_f$  we increase the K loading time, which increases  $N_b$  and reduces  $N_f$ . We tune  $N_b$  from  $6.6 \times 10^3$  to  $2.3 \times 10^4$  while the corresponding  $N_f$  is between  $2.2 \times 10^5$  and  $1.0 \times 10^5$ .

### 7.5.4 other modes and the attractive side of the Feshbach resonance

We briefly report some further observations in our system. First we look into the radial breathing mode frequency at negative  $a_{bf}$  values. Our measurements on the attractive side of the Feshbach resonance are limited to  $|a_{bf}| \lesssim 600$ . For very strong attractive interactions the oscillations are not well-defined, because the mixture is close to the regime where the BEC undergoes collapse [Osp06a, Zac06] and rapidly decays. In this complex regime we see a small upshift in frequency, which reaches a maximum value of 6(2)%.

Secondly, we measure the frequency of the radial dipole mode at positive scattering lengths. We excite this oscillation by shortly switching on an additional trapping beam, which is slightly displaced and parallel to the beam that provides the radial confinement in the crossed optical dipole trap. This displaces the center of mass of the cloud. By switching off this excitation beam we release the sample into the original trap and record the oscillation. Our observations show that there is no interaction-induced shift on the level of 0.5%.

It would be interesting to study also frequency shifts in the low-lying axial modes, i.e. the axial dipole and the quadrupole mode. Due to their surface character these shifts are

expected to be small. For the slow axial mode that we clearly observe in both panels in Fig. 7.5, the oscillations are of opposite phase. This points to the fact that the mode, as expected [Mew96], is mainly a quadrupole mode and thus has predominant surface character. However, two reasons hinder the observation of the frequency shifts in our system. As mentioned before, the timescale of the axial modes is much longer than that of the radial modes. Consequently in the interesting regime, where the interaction is strong and frequency shifts may occur, the fast decay of the atom number leads to large errors in the frequency measurements and prevents us from resolving a frequency shift there. A large uncertainty in these measurements results from the excitation scheme in our experiment. In the time evolution of the axial dipole mode, for example, we observe various hints for higher-order excitations. For these reasons we can only state within an uncertainty of 8% that we do not see a frequency shift for these modes.



## Chapter 8

# Publication: Stability and breakdown of Fermi polarons in a strongly interacting Fermi-Bose mixture

Journal: Physical Review A, Vol: **103**, Issue 053314

Published: 17. May 2021

DOI: [10.1103/PhysRevA.103.053314](https://doi.org/10.1103/PhysRevA.103.053314)

Isabella Fritsche<sup>1,2</sup>, Cosetta Baroni<sup>1,2</sup>, Erich Dobler<sup>1,2</sup>, Emil Kirilov<sup>1,2</sup>, Bo Huang<sup>1,2</sup>, Rudolf Grimm<sup>1,2</sup>, Georg M. Bruun<sup>3,4</sup> and Pietro Massignan<sup>5</sup>

<sup>1</sup> Institut für Quantenoptik und Quanteninformation, Österreichische Akademie der Wissenschaften, 6020 Innsbruck, Austria.

<sup>2</sup> Institut für Experimentalphysik, Universität Innsbruck, 6020 Innsbruck, Austria.

<sup>3</sup> Center for Complex Quantum Systems, Department of Physics and Astronomy, Aarhus University, Ny Munkegade 120, DK-8000 Aarhus C, Denmark

<sup>4</sup> Shenzhen Institute for Quantum Science and Engineering and Department of Physics, Southern University of Science and Technology, Shenzhen 518055, China

<sup>5</sup> Departament de Física, Universitat Politècnica de Catalunya, Campus Nord B4-B5, 08034 Barcelona, Spain

Contribution to the publication: I took the leading role in preparing the system, developing and implementing excitation schemes, and taking the measurements. Furthermore I analyzed the data and wrote the main part of the manuscript.

Note on the present version of the publication: This version can vary from the published version since final changes by the editor are not included. Typos have been corrected. The sections structure has been introduced for better readability and references have been updated.

## 8.1 Abstract

We investigate the properties of a strongly interacting imbalanced mixture of bosonic  $^{41}\text{K}$  impurities immersed in a Fermi sea of ultracold  $^6\text{Li}$  atoms. This enables us to explore the Fermi polaron scenario for large impurity concentrations including the case where they form a Bose-Einstein condensate. The system is characterized by means of radio-frequency injection spectroscopy and interspecies interactions are widely tunable by means of a well-characterized Feshbach resonance. We find that the energy of the Fermi polarons formed in the thermal fraction of the impurity cloud remains rather insensitive to the impurity concentration, even as we approach equal densities for both species. The apparent insensitivity to high concentration is consistent with a theoretical prediction, based on Landau's quasiparticle theory, of a weak effective interaction between the polarons. The condensed fraction of the bosonic  $^{41}\text{K}$  gas is much denser than its thermal component, which leads to a break-down of the Fermi polaron description. Instead, we observe a new branch in the radio-frequency spectrum with a small energy shift, which is consistent with the presence of Bose polarons formed by  $^6\text{Li}$  fermions inside the  $^{41}\text{K}$  condensate. A closer investigation of the behavior of the condensate by means of Rabi oscillation measurements support this observation, indicating that we have realized Fermi and Bose polarons, two fundamentally different quasiparticles, in one cloud.

## 8.2 Introduction

Quantum many-body systems may greatly vary in the nature of their elementary participants and in energy scales, descending from nuclear and quark-gluon plasmas, electrons in condensed matter, down to liquid helium and ultracold gases. Nonetheless, the theoretical approaches used to tackle them are remarkably similar [Lan33, Str18, Wöl18, Bow73, Mas14]. One of the most important tools developed to deal with the many-body problem, and to simplify it drastically, is Landau's celebrated idea of quasiparticles [Lan33]. It turns out that the low energy excitations of a large class of many-body systems can be described in terms of particle-like entities denoted quasiparticles. This leads to a relatively simple yet powerful description of interacting many-body systems, and as a consequence the quasiparticle framework is an indispensable tool in our understanding of nature [Bay91]. Indeed, while exotic new materials such as unconventional superconductors [Nor11] or singular Fermi liquids [Var02] may defy this quasiparticle description, Landau's framework has in general been spectacularly successful in describing a wide range of systems in nature.

Multi-component ultracold gases offer an excellent test bed to investigate quantum many-body systems [Blo08]. In particular, strongly imbalanced quantum mixtures represent an ideal system to study the limits of Landau's quasiparticle paradigm. In these systems, the minority component represents impurities interacting with the surrounding majority component to form quasiparticles. Since early experiments in 2009 [Sch09, Nas09], the case of dilute impurities in a large Fermi sea realizing quasiparticles coined Fermi polarons has been intensively studied in many experiments [Koh12, Cet15, Cet16,

[Sca17, DO19, Nes20, Adl20]. Thanks to the flexibility provided by ultracold atom experiments, also the complementary case of Bose polarons, i.e. quasiparticles formed by embedding mobile impurities in a bosonic environment, has been investigated [Hu16, Jør16, PA19, Yan20a, Sko21].

In the single impurity limit, the quantum statistics of the minority species, i.e. whether it is a fermion or a boson, is irrelevant for the behavior of the ensemble. Theoretical predictions based on Landau's approach have shown excellent agreement with experimental observations in this regime [Che10, Mas14, Lev15a, Sch18]. Even for moderate impurity concentration, a description in terms of quasiparticles has proved accurate. However, as the concentration is further increased, the quantum statistics of the impurities will determine the fate of the polaron. In Fermi-Fermi systems the impurities first form a Fermi sea of polarons [Sca17], and finally the whole system undergoes a transition to a paired superfluid as the concentration is increased beyond a critical value for attractive interactions [Pit16, Kin18a]. In contrast, bosonic impurities at large concentration and low temperature will form a Bose-Einstein condensate (BEC), as we have shown in previous work [Lou17, Lou18b, Hua19]. Employing resonantly tunable interactions, a strongly interacting Fermi-Bose mixture, embedded in the Fermi sea, can then be created. Furthermore, an intrinsic property of quasiparticles such as polarons is that they interact via density modulations in the surrounding medium [Bay91]. Such induced interactions between bosonic impurities will in general be attractive, in contrast to fermionic impurities [Mor10, Yu10, Yu12, Cam18a], and may lead to the formation of bound dimer states [Cam18b].

In this Article, we present our experimental observations regarding polaron physics in Fermi-Bose mixtures, where the bosons ( $^{41}\text{K}$  atoms) represent the minority species immersed in a sea of ultracold fermions ( $^6\text{Li}$  atoms). We explore different density regimes and show that both the Fermi and the Bose polaron can be realized in our system. In Sec. 8.3 we discuss the basic properties of the impurities as a function of their concentration, and the differences with respect to the previously investigated Fermi-Fermi case of  $^{40}\text{K}$  impurities in a  $^6\text{Li}$  gas [Koh12, Cet15, Cet16]. After this we introduce our experimental procedures and the relevant parameters in Sec. 8.4. Then our experimental results are presented and discussed in Sec. 8.5 before we conclude in Sec. 8.6.

### 8.3 Bosonic Impurities in a fermionic environment

In this Section, we discuss our basic approach of immersing bosonic potassium atoms,  $^{41}\text{K}$ , as a minority component into a Fermi sea of ultracold lithium atoms,  $^6\text{Li}$ , in the presence of strong interspecies interactions. We introduce the three different density regimes accessible in our system. Then we compare the current experimental approach with our previous work, in which we investigated a system where the impurity was represented by the fermionic isotope  $^{40}\text{K}$  [Koh12, Cet15, Cet16].

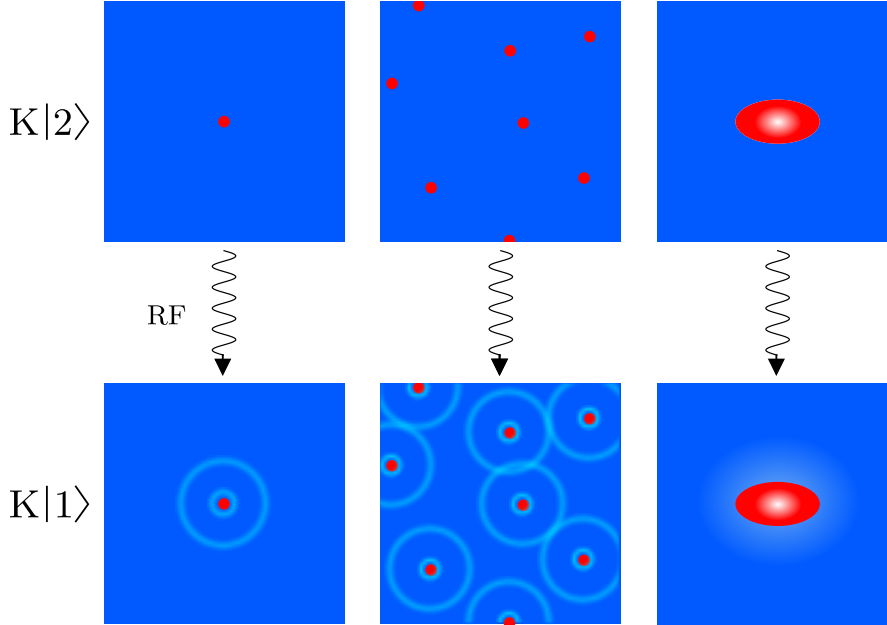


FIGURE 8.1: Illustration of the Fermi-Bose mixture in three different impurity density regimes. The upper (lower) row shows the non-interacting (interacting) impurities, immersed in a Fermi sea, which is represented by the blue background. The interaction between the impurities and the Fermi sea gives rise to density modulations as illustrated by the light blue circular rings around the K atoms. A radio-frequency (RF) pulse brings the system from a non-interacting to a strongly interacting state. The three columns illustrate three different regimes. From left to right we increase the bosonic density from a single impurity, to high densities, and finally to a mixed phase containing a large BEC component.

### 8.3.1 From a single impurity to a BEC

Our main motivation is to investigate density-dependent effects of Fermi polarons emerging from bosonic impurities. The three different regimes of impurity densities in our Fermi-Bose (FB) mixture are illustrated in Fig. 8.1. The blue background and the red dots represent the Li Fermi sea and the K impurities, respectively. As in our previous work on the Fermi-Fermi (FF) system [Koh12], we use radio-frequency (RF) injection spectroscopy to transfer atoms from a non-interacting spin state  $K|2\rangle$  into a state  $K|1\rangle$  that interacts with the fermionic medium.

In the case of a single impurity (left column), the K atom is dressed by particle-hole excitations of the Fermi sea, which lead to local density modulations in the medium and to the formation of the Fermi polaron. In this low concentration regime, the quantum statistics of the impurity does not matter. The situation is accurately described in terms of a variational ansatz [Che06], which has been widely applied in the field [Mas12, Mas14, Par16, Sch18].

As we add more K atoms, we expect to introduce polaron-polaron interactions into our system, as depicted in the middle column of Fig. 8.1. In this density regime, the spatial overlap of the density modulations around the impurities will result in an effective interaction between the quasiparticles mediated by the fermions, which is attractive due

to the bosonic nature of the  $^{41}\text{K}$  atoms [Mor10, Yu10, Yu12, Cam18a, San08, Hu18, Cam18b, Taj18, DeS19, Edr20], see also Appendix 8.9. This effective interaction plays a key role in Landau's quasiparticle theory, but experimental observations in quantum-degenerate gases are still scarce [Cet16].

In the high-density regime (right column), the impurities form a BEC in the center of the trap. As we shall see, the density of this BEC exceeds that of the fermionic density by a large factor of  $\sim 36$ . In this case, the two species interchange their roles and, locally, the Li atoms can be considered as impurities in the K-BEC. Such a scenario is commonly described in terms of Bose polarons [Hu16, Jør16]. Therefore, as we vary the K density from a thermal cloud to a BEC, we can realize the transition from a system of Fermi polarons to a system of Bose polarons.

### 8.3.2 Comparison with previous experiments

Here we discuss the basic situation investigated in our present work in comparison with our previous experiments. The main difference is the change in the quantum statistics of the impurity species, i.e. bosonic  $^{41}\text{K}$  atoms instead of fermionic  $^{40}\text{K}$  atoms. The Fermi sea of  $^6\text{Li}$  stays essentially the same, only with minor changes of the particular experimental parameters. This similarity enables us to focus on the effects of the quantum statistics of the impurity.

The tunability of the interspecies interaction strength in our experiment is given by a Feshbach resonance (FR) [Chi10] between the lowest Zeeman sublevels of K and Li. The parameters characterizing the FR are very similar in the FB and FF case, see App. 8.8 and Supp. Mat. of Ref. [Cet16]. A quantitative difference is the Fermi energy, which in the present case is somewhat lower and therefore modifies the influence of the finite effective range on the interspecies interaction. This fact is taken into account in our theoretical approach, which is presented in detail in App. 8.9.

Another difference between the two systems, which is connected with the FR, is the choice of spin states we work with. In the FF system, we tune the interactions between the lowest and the third-to-lowest spin state of Li and K, respectively. Therefore, dipolar relaxation [Nai11] can lead to decay into lower lying Zeeman sublevels, which is relevant, in particular, if molecules are formed [Jag16]. In the FB case, the interacting atoms occupy the lowest spin channel, which suppresses the two-body process of dipolar relaxation.

When considering few-body processes [Nai17, Gre17a], we find that the quantum statistics of the impurities plays a crucial role. In contrast to the FF system, inelastic few-body scattering processes are not suppressed by Pauli blocking in the present case. Therefore, three-body processes involving one fermion (Li) and two bosons (K) can lead to strong resonant losses [Häf17, Joh17]. Other few-body processes, like, e.g., atom-dimer resonances [Jag14], sensitively depend on the quantum statistics.

As we increase the K density and generate a BEC, which is only possible if the impurities are bosonic, the character of the whole system changes qualitatively. As described in our previous publications [Lou18b, Hua19, Hua20], already for moderate repulsive

interspecies interactions we enter the regime of phase separation. Here the BEC separates from the Fermi gas and behaves as an almost pure BEC. On the other hand, for moderate attractive interactions the BEC is supposed to undergo collapse [Osp06a, Zac06].

Owing to the fact that the Li-K mixture offers very similar interaction tunability for  $^{40}\text{K}$  and  $^{41}\text{K}$ , it provides an excellent test bed for investigating the differences between strongly interacting FF and FB systems.

## 8.4 Experimental procedures

In this Section, we outline the experimental procedures for preparing a mixture of ultracold  $^6\text{Li}$  and  $^{41}\text{K}$  atoms in the vicinity of an interspecies FR. After describing the preparation of our sample (8.4.1), we introduce experimental parameters relevant for the data analysis (8.4.2) and our method of tuning the interspecies interaction (8.4.3). Finally we explain the RF excitation scheme (8.4.4).

### 8.4.1 Sample preparation and detection

We use an all-optical approach [Spi10] to prepare our system in a crossed-beam optical dipole trap (CODT), operated with 1064-nm light. Following the evaporation and spin preparation scheme described in detail in the Supplemental Material of Refs. [Lou18b, Lou18a], we obtain a mixture of lithium atoms in the lowest hyperfine spin state  $|\text{Li}|1\rangle$  ( $F = 1/2, m_F = 1/2$ ) and potassium atoms in the second to lowest hyperfine spin state  $|\text{K}|2\rangle$  ( $F = 1, m_F = 0$ ) in thermal equilibrium.

At the end of each experimental cycle we switch off the optical dipole trap, let the atoms expand for an adjustable time and detect them using state-selective absorption imaging. This allows us to image the atoms in two spin states per species for each experimental cycle. Details on the imaging technique and on how to obtain the atom number are provided in the Supplemental Material of Ref. [Cet15].

We conduct our measurements in two different regimes, in which we either prepare a thermal cloud (THC) or a partially condensed cloud (PBEC) of K atoms immersed in a degenerate Fermi sea of Li atoms. We keep the same trap setting for both regimes in order to avoid complications arising from different trap depths and different light shifts of the center of the Feshbach resonance. We achieve this by altering the preparation stage for the PBEC with respect to the THC in two ways. First, we increase the initially loaded atom numbers and second we apply an additional evaporation step where we further ramp down the power of our CODT and slowly (within 1s) recompress it to the initial values in the end. With this procedure, we ensure a two-fold increase in the number of K atoms and thus an increase of the critical temperature for condensation by about 30%. The condensed fraction is typically of the order of  $\beta \approx 0.5$ .

The finally prepared system consists of roughly  $10^5$   $\text{Li}|1\rangle$  and  $10^4$   $\text{K}|2\rangle$  atoms<sup>1</sup> with temperatures of  $T \approx 100$  nK at a magnetic field of  $B \approx 335$  G, where the only relevant effect of the weak interaction is the thermalization of the sample with an interspecies scattering length of about  $\sim 60 a_0$ <sup>2</sup>,  $a_0$  being the Bohr radius. The atoms are trapped in a CODT with radial trap frequencies  $\omega_{\text{rad,K}} = 2\pi \times 227 \text{ s}^{-1}$  and  $\omega_{\text{rad,Li}} = 2\pi \times 382 \text{ s}^{-1}$ , as well as axial frequencies  $\omega_{\text{ax,K}} = 2\pi \times 31 \text{ s}^{-1}$  and  $\omega_{\text{ax,Li}} = 2\pi \times 49.5 \text{ s}^{-1}$  for K and Li, respectively. The resulting elongated trap has an aspect ratio of  $\sim 7$  with the weak axis oriented horizontally. The differential gravitational sag [Lou17] amounts to about  $3 \mu\text{m}$  and can be neglected since the Fermi sea is much larger. These are the initial conditions for all the measurements presented in this Article.

#### 8.4.2 Relevant parameters

The procedure for thermometry in our mixture of  $^{41}\text{K}$  and  $^6\text{Li}$  atoms is different for the two experimental regimes. In the case of THC we determine the temperature in a standard way by ballistic expansion of the K atoms after releasing them from the trap. In the case of PBEC we follow the approach described in Ref. [Lou17], where we release the atoms from the trap to determine the condensate fraction of the K atoms. From this and the known atom numbers and trap frequencies, we calculate the temperature. For a PBEC, this thermometry method proved to be more accurate than the standard ballistic expansion method [Lou17]. The density profiles of both the degenerate Li Fermi gas and the bosonic K cloud are calculated using standard textbook relations [Pit16]. We neglect small finite-size or interaction corrections for the condensate [Lou18b]. In order to determine the relevant parameters of our system we take into account that the Fermi pressure acts on the Li atoms, and that the optical potential is about two times deeper for K. This leads to the potassium sample being much smaller than the spatial extent of the lithium cloud, which allows us to treat the latter as an essentially homogeneous environment [Koh12]. Since we obtain our spectroscopic signal from the K component, we introduce the K-averaged atom number densities,  $\bar{n}_{\text{Li}}$  and  $\bar{n}_{\text{K}}$ , for both species,

$$\bar{n}_{\text{Li,K}} = \frac{1}{N_{\text{K}}} \int n_{\text{Li,K}}(\mathbf{r}) n_{\text{K}}(\mathbf{r}) d^3\mathbf{r}, \quad (8.1)$$

with  $n_{\text{Li,K}}(\mathbf{r})$  being the local number density at position  $\mathbf{r}$  of Li and K, respectively. Similarly we define the effective Fermi energy as

$$\epsilon_{\text{F}} = \frac{1}{N_{\text{K}}} \int E_{\text{F}}(\mathbf{r}) n_{\text{K}}(\mathbf{r}) d^3\mathbf{r}, \quad (8.2)$$

where the local Fermi energy at position  $\mathbf{r}$  is given by

$$E_{\text{F}}(\mathbf{r}) = \frac{\hbar^2 (6\pi^2 n_{\text{Li}}(\mathbf{r}))^{2/3}}{2m_{\text{Li}}}. \quad (8.3)$$

<sup>1</sup>Note that the atom numbers in the PBEC and in the THC slightly differ, due to the different preparation methods.

<sup>2</sup>Hanna, T. and Tiesinga, E.(private communication)

Finally, we define the effective Fermi wave number as  $\kappa_F = \sqrt{2m_{\text{Li}}\epsilon_F}/\hbar$ .

In Table 8.1 we present an overview of typical values for important experimental parameters, which we adjust to measure the polaron spectra, as discussed in Sec. 8.5.1. Since such a measurement consists of many individual spectra, the given uncertainties reflect the standard deviation for all spectra. We introduce the dimensionless range parameter  $\kappa_F R^*$  [Pet04], which quantifies the character of the Feshbach resonance (open- or closed-channel dominated), and the reduced temperature of the sample  $k_B T/\epsilon_F$ , where  $k_B$  is the Boltzmann constant. The total atom numbers of Li ( $N_{\text{Li}}$ ) and K ( $N_{\text{K}}$ ) are listed, and we give the concentrations  $\mathcal{C}_{\text{K2}} = \bar{n}_{\text{K2}}/\bar{n}_{\text{Li}}$  and  $\mathcal{C}_{\text{K2,BEC}} = \bar{n}_{\text{K2,BEC}}/\bar{n}_{\text{Li}}$  for the thermal and the condensed part of the non-interacting sample, respectively. Note that in the majority of our measurements, we state the concentration of the non-interacting sample. The value for the interacting case  $\mathcal{C}_{\text{K1}} = \bar{n}_{\text{K1}}/\bar{n}_{\text{Li}}$  is experimentally not directly accessible because of interaction effects on the spatial distribution and can thus only be estimated in Sec. 8.5.2.

TABLE 8.1: Table of experimental parameter values for measurements on the thermal cloud (THC) and partial BEC (PBEC).

parameter	THC	PBEC
$\epsilon_F$	$k_B \times 930(60)$ nK	$k_B \times 620(50)$ nK
$1/\kappa_F$	4000(130) $a_0$	4800(200) $a_0$
$\kappa_F R^*$	0.57(2)	0.47(2)
$T$	130(13) nK	118(21) nK
$k_B T/\epsilon_F$	0.14(1)	0.19(3)
$N_{\text{Li}}$	$2.8(2) \times 10^5$	$1.2(1) \times 10^5$
$N_{\text{K}}$	$1.2(1) \times 10^4$	$2.7(3) \times 10^4$
$\bar{n}_{\text{Li}}$	$1.9(2) \times 10^{12} \text{cm}^{-3}$	$1.0(1) \times 10^{12} \text{cm}^{-3}$
$\bar{n}_{\text{K}}$	$0.92(7) \times 10^{12} \text{cm}^{-3}$	$1.4(1) \times 10^{12} \text{cm}^{-3}$
$\bar{n}_{\text{K,BEC}}$	–	$3.8(1) \times 10^{13} \text{cm}^{-3}$
$\mathcal{C}_{\text{K2}}$	0.61(7)	1.5(5)
$\mathcal{C}_{\text{K2,BEC}}^3$	–	36(6)
$\beta$	–	0.46(7)

### 8.4.3 Interaction tuning

An interspecies Feshbach resonance (FR) centered at  $B_0 = 335.080(1)$  G between the atoms in states  $\text{Li}|1\rangle$  and  $\text{K}|1\rangle$  ( $F = 1, m_F = 1$ ) enables us to tune the  $s$ -wave interaction by varying the magnetic field. In Appendix 8.8 we report on the accurate determination of  $B_0$ , including our trap-specific light shift [Lou18b]. This allows us to adjust the interspecies scattering length  $a$  according to the relation [Chi10]

$$a = a_{\text{bg}} \left( 1 - \frac{\Delta}{B - B_0} \right), \quad (8.4)$$

where  $\Delta = 0.9487$  G is the width and  $a_{\text{bg}} = 60.865 a_0$  is the background scattering length of the Feshbach resonance, as explained in detail in the Supplemental Material of Ref. [Lou18b].

In order to quantify the interspecies interaction strength in our system we introduce the dimensionless interaction parameter  $X = -1/(\kappa_F a)$ . Most of the measurements presented in this Article are conducted in the strongly interacting regime ( $-1 \lesssim X \lesssim 1$ ), which raises the question of accuracy and precision in our knowledge of the magnetic field strength. Therefore, we experimentally determined the residual fluctuations around the target value, resulting in a statistical uncertainty of  $\sigma_B = 0.5$  mG, which translates to a corresponding uncertainty  $\sigma_X < 0.035$  of the interaction parameter. Furthermore, we observe a slow drift of the magnetic field strength, which we take into account by taking the average value of the magnetic field determined before and after each measurement. We disregard all measurements that exceed a magnetic field drift of 3 mG.

The uncertainty in the B field and the fact that our FR is extending over a rather small magnetic field region set the resolution we can achieve for  $X$ . For this reason, we discretize the variation of the interaction parameter and divide a region between  $-1.5 < X < 1.5$  into 12 bins, each having a width of  $\sim 0.25$ . Individual bins in the full spectrum, presented in Fig. 8.2, contain averages of 1-4 measurements.

#### 8.4.4 Radio-frequency excitation scheme

In order to probe the spectral function of our K atoms across the Feshbach resonance we use radio-frequency (RF) spectroscopy. There are two main schemes, referred to as “injection” and “ejection” spectroscopy, which shed light on different aspects of the system [Mas14, Liu20]. We choose the former, in which we transfer the minority atoms from a state that is to a good approximation non-interacting into an interacting state. One advantage of this method is that the system can be transferred to a strongly interacting state that is not necessarily the ground state of the system. It therefore enables us to study the repulsive polaron as a metastable state [Mas11, Koh12] along with its non-equilibrium evolution.

The system is excited by an RF pulse that transfers atoms from the non-interacting  $K|2\rangle$  to the interacting  $K|1\rangle$  state in the presence of  $Li|1\rangle$ . In order to avoid side lobes in the spectrum we use a Blackman-shaped pulse. We adjust it to be a resonant  $\pi$ -pulse for a bare K cloud, i.e. in the absence of the Li atoms. The power is chosen such that at the resonance frequency  $\nu_0$ , where the maximum transfer occurs, we have a pulse duration of  $\tau_{\text{RF}} = 1$  ms. This duration was chosen as a compromise between spectral resolution and lifetime. The former is set by the spectral width of the RF pulse  $\sigma_{\text{RF}} = 0.7$  kHz, which, depending on the specific sample preparation, is around  $\sigma_{\text{RF}} \approx 0.04 \epsilon_F/\hbar$ . The latter is given by the shortest lifetime of the polaron, which we estimated to be around 1 ms.

The presence of Li changes the frequency of maximum transfer because of interactions between the two species. In most of our measurement we vary the frequency detuning  $\Delta\nu = \nu_0 - \nu$ , keeping the pulse power unchanged, and observe the transferred fraction of potassium atoms  $N_{K1}/N_{\text{tot}}$ , where  $N_{K1}$  is the atom number in the  $K|1\rangle$  state and  $N_{\text{tot}} = N_{K1} + N_{K2}$  is the total atom number in both states. The dependence of the spectroscopic signal  $N_{K1}/N_{\text{tot}}$  on  $\Delta\nu$  reflects the energy spectrum of our strongly interacting system

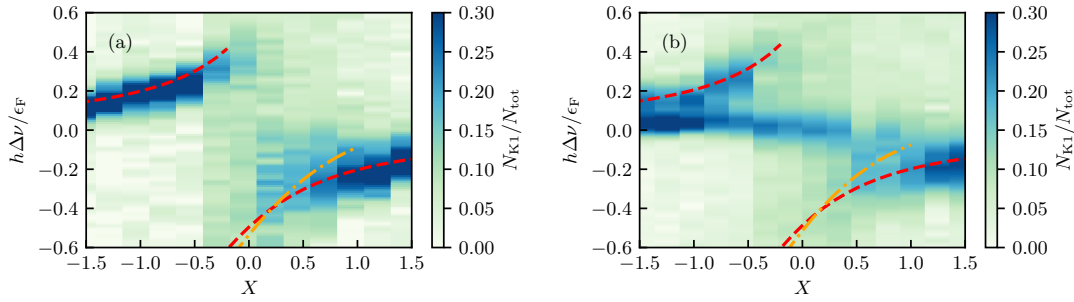


FIGURE 8.2: Spectral response of a bosonic  $^{41}\text{K}$  sample immersed in a  $^6\text{Li}$  Fermi sea. Panels (a) and (b) show the measured excitation spectra in the thermal cloud (THC) regime and the partially condensed (PBEC) regime, respectively. The spectra are shown as a function of the interaction parameter  $X = -1/(\kappa_F a)$  and the dimensionless RF detuning  $h\Delta\nu/\epsilon_F$ . The color map refers to the transferred fraction of atoms from  $\text{K}|2\rangle$  to  $\text{K}|1\rangle$ . Red dashed and orange dash-dotted lines illustrate our theoretical predictions for the polaron and molecule energies in the single-impurity limit, respectively.

of  $\text{K}|1\rangle$  atoms immersed in a  $\text{Li}|1\rangle$  Fermi sea. We determine the uncertainty of the atom numbers from the standard deviation of repeated measurements. A small non-zero background, especially in the PBEC regime, may be attributed to imaging artefacts<sup>4</sup> and is directly subtracted from the data.

## 8.5 Experimental results

In this Section, we present our experimental observations. In Sec. 8.5.1, we discuss our RF measurements of the spectral response of the K atoms. Following this, we describe in Sec. 8.5.2 our findings on the energy of the repulsive Fermi polaron as we vary the density of the thermal K atoms of a partial BEC. The emergence of Bose polarons in the condensed component is discussed in Sec. 8.5.3. Then we present our observations on the lifetime of the repulsive Fermi polaron and discuss possible decay channels in Sec. 8.5.4, before we finally examine the behavior of the K atoms in the PBEC regime on the basis of Rabi oscillation measurements in Sec. 8.5.5.

### 8.5.1 Spectral response

In order to investigate the full spectral response of the system across the strongly interacting regime, we combine RF spectra taken at different values of  $X$ . The spectra, recorded in the thermal (THC) and partially condensed (PBEC) regime, are depicted in Figs. 8.2(a) and (b). The  $x$ -axis represents the discretized dimensionless interaction parameter  $X$ , as discussed in Sec. 8.4.3. Each bin shows the transferred fraction  $N_{\text{K}1}/N_{\text{tot}}$  as a function of the energy detuning of the RF pulse  $h\Delta\nu$  normalized to  $\epsilon_F$ . The theoretical predictions, red dashed and orange dash-dotted lines, denote a

<sup>4</sup>Attributed to imaging artefacts, our absorption pictures show a residual signal in  $\text{K}|1\rangle$  when imaging a BEC in  $\text{K}|2\rangle$ . We explain this by scattering off-resonant light from a very dense atomic sample and subtract the resulting signal from the real atom number.

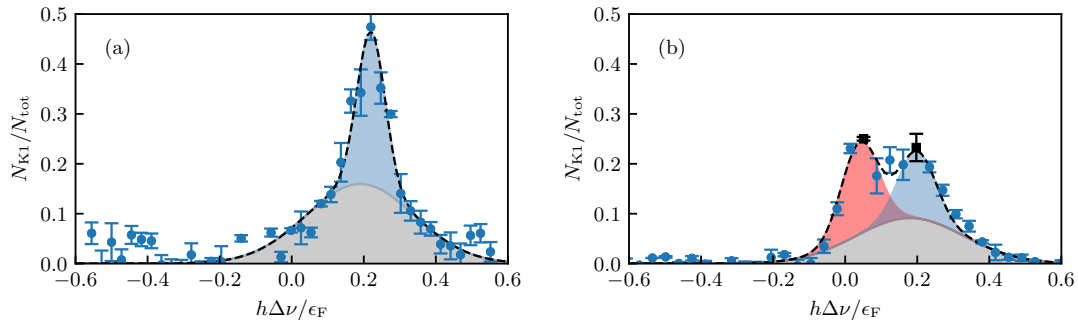


FIGURE 8.3: Typical polaron spectra in the THC (a) and PBEC (b) regime. We show the fraction of transferred atoms as a function of the frequency detuning  $\Delta\nu$  of the applied RF pulse at an interaction strength of  $X \approx -0.7$ . The shaded areas under the curves illustrate the contributions resulting from a fit by a double-Gaussian (THC, left) and triple-Gaussian (PBEC, right) function. Black dashed lines depict their sum. The width of the narrow peaks is fixed to the Fourier width of the applied pulse. The measurement points marked by black squares in (b) are further investigated in Fig. 8.4.

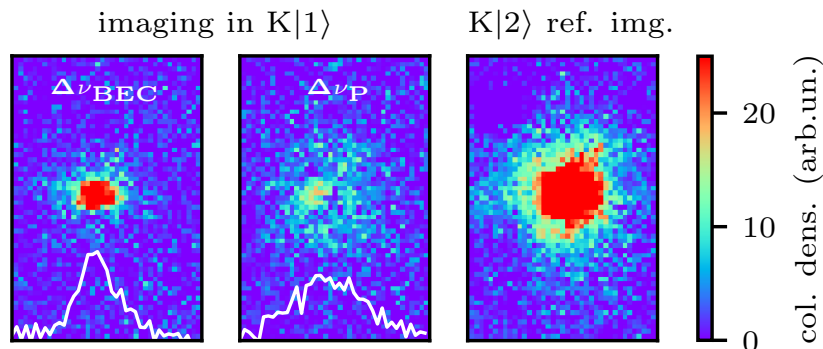


FIGURE 8.4: Absorption images of  $K|1\rangle$  corresponding to the two measurements, marked by black squares in Fig. 8.3(b) and a  $K|2\rangle$  reference image after a short time of flight of 6 ms and 4 ms, respectively. The left panel and the middle panel show the atoms at the transfer frequencies  $\Delta\nu_{\text{BEC}}$  and  $\Delta\nu_{\text{P}}$ , respectively. The color map depicts the column density in arbitrary units. The field-of-view of all images is about  $(150 \times 230) \mu\text{m}$ . The white solid lines show the corresponding projected line-density profiles. A reference picture of the  $K|2\rangle$  cloud, before transfer, with  $\beta \approx 0.5$  is shown in the panel on the right.

variational calculation describing a single impurity interacting with a Fermi sea using a two-channel model [Koh12, Mas12]. The dimensionless range parameter in the two regimes is  $\kappa_{\text{F}}R^* = 0.57(2)$  and  $\kappa_{\text{F}}R^* = 0.47(2)$ , respectively.

In Fig. 8.2(a) we show the full spectral response in the THC regime. We observe a typical polaron spectrum consisting of the repulsive and the attractive branch exhibiting a positive and negative energy shift, respectively, and a decrease of contrast as the interaction is tuned close to  $X = 0$ . The obtained polaron energies are in good agreement with the theoretical predictions for the single impurity scenario, represented by the red dashed lines, although the concentration  $\mathcal{C}_{\text{K}2} = 0.61(7)$  in this measurement is fairly high.

Figure 8.2(b) shows the spectrum in the PBEC regime. A striking difference between the THC and PBEC spectra is that in the latter a new branch, which shows almost no energy shift, emerges in the spectrum. The bimodal spectral response is a consequence of different resonance frequencies of the transfer to the  $K|1\rangle$  state for the two components of the gas. The thermal part of the K cloud appears to behave like in the single impurity limit, even though the K density is similar to the Li density. In stark contrast to this, the condensed part is transferred at a frequency close to the non-interacting value  $\Delta\nu = 0$ , with a small but consistent upshift corresponding to a few percent of the Fermi energy. As we discuss in Sec. 8.5.3, this shift can be attributed to the formation of Bose polarons, where the Li atoms are now the impurities.

In order to further investigate the differences between the THC and PBEC regimes we show two sample spectra at an interaction strength of  $X \approx -0.7$  in Figs. 8.3(a) and (b), respectively. In the THC regime we find a single narrow peak, which we attribute to the Fermi polaron, along with a broader pedestal, which we interpret as a many-body continuum of states. The observed spectrum can be well approximated by a double Gaussian fit  $G_p(\Delta\nu) + G_{bg}(\Delta\nu)$ , as also used in our previous work [Koh12]. The function takes the form  $G_\alpha(\Delta\nu) = A_\alpha e^{-(\Delta\nu - \Delta\nu_\alpha)^2 / (2\sigma_\alpha^2)}$ , with  $A_\alpha$ ,  $\Delta\nu_\alpha$ ,  $\sigma_\alpha$  representing the amplitude, center and width of the Gaussian for  $\alpha = p, bg$ . The polaron peak,  $\alpha = p$ , is fixed to a spectral pulse width of  $\sigma_p = 0.7 \text{ kHz} \approx 0.04 \epsilon_F / h$ , which corresponds to the Fourier width resulting from the finite duration of the 1-ms RF pulse. The background,  $\alpha = bg$ , is marked by the gray, broad Gaussian. We transfer about 50% of the atoms into the interacting state at a frequency detuning corresponding to  $h\Delta\nu \approx 0.2\epsilon_F$ .

In the PBEC regime, depicted in Fig. 8.3(b), we identify a maximum transfer at two well-defined frequencies. We approximate the lineshape of the whole spectrum by a triple-Gaussian function. The first two parts stem from the polaron and the many-body continuum  $\tilde{G}_p(\Delta\nu) + \tilde{G}_{bg}(\Delta\nu)$ . We assume that the ratio of the two amplitudes stays the same as determined in Fig. 8.3(a), but their absolute values are reduced corresponding to the fraction of non-condensed atoms, as  $\tilde{G}_{p,bg}(\Delta\nu) = G_{p,bg}(\Delta\nu) \times (1 - \beta)$ . The third part describes the transfer of the condensed fraction  $\tilde{G}_{BEC}(\Delta\nu) = G_{BEC}(\Delta\nu) \times \beta$  at a small energy shift.

In the two panels on the left of Fig. 8.4, we show absorption images of atoms in  $K|1\rangle$ , after a short time of flight of 6 ms, which were released from the trap within  $\sim 10 \mu\text{s}$  after the RF pulse. The two pictures correspond to the measurements for the two frequency detunings  $\Delta\nu_{BEC}$  and  $\Delta\nu_p$ , for which we have observed maximum transfer of the BEC and the thermal cloud, respectively. These two detunings are marked by black squares in Fig 8.3(b). The atomic clouds in the images have the same atom number, but very different spatial distributions. The left panel shows a dense cloud that only extends over about  $40 \mu\text{m}$ , whereas the middle panel shows dilute atoms that are distributed over the whole picture. In the right image we present a reference picture of a  $K|2\rangle$  cloud before transfer, with a BEC fraction of  $\beta \approx 0.5$ . Comparing these images shows that a fraction of the non-condensed part is transferred in the middle picture and a fraction of the condensed part is transferred in the left picture. This strongly supports our interpretation that the two different frequencies correspond to the resonance frequencies of the two components of the partial BEC.

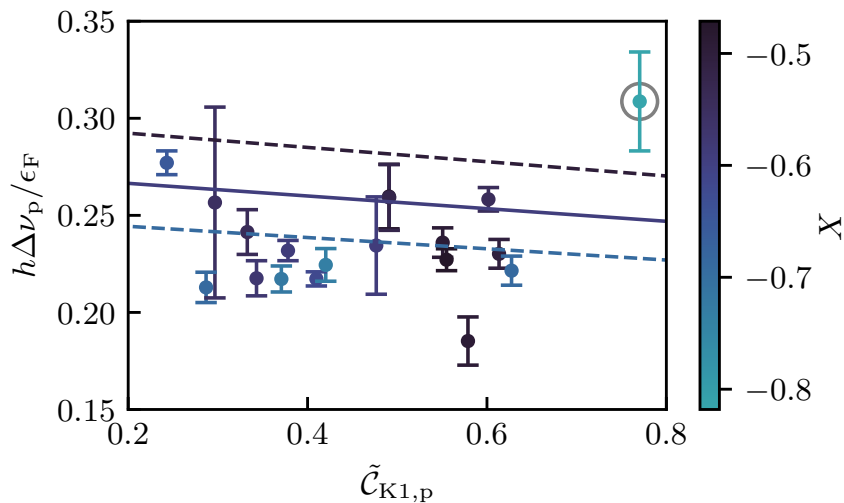


FIGURE 8.5: Concentration dependence of the energy of the repulsive Fermi polaron. The color code refers to the interaction strength  $X$ . The solid and dashed lines show the theoretical predictions including polaron-polaron interactions, according to Eq. (8.32), for the mean value and its standard deviation of  $X = -0.6 \pm 0.1$ . The grey circle marks the measurement with the highest temperature  $k_B T / \epsilon_F = 0.27$  (see discussion in text).

To conclude this part, our observations show that the spectra for the THC and the non-condensed part of the PBEC sample are consistent with a theoretical description of the Fermi polaron, and with our previous measurements on the Fermi polaron with fermionic impurities [Koh12]. In contrast, the condensed part of the partial BEC, which has a very large concentration of K atoms with  $C_{K2} \approx 36$ , shows a much smaller energy shift that seems unrelated to the Fermi polaron.

### 8.5.2 Concentration variation

We now investigate closer the effects of a finite impurity concentration. In particular, we expect on general grounds that there are interactions between the polarons, which should show up as a change in their energy as a function of their concentration [Bay91]. In order to explore this, we take a set of spectra for densities in the range  $0 < C_{K2} < 45$  at an interaction strength  $X = -0.6(1)$ . Here, the uncertainty denotes the standard deviation that characterizes typical experimental fluctuations. We vary the concentration by changing various parameters such as the loading time and the evaporation endpoint in our preparation sequence.

Since only a fraction of the atoms in  $K|2\rangle$  is transferred and only atoms in  $K|1\rangle$  can be responsible for interaction effects, the concentration  $C_{K1}$  is the relevant parameter. This, however, cannot be obtained directly because of our incomplete knowledge of interaction effects on the spatial distribution during the RF pulse. We therefore introduce estimated concentrations, obtained by multiplying the concentration of  $K|2\rangle$  by the estimated transferred fraction at the resonance frequency. The measurements presented here are conducted in the PBEC regime and we can therefore obtain two concentrations  $\tilde{C}_{K1,p} = C_{K2} \times (\tilde{A}_p + \tilde{A}_{bg}) / (1 - \beta)$  and  $\tilde{C}_{K1,BEC} = C_{K2} \times \tilde{A}_{BEC} / \beta$  for the non-condensed

and the condensed component of the K-atoms, respectively. The amplitudes  $\tilde{A}_\alpha$  correspond to the fitting amplitudes, as discussed in Sec. 8.5.1.

In Fig. 8.5 we show our results regarding the density variation of the energy of the repulsive polaron. The color scale indicates the particular values of the interaction parameter  $X$  for each data point. From Fermi liquid theory we know that there is an effective interaction  $f$  between the polarons mediated by the Fermi gas [Bay91]. As shown in Ref. [Yu12] (see also App. 8.9), the effective interaction has a direct and an exchange contribution. For low temperature and arbitrary Bose-Fermi interaction strength, it can be calculated from the density of states  $\mathcal{N}$  at the Fermi surface of the Li atoms and from the number  $\Delta N$  of Li atoms in the dressing cloud of the polaron as  $f = -\Delta N^2/\mathcal{N} + g_1$ . Here,  $g_1 = 4\pi\hbar^2 a_{11}/m_K$  represents the direct interaction between two  $K|1\rangle$  atoms, where  $a_{11}$  is the corresponding scattering length. Note that the induced interaction  $-\Delta N^2/\mathcal{N}$ , mediated by the Fermi gas, is attractive since the K atoms are bosonic. Taking into account that the RF injection spectroscopy gradually increases the impurity concentration, so that the signal is averaged from zero to the final K density, the observed average energy shift is  $E(n) = E(0) + fn/2$ , see App. 8.9 for details. The lines in Fig. 8.5 are obtained from this formula where the solid and dashed lines correspond to an interaction strength of  $X = -0.6$  and  $\pm$  its standard experimental deviation of 0.1. We note that due to the small value of the scattering length  $a_{11}$  between the atoms in  $K|1\rangle$ , the negative slope of these lines is essentially only due to the mediated interaction  $-\Delta N^2/\mathcal{N}$ .

From Fig. 8.5 we see that our experimental observations are consistent with the predicted concentration dependence of the polaron energy. The mean temperature of the measurements presented is  $k_B T/\epsilon_F = 0.17(2)$  so that we expect the result to be fairly close to the zero-temperature limit assumed by the theory. The measurement marked by the grey circle has an exceptionally high temperature of  $k_B T/\epsilon_F = 0.27$ . We therefore suspect that this data point is subject to a significant finite-temperature shift and may thus be considered an outlier.

Given the large fluctuations in the data and the predicted small influence of the effective interaction, we cannot provide conclusive evidence of its presence. Instead, the comparison shows that future improved experiments may indeed open up the possibility to observe the effect of polaron-polaron interactions, for which a clear observation is still missing in the field of ultracold quantum gases.

### 8.5.3 Bose polarons

We now turn to the low-energy peak, which, as we have shown, comes from the condensed fraction of the K atoms. In Fig. 8.6, the position of this peak is shown as a function of the impurity concentration, extracted from the same dataset as presented in Sec. 8.5.2. We observe a small and consistent energy shift of  $\sim 0.04$ . An estimation of this energy shift may be obtained as follows.

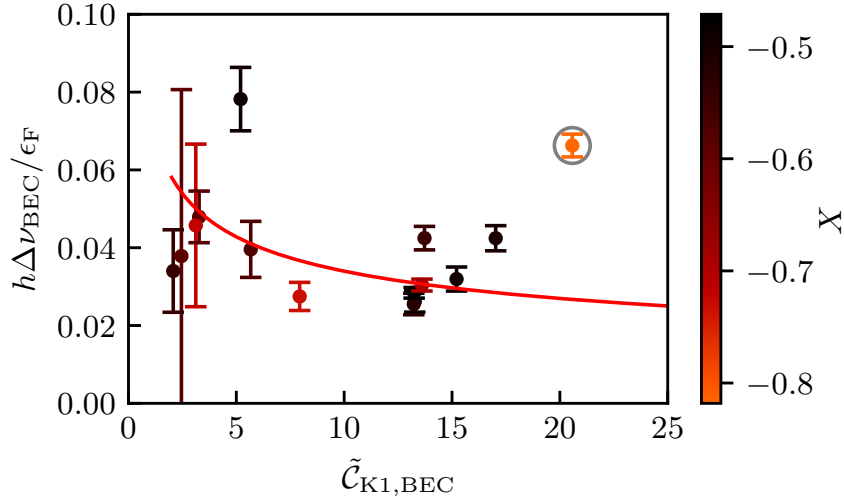


FIGURE 8.6: Concentration dependence of the observed BEC peak position. The color code refers to the interaction strength  $X$  and the grey circle marks the measurement with highest temperature, as in Fig. 8.5. A fit to the data of the theoretical prediction according to Eq. (8.5) is shown as the red solid line. The error bars of the data points represent the uncertainties of the fits.

First, since the three scattering lengths between the K atoms in the two spin states ( $a_{11}$ ,  $a_{22}$  and  $a_{12}$ ) differ by less than 0.3%<sup>5</sup>, the energy shift must be attributed mostly to K-Li interactions. Second, since the density of the condensed part of the K atoms is much higher than for the Li atoms in the center of the trap, the situation is reversed in the sense that one can now regard the Li atoms as impurities in a BEC of K atoms. A suitable framework to analyze this is therefore the one of Bose polarons, formed by Li atoms in the  $K|1\rangle$  BEC, rather than the one of Fermi polarons. The total energy shift can therefore be estimated as  $\Delta E_{\text{tot}} = N_{\text{Li}} E_{\text{Li}}$ , where  $N_{\text{Li}}$  is the number of Li atoms inside the  $K|1\rangle$  BEC, and  $E_{\text{Li}}$  is the energy of a single Bose polaron. In the strongly interacting region on the BEC side of the resonance ( $X \approx -0.6$ ), a repulsive Bose polaron has a typical energy  $E_{\text{Li}} = \xi \epsilon_n$ , where  $\xi$  is a constant of order unity [Hu16, Jør16, PA19, Yan20a, Sko21]. The energy scale  $\epsilon_n$  of the Bose gas is defined, in analogy with the Fermi energy, as  $\epsilon_n = \hbar^2 \kappa_n^2 / (2m_{\text{K}})$ , with  $\kappa_n = (6\pi \bar{n}_{\text{K1,BEC}})^{1/3}$  so that  $\epsilon_n / \epsilon_{\text{F}} = (m_{\text{Li}} / m_{\text{K}}) (\mathcal{C}_{\text{K1,BEC}})^{2/3}$ . The relevant concentration is that of the  $K|1\rangle$  BEC that interacts with the Li atoms, which we approximate as  $\mathcal{C}_{\text{K1,BEC}} \approx \tilde{\mathcal{C}}_{\text{K1,BEC}}$ . Since RF spectroscopy measures the energy shift per atom transferred from  $K|2\rangle$  to  $K|1\rangle$ , the relevant quantity is the energy shift per K atom in the  $K|1\rangle$  BEC, which is given by

$$\Delta E_{\text{tot}} / N_{\text{K1,BEC}} = (6/41) (\tilde{\mathcal{C}}_{\text{K1,BEC}})^{-1/3} \xi \epsilon_{\text{F}}. \quad (8.5)$$

With  $\xi$  as the only free parameter, Eq. (8.5) can then be fitted to the experimental data displayed in Fig. 8.6, which yields  $\xi \approx 0.5$ . The resulting curve, shown by the solid line in Fig. 8.6, reasonably agrees with the data. We should however mention a few caveats. First, the  $K|1\rangle$  BEC is only formed above a certain critical concentration, but the RF probe transfers the atoms gradually into the  $K|1\rangle$  state. This effect is further

<sup>5</sup>Eberhard Tiemann (private communication)

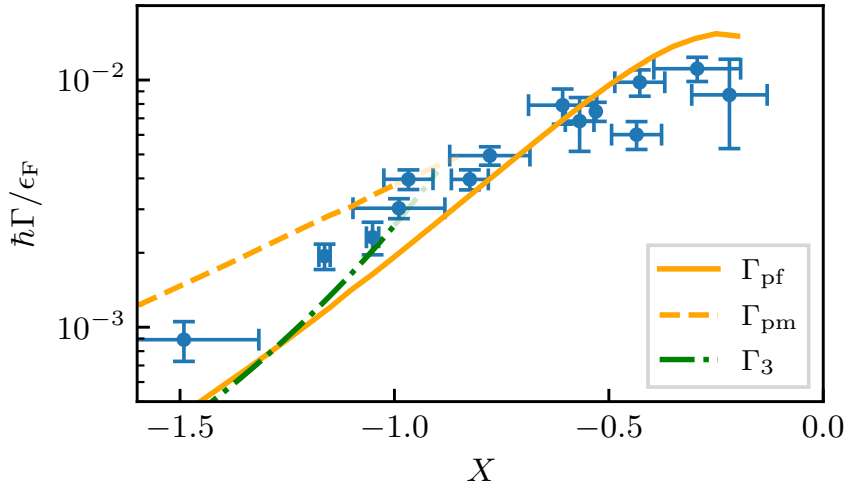


FIGURE 8.7: Decay rate of the polaron for different interaction strengths  $X$ . Blue circles depict the measured lifetimes of the polaron. The orange solid and dashed lines show theoretical calculations of the two- and three-body decay, respectively. The three-body recombination rate in vacuum is depicted by the green dash-dotted line. See App. 8.9 for details.

explored in Sec. 8.5.5. It follows that the observed behavior is presumably a result of an average BEC density experienced by the Li atoms during the RF probe. Second, the bosons and the fermions will eventually phase separate for the given interaction strength [Lou18b, Hua19], which also complicates the interpretation of the experiment. Nevertheless, the agreement between theory and experiment for a reasonable value of the fit parameter,  $\xi \approx 0.5$ , suggests that the observed shift of the BEC energy is, indeed, due to the formation of Bose polarons in the center of trap.

#### 8.5.4 Lifetime of repulsive polaron

The repulsive Fermi polaron is a metastable quasiparticle, which can decay via two- or three-body processes into lower energy states [Mas11, Mas14]. In order to determine its lifetime, we carry out measurements in the THC regime for  $X < 0$ . The repulsive polaron is populated by applying a  $\pi$ -pulse with a duration  $\tau = 0.3$  ms (instead of the 1 ms used in all measurements shown before) and frequency detuning  $\Delta\nu_p$ . In this way, we resonantly excite the quasiparticle with a short pulse in order to maximize the number of transferred atoms. After this excitation, about  $\sim 50\%$  of the atoms are found to remain in  $K|2\rangle$ . We therefore apply a  $10\ \mu\text{s}$  resonant “cleaning” light pulse to remove them from the trap, thus creating a pure sample of strongly interacting  $K|1\rangle$  and  $\text{Li}|1\rangle$  atoms. At this point, we wait for a variable time before applying another RF pulse, identical to the first one, which only addresses the polarons that have not yet decayed. In contrast to all measurements presented so far, the measured signal is now the fraction of atoms transferred back into the non-interacting state  $K|2\rangle$ . We fit an exponential decay to the data sets obtained for various values of  $X$  and extract the  $1/e$  decay time  $\tau_p$ , which represents the lifetime of the polaron.

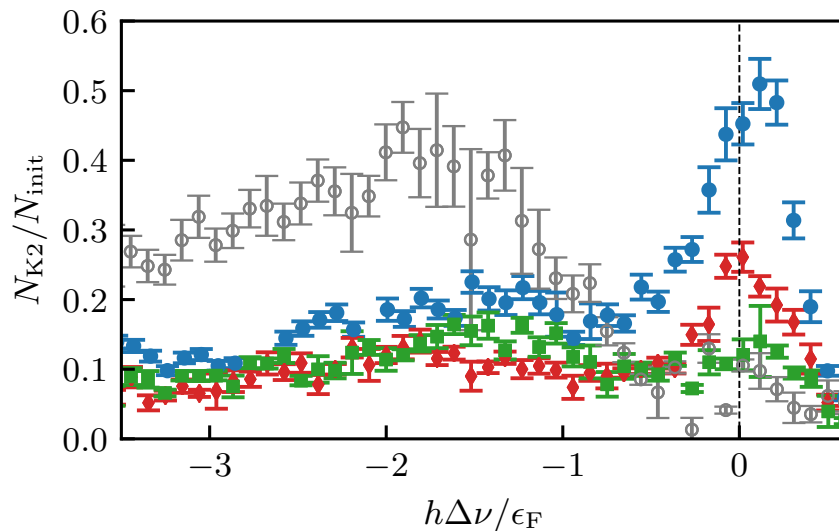


FIGURE 8.8: Ejection spectra of the repulsive polaron and its decay products. We show the fraction of atoms transferred from  $K|1\rangle$  to  $K|2\rangle$  as a function of the applied RF signal. The blue circles, red diamonds, green squares show the spectrum after a decay time of 1.2 ms, 2.2 ms, 5.2 ms. These three measurements are normalized to the total atom number of the measurements with the shortest wait time (blue circles). As a comparison, we also show a molecule spectrum (gray empty circles).

The blue circles in Fig. 8.7 show the repulsive polaron decay rate  $\Gamma = 1/\tau_p$  as a function of the interaction strength. Approaching the resonance, the decay rate rises from  $10^{-3} \epsilon_F/\hbar$  at  $X = -1.5$  to about  $10^{-2} \epsilon_F/\hbar$  at  $X \approx -0.2$ . This corresponds to polaron lifetimes between  $\sim 10$  ms and  $\sim 1$  ms and is in excellent agreement with our previous experiments on Fermi polarons with fermionic impurities [Koh12].

The solid line in Fig. 8.7 is a theoretical prediction based on the assumption that the repulsive polaron decays via a two-body process into the attractive polaron, which due to its high kinetic energy can be approximated by a free particle. The dashed line gives, on the other hand, the three-body decay rate into the molecule, taking into account medium effects in the perturbative regime. Finally, the green dash-dotted line shows the three-body decay rate in a vacuum for a broad resonance [Pet03], adapted here to describe a narrow resonance. For details on the calculations of these rates, see App. 8.9. By comparing these theory lines with the data, we see that two-body decay into the attractive polaron seems to be the main loss channel for strong interactions. However, for weaker interactions the attractive polaron is ill-defined, due to the smallness of its residue and decay into the molecular states. In this regime, three-body decay processes become dominant. This is consistent with the observations for the case of fermionic impurities [Koh12, Sca17].

We observe a residual signal remaining in  $K|1\rangle$  after the second RF pulse, which transfers the repulsive polarons into  $K|2\rangle$ . It consists of remaining polarons and its decay products. In order to investigate the nature of the residual component, we let the polaron decay for a time  $t$  and then we apply ejection spectroscopy. In contrast to the measurement described so far, we now vary the frequency of the second RF pulse, which transfers  $K|1\rangle$

atoms back to  $K|2\rangle$ ). In Fig. 8.8 we show such measurements for the three decay times  $t_1 = 1.2$  ms,  $t_2 = 2.2$  ms, and  $t_3 = 5.2$  ms, all taken at the same interaction strength  $X = -0.80(2)$ . We show the transferred fraction  $N_{K2}/N_{\text{init}}$  normalized to the total atom number  $N_{\text{init}} = N_{K1}(t_1) + N_{K2}(t_1)$  after a wait time of  $t_1$ . The blue circles, red diamonds, and green squares represent the ejection spectra recorded after waiting times of  $t_1$ ,  $t_2$ , and  $t_3$ , respectively.

We expect that the decay product consists of molecules, since this is the predicted ground state for  $X = -0.80$ . In order to check this, we compare the ejection spectra with a molecule dissociation spectrum, shown by the gray open circles in Fig. 8.8. To obtain this spectrum, we start with a THC sample in the non-interacting state. Then we associate molecules by applying a  $3\pi$  pulse to  $K|2\rangle$  at a frequency adjusted such that it corresponds to the binding energy of the molecule at  $X = -0.80$  (see App. 8.8). Since we do not transfer all  $K|2\rangle$  atoms into the molecular state, we apply a resonant ‘‘cleaning’’ light pulse, which removes the remaining atoms from the trap. This leaves us with a mixed sample of  $\text{Li}|1\rangle$ - $K|1\rangle$  molecules and bare  $\text{Li}|1\rangle$  atoms. Then we perform ejection spectroscopy to probe the spectrum of the molecule. This is achieved by applying another  $3\pi$  pulse to dissociate the molecules, where we vary the frequency. Note that this particular spectrum is normalized to its own total atom number  $N_{\text{init}} = N_{\text{tot}}$ .

Let us now compare the four ejection spectra presented in Fig. 8.8. In the measurement at the shortest decay time (blue circles) we recognize a narrow peak at positive energies, which we identify as the repulsive polaron. The broad pedestal at negative energies on the other hand reflects the response of the molecules, since it is similar to the bare molecular spectrum. As we increase the wait time from  $t_1$  to  $t_2$  and then to  $t_3$ , we observe a decrease of transferred atoms at the repulsive polaron frequency, as a consequence of its decay.

Given that the polarons decay into molecules, we would expect a corresponding increase in their spectral signal, i.e. the broad pedestal. This is however not observed. Instead, as the wait time of the measurements in Fig. 8.8 is increased from  $t_1$  to  $t_3$ , we see a reduction of K atoms in the trap by a factor of  $\sim 2$ , while the broad pedestal is unchanged. From this, and the measurements presented in Fig. 8.7, we speculate that the repulsive polarons decay into molecules, which themselves undergo relatively fast collisional decay into lower lying molecular states, where the excess energy of the latter is sufficient to remove the atoms from the trap. We believe Bose-Fermi dimers are less robust against collisions as compared to Fermi-Fermi dimers, for which we have demonstrated a Pauli suppression effect in Ref. [Jag16].

### 8.5.5 Rabi oscillation measurements

We now further investigate the nature of the thermal and condensed parts of the K cloud by performing Rabi oscillation measurements, as shown in Fig. 8.9. A 1-ms RF pulse is applied to transfer atoms from  $K|2\rangle$  into  $K|1\rangle$ . The transferred fraction of atoms is then measured as a function of the pulse area  $\mathcal{A} = \sqrt{P/P_\pi}$ , where the peak RF power  $P$  of our Blackman pulse is the experimentally controlled variable and  $P_\pi$  is

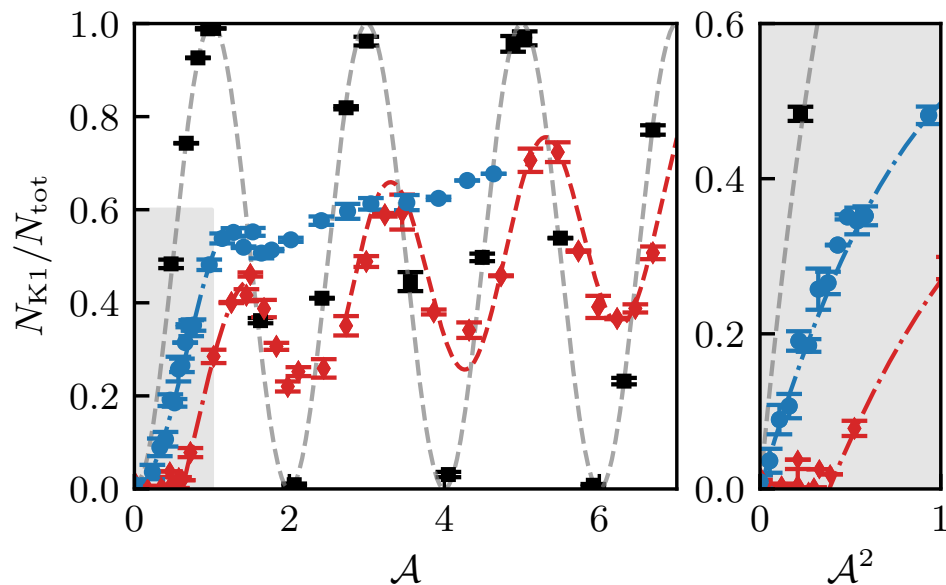


FIGURE 8.9: Rabi oscillation measurements. We show the dependence of the transferred fraction on the pulse area, normalized to a 1-ms RF  $\pi$ -pulse in the non-interacting case. The black squares show the Rabi oscillations of a non-interacting sample. The two further measurements are conducted in the THC and the PBEC regime at  $\nu_p$  (blue circles) and  $\nu_{\text{BEC}}$  (red diamonds), respectively. The black and red dashed lines show a  $\sin^2$  oscillation at the non-interacting Rabi frequency, where the latter has a reduced amplitude by the factor  $\beta$ , corresponding to the BEC fraction. The blue and red dash-dotted curve show the initial transient of a  $\sin^2$  oscillation with Rabi frequencies reduced by the interaction. Right-hand panel: the region of weaker RF pulses, marked by the shaded area, is plotted against the square of the pulse area  $\mathcal{A}^2$ .

the corresponding power to achieve a  $\pi$ -pulse in a non-interacting case. First, we take a reference measurement with Li removed from the trap. As we vary the RF power the black squares show the Rabi oscillations of the non-interacting sample, which are well fitted with a  $\sin^2$  function, as illustrated by the black dashed line. After this, we prepare our atoms in the THC at  $X \approx -0.5$  and tune the radio frequency to the polaron peak at  $\nu_p$  (blue circles). We observe an initial increase in the signal that follows a  $\sin^2$  behavior (dash-dotted blue line). For  $\mathcal{A} \gtrsim 1$ , this changes into a steady increase in the transferred fraction with no clear oscillations. We can explain this effect by the decay of the polaron to other states, such as molecules [Mas12]. Such states have a reduced overlap with the non-interacting state. Therefore, the transfer probability from  $\text{K}|2\rangle$  to  $\text{K}|1\rangle$  is higher than the backtransfer from the dressed molecular state to  $\text{K}|2\rangle$ . This results in a growing population in  $\text{K}|1\rangle$  with increasing RF power.

When we prepare a PBEC sample and tune the frequency of the RF pulse to  $\nu_{\text{BEC}}$  (red diamonds) the system behaves in a very different way. In the region  $\mathcal{A} \gtrsim 1$  of Fig. 8.9, we observe a clear oscillating behavior, depicted by the red dashed line. The frequency is the same as for the non-interacting case, but the amplitude is reduced by a factor that is close to the BEC fraction  $\beta$ . This is consistent with a BEC of K atoms oscillating between the  $|1\rangle$  and  $|2\rangle$  states, in a way, largely unaffected by the small concentration of

Li atoms. The increasing background can be attributed to an off-resonant contribution originated from the non-condensed component.

A remarkable feature shows up in the behavior of the condensate for weak RF pulses. For  $0 < \mathcal{A} \lesssim 1$ , we find that the atom transfer is inhibited. In order to highlight this striking effect, we plot the transferred fraction in the region of small pulse areas, marked by the shaded region, as a function of  $\mathcal{A}^2$  in the right panel of Fig. 8.9. This representation turns an initial quadratic dependence on  $\mathcal{A}$ , typical for the coherent evolution of a quantum system, into a linear dependence on  $\mathcal{A}^2$ . Such a behavior is nicely visible in all three data sets. However the red diamonds show a transfer of the BEC only after a critical value of  $\mathcal{A}^2 \approx 0.4$  is reached.

This peculiar effect likely arises from a density-dependent shift of the resonance frequency. In the regime of low concentration  $C_{K1}$  the final state of the system is the Fermi polaron. This results in almost no transfer, for small  $\mathcal{A}$  in Fig. 8.9, since the detuning of the RF pulse to the polaron energy is about  $\sim 4\Gamma_p$ , where  $\Gamma_p$  is the spectral width of the polaron peak and the Fourier width of the RF pulse is  $1/\tau_{\text{RF}} \approx \Gamma_p$ . On the other hand, when the RF pulse transfers enough atoms to create a  $K|1\rangle$  BEC, the resonance frequency shifts to the one determined by the Bose polarons and permits the transfer to start.

On top of this effect, as the BEC density increases in  $K|1\rangle$ , phase separation may occur and can remove the fermions from the spatial region occupied by the bosons [Lou18b, Hua19]. We estimate this effect to take place while the RF pulse is applied, since there is no clear separation of the corresponding time scales in our experiment. In this scenario, the two species will separate at an RF power that is high enough for a significant fraction of the BEC to be transferred. After this, the K cloud will exhibit Rabi oscillations similar to the non-interacting case.

The origin of the observed inhibition of Rabi oscillations of an RF-coupled BEC in the environment of a Fermi sea is an interesting many-body phenomenon and needs further investigation in future work.

## 8.6 Summary and conclusion

We have presented first observations concerning the Fermi polaron with bosonic impurities and its differences with respect to fermionic impurities. The quantum-statistical nature of the impurities, which does not matter in the single-particle limit, enters the problem at higher concentration and can profoundly change the properties of the system. We have explored the case of high densities below and above the threshold for Bose-Einstein condensation of the impurity cloud and found very different behavior.

For a thermal impurity cloud we have probed the energy of the attractive and the repulsive quasiparticle branch across the strongly interacting regime and found properties

very similar to those of the previously investigated Fermi-Fermi system. Our observations are, within the experimental uncertainties, fully consistent with the single-impurity theoretical predictions despite the fact that the concentration is near unity.

In order to increase the impurity concentration we have cooled the sample further to create a partial BEC. The spectral response of this dense system reveals a drastic change of the spectrum. We find that, in addition to the signature of the repulsive and attractive polaron, a new branch, the BEC branch, emerges in the spectrum, which shows no sign of the Fermi polaron anymore. Instead we find a small positive shift in energy over a wide range of interactions. We speculate that, since the concentration far exceeds unity, this effect may be explained by an interchange of the role of the two atomic species, where the BEC and the Fermi sea represent the environment and the impurities, respectively. Such a scenario is usually described by the Bose polaron [Hu16, Jør16]. This suggests that the Fermi and the Bose polaron appear as different branches of one spectrum.

We have dedicated particular attention to the region of positive scattering lengths, where the repulsive Fermi polaron is realized. As we vary the concentration, the energy shift of the condensed component of the partial BEC remains small and positive. We find good qualitative agreement with a Bose polaron description, where the back action of the Bose polarons on the surrounding results in a small, but clearly observable energy shift.

As we investigate the concentration dependence of the thermal component of the partial BEC closer, at strong repulsive interactions, our results indicate a slightly smaller energy of the Fermi polaron than expected from a single-impurity prediction. The experimental uncertainty in the determination of the interaction strength, which is very sensitive to magnetic field fluctuations, renders a qualitative analysis impossible. However, theoretical calculations, including polaron-polaron interactions, predict a decreasing energy shift with increasing concentration, which is consistent with our experimental data. This suggests that interaction effects amongst polarons could be observed in future more precise measurements.

In order to further characterize the metastable repulsive Fermi polaron, we have measured its decay rate and compared it to theoretical predictions of different decay channels. Our observations close to the center of the FR are in very good agreement with two-body scattering processes, where the repulsive polaron decays into a bare particle. Furthermore we find qualitative agreement between the measured decay rates for moderate interactions and our theoretical calculations of three-body decay.

In order to gain further insight into the transitional behavior from low to high concentration, we vary the strength of the spectroscopy pulse that transfers the partial BEC into the state strongly interacting with the fermionic medium. For low pulse strengths, we observe a peculiar interaction-induced inhibition of the transfer, whereas for high pulse strengths we essentially recover the behavior of a non-interacting cloud. This striking result suggests a shift of the resonance frequency with changing concentration, which supports our interpretation of a transition of our mixture between regimes governed by two fundamental quasiparticles, the Fermi and the Bose polaron.

Our capability of creating a partial BEC, which interacts strongly with a surrounding Fermi sea, allows us to investigate the behavior of vastly different concentration regimes, in the same setup. Future measurements focused on the transition between the two fundamentally different polarons could shed light on the largely unknown physics beyond the single quasiparticle picture, where polaron-polaron interactions play a significant role. Conducting measurements on that order of precision will require even better magnetic field control and more stable conditions, which seems feasible with further technical improvements. In addition, time-domain methods [Cet15, Cet16] may provide deeper insight into density-dependent behavior. The unambiguous observation of such effects would represent a major step, since effective interactions are an integral part of Landau's theory of quasiparticles leading to many of its non-trivial predictions.

## 8.7 Acknowledgment

We acknowledge fruitful discussions with Richard Schmidt and his group at the Max-Planck-Institute for Quantum Optics, and with Jook Walraven. We acknowledge financial support within the Doktoratskolleg ALM (W1259-N27), funded by the Austrian Science Fund FWF, and within the Innsbruck Laser Core Facility, financed by the Austrian Federal Ministry of Education, Science and Research. G.M.B. acknowledges support from DNRF through the Center for Complex Quantum Systems (Grant agreement No. DNRF156) and the Independent Research Fund Denmark-Natural Sciences (Grant No. DFF-8021-00233B). P.M. further acknowledges support by the Spanish MINECO (FIS2017-84114-C2-1-P), and EU FEDER Quantumcat.

## 8.8 Appendix: Accurate determination of the Feshbach resonance center

In all measurements described in this manuscript we tune the inter-particle interaction by means of a particular Feshbach resonance (FR). The exact determination of the Feshbach resonance center  $B_0$  of the FR on the mG scale is crucial in our experiment since the strongly interacting regime is only about  $\pm 12$  mG wide. Our previous determinations of the FR parameters are explained in detail in the Supplemental Material of [Lou18b]. Following a slightly different technique, we determine the molecule's binding energy  $E_b$ , in vacuum, at different interaction strengths and fit it with

$$E_b = \frac{\hbar^2}{8(R^*)^2 m_r} \left( \sqrt{1 - \frac{4R^*(B - B_0)}{a_{bg}\Delta}} - 1 \right)^2, \quad (8.6)$$

derived in [Pet04, Lev11]. The reduced mass  $m_r = m_F m_B / (m_F + m_B)$ , the resonance width  $\Delta = 0.9487$  G, the range parameter [Pet04]  $R^* = 2241(7) a_0$ , and the background scattering length  $a_{bg} = 60.865 a_0$  are known, which leaves  $B_0$  as the only fitting parameter in this model. It is important to note, that Eq. (8.6) describes the binding energy

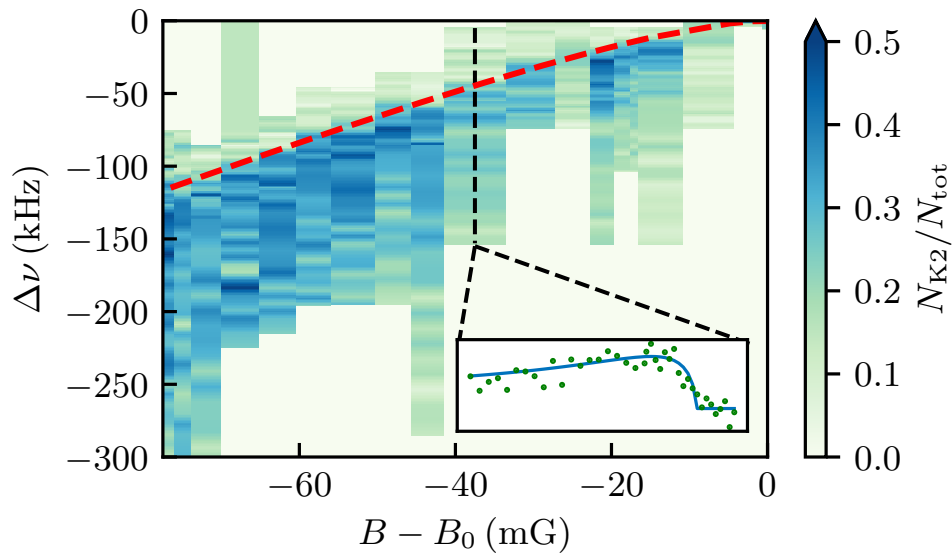


FIGURE 8.10: Molecule dissociation measurement. The transferred fraction to  $K|2\rangle$  (color scale) is shown in dependence of magnetic field and radio-frequency detuning for various magnetic fields around the center of the Feshbach resonance. The inset shows an example spectrum, taken at  $B - B_0 \approx -37$  mG. After determining the binding energy of the molecules as a function of the interaction strength we fit the resulting data by Eq. (8.6), shown by the red dashed line, with  $B_0$  as the only fitting parameter.

of molecules in vacuum. Interactions with the remaining Fermi sea are not included and can lead to a systematic shift on the order of 5 mG.

In contrast to our previous method (see Appendix of [Lou18b]),  $B_0$  is determined by molecule dissociation *in vacuum* via ejection spectroscopy. The measurement consists of the creation of molecules in the THC regime at  $X \approx -0.8$  by applying an RF pulse to the  $K|2\rangle$  atoms at a frequency that corresponds to the binding energy  $\nu_{RF} \approx E_b/h$ , which we optimize roughly on maximum molecule association efficiency. Then, we ramp the magnetic field to lower  $X$  values and therefore increase the binding energy. This procedure prevents the molecules from dissociating as we apply an RF pulse to transfer the remaining unbound  $Li|1\rangle$  atoms into  $Li|2\rangle$ . To be sure that no particles, except the molecules, are present we apply a  $10 \mu s$  resonant cleaning pulse to  $Li|2\rangle$  and another one to  $K|2\rangle$ . Then we ramp back the magnetic field to reach the final interaction strength  $X$  for which we want to determine the binding energy. At this field we apply another RF pulse to transfer the  $K1$  atoms into  $K2$  and consequently dissociate the molecules. As we vary the frequency of this last pulse, we obtain the dissociation spectrum with a line shape determined by the frequency-dependence of the Franck-Condon factor, as described in Ref. [Chi05]. The inset of Fig. 8.10 shows a sample spectrum at a magnetic detuning  $B - B_0 \approx -37$  mG and the corresponding fit to extract the binding energy. We record dissociation spectra in a range of about 80 mG where we expect molecules to exist. These measurements are presented in Fig. 8.10. A fit to the binding energies following Eq. (8.6) is illustrated by the red dashed line. The resulting value for the center of the Feshbach resonance is  $B_0 = 335.080(1)$  mG. Note that this value refers to our particular trap setting and includes a light shift of about 25 mG. All experiments

reported here were carried out for the same trap setting, so that we have the same  $B_0$  for all our measurements.

## 8.9 Appendix: Quasiparticle properties of Fermi polarons

In this Appendix, we present the calculations from which we infer the quasiparticle properties of isolated Fermi polarons and the strength of their mutual interactions.

### 8.9.1 Properties of isolated polarons

A single impurity with momentum  $\mathbf{p}$  immersed in a homogeneous Fermi sea may be described as a quasiparticle, whose dressing is composed of a superposition of particle-hole excitations in the Fermi sea. Such a state can be accurately modeled by the variational Ansatz [Che06]

$$|\psi\rangle = \phi c_{\mathbf{p}\downarrow}^\dagger |\text{FS}\rangle + \sum_{\substack{k > k_F \\ q < k_F}} \phi_{\mathbf{k}\mathbf{q}} c_{\mathbf{p}+\mathbf{q}-\mathbf{k}\downarrow}^\dagger c_{\mathbf{k}\uparrow}^\dagger c_{\mathbf{q}\uparrow} |\text{FS}\rangle \quad (8.7)$$

Here  $c_{\mathbf{p}\sigma}^\dagger$  creates an impurity ( $\sigma = \downarrow$ ) or a majority atom ( $\sigma = \uparrow$ ) with momentum  $\mathbf{p}$ , and  $|\text{FS}\rangle$  denotes the unperturbed Fermi sea. We warn the reader that, to avoid clutter, the notation adopted here slightly differs from the one used in the manuscript.

The minimization of the energy based on this variational Ansatz yields an identical result to the diagrammatic calculation within the ‘‘ladder’’ (or ‘‘forward-scattering’’) approximation [Com07], but the latter (once properly analytically continued [Mas11]) allows also to investigate the properties of the repulsive branch, and eventually the effects of non-zero temperature, in a straightforward way. The retarded self-energy of a single impurity of mass  $m_\downarrow$ , with momentum  $\mathbf{p}$  and energy  $\omega$  in a Fermi sea of particles with mass  $m_\uparrow$  reads ( $\hbar = k_B = 1$ )

$$\Sigma(\mathbf{p}, \omega) = \sum_{\mathbf{q}} f(\xi_{\mathbf{q}\uparrow}) T(\mathbf{p} + \mathbf{q}, \omega + \xi_{\mathbf{q}\uparrow}) \quad (8.8)$$

$$= \sum_{\mathbf{q}} \frac{f(\xi_{\mathbf{q}\uparrow})}{\frac{m_r}{2\pi\tilde{a}} - \sum_{\mathbf{k}} \left[ \frac{1-f(\xi_{\mathbf{k}\uparrow})}{\omega - (\epsilon_{\mathbf{p}+\mathbf{q}-\mathbf{k}\downarrow} + \epsilon_{\mathbf{k}\uparrow} - \epsilon_{\mathbf{q}\uparrow}) + i0_+} + \frac{2m_r}{k^2} \right]}, \quad (8.9)$$

where  $f(x) = 1/[\exp(\beta x) + 1]$  is the Fermi function at inverse temperature  $\beta$ , and  $T(\mathbf{P}, \Omega)$  is the  $T$ -matrix describing the scattering of an  $\uparrow\downarrow$  pair of atoms with total momentum  $\mathbf{P}$  and total energy  $\Omega$ . Here we introduced the kinetic energy of a  $\sigma$  atom measured with respect to the chemical potential  $\xi_{\mathbf{k}\sigma} = \epsilon_{\mathbf{k}\sigma} - \mu_\sigma = k^2/2m_\sigma - \mu_\sigma$ , the reduced mass  $m_r = m_\uparrow m_\downarrow / (m_\uparrow + m_\downarrow)$ , and the energy-dependent quantity

$$\frac{1}{\tilde{a}(\omega, K)} = \frac{1}{a} + R^* k_r^2, \quad (8.10)$$

where  $k_r = \sqrt{2m_r[\omega - K^2/(2M) + E_F]}$  (with  $K = |\mathbf{p} + \mathbf{q}|$  and  $M = m_\uparrow + m_\downarrow$ ) is the relative momentum of the colliding pair, and  $E_F$  is the Fermi energy of the homogeneous

Fermi sea. Since we consider the properties of a single  $\downarrow$  particle, we have set its chemical potential to zero.

The Green's function of the impurity reads

$$G_{\downarrow}(\mathbf{p}, \omega) = \frac{1}{\omega - \epsilon_{\mathbf{p}\downarrow} - \Sigma(\mathbf{p}, \omega) + i0_+}. \quad (8.11)$$

Its spectral function  $A = -2\text{Im}[G_{\downarrow}]$  features two branches of excitations, one at negative and one at positive energies. In the vicinity of these sharp excitations, the Green's function at small momenta may be approximated as

$$G_{\downarrow}(\mathbf{p}, \omega) \approx \frac{Z_{\pm}}{\omega - E_{\pm} - \frac{p^2}{2m_{\pm}^*} - iZ_{\pm}\text{Im}[\Sigma(\mathbf{p}, E_{\pm})]}. \quad (8.12)$$

The energy of an attractive ( $-$ ) polaron at zero momentum is the purely real solution at negative energies of

$$E_- = \Sigma(0, E_-), \quad (8.13)$$

while the energy of the repulsive  $\mathbf{p} = 0$  polaron is the positive energy solution of

$$E_+ = \text{Re}[\Sigma(0, E_+)]. \quad (8.14)$$

The quasiparticle residues  $Z$  are defined as

$$Z_{\pm} = \frac{1}{1 - \text{Re}[\partial_{\omega}\Sigma(0, \omega = E_{\pm})]}, \quad (8.15)$$

and the effective masses are given by

$$m_{\pm}^* = \frac{m_{\downarrow}/Z_{\pm}}{1 + \text{Re}[\partial_{\epsilon_{\downarrow\mathbf{p}}}\Sigma(0, E_{\pm})]}. \quad (8.16)$$

The energy, residue, and effective mass obtained in this way compare very favorably with both MC simulations and experiments [Pro08, Sch09, Nas09, Koh12, Kos12, Sca17]. The energies of dressed molecules are instead computed from a related Ansatz, describing a bare molecule dressed by particle-hole excitations in the medium [Mor09, Pun09, Com09, Mas12, Tre12, Qi12].

### 8.9.1.1 Polaron decay

The repulsive polaron is unstable towards decay into lower-lying excitations, but it remains a well-defined quasi-particle as long as its decay rate  $\Gamma$  is small [Bru10, Mas11, Koh12, Sca17]. The population decay rate for the 2-body process leading a polaron to decay onto free particles (pf) is given by

$$\Gamma_{\text{pf}} = -2Z_+\text{Im}[\tilde{\Sigma}(0, E_{\downarrow+})], \quad (8.17)$$

where  $\tilde{\Sigma}$  is defined in Eq. (S.16) of Ref. [Sca17]. The competing process leading a polaron to decay onto a dressed molecule is instead given by [Koh12]

$$\Gamma_{\text{pm}} = \frac{64k_F a}{45\pi^3} (Z_+^3 Z_M) \left(\frac{m_\uparrow}{m_+^*}\right)^2 \left(1 + \frac{m_\uparrow}{m_\uparrow + m_\downarrow}\right)^{3/2} \times \left(\frac{E_F}{E_+ - E_M}\right)^{5/2} \frac{a}{a^* \sqrt{1 + 4R^*/a^*}} E_F, \quad (8.18)$$

where  $E_M$  is the energy of a dressed molecule (found by a variational Ansatz à la Chevy), and  $a^* = \sqrt{2m_r E_b}$  is the typical size of a vacuum dimer at a narrow resonance.

In the extreme BEC limit, where medium effects become negligible, and in presence of a broad resonance, the three-body recombination proceeds at a rate [Pet03]

$$\Gamma_3 = \left(\frac{\bar{\epsilon}_\uparrow}{\epsilon}\right) \alpha n_\uparrow^2. \quad (8.19)$$

Here,  $\bar{\epsilon}_\uparrow$  is the average kinetic energy of majority atoms,  $\epsilon$  is the binding energy of the  $\uparrow\downarrow$  dimer, and  $\alpha$  is a constant which for our mass ratio takes the value

$$\alpha_\uparrow = 2.57 \frac{\hbar^5}{m_\uparrow^3 \epsilon^2}. \quad (8.20)$$

We plot for comparison this formula in Fig. 8.7, using for the majority kinetic energy the  $T = 0$  value  $\bar{\epsilon}_\uparrow = 3E_F/5$ , and for the dimer binding energy its value at a narrow resonance, given by Eq. (8.6).

### 8.9.2 Polaron-polaron interactions

An intrinsic property of quasiparticles is that they interact. Within Fermi liquid theory [Mor10, Yu10, Yu12], the total energy density of a gas containing  $N_\downarrow \ll N_\uparrow$  impurities in a large sea of  $N_\uparrow$  ideal fermions may be written as

$$\mathcal{E}(n_\uparrow, n_\downarrow) = \frac{3}{5} E_F n_\uparrow + E_\downarrow n_\downarrow + \frac{1}{2} f n_\downarrow^2. \quad (8.21)$$

The first term in this expression represents the energy of the unperturbed Fermi sea, the second is the contribution of isolated polarons, and the third term is the polaron-polaron interaction. We have neglected the mean kinetic energy of the impurities, which is expected to be very small when impurities are bosonic.

The effective interaction  $f$  between Landau quasiparticles contains two contributions:  $f = g_1 + f_x$ . The first one is the direct (or mean-field) interaction,  $g_1 = 4\pi\hbar^2 a_{11}/m_\downarrow$ , where  $a_{11}$  is the scattering length between bare impurities. The second term instead describes an exchange contribution, mediated by particle-hole excitations in the Fermi sea. At  $T = 0$ , this induced interaction between bosonic impurities is given by [Yu12]

$$f_x = -\frac{(\Delta N)^2}{\mathcal{N}}. \quad (8.22)$$

Here  $\mathcal{N} = \frac{3n_\uparrow}{2E_F}$  is the density of states at the Fermi energy, and  $\Delta N$  is the number of particles in the dressing cloud of a polaron, given by [Mas11]

$$\Delta N \equiv \left. \frac{\partial n_\uparrow}{\partial n_\downarrow} \right|_{\mu_\uparrow} = - \left( \frac{\partial \mu_\downarrow}{\partial n_\uparrow} \right)_{n_\downarrow} / \left( \frac{\partial \mu_\uparrow}{\partial n_\uparrow} \right)_{n_\downarrow} \approx - \frac{\partial \mu_\downarrow}{\partial E_F}. \quad (8.23)$$

In the last step, we used that  $\mu_\uparrow \approx E_F$ .

We present here a compact derivation of Eq. (8.22), following the lines of the elegant presentation given in Ref. [Yu12]. Within Landau theory, a  $\uparrow$  atom and a  $\downarrow$  polaron interact with a coupling constant  $g_x$  given by

$$g_x = \frac{\partial^2 \mathcal{E}}{\partial n_\uparrow \partial n_\downarrow} = \frac{\partial \mu_\uparrow}{\partial n_\downarrow}. \quad (8.24)$$

To second order in  $g_x$ , the polaron-polaron interaction is then given by

$$\mathcal{E}^{(2)} = - \frac{g_x^2}{V^3} \sum_{\mathbf{p}_\uparrow, \mathbf{p}_\downarrow, \mathbf{q}} \frac{(1 - f_{\mathbf{p}_\uparrow + \mathbf{q}})(1 + f_{\mathbf{p}_\downarrow - \mathbf{q}}^{(b)}) f_{\mathbf{p}_\downarrow}^{(b)} f_{\mathbf{p}_\uparrow}}{\frac{(\mathbf{p}_\uparrow + \mathbf{q})^2}{2m_\uparrow} + \frac{(\mathbf{p}_\downarrow - \mathbf{q})^2}{2m_\downarrow^*} - \frac{p_\downarrow^2}{2m_\downarrow^*} - \frac{p_\uparrow^2}{2m_\uparrow}}, \quad (8.25)$$

where  $f^{(b)}$  indicates Bose functions since we are assuming a bosonic impurity. The exchange contribution to Landau's polaron-polaron interaction can be calculated from this as

$$f_x = \frac{\delta^2 \mathcal{E}^{(2)}}{\delta f_{\mathbf{p}_\downarrow}^{(b)} \delta f_{\mathbf{p}_\downarrow - \mathbf{q}}^{(b)}} \quad (8.26)$$

where both  $\mathbf{p}_\downarrow$  and  $\mathbf{q}$  are vanishingly small. This gives

$$f_x = - \frac{g_x^2}{V} \left( \sum_{\mathbf{p}_\uparrow} \frac{f_{\mathbf{p}_\uparrow} - f_{\mathbf{p}_\uparrow + \mathbf{q}}}{\frac{(\mathbf{p}_\uparrow + \mathbf{q})^2}{2m_\uparrow} - \frac{p_\uparrow^2}{2m_\uparrow}} \right)_{q \rightarrow 0} = g_x^2 \chi, \quad (8.27)$$

where  $\chi$  is the so-called Lindhard function. At zero temperature,  $\chi$  equals simply the density of states at the Fermi surface  $\mathcal{N} = \frac{\partial n_\uparrow}{\partial \mu_\uparrow} = \frac{3n_\uparrow}{2E_F}$ . Collecting the above results, at zero temperature we have

$$\begin{aligned} f_x &= -g_x^2 \mathcal{N} = - \left( \frac{\partial \mu_\uparrow}{\partial n_\downarrow} \right)^2 \frac{\partial n_\uparrow}{\partial \mu_\uparrow} = - \left[ - \frac{\left( \frac{\partial \mu_\uparrow}{\partial n_\downarrow} \right)}{\left( \frac{\partial \mu_\uparrow}{\partial n_\uparrow} \right)} \right]^2 \frac{\partial \mu_\uparrow}{\partial n_\uparrow} \\ &= - \frac{(\Delta N)^2}{\mathcal{N}}. \end{aligned} \quad (8.28)$$

In the last step we used  $\left( \frac{\partial x}{\partial y} \right)_z \left( \frac{\partial y}{\partial z} \right)_x \left( \frac{\partial z}{\partial x} \right)_y = -1$ .

When the impurities are fermionic, an almost identical calculation leads to  $f_x^{(f)} = -f_x$ . Physically, this comes from the Pauli repulsion between identical fermions or alternatively, because the effective interaction involves the exchange of the impurities, which leads to a sign change for fermions as compared to bosons [Mor10, Yu10, Yu12, Cam18a].

The Landau interaction  $f$  between bosonic impurities is finally given by

$$f = -\frac{(\Delta N)^2}{\mathcal{N}} + g_1. \quad (8.29)$$

Note that the Landau polaron-polaron induced interaction (which is the first term in the latter expression) is always attractive for bosonic impurities (and repulsive for fermionic ones), irrespective of whether the impurity-bath interaction is attractive or repulsive.

Introducing the impurity concentration  $\mathcal{C} = n_\downarrow/n_\uparrow$ , the increase of the energy of the gas when adding one impurity is found to be

$$\mu_\downarrow = \frac{\partial \mathcal{E}}{\partial n_\downarrow} = E_\downarrow - \frac{2}{3}(\Delta N)^2 \mathcal{C} E_F + g_1 n_\downarrow. \quad (8.30)$$

In RF injection, we are gradually increasing the number of impurities, and therefore the polaron-polaron interactions. Taking a simple average, one gets

$$\bar{\mu}_\downarrow = \frac{1}{N_\downarrow} \int_0^{N_\downarrow} \mu_\downarrow(N'_\downarrow) dN'_\downarrow = \Delta E, \quad (8.31)$$

where  $\Delta E$  is the energy shift per impurity

$$\Delta E = \frac{\mathcal{E} - \frac{3}{5}E_F n_\uparrow}{n_\downarrow} = E_\downarrow - \frac{1}{3}(\Delta N)^2 \mathcal{C} E_F + \frac{g_1 n_\downarrow}{2}. \quad (8.32)$$

# 9 Chapter 9

## Outlook

Many intriguing experiments have already been conducted in the FeLiKx laboratory and many are yet to come. The measurements presented in this thesis opened up a variety of new questions, which will eventually be tackled in the future. In this chapter I will present some future perspectives of FeLiKx and in the course of this I will also propose some technical extensions.

### Near future projects

Our most recent measurements on the Fermi-Bose mixture, presented in Ch. 8, revealed the behavior of the Fermi polaron as the impurity concentration approaches its limiting values  $\mathcal{C} \rightarrow 0$  (Fermi polaron) and  $\mathcal{C} \rightarrow \infty$  (Bose polaron). The physical nature of the underlying process that marks the transition between these two regimes is largely unknown, due to the complexity of the system. Therefore the exploration of the intermediate regime around  $\mathcal{C} \approx 1$  could shed light onto the limits of Landau's quasiparticle theory. However, for the fact that the impurities are bosons the atoms will form a BEC as a certain critical density is reached. We assume the interaction mechanisms of a thermal cloud and a condensed cloud to be quite distinct and therefore we want to strictly separate those two regimes. In our case, the bosons begin to form a BEC at a concentration of  $\mathcal{C} \lesssim 1$ . For this reason we can choose two different strategies to probe the transition:

- THE BOTTOM-UP APPROACH: Within this method we generate a sample of atoms with low impurity concentration and increase it until the critical impurity density is reached. So far we could not access the desired regimes for technical reasons. The instability of the magnetic field rendered an exact analysis impossible. However, in very recent experiments after completion of the work for this thesis we resolved this issue and reached better resolution. A first dataset, taken under improved conditions, looks promising and shows evidence for a steep decrease (beyond theoretical predictions) in the energy of the repulsive polaron as the impurity density is increased.
- THE TOP-DOWN APPROACH: In this scenario we start with a pure BEC that is immersed into the Li Fermi sea and decrease the K density by applying incomplete RF transfer. Our measurements presented in Fig. 8.9 of Ch. 8 show that as the power of the RF pulse is changed, the resonance frequency, which represents the energy of K in the final state, changes. If the initial state would be represented by a pure BEC, rather than a partial BEC, we could apply an even shorter RF pulse

and probe the transition between the full BEC transfer and a polaronic transfer. Furthermore by varying the RF-pulse length we could, if three-body loss allows for it, even potentially probe the timescale of the break down of the polaron due to density-induced interactions.

These are possible near future projects. They are relatively easy to implement and the current status of the machine could allow for these experiments to be conducted, until technical changes (a change of the oven section) are unavoidable.

### Technical upgrades of FeLiKx

In order to match the ever bigger growing demands of a state-of-the art experiment the FeLiKx experiment should be upgraded in foreseeable time. Some technical changes are necessary for the controlled operation and some hold great potential for future measurements. Over the next years I suggest to implement:

- NEW OVEN SECTION: As mentioned earlier, we suspect that our oven is clogged, and at the moment we cannot locate the part of the oven from which we are loading our atoms. This is a degree of control that we want to gain back. Therefore, right now we are designing a new oven section without microtubes (see [Wil09]), which will hopefully be operational by the end of this year.
- MICROSCOPE: Our imaging system covers a wide range of possibilities, but during recent experiments we started to realize its limit. An insitu image of a BEC is only approximately two pixels wide and possible density modulations in the Fermi sea due to the bosons with a spatially small extension are hard/impossible to observe. Therefore, we (more precisely: Emil Kirilov) designed a new microscope that can be implemented into the experiment (theoretically) without any major reconstruction [Ött19].
- SPECIES-SELECTIVE POTENTIAL: A very advantageous tool that would open another chapter of this experiment would be a species-selective optical potential for our K atoms. Since Li represents the second species that shall not be perturbed by the optical potential we would implement a new laser that is close in wavelength to the K transition at 767 nm.

### Other future projects

The chapter of Fermi polarons is not quite closed since many questions are yet to be studied. The FeLiKx experiment presents an ideal platform to investigate these quasi-particles and further upgrades enable us to gain more insight into various questions:

- MOMENTUM DEPENDENCE OF THE FERMI POLARON: With the aid of a species-selective potential, we could selectively excite K without influencing Li. This tool enables us to vary the motional degree of freedom of the impurities and probe the sensitivity of the polaron on the impurities momentum, which is so far unknown.

- LIMITS OF QUASIPARTICLE THEORY: One major difference of using bosonic rather than fermionic K is that if compressed, the  $^{41}\text{K}$  atoms will condense and form a very dense degenerate sample of small spatial extent. Fermions, on the other hand, are limited by Fermi pressure. By switching to the fermionic isotope  $^{40}\text{K}$ , we could modify the impurity density without perturbing Li and achieve limits beyond of what we can achieve now. In addition to that we could investigate the influence of a degenerate sample of impurities (DFG) with respect to a thermal sample of impurities.
- INFINITE IMPURITY MASS: One nifty usage of a species-selective potential would be a species-selective optical lattice. By splitting the laser light that creates the optical potential, into two beams and superimposing them from opposite directions we could pin down the K atoms and design a lattice of impurities with infinite mass. This could lead to the first observation of the orthogonality catastrophe (OC) [And67]. Admittedly, our mass imbalance is already quite large and right now the limiting factor to not seeing the OC is probably our high temperature. However, in the case of a repaired oven section and a resulting increase in the final atomic number (by a significant amount), the elimination of the impurity recoil could be the final step towards investigating the orthogonality catastrophe.

There are of course many more projects that can be realized with the FeLiKx machine, however, there is only limited space to write them down. With this I want to finish this chapter and wish the future FeLiKx teams all the best.



# Bibliography

- [Abr75] A. A. Abrikosov. *Methods of Quantum Field Theory in Statistical Physics*. English. Rev English ed. edition. New York: Dover Publications (1975).
- [Ada21] D. Adam, Q. Bouton, J. Nettersheim, S. Burgardt, and A. Widera. “Coherent and Dephasing Spectroscopy for Single-Impurity Probing of an Ultracold Bath”, *arXiv:2105.03331* (2021). arXiv: [2105.03331](#).
- [Adl20] H. S. Adlong, W. E. Liu, F. Scazza, M. Zaccanti, N. D. Opping, S. Fölling, M. M. Parish, and J. Levinsen. “Quasiparticle Lifetime of the Repulsive Fermi Polaron”, *Physical Review Letters* **125**, 133401 (2020).
- [Aik14] K. Aikawa, S. Baier, A. Frisch, M. Mark, C. Ravensbergen, and F. Ferlaino. “Observation of Fermi Surface Deformation in a Dipolar Quantum Gas”, *Science* **345**, 1484–1487 (2014).
- [Alt07a] A. Altmeyer, S. Riedl, C. Kohstall, M. J. Wright, R. Geursen, M. Bartenstein, C. Chin, J. Hecker Denschlag, and R. Grimm. “Precision Measurements of Collective Oscillations in the BEC-BCS Crossover”, *Physical Review Letters* **98**, 040401, 040401 (2007).
- [Alt07b] A. Altmeyer, S. Riedl, M. J. Wright, C. Kohstall, J. Hecker Denschlag, and R. Grimm. “Dynamics of a Strongly Interacting Fermi Gas: The Radial Quadrupole Mode”, *Physical Review A* **76**, 033610, 033610 (2007).
- [Ami21] L. Amico, M. Boshier, G. Birkl, A. Minguzzi, C. Miniatura, L.-C. Kwek, D. Aghamalyan, V. Ahufinger, D. Anderson, N. Andrei, A. S. Arnold, M. Baker, T. A. Bell, T. Bland, J. P. Brantut, D. Cassettari, W. J. Chetcuti, F. Chevy, R. Citro, S. De Palo, R. Dumke, M. Edwards, R. Folman, J. Fortagh, S. A. Gardiner, B. M. Garraway, G. Gauthier, A. Günther, T. Haug, C. Hufnagel, M. Keil, W. von Klitzing, P. Ireland, M. Lebrat, W. Li, L. Longchambon, J. Mompart, O. Morsch, P. Naldesi, T. W. Neely, M. Olshanii, E. Orignac, S. Pandey, A. Pérez-Obiol, H. Perrin, L. Piroli, J. Polo, A. L. Pritchard, N. P. Proukakis, C. Rylands, H. Rubinsztein-Dunlop, F. Scazza, S. Stringari, F. Tosto, A. Trombettoni, N. Victorin, D. Wilkowski, K. Khani, and A. Yakimenko. “State of the Art and Perspective on Atomtronics”, *arXiv:2008.04439 [cond-mat, physics:quant-ph]* (2021). arXiv: [2008.04439 \[cond-mat, physics:quant-ph\]](#).
- [And95] M. H. Anderson, J. R. Ensher, M. R. Matthews, C. E. Wieman, and E. A. Cornell. “Observation of Bose-Einstein Condensation in Dilute Atomic Vapor”, *Science* **269**, 198–201 (1995).
- [And67] P. W. Anderson. “Infrared Catastrophe in Fermi Gases with Local Scattering Potentials”, *Physical Review Letters* **18**, 1049–1051 (1967).
- [Ata13] M. Atala, M. Aidelsburger, J. T. Barreiro, D. Abanin, T. Kitagawa, E. Demler, and I. Bloch. “Direct Measurement of the Zak Phase in Topological Bloch Bands”, *Nature Physics* **9**, 795–800 (2013).
- [Baa10] J. E. Baarsma, K. B. Gubbels, and H. T. C. Stoof. “Population and Mass Imbalance in Atomic Fermi Gases”, *Physical Review A* **82**, 013624 (2010).
- [Bar08a] M. A. Baranov. “Theoretical Progress in Many-Body Physics with Ultracold Dipolar Gases”, *Physics Reports* **464**, 71–111 (2008).
- [Bar08b] M. A. Baranov, C. Lobo, and G. V. Shlyapnikov. “Superfluid Pairing between Fermions with Unequal Masses”, *Physical Review A* **78**, 033620 (2008).
- [Bar14] A. B. Bardou, S. Beattie, C. Luciuk, W. Cairncross, D. Fine, N. S. Cheng, G. J. A. Edge, E. Taylor, S. Zhang, S. Trotzky, and J. H. Thywissen. “Transverse Demagnetization Dynamics of a Unitary Fermi Gas”, *Science* **344**, 722–724 (2014).

- [Bar04a] M. Bartenstein, A. Altmeyer, S. Riedl, S. Jochim, C. Chin, J. H. Denschlag, and R. Grimm. “Crossover from a Molecular Bose-Einstein Condensate to a Degenerate Fermi Gas”, *Physical Review Letters* **92**, 120401 (2004).
- [Bar04b] M. Bartenstein, A. Altmeyer, S. Riedl, S. Jochim, C. Chin, J. Hecker Denschlag, and R. Grimm. “Collective Excitations of a Degenerate Gas at the BEC-BCS Crossover”, *Physical Review Letters* **92**, 203201 (2004).
- [Bau11] F. Baumer, F. Münchow, A. Görlitz, S. E. Maxwell, P. S. Julienne, and E. Tiesinga. “Spatial Separation in a Thermal Mixture of Ultracold  $^{174}\text{Yb}$  and  $^{87}\text{Rb}$  Atoms”, *Physical Review A* **83**, 040702 (2011).
- [Bay91] G. Baym and C. Pethick. *Landau Fermi-Liquid Theory: Concepts and Applications*. Wiley-VCH (1991).
- [Ber13] G. Bertaina, E. Fratini, S. Giorgini, and P. Pieri. “Quantum Monte Carlo Study of a Resonant Bose-Fermi Mixture”, *Physical Review Letters* **110**, 115303 (2013).
- [Bie16] T. Bienaimé, E. Fava, G. Colzi, C. Mordini, S. Serafini, C. Qu, S. Stringari, G. Lamporesi, and G. Ferrari. “Spin-Dipole Oscillation and Polarizability of a Binary Bose-Einstein Condensate near the Miscible-Immiscible Phase Transition”, *Physical Review A* **94**, 063652 (2016).
- [Bij00] M. J. Bijlsma, B. A. Heringa, and H. T. C. Stoof. “Phonon Exchange in Dilute Fermi-Bose Mixtures: Tailoring the Fermi-Fermi Interaction”, *Physical Review A* **61**, 053601 (2000).
- [Bin84] K. Binder and D. P. Landau. “Finite-Size Scaling at First-Order Phase Transitions”, *Physical Review B* **30**, 1477–1485 (1984).
- [Blo08] I. Bloch, J. Dalibard, and W. Zwerger. “Many-Body Physics with Ultracold Gases”, *Reviews of Modern Physics* **80**, 885 (2008).
- [Blo13] I. Bloch. “Quantum Simulations Using Ultracold Atoms”. In: *2013 Conference on Lasers Electro-Optics Europe International Quantum Electronics Conference CLEO EUROPE/IQEC* (2013), 1–1.
- [Bom19] R. Bombín, T. Comparin, G. Bertaina, F. Mazzanti, S. Giorgini, and J. Boronat. “Two-Dimensional Repulsive Fermi Polarons with Short- and Long-Range Interactions”, en. *Physical Review A* **100**, 023608 (2019).
- [Bos24] S. N. Bose. “Plancksches Gesetz Und Lichtquantenhypothese”, *Zeitschrift für Physik* **26**, 178 (1924).
- [Böt19] F. Böttcher, J.-N. Schmidt, M. Wenzel, J. Hertkorn, M. Guo, T. Langen, and T. Pfau. “Transient Supersolid Properties in an Array of Dipolar Quantum Droplets”, *Physical Review X* **9**, 011051 (2019).
- [Bou03] T. Bourdel, J. Cubizolles, L. Khaykovich, K. M. F. Magalhães, S. J. J. M. F. Kokkelmans, G. V. Shlyapnikov, and C. Salomon. “Measurement of the Interaction Energy near a Feshbach Resonance in a  $^6\text{Li}$  Fermi Gas”, *Physical Review Letters* **91**, 020402 (2003).
- [Bou04] T. Bourdel, L. Khaykovich, J. Cubizolles, J. Zhang, F. Chevy, M. Teichmann, L. Tarruell, S. J. J. M. F. Kokkelmans, and C. Salomon. “Experimental Study of the BEC-BCS Crossover Region in Lithium 6”, *Physical Review Letters* **93**, 050401 (2004).
- [Bow73] R. M. Bowley. “Microscopic Theory of Impurities in Liquid Helium. III.”, *Progress in Particle and Nuclear Physics, Vol 63, No 1* **10**, 481–501 (1973).
- [Bra97] M. Brack and R. K. Bhaduri. *Semiclassical Physics*. Addison-Wesley Publishing Company, Inc. (1997).
- [Bré85] E. Brézin and J. Zinn-Justin. “Finite Size Effects in Phase Transitions”, *Nuclear Physics B* **257**, 867–893 (1985).
- [Bru10] G. M. Bruun and P. Massignan. “Decay of Polarons and Molecules in a Strongly Polarized Fermi Gas”, *Physical Review Letters* **105**, 020403 (2010).
- [Bru04] G. M. Bruun and C. J. Pethick. “Effective Theory of Feshbach Resonances and Many-Body Properties of Fermi Gases”, *Physical Review Letters* **92**, 140404 (2004).

- [Bug05] C. Buggle, P. Pedri, W. von Klitzing, and J. T. M. Walraven. “Shape Oscillations in Non-degenerate Bose Gases: Transition from the Collisionless to the Hydrodynamic Regime”, *Physical Review A* **72**, 043610 (2005).
- [Bur14] A. Burchianti, G. Valtolina, J. A. Seman, E. Pace, M. De Pas, M. Inguscio, M. Zaccanti, and G. Roati. “Efficient All-Optical Production of Large  $^6\text{Li}$  Quantum Gases Using  $D_1$  Gray-Molasses Cooling”, *Physical Review A* **90**, 043408 (2014).
- [Bur16] N. Q. Burdick, Y. Tang, and B. L. Lev. “Long-Lived Spin-Orbit-Coupled Degenerate Dipolar Fermi Gas”, *Physical Review X* **6**, 031022 (2016).
- [Bur97] E. A. Burt, R. W. Ghrist, C. J. Myatt, M. J. Holland, E. A. Cornell, and C. E. Wieman. “Coherence, Correlations, and Collisions: What One Learns about Bose-Einstein Condensates from Their Decay”, *Physical Review Letters* **79**, 337–340 (1997).
- [Bus97] T. Busch, J. I. Cirac, V. M. Pérez-García, and P. Zoller. “Stability and Collective Excitations of a Two-Component Bose-Einstein Condensed Gas: A Moment Approach”, *Physical Review A* **56**, 2978–2983 (1997).
- [Cam18a] A. Camacho-Guardian and G. M. Bruun. “Landau Effective Interaction between Quasiparticles in a Bose-Einstein Condensate”, *Physical Review X* **8**, 031042 (2018).
- [Cam18b] A. Camacho-Guardian, L. A. Peña Ardila, T. Pohl, and G. M. Bruun. “Bipolarons in a Bose-Einstein Condensate”, *Physical Review Letters* **121**, 013401 (2018).
- [Cap01] P. Capuzzi and E. S. Hernández. “Zero-Sound Density Oscillations in Fermi-Bose Mixtures”, *Physical Review A* **64**, 043607 (2001).
- [Car17] M. A. Caracanhas, F. Schreck, and C. M. Smith. “Fermi-Bose Mixture in Mixed Dimensions”, *New Journal of Physics* **19**, 115011 (2017).
- [Cat19] G. Catelani and D. Basko. “Non-Equilibrium Quasiparticles in Superconducting Circuits: Photons vs. Phonons”, en. *SciPost Physics* **6**, 013 (2019).
- [Cet16] M. Cetina, M. Jag, R. S. Lous, I. Fritsche, J. T. M. Walraven, R. Grimm, J. Levinsen, M. M. Parish, R. Schmidt, M. Knap, and E. Demler. “Ultrafast Many-Body Interferometry of Impurities Coupled to a Fermi Sea”, *Science* **354**, 96–99 (2016).
- [Cet15] M. Cetina, M. Jag, R. S. Lous, J. T. M. Walraven, R. Grimm, R. S. Christensen, and G. M. Bruun. “Decoherence of Impurities in a Fermi Sea of Ultracold Atoms”, *Physical Review Letters* **115**, 135302 (2015).
- [Che18] J.-G. Chen, Y.-R. Shi, X. Zhang, and W. Zhang. “Polarons in Alkaline-Earth-like Atoms with Multi Background Fermi Surfaces”, en. *arXiv:1801.09375 [cond-mat]* (2018). arXiv: [1801.09375 \[cond-mat\]](https://arxiv.org/abs/1801.09375).
- [Che06] F. Chevy. “Universal Phase Diagram of a Strongly Interacting Fermi Gas with Unbalanced Spin Populations”, *Physical Review A* **74**, 063628 (2006).
- [Che02] F. Chevy, V. Bretin, P. Rosenbusch, K. W. Madison, and J. Dalibard. “Transverse Breathing Mode of an Elongated Bose-Einstein Condensate”, *Physical Review Letters* **88**, 250402, 250402 (2002).
- [Che10] F. Chevy and C. Mora. “Ultra-Cold Polarized Fermi Gases”, *Reports on Progress in Physics* **73**, 112401 (2010).
- [Chi10] C. Chin, R. Grimm, P. S. Julienne, and E. Tiesinga. “Feshbach Resonances in Ultracold Gases”, *Reviews of Modern Physics* **82**, 1225–1286 (2010).
- [Chi05] C. Chin and P. S. Julienne. “Radio-Frequency Transitions on Weakly Bound Ultracold Molecules”, *Physical Review A* **71**, 012713 (2005).
- [Cho19] L. Chomaz, D. Petter, P. Ilzhöfer, G. Natale, A. Trautmann, C. Politi, G. Durastante, R. M. W. van Bijnen, A. Patscheider, M. Sohmen, M. J. Mark, and F. Ferlaino. “Long-Lived and Transient Supersolid Behaviors in Dipolar Quantum Gases”, *Physical Review X* **9**, 021012 (2019).
- [Chu97] S. Chu, C. Cohen-Tannoudji, and W. D. Phillips. *The Nobel Prize in Physics*. <https://www.nobelprize.org/prizes/physics/1997/summary/> (1997).

- [Com08] R. Combescot and S. Giraud. “Normal State of Highly Polarized Fermi Gases: Full Many-Body Treatment”, *Physical Review Letters* **101**, 050404 (2008).
- [Com09] R. Combescot, S. Giraud, and X. Leyronas. “Analytical Theory of the Dressed Bound State in Highly Polarized Fermi Gases”, *EPL (Europhysics Letters)* **88**, 60007 (2009).
- [Com07] R. Combescot, A. Recati, C. Lobo, and F. Chevy. “Normal State of Highly Polarized Fermi Gases: Simple Many-Body Approaches”, *Physical Review Letters* **98**, 180402 (2007).
- [Cor01] E. A. Cornell, W. Ketterle, and C. E. Wieman. *The Nobel Prize in Physics*. <https://www.nobelprize.org/prizes/physics/2001/summary/> (2001).
- [Cro09] A. D. Cronin, J. Schmiedmayer, and D. E. Pritchard. “Optics and Interferometry with Atoms and Molecules”, *Reviews of Modern Physics* **81**, 1051–1129 (2009).
- [Cui10] X. Cui and H. Zhai. “Stability of a Fully Magnetized Ferromagnetic State in Repulsively Interacting Ultracold Fermi Gases”, *Physical Review A* **81**, 041602 (2010).
- [Dal99] F. Dalfovo, S. Giorgini, L. P. Pitaevskii, and S. Stringari. “Theory of Bose-Einstein Condensation in Trapped Gases”, *Reviews of Modern Physics* **71**, 463–512 (1999).
- [Dal11] J. Dalibard, F. Gerbier, G. Juzeliunas, and P. Öhberg. “Artificial Gauge Potentials for Neutral Atoms”, *Reviews of Modern Physics* **83**, 1523–1543 (2011).
- [Dan08] J. G. Danzl, E. Haller, M. Gustavsson, M. J. Mark, R. Hart, N. Bouloufa, O. Dulieu, H. Ritsch, and H.-C. Nägerl. “Quantum Gas of Deeply Bound Ground State Molecules”, *Science* **321**, 1062–1066 (2008).
- [DO19] N. Darkwah Oppong, L. Riegger, O. Bettermann, M. Höfer, J. Levinsen, M. M. Parish, I. Bloch, and S. Fölling. “Observation of Coherent Multiorbital Polarons in a Two-Dimensional Fermi Gas”, *Physical Review Letters* **122**, 193604 (2019).
- [Das65] P. Das, R. B. de Ouboter, and K. W. Taconis. “A Realization of a London-Clarke-Mendoza Type Refrigerator”. In: *Low Temperature Physics LT9: Proceedings of the IXth International Conference on Low Temperature Physics Columbus, Ohio, August 31 – September 4, 1964*. Ed. by J. G. Daunt, D. O. Edwards, F. J. Milford, and M. Yaqub. Boston, MA: Springer US (1965), 1253–1255.
- [Dav96] H. Davis. *Statistical Mechanics of Phases, Interfaces and Thin Films*. Advances in Interfacial Engineering Series. Wiley (1996).
- [Dav95] K. B. Davis, M. O. Mewes, M. R. Andrews, N. J. van Druten, D. S. Durfee, D. M. Kurn, and W. Ketterle. “Bose-Einstein Condensation in a Gas of Sodium Atoms”, *Physical Review Letters* **75**, 3969–3973 (1995).
- [Dei08] J. Deiglmayr, A. Grochola, M. Repp, K. Mörtlbauer, C. Glück, J. Lange, O. Dulieu, R. Wester, and M. Weidemüller. “Formation of Ultracold Polar Molecules in the Rovibrational Ground State”, *Physical Review Letters* **101**, 133004 (2008).
- [Del15] M. DeLahaye, S. Laurent, I. Ferrier-Barbut, S. Jin, F. Chevy, and C. Salomon. “Critical Velocity and Dissipation of an Ultracold Bose-Fermi Counterflow”, *Physical Review Letters* **115**, 265303 (2015).
- [DeM99] B. DeMarco and D. S. Jin. “Onset of Fermi Degeneracy in a Trapped Atomic Gas”, *Science* **285**, 1703–1706 (1999).
- [Den18] T.-S. Deng, Z.-C. Lu, Y.-R. Shi, J.-G. Chen, W. Zhang, and W. Yi. “Repulsive Polarons in Alkaline-Earth-Metal-like Atoms across an Orbital Feshbach Resonance”, *Physical Review A* **97**, 013635 (2018).
- [D’E07] C. D’Errico, M. Zaccanti, M. Fattori, G. Roati, M. Inguscio, G. Modugno, and A. Simoni. “Feshbach Resonances in Ultracold  $^{39}\text{K}$ ”, *New Journal of Physics* **9**, 223 (2007).
- [DeS19] B. J. DeSalvo, K. Patel, G. Cai, and C. Chin. “Observation of Fermion-Mediated Interactions between Bosonic Atoms”, *Nature* **568**, 61–64 (2019).
- [Don01] E. A. Donley, N. R. Clausen, S. L. Cornish, J. L. Roberts, E. A. Cornell, and C. E. Wieman. “Dynamics of Collapsing and Exploding Bose-Einstein Condensates”, *Nature (London)* **412**, 295–299 (2001).

- [Dub13] J. Dubois, T. Jullien, F. Portier, P. Roche, A. Cavanna, Y. Jin, W. Wegscheider, P. Roulleau, and D. C. Glattli. “Minimal-Excitation States for Electron Quantum Optics Using Levitons”, *Nature* **502**, 659–663 (2013).
- [Dzs20] D. Dzsotjan, R. Schmidt, and M. Fleischhauer. “Dynamical Variational Approach to Bose Polarons at Finite Temperatures”, *Physical Review Letters* **124**, 223401 (2020).
- [Ebn71] C. Ebner and D. Edwards. “The Low Temperature Thermodynamic Properties of Superfluid Solutions of  $^3\text{He}$  in  $^4\text{He}$ ”, *Physics Reports* **2**, 77–154 (1971).
- [Edr20] H. Edri, B. Raz, N. Matzliah, N. Davidson, and R. Ozeri. “Observation of Spin-Spin Fermion-Mediated Interactions between Ultracold Bosons”, *Physical Review Letters* **124**, 163401 (2020).
- [Efi70] V. Efimov. “Energy Levels Arising from Resonant Two-Body Forces in a Three-Body System”, *Physics Letters B* **33**, 563–564 (1970).
- [Efr02] D. V. Efremov and L. Viverit. “ $p$ -Wave Cooper Pairing of Fermions in Mixtures of Dilute Fermi and Bose Gases”, *Physical Review B* **65**, 134519 (2002).
- [Ein24] A. Einstein. “Quantentheorie Des Einatomigen Idealen Gases I”, *Sitzungsberichte der Preussischen Akademie der Wissenschaften* **21**, 261 (1924).
- [Ens09] T. Enss and W. Zwerger. “Superfluidity near Phase Separation in Bose-Fermi Mixtures”, *The European Physical Journal B* **68**, 383–389 (2009).
- [Esr98] B. D. Esry and C. H. Greene. “Low-Lying Excitations of Double Bose-Einstein Condensates”, *Physical Review A* **57**, 1265–1271 (1998).
- [Esr01] B. D. Esry, C. H. Greene, and H. Suno. “Threshold Laws for Three-Body Recombination”, *Physical Review A* **65**, 010705 (2001).
- [Fer08] F. Ferlino, S. Knoop, and R. Grimm. “Ultracold Feshbach Molecules”, *arXiv:0809.3920 [cond-mat, physics:quant-ph]* (2008). arXiv: 0809.3920 [cond-mat, physics:quant-ph].
- [Fer14] I. Ferrier-Barbut, M. Delehaye, S. Laurent, A. T. Grier, M. Pierce, B. S. Rem, F. Chevy, and C. Salomon. “A Mixture of Bose and Fermi Superfluids”, *Science* **345**, 1035–1038 (2014).
- [Fie20] B. Field, J. Levinsen, and M. M. Parish. “Fate of the Bose Polaron at Finite Temperature”, *Physical Review A* **101**, 013623 (2020).
- [Fra10] E. Fratini and P. Pieri. “Pairing and Condensation in a Resonant Bose-Fermi Mixture”, *Physical Review A* **81**, 051605 (2010).
- [Fri15] I. Fritsche. “Sub-Doppler Cooling of Fermionic Lithium”. PhD thesis. University of Innsbruck, Austria (2015).
- [Frö54] H. Fröhlich. “Electrons in Lattice Fields”, *Advances in Physics* **3**, 325–361 (1954).
- [Gal19] V. Galitski, G. Juzeliūnas, and I. B. Spielman. “Artificial Gauge Fields with Ultracold Atoms”, *Physics Today* **72**, 38–44 (2019).
- [Gal13] V. Galitski and I. B. Spielman. “Spin-Orbit Coupling in Quantum Gases”, *Nature (London)* **494**, 49 (2013).
- [Gen01] S. D. Gensemer and D. S. Jin. “Transition from Collisionless to Hydrodynamic Behavior in an Ultracold Fermi Gas”, *Physical Review Letters* **87**, 173201 (2001).
- [Gia04] T. Giamarchi. “Theoretical Framework for Quasi-One Dimensional Systems”, *Chemical Reviews* **104**, 5037–5056 (2004).
- [Gio96] S. Giorgini, L. P. Pitaevskii, and S. Stringari. “Condensate Fraction and Critical Temperature of a Trapped Interacting Bose Gas”, *Physical Review A* **54**, R4633–R4636 (1996).
- [Gir09] S. Giraud and R. Combescot. “Highly Polarized Fermi Gases: One-Dimensional Case”, *Physical Review A* **79**, 043615 (2009).
- [Goo11] J. Goold, T. Fogarty, N. Lo Gullo, M. Paternostro, and T. Busch. “Orthogonality Catastrophe as a Consequence of Qubit Embedding in an Ultracold Fermi Gas”, *Physical Review A* **84**, 063632 (2011).

- [Gor04] K. Goral, T. Göhler, S. A. Gardiner, E. Tiesinga, and P. S. Julienne. “Adiabatic Association of Ultracold Molecules via Magnetic-Field Tunable Interactions”, *Journal of Physics B* **37**, 3457 (2004).
- [Gre17a] C. H. Greene, P. Giannakeas, and J. Pérez-Ríos. “Universal Few-Body Physics and Cluster Formation”, *Reviews of Modern Physics* **89**, 035006 (2017).
- [Gre17b] J. Greensite. *An Introduction to Quantum Theory*. en. 2053-2563. IOP Publishing (2017).
- [Gre05] M. Greiner, C. A. Regal, and D. S. Jin. “Probing the Excitation Spectrum of a Fermi Gas in the BCS-BEC Crossover Regime”, *Physical Review Letters* **94**, 070403 (2005).
- [Gri13] A. T. Grier, I. Ferrier-Barbut, B. S. Rem, M. Delehay, L. Khaykovich, F. Chevy, and C. Salomon. “ $\Lambda$ ”, *Physical Review A* **87**, 063411 (2013).
- [Gri00] R. Grimm, M. Weidemüller, and Y. B. Ovchinnikov. “Optical Dipole Traps for Neutral Atoms”, *Adv. At. Mol. Opt. Phys.* **42**, 95 (2000).
- [Gri12] M. Gring, M. Kuhnert, T. Langen, T. Kitagawa, B. Rauer, M. Schreitl, I. Mazets, D. A. Smith, E. Demler, and J. Schmiedmayer. “Relaxation and Prethermalization in an Isolated Quantum System”, *Science* **337**, 1318–1322 (2012).
- [Gru15] F. Grusdt and E. Demler. “New Theoretical Approaches to Bose Polarons”, *arXiv:1510.04934 [cond-mat]* (2015). arXiv: [1510.04934](https://arxiv.org/abs/1510.04934) [cond-mat].
- [Gue18] N.-E. Guenther, P. Massignan, M. Lewenstein, and G. M. Bruun. “Bose Polarons at Finite Temperature and Strong Coupling”, *Physical Review Letters* **120**, 050405 (2018).
- [Had06] Z. Hadzibabic, P. Krüger, M. Cheneau, B. Battelier, and J. Dalibard. “Berezinskii–Kosterlitz–Thouless Crossover in a Trapped Atomic Gas”, *Nature* **441**, 1118–1121 (2006).
- [Häf17] S. Häfner, J. Ulmanis, E. D. Kuhnle, Y. Wang, C. H. Greene, and M. Weidemüller. “Role of the Intraspecies Scattering Length in the Efimov Scenario with Large Mass Difference”, *Physical Review A* **95**, 062708 (2017).
- [Hah50] E. L. Hahn. “Spin Echoes”, *Physical Review* **80**, 580 (1950).
- [Hal11] E. Haller, M. Rabie, M. J. Mark, J. G. Danzl, R. Hart, K. Lauber, G. Pupillo, and H.-C. Nägerl. “Three-Body Correlation Functions and Recombination Rates for Bosons in Three Dimensions and One Dimension”, *Physical Review Letters* **107**, 230404 (2011).
- [Han01] D. J. Han, M. T. DePue, and D. S. Weiss. “Loading and Compressing Cs Atoms in a Very Far-off-Resonant Light Trap”, *Physical Review A* **63**, 023405 (2001).
- [Han13] J.-P. Hansen and I. R. McDonald. “Index”. In: *Theory of Simple Liquids (Fourth Edition)*. 4th Edition. Oxford: Academic Press (2013).
- [Har15] R. A. Hart, P. M. Duarte, T.-L. Yang, X. Liu, T. Paiva, E. Khatami, R. T. Scalettar, N. Trivedi, D. A. Huse, and R. G. Hulet. “Observation of Antiferromagnetic Correlations in the Hubbard Model with Ultracold Atoms”, *Nature (London)* **519**, 211–214 (2015).
- [Hau07] R. Haussmann, W. Rantner, S. Cerrito, and W. Zwerger. “Thermodynamics of the BCS-BEC Crossover”, *Physical Review A* **75**, 023610 (2007).
- [Hei00] H. Heiselberg, C. J. Pethick, H. Smith, and L. Viverit. “Influence of Induced Interactions on the Superfluid Transition in Dilute Fermi Gases”, *Physical Review Letters* **85**, 2418–2421 (2000).
- [Hir20] A. Hirohata, K. Yamada, Y. Nakatani, I.-L. Prejbeanu, B. Diény, P. Pirro, and B. Hillebrands. “Review on Spintronics: Principles and Device Applications”, en. *Journal of Magnetism and Magnetic Materials* **509**, 166711 (2020).
- [Ho98] T.-L. Ho. “Spinor Bose Condensates in Optical Traps”, *Physical Review Letters* **81**, 742–745 (1998).
- [Ho04] T.-L. Ho. “Universal Thermodynamics of Degenerate Quantum Gases in the Unitarity Limit”, *Physical Review Letters* **92**, 090402 (2004).
- [Hol00] M. J. Holland, B. DeMarco, and D. S. Jin. “Evaporative Cooling of a Two-Component Degenerate Fermi Gas”, *Physical Review A* **61**, 053610 (2000).

- [Hu18] H. Hu, B. C. Mulkerin, J. Wang, and X.-J. Liu. “Attractive Fermi Polarons at Nonzero Temperatures with a Finite Impurity Concentration”, *Physical Review A* **98**, 013626 (2018).
- [Hu16] M.-G. Hu, M. J. Van de Graaff, D. Kedar, J. P. Corson, E. A. Cornell, and D. S. Jin. “Bose Polarons in the Strongly Interacting Regime”, *Physical Review Letters* **117**, 055301 (2016).
- [Hua19] B. Huang, I. Fritsche, R. S. Lous, C. Baroni, J. T. M. Walraven, E. Kirilov, and R. Grimm. “Breathing Mode of a Bose-Einstein Condensate Repulsively Interacting with a Fermionic Reservoir”, *Physical Review A* **99**, 041602(R) (2019).
- [Hua20] B. Huang. “Bose-Einstein Condensate Immersed in a Fermi Sea: Theory of Static and Dynamic Behavior across Phase Separation”, *Physical Review A* **101**, 063618 (2020).
- [Hun08] C.-L. Hung, X. Zhang, N. Gemelke, and C. Chin. “Accelerating Evaporative Cooling of Atoms into Bose-Einstein Condensation in Optical Traps”, *Physical Review A* **78**, 011604(R) (2008).
- [Ima06] A. Imambekov, C. J. Bolech, M. Lukin, and E. Demler. “Breakdown of the Local Density Approximation in Interacting Systems of Cold Fermions in Strongly Anisotropic Traps”, *Physical Review A* **74**, 053626 (2006).
- [Isk06] M. Iskin and C. A. R. S. de Melo. “Two-Species Fermion Mixtures with Population Imbalance”, *Physical Review Letters* **97**, 100404, 100404 (2006).
- [Jag16] M. Jag, M. Cetina, R. S. Lous, R. Grimm, J. Levinsen, and D. S. Petrov. “Lifetime of Feshbach Dimers in a Fermi-Fermi Mixture of  $^6\text{Li}$  and  $^{40}\text{K}$ ”, *Physical Review A* **94**, 062706 (2016).
- [Jag14] M. Jag, M. Zaccanti, M. Cetina, R. S. Lous, F. Schreck, R. Grimm, D. S. Petrov, and J. Levinsen. “Observation of a Strong Atom-Dimer Attraction in a Mass-Imbalanced Fermi-Fermi Mixture”, *Physical Review Letters* **112**, 075302 (2014).
- [Jal01] R. A. Jalabert and H. M. Pastawski. “The Semiclassical Tool in Complex Physical Systems: Mesoscopics and Decoherence”, *Advances in Solid State Physics, Vol 48* **41**, 483–496 (2001).
- [Jin96] D. S. Jin, J. R. Ensher, M. R. Matthews, C. E. Wieman, and E. A. Cornell. “Collective Excitations of a Bose-Einstein Condensate in a Dilute Gas”, *Physical Review Letters* **77**, 420–423 (1996).
- [Jo09] G.-B. Jo, Y.-R. Lee, J.-H. Choi, C. A. Christensen, T. H. Kim, J. H. Thywissen, D. E. Pritchard, and W. Ketterle. “Itinerant Ferromagnetism in a Fermi Gas of Ultracold Atoms”, en. *Science* **325**, 1521–1524 (2009).
- [Joc03] S. Jochim, M. Bartenstein, A. Altmeyer, G. Hendl, S. Riedl, C. Chin, J. Hecker Denschlag, and R. Grimm. “Bose-Einstein Condensation of Molecules”, *Science* **302**, 2101–2103 (2003).
- [Joh17] J. Johansen, B. J. DeSalvo, K. Patel, and C. Chin. “Testing Universality of Efimov Physics across Broad and Narrow Feshbach Resonances”, *Nature Physics* **13**, 731–735 (2017).
- [Jør16] N. B. Jørgensen, L. Wacker, K. T. Skalmstang, M. M. Parish, J. Levinsen, R. S. Christensen, G. M. Bruun, and J. J. Arlt. “Observation of Attractive and Repulsive Polarons in a Bose-Einstein Condensate”, *Physical Review Letters* **117**, 055302 (2016).
- [Kad16] H. Kadau, M. Schmitt, M. Wenzel, C. Wink, T. Maier, I. Ferrier-Barbut, and T. Pfau. “Observing the Rosensweig Instability of a Quantum Ferrofluid”, *Nature (London)* **530**, 194–197 (2016).
- [Kag85] Y. Kagan, B. V. Svistunov, and G. V. Shlyapnikov. “Effect of Bose Condensation on Inelastic Processes in Gases”, *JETP Letters* **42** (1985).
- [Kai14] B. Kain and H. Y. Ling. “Polarons in a Dipolar Condensate”, *Physical Review A* **89**, 023612 (2014).
- [Kas92] M. Kasevich and S. Chu. “Laser Cooling below a Photon Recoil with Three-Level Atoms”, *Physical Review Letters* **69**, 1741–1744 (1992).
- [Kau21] H. Kaur, H. Kaur, and A. Sharma. “A Review of Recent Advancement in Superconductors”, en. *Materials Today: Proceedings. International Conference on Newer Trends and Innovation in Mechanical Engineering: Materials Science* **37**, 3612–3614 (2021).

- [Ket99] W. Ketterle, D. S. Durfee, and D. M. Stamper-Kurn. “Making, Probing and Understanding Bose-Einstein Condensates”, *arXiv:cond-mat/9904034* (1999). eprint: [cond-mat/9904034](#).
- [Ket08] W. Ketterle and M. W. Zwierlein. “Making, Probing and Understanding Ultracold Fermi Gases”, *La Rivista del Nuovo Cimento* **31**, 247–422 (2008). eprint: [0801.2500](#).
- [Kin04] J. Kinast, S. L. Hemmer, M. E. Gehm, A. Turlapov, and J. E. Thomas. “Evidence for Superfluidity in a Resonantly Interacting Fermi Gas”, *Physical Review Letters* **92**, 150402 (2004).
- [Kin15] J. J. Kinnunen and G. M. Bruun. “Induced Interactions in a Superfluid Bose-Fermi Mixture”, *Physical Review A* **91**, 041605 (2015).
- [Kin18a] J. J. Kinnunen, J. E. Baarsma, J.-P. Martikainen, and P. Törmä. “The Fulde–Ferrell–Larkin–Ovchinnikov State for Ultracold Fermions in Lattice and Harmonic Potentials: A Review”, *Reports on Progress in Physics* **81**, 046401 (2018).
- [Kin18b] J. J. Kinnunen, Z. Wu, and G. M. Bruun. “Induced  $s$ -Wave Pairing in Bose-Fermi Mixtures”, *Physical Review Letters* **121**, 253402 (2018).
- [Kir57] D. Kirzhnits. “Quantum Corrections to the Thomas–Fermi Equation”, *Soviet Physics–JETP [translation of Zhurnal Eksperimentalnoi i Teoreticheskoi Fiziki]* **5**, 64 (1957).
- [Kli03] I. Klich. *Quantum Noise in Mesoscopic Physics*. Springer Netherlands (2003), 397–402.
- [Kna12] M. Knap, A. Shashi, Y. Nishida, A. Imambekov, D. A. Abanin, and E. Demler. “Time-Dependent Impurity in Ultracold Fermions: Orthogonality Catastrophe and Beyond”, *Physical Review X* **2**, 041020 (2012).
- [Köh06] T. Köhler, K. Goral, and P. S. Julienne. “Production of Cold Molecules via Magnetically Tunable Feshbach Resonances”, *Reviews of Modern Physics* **78**, 1311 (2006).
- [Koh12] C. Kohstall, M. Zaccanti, M. Jag, A. Trenkwalder, P. Massignan, G. M. Bruun, F. Schreck, and R. Grimm. “Metastability and Coherence of Repulsive Polarons in a Strongly Interacting Fermi Mixture”, *Nature (London)* **485**, 615–618 (2012).
- [Kon16] H. Konishi, F. Schäfer, S. Ueda, and Y. Takahashi. “Collisional Stability of Localized  $\text{Yb}^3\text{P}_2$  Atoms Immersed in a Fermi Sea of  $\text{Li}$ ”, *New Journal of Physics* **18**, 103009 (2016).
- [Kor50] J. Korringa. “Nuclear Magnetic Relaxation and Resonance Line Shift in Metals”, *Physica* **16**, 601–610 (1950).
- [Kos12] M. Koschorreck, D. Pertot, E. Vogt, B. Fröhlich, M. Feld, and M. Köhl. “Attractive and Repulsive Fermi Polarons in Two Dimensions”, en. *Nature* **485**, 619–622 (2012).
- [Kos13] M. Koschorreck, D. Pertot, E. Vogt, and M. Köhl. “Universal Spin Dynamics in Two-Dimensional Fermi Gases”, *Nature Physics* **9**, 405–409 (2013).
- [Kra06] T. Kraemer, M. Mark, P. Waldburger, J. G. Danzl, C. Chin, B. Engeser, A. D. Lange, K. Pilch, A. Jaakkola, H.-C. Nägerl, and R. Grimm. “Evidence for Efimov Quantum States in an Ultracold Gas of Caesium Atoms”, *Nature (London)* **440**, 315–318 (2006).
- [Kra09] F. Krausz and M. Ivanov. “Attosecond Physics”, *Reviews of Modern Physics* **81**, 163–234 (2009).
- [Ku12] M. J. H. Ku, A. T. Sommer, L. W. Cheuk, and M. W. Zwierlein. “Revealing the Superfluid Lambda Transition in the Universal Thermodynamics of a Unitary Fermi Gas”, *Science* **335**, 563–567 (2012).
- [Lah09] T. Lahaye, C. Menotti, L. Santos, M. Lewenstein, and T. Pfau. “The Physics of Dipolar Bosonic Quantum Gases”, *Reports on Progress in Physics* **72**, 126401 (2009).
- [Lan14] Z. Lan and C. Lobo. “A Single Impurity in an Ideal Atomic Fermi Gas: Current Understanding and Some Open Problems”, en. *Journal of the Indian Institute of Science* **94**, 179–188 (2014).
- [Lan33] L. D. Landau. “Über Die Bewegung Der Elektronen in Kristallgitter”, *Physikalische Zeitschrift der Sowjetunion* **3**, 644 (1933).

- [Lan48] L. D. Landau and S. I. Pekar. “Effective Mass of a Polaron”, *Zh. Eksp. Teor. Fiz.* **18**, 419–423 (1948).
- [Lan08] F. Lang, K. Winkler, C. Strauss, R. Grimm, and J. Hecker Denschlag. “Ultracold Triplet Molecules in the Rovibrational Ground State”, *Physical Review Letters* **101**, 133005, 133005 (2008).
- [Lau98] R. B. Laughlin, H. L. Störmer, and D. C. Tsui. *The Nobel Prize in Physics 1998*. en-US. <https://www.nobelprize.org/prizes/physics/1998/summary/> (1998).
- [LeB07] L. J. LeBlanc and J. H. Thywissen. “Species-Specific Optical Lattices”, *Physical Review A* **75**, 053612 (2007).
- [Lee16] K. L. Lee, N. B. Jørgensen, I.-K. Liu, L. Wacker, J. J. Arlt, and N. P. Proukakis. “Phase Separation and Dynamics of Two-Component Bose-Einstein Condensates”, *Physical Review A* **94**, 013602 (2016).
- [Les10] M. J. Leskinen, O. H. T. Nummi, F. Massel, and P. Törmä. “Fermi-Polaron-like Effects in a One-Dimensional (1D) Optical Lattice”, en. *New Journal of Physics* **12**, 073044 (2010).
- [Lev11] J. Levinsen and D. Petrov. “Atom-Dimer and Dimer-Dimer Scattering in Fermionic Mixtures near a Narrow Feshbach Resonance”, *The European Physical Journal D* **65**, 67–82 (2011).
- [Lev15a] J. Levinsen and M. M. Parish. “Strongly Interacting Two-Dimensional Fermi Gases”. In: *Annual Review of Cold Atoms and Molecules*. Vol. 3. Singapore: World Scientific (2015), 1–75.
- [Lev15b] J. Levinsen, M. M. Parish, and G. M. Bruun. “Impurity in a Bose-Einstein Condensate and the Efimov Effect”, *Physical Review Letters* **115**, 125302 (2015).
- [Lev17] J. Levinsen, M. M. Parish, R. S. Christensen, J. J. Arlt, and G. M. Bruun. “Finite-Temperature Behavior of the Bose Polaron”, *Physical Review A* **96**, 063622 (2017).
- [Lev93] L. Levitov and G. Lesovik. “Charge distribution in quantum shot noise”, *JETP Letters* **58**, 230 (1993).
- [Lev96] L. S. Levitov, H. Lee, and G. B. Lesovik. “Electron Counting Statistics and Coherent States of Electric Current”, *Journal of Mathematical Physics* **37**, 4845–4866 (1996).
- [Lin14] M. G. Lingham, K. Fenech, S. Hoinka, and C. J. Vale. “Local Observation of Pair Condensation in a Fermi Gas at Unitarity”, *Physical Review Letters* **112**, 100404 (2014).
- [Liu16] I.-K. Liu, R. W. Pattinson, T. P. Billam, S. A. Gardiner, S. L. Cornish, T.-M. Huang, W.-W. Lin, S.-C. Gou, N. G. Parker, and N. P. Proukakis. “Stochastic Growth Dynamics and Composite Defects in Quenched Immiscible Binary Condensates”, *Physical Review A* **93**, 023628 (2016).
- [Liu03a] W. V. Liu and F. Wilczek. “Interior Gap Superfluidity”, *Physical Review Letters* **90**, 047002 (2003).
- [Liu19] W. E. Liu, J. Levinsen, and M. M. Parish. “Variational Approach for Impurity Dynamics at Finite Temperature”, *Physical Review Letters* **122**, 205301 (2019).
- [Liu20] W. E. Liu, Z.-Y. Shi, M. M. Parish, and J. Levinsen. “Theory of Radio-Frequency Spectroscopy of Impurities in Quantum Gases”, *Physical Review A* **102**, 023304 (2020).
- [Liu03b] X.-J. Liu and H. Hu. “Collisionless and Hydrodynamic Excitations of Trapped Boson-Fermion Mixtures”, *Physical Review A* **67**, 023613 (2003).
- [Lob06] C. Lobo, A. Recati, S. Giorgini, and S. Stringari. “Normal State of a Polarized Fermi Gas at Unitarity”, *Physical Review Letters* **97**, 200403 (2006).
- [Löf01] T. Löfwander, V. S. Shumeiko, and G. Wendin. “Andreev Bound States in High-T<sub>c</sub> Superconducting Junctions”, *Superconductor Science and Technology* **14**, R53–R77 (2001).
- [Los76] J. Loschmidt. “Über Den Zustand Des Wärmegleichgewichts Eines Systems von Körpern Mit Rücksicht Auf Die Schwerkraft”, *Sitzungsber. Akad. Wissenschaften, Wien* **73**, 128–142 (1876).

- [Lou18a] R. S. Lous. “Tunable Bose-Fermi and Fermi-Fermi Mixtures of Potassium and Lithium: Phase Separation, Polarons, and Molecules”. PhD thesis. University of Innsbruck (2018).
- [Lou17] R. S. Lous, I. Fritsche, M. Jag, B. Huang, and R. Grimm. “Thermometry of a Deeply Degenerate Fermi Gas with a Bose-Einstein Condensate”, *Physical Review A* **95**, 053627 (2017).
- [Lou18b] R. S. Lous, I. Fritsche, M. Jag, F. Lehmann, E. Kirilov, B. Huang, and R. Grimm. “Probing the Interface of a Phase-Separated State in a Repulsive Bose-Fermi Mixture”, *Physical Review Letters* **120**, 243403 (2018).
- [Lud11] D. Ludwig, S. Floerchinger, S. Moroz, and C. Wetterich. “Quantum Phase Transition in Bose-Fermi Mixtures”, *Physical Review A* **84**, 033629 (2011).
- [Luo07] L. Luo, B. Clancy, J. Joseph, J. Kinast, and J. E. Thomas. “Measurement of the Entropy and Critical Temperature of a Strongly Interacting Fermi Gas”, *Physical Review Letters* **98**, 080402 (2007).
- [Lut63] J. M. Luttinger. “An Exactly Soluble Model of a Many-Fermion System”, *Journal of Mathematical Physics* **4**, 1154–1162 (1963).
- [Mad00] P. Maddaloni, M. Modugno, C. Fort, F. Minardi, and M. Inguscio. “Collective Oscillations of Two Colliding Bose-Einstein Condensates”, *Physical Review Letters* **85**, 2413–2417 (2000).
- [Mah90] G. D. Mahan. “Physics of Solids and Liquids”, *Plenum New York NY Many-particle physics* (1990).
- [Mar08] F. M. Marchetti, C. J. M. Mathy, D. A. Huse, and M. M. Parish. “Phase Separation and Collapse in Bose-Fermi Mixtures with a Feshbach Resonance”, *Physical Review B* **78**, 134517 (2008).
- [Mar19] L. D. Marco, G. Valtolina, K. Matsuda, W. G. Tobias, J. P. Covey, and J. Ye. “A Degenerate Fermi Gas of Polar Molecules”, en. *Science* **363**, 853–856 (2019).
- [Mar88] A. G. Martin, K. Helmerson, V. S. Bagnato, G. P. Lafyatis, and D. E. Pritchard. “Rf Spectroscopy of Trapped Neutral Atoms”, en. *Physical Review Letters* **61**, 2431–2434 (1988).
- [Mar13] T. Maruyama and H. Yabu. “Longitudinal and Transverse Breathing Oscillations in Bose-Fermi Mixtures of Yb Atoms at Zero Temperature in the Largely Prolate Deformed Traps”, *Journal of Physics B: Atomic, Molecular and Optical Physics* **46**, 055201 (2013).
- [Mas12] P. Massignan. “Polarons and Dressed Molecules near Narrow Feshbach Resonances”, en. *EPL (Europhysics Letters)* **98**, 10012 (2012).
- [Mas11] P. Massignan and G. M. Bruun. “Repulsive Polarons and Itinerant Ferromagnetism in Strongly Polarized Fermi Gases”, *The European Physical Journal D* **65**, 83–89 (2011).
- [Mas14] P. Massignan, M. Zaccanti, and G. M. Bruun. “Polarons, Dressed Molecules and Itinerant Ferromagnetism in Ultracold Fermi Gases”, en. *Reports on Progress in Physics* **77**, 034401 (2014).
- [Mat11] C. J. M. Mathy, M. M. Parish, and D. A. Huse. “Trimers, Molecules, and Polarons in Mass-Imbalanced Atomic Fermi Gases”, *Physical Review Letters* **106**, 166404 (2011).
- [Mat98] M. R. Matthews, D. S. Hall, D. S. Jin, J. R. Ensher, C. E. Wieman, E. A. Cornell, F. Dalfovo, C. Minniti, and S. Stringari. “Dynamical Response of a Bose-Einstein Condensate to a Discontinuous Change in Internal State”, *Physical Review Letters* **81**, 243–247 (1998).
- [MW03] C. Z. Matthias Weidemüller. *Interactions in Ultracold Gases: From Atoms to Molecules* (2003).
- [Mat92] R. D. Mattuck. *A Guide to Feynman Diagrams in the Many-Body Problem*. en. Courier Corporation (1992).
- [McC11] D. J. McCarron, H. W. Cho, D. L. Jenkin, M. P. Köppinger, and S. L. Cornish. “Dual-Species Bose-Einstein Condensate of  $^{87}\text{Rb}$  and  $^{133}\text{Cs}$ ”, *Physical Review A* **84**, 011603 (2011).
- [Mew96] M.-O. Mewes, M. R. Andrews, N. J. van Druten, D. M. Kurn, D. S. Durfee, C. G. Townsend, and W. Ketterle. “Collective Excitations of a Bose-Einstein Condensate in a Magnetic Trap”, *Physical Review Letters* **77**, 988–991 (1996).

- [Mis19] S. I. Mistakidis, G. C. Katsimiga, G. M. Koutentakis, T. Busch, and P. Schmelcher. “Quench Dynamics and Orthogonality Catastrophe of Bose Polarons”, *Physical Review Letters* **122**, 183001 (2019).
- [Mod02] G. Modugno, G. Roati, F. Riboli, F. Ferlaino, R. Brecha, and M. Inguscio. “Collapse of a Degenerate Fermi Gas”, *Science* **297**, 2240–2243 (2002).
- [Moe95] A. J. Moerdijk, B. J. Verhaar, and A. Axelsson. “Resonances in Ultracold Collisions of  $^6\text{Li}$ ,  $^7\text{Li}$ , and  $^{23}\text{Na}$ ”, *Physical Review A* **51**, 4852–4861 (1995).
- [Møl98] K. Mølmer. “Bose Condensates and Fermi Gases at Zero Temperature”, *Physical Review Letters* **80**, 1804–1807 (1998).
- [Mor11] C. Mora, Y. Castin, and L. Pricoupenko. “Integral Equations for the Four-Body Problem”, *Compt. Rend. Phys.* **12**, 1 (2011).
- [Mor09] C. Mora and F. Chevy. “Ground State of a Tightly Bound Composite Dimer Immersed in a Fermi Sea”, *Physical Review A* **80**, 033607 (2009).
- [Mor10] C. Mora and F. Chevy. “Normal Phase of an Imbalanced Fermi Gas”, *Physical Review Letters* **104**, 230402 (2010).
- [Mos01] A. Mosk, S. Kraft, M. Mudrich, K. Singer, W. Wohlleben, R. Grimm, and M. Weidemüller. “Mixture of Ultracold Lithium and Cesium Atoms in an Optical Dipole Trap”, *Applied Physics B* **73**, 791 (2001).
- [Mud02] M. Mudrich, S. Kraft, K. Singer, R. Grimm, A. Mosk, and M. Weidemüller. “Sympathetic Cooling with Two Atomic Species in an Optical Trap”, *Physical Review Letters* **88**, 253001 (2002).
- [Muk19] B. Mukherjee, P. B. Patel, Z. Yan, R. J. Fletcher, J. Struck, and M. W. Zwierlein. “Spectral Response and Contact of the Unitary Fermi Gas”, *Physical Review Letters* **122**, 203402 (2019).
- [Mul19] B. C. Mulkerin, X.-J. Liu, and H. Hu. “Breakdown of the Fermi Polaron Description near Fermi Degeneracy at Unitarity”, *Annals of Physics* **407**, 29–45 (2019).
- [Nai17] P. Naidon and S. Endo. “Efimov Physics: A Review”, *Reports on Progress in Physics* **80**, 056001 (2017).
- [Nai11] D. Naik, A. Trenkwalder, C. Kohstall, F. M. Spiegelhalter, M. Zaccanti, G. Hendl, F. Schreck, R. Grimm, T. Hanna, and P. Julienne. “Feshbach Resonances in the  $^6\text{Li}$ - $^{40}\text{K}$  Fermi-Fermi Mixture: Elastic versus Inelastic Interactions”, *The European Physical Journal D* **65**, 55–65 (2011).
- [Nas10] S. Nascimbène, N. Navon, K. J. Jiang, F. Chevy, and C. Salomon. “Exploring the Thermodynamics of a Universal Fermi Gas”, *Nature (London)* **463**, 1057–1061 (2010).
- [Nas09] S. Nascimbène, N. Navon, K. J. Jiang, L. Tarruell, M. Teichmann, J. McKeever, F. Chevy, and C. Salomon. “Collective Oscillations of an Imbalanced Fermi Gas: Axial Compression Modes and Polaron Effective Mass”, *Physical Review Letters* **103**, 170402 (2009).
- [Nav10] N. Navon, S. Nascimbène, F. Chevy, and C. Salomon. “The Equation of State of a Low-Temperature Fermi Gas with Tunable Interactions”, *Science* **328**, 729–732 (2010).
- [Nes20] G. Ness, C. Shkedrov, Y. Florshaim, O. K. Diessel, J. von Milczewski, R. Schmidt, and Y. Sagi. “Observation of a Smooth Polaron-Molecule Transition in a Degenerate Fermi Gas”, *Physical Review X* **10**, 041019 (2020).
- [Ni08] K.-K. Ni, S. Ospelkaus, M. H. G. de Miranda, A. Pe’er, B. Neyenhuis, J. J. Zirbel, S. Kotochigova, P. S. Julienne, D. S. Jin, and J. Ye. “A High Phase-Space-Density Gas of Polar Molecules”, *Science* **322**, 231–235 (2008).
- [Nis21] K. Nishimura, E. Nakano, K. Iida, H. Tajima, T. Miyakawa, and H. Yabu. “Ground State of the Polaron in an Ultracold Dipolar Fermi Gas”, en. *Physical Review A* **103**, 033324 (2021).
- [NIS18] NIST/SEMATECH. *E-Handbook of Statistical Methods* (2018).
- [Nor11] M. R. Norman. “The Challenge of Unconventional Superconductivity”, *Science* **332**, 196–200 (2011).

- [Noz69] P. Nozières and C. T. de Dominicis. “Singularities in the X-Ray Absorption and Emission of Metals. III. One-Body Theory Exact Solution”, *Physical Review* **178**, 1097–1107 (1969).
- [O’H02] K. M. O’Hara, S. L. Hemmer, M. E. Gehm, S. R. Granade, and J. E. Thomas. “Observation of a Strongly Interacting Degenerate Fermi Gas”, *Science* **298**, 2179–2182 (2002).
- [Oht90] K. Ohtaka and Y. Tanabe. “Theory of the Soft-x-Ray Edge Problem in Simple Metals: Historical Survey and Recent Developments”, *Reviews of Modern Physics* **62**, 929–991 (1990).
- [Ono16] R. Onofrio. “Physics of Our Days: Cooling and Thermometry of Atomic Fermi Gases”, *Physics-Uspekhi* **59**, 1129 (2016).
- [Tan] “Optical Bloch Equations”. en. In: *Atom—Photon Interactions*. John Wiley & Sons, Ltd (1998). Chap. 5, 353–405.
- [Osp06a] C. Ospelkaus, S. Ospelkaus, K. Sengstock, and K. Bongs. “Interaction-Driven Dynamics of  $^{40}\text{K}$ - $^{87}\text{Rb}$  Fermion-Boson Gas Mixtures in the Large-Particle-Number Limit”, *Physical Review Letters* **96**, 020401, 020401 (2006).
- [Osp06b] S. Ospelkaus, C. Ospelkaus, L. Humbert, K. Sengstock, and K. Bongs. “Tuning of Heteronuclear Interactions in a Degenerate Fermi-Bose Mixture”, *Physical Review Letters* **97**, 120403 (2006).
- [Ött19] T. Öttl. “Designing and Testing an Objective for Imaging Ultracold Quantum Gases / Thomas Öttl”. en. PhD thesis. Universität Innsbruck (2019).
- [Pap08] S. B. Papp, J. M. Pino, and C. E. Wieman. “Tunable Miscibility in a Dual-Species Bose-Einstein Condensate”, *Physical Review Letters* **101**, 040402 (2008).
- [Par07] M. M. Parish, F. M. Marchetti, A. Lamacraft, and B. D. Simons. “Polarized Fermi Condensates with Unequal Masses: Tuning the Tricritical Point”, *Physical Review Letters* **98**, 160402 (2007).
- [Par11] M. M. Parish. “Polaron-Molecule Transitions in a Two-Dimensional Fermi Gas”, *Physical Review A* **83**, 051603 (2011).
- [Par13] M. M. Parish and J. Levinsen. “Highly Polarized Fermi Gases in Two Dimensions”, *Physical Review A* **87**, 033616 (2013).
- [Par16] M. M. Parish and J. Levinsen. “Quantum Dynamics of Impurities Coupled to a Fermi Sea”, *Physical Review B* **94**, 184303 (2016).
- [Par17] J. W. Park, Z. Z. Yan, H. Loh, S. A. Will, and M. W. Zwierlein. “Second-Scale Nuclear Spin Coherence Time of Ultracold  $^{23}\text{Na}$ / $^{40}\text{K}$  Molecules”, en. *Science* **357**, 372–375 (2017).
- [Pat14] H. J. Patel, C. L. Blackley, S. L. Cornish, and J. M. Hutson. “Feshbach Resonances, Molecular Bound States, and Prospects of Ultracold-Molecule Formation in Mixtures of Ultracold K and Cs”, *Physical Review A* **90**, 032716 (2014).
- [Paz15] R. Pazourek, S. Nagele, and J. Burgdörfer. “Attosecond Chronoscopy of Photoemission”, *Reviews of Modern Physics* **87**, 765–802 (2015).
- [PA19] L. A. Peña Ardila, N. B. Jørgensen, T. Pohl, S. Giorgini, G. M. Bruun, and J. J. Arlt. “Analyzing a Bose Polaron across Resonant Interactions”, *Physical Review A* **99**, 063607 (2019).
- [Pet02] C. J. Pethick and H. Smith. *Bose-Einstein Condensation in Dilute Gases*. Cambridge University Press (2002).
- [Pet03] D. S. Petrov. “Three-Body Problem in Fermi Gases with Short-Range Interparticle Interaction”, *Physical Review A* **67**, 010703, 010703(R) (2003).
- [Pet04] D. S. Petrov. “Three-Boson Problem near a Narrow Feshbach Resonance”, *Physical Review Letters* **93**, 143201 (2004).
- [Pir14] R. Pires, J. Ulmanis, S. Häfner, M. Repp, A. Arias, E. D. Kuhnle, and M. Weidemüller. “Observation of Efimov Resonances in a Mixture with Extreme Mass Imbalance”, *Physical Review Letters* **112**, 250404 (2014).
- [Pit03] L. Pitaevskii and S. Stringari. *Bose-Einstein Condensation*. Oxford University Press (2003).

- [Pit16] L. Pitaevskii and S. Stringari. *Bose-Einstein Condensation and Superfluidity*. Oxford University Press (2016).
- [Pob07] F. Pobell. “The 3He-4He Dilution Refrigerator”. In: *Matter and Methods at Low Temperatures*. Springer-Verlag, Berlin (2007), 149.
- [Pol10] S. E. Pollack, D. Dries, R. G. Hulet, K. M. F. Magalhães, E. A. L. Henn, E. R. F. Ramos, M. A. Caracanhas, and V. S. Bagnato. “Collective Excitation of a Bose-Einstein Condensate by Modulation of the Atomic Scattering Length”, *Physical Review A* **81**, 053627 (2010).
- [Pow05] S. Powell, S. Sachdev, and H. P. Büchler. “Depletion of the Bose-Einstein Condensate in Bose-Fermi Mixtures”, *Physical Review B* **72**, 024534 (2005).
- [Pro08] N. Prokof’ev and B. Svistunov. “Fermi-Polaron Problem: Diagrammatic Monte Carlo Method for Divergent Sign-Alternating Series”, *Physical Review B* **77**, 020408 (2008).
- [Pu02] H. Pu, W. Zhang, M. Wilkens, and P. Meystre. “Phonon Spectrum and Dynamical Stability of a Dilute Quantum Degenerate Bose-Fermi Mixture”, *Physical Review Letters* **88**, 070408 (2002).
- [Pun09] M. Punk, P. T. Dumitrescu, and W. Zwerger. “Polaron-to-Molecule Transition in a Strongly Imbalanced Fermi Gas”, *Physical Review A* **80**, 053605 (2009).
- [Qi12] R. Qi and H. Zhai. “Highly Polarized Fermi Gases across a Narrow Feshbach Resonance”, *Physical Review A* **85**, 041603(R) (2012).
- [Ran06] J. Ranninger and A. Romano. “Resonating Bipolarons”, en. *EPL (Europhysics Letters)* **75**, 461 (2006).
- [Rav18] C. Ravensbergen, V. Corre, E. Soave, M. Kreyer, E. Kirilov, and R. Grimm. “Production of a Degenerate Fermi-Fermi Mixture of Dysprosium and Potassium Atoms”, *Physical Review A* **98**, 063624 (2018).
- [Reg04] C. A. Regal, M. Greiner, and D. S. Jin. “Observation of Resonance Condensation of Fermionic Atom Pairs”, *Physical Review Letters* **92**, 040403 (2004).
- [Rev16] M. C. Revelle, J. A. Fry, B. A. Olsen, and R. G. Hulet. “1D to 3D Crossover of a Spin-Imbalanced Fermi Gas”, *Physical Review Letters* **117**, 235301 (2016).
- [Roa02] G. Roati, F. Riboli, G. Modugno, and M. Inguscio. “Fermi-Bose Quantum Degenerate k-Rb Mixture with Attractive Interaction”, *Physical Review Letters* **89**, 150403 (2002).
- [Rod04] M. Rodríguez, P. Pedri, P. Törmä, and L. Santos. “Scissors Modes of Two-Component Degenerate Gases: Bose-Bose and Bose-Fermi Mixtures”, *Physical Review A* **69**, 023617 (2004).
- [Ros99] A. Rosch. “Quantum-Coherent Transport of a Heavy Particle in a Fermionic Bath”, *Advances in Physics* **48**, 295–394 (1999).
- [Rot02] R. Roth. “Structure and Stability of Trapped Atomic Boson-Fermion Mixtures”, *Physical Review A* **66**, 013614 (2002).
- [Roy17] R. Roy, A. Green, R. Bowler, and S. Gupta. “Two-Element Mixture of Bose and Fermi Superfluids”, *Physical Review Letters* **118**, 055301 (2017).
- [Saf13] M. S. Safronova, U. I. Safronova, and C. W. Clark. “Magic Wavelengths for Optical Cooling and Trapping of Potassium”, *Physical Review A* **87**, 052504 (2013).
- [Sag05] J. M. Sage, S. Sainis, T. Bergeman, and D. DeMille. “Optical Production of Ultracold Polar Molecules”, *Physical Review Letters* **94**, 203001, 203001 (2005).
- [San12] C. Sanner, E. J. Su, W. Huang, A. Keshet, J. Gillen, and W. Ketterle. “Correlations and Pair Formation in a Repulsively Interacting Fermi Gas”, *Physical Review Letters* **108**, 240404 (2012).
- [San08] D. H. Santamore and E. Timmermans. “Fermion-Mediated Interactions in a Dilute Bose-Einstein Condensate”, *Physical Review A* **78**, 013619 (2008).
- [Sar21] S. D. Sarma and Y. Liao. “Know the Enemy: 2D Fermi Liquids”, *Annals of Physics*, 168495 (2021).

- [Sat17] M. Sato and Y. Ando. “Topological Superconductors: A Review”, en. *Reports on Progress in Physics* **80**, 076501 (2017).
- [Sav97] T. A. Savard, K. M. O’Hara, and J. E. Thomas. “Laser-Noise-Induced Heating in Far-off Resonance Optical Traps”, *Physical Review A* **56**, R1095–R1098 (1997).
- [Sca17] F. Scazza, G. Valtolina, P. Massignan, A. Recati, A. Amico, A. Burchianti, C. Fort, M. Inguscio, M. Zaccanti, and G. Roati. “Repulsive Fermi Polarons in a Resonant Mixture of Ultracold  ${}^6\text{Li}$  Atoms”, *Physical Review Letters* **118**, 083602 (2017).
- [Sch10] A. Schirotzek. “Radio-Frequency Spectroscopy of Ultracold Atomic Fermi Gases”. eng. Thesis. Massachusetts Institute of Technology (2010).
- [Sch09] A. Schirotzek, C.-H. Wu, A. Sommer, and M. W. Zwierlein. “Observation of Fermi Polarons in a Tunable Fermi Liquid of Ultracold Atoms”, *Physical Review Letters* **102**, 230402 (2009).
- [Sch18] R. Schmidt, M. Knap, D. A. Ivanov, J.-S. You, M. Cetina, and E. Demler. “Universal Many-Body Response of Heavy Impurities Coupled to a Fermi Sea: A Review of Recent Progress”, *Reports on Progress in Physics* **81**, 024401 (2018).
- [Sch12a] R. Schmidt, S. Rath, and W. Zwerger. “Efimov Physics beyond Universality”, *The European Physical Journal B* **85**, 1–6 (2012).
- [Sch12b] P.-I. Schneider and A. Saenz. “Quantum Computation with Ultracold Atoms in a Driven Optical Lattice”, *Physical Review A* **85**, 050304 (2012).
- [Sch00] G. Schön. “Superconducting Nanowires”, *Nature* **404**, 948–949 (2000).
- [Sch01a] F. Schreck, G. Ferrari, K. L. Corwin, J. Cubizolles, L. Khaykovich, M.-O. Mewes, and C. Salomon. “Sympathetic Cooling of Bosonic and Fermionic Lithium Gases towards Quantum Degeneracy”, *Physical Review A* **64**, 011402 (2001).
- [Sch01b] J. Schuster, A. Marte, S. Amtage, B. Sang, G. Rempe, and H. C. W. Beijerinck. “Avalanches in a Bose-Einstein Condensate”, *Physical Review Letters* **87**, 170404 (2001).
- [Shi08] Y.-i. Shin, C. H. Schunck, A. Schirotzek, and W. Ketterle. “Phase Diagram of a Two-Component Fermi Gas with Resonant Interactions”, *Nature (London)* **451**, 689–694 (2008).
- [Sid17] M. Sidler, P. Back, O. Cotlet, A. Srivastava, T. Fink, M. Kroner, E. Demler, and A. Imamoglu. “Fermi Polaron-Polaritons in Charge-Tunable Atomically Thin Semiconductors”, en. *Nature Physics* **13**, 255–261 (2017).
- [Sie15] F. Sievers, N. Kretzschmar, D. R. Fernandes, D. Suchet, M. Rabinovic, S. Wu, C. V. Parker, L. Khaykovich, C. Salomon, and F. Chevy. “Simultaneous Sub-Doppler Laser Cooling of Fermionic  ${}^6\text{Li}$  and  ${}^{40}\text{K}$  on the  $D_1$  Line: Theory and Experiment”, *Physical Review A* **91**, 023426 (2015).
- [Sim11] J. Simon, W. S. Bakr, R. Ma, M. E. Tai, P. M. Preiss, and M. Greiner. “Quantum Simulation of Antiferromagnetic Spin Chains in an Optical Lattice”, en. *Nature* **472**, 307–312 (2011).
- [Sko21] M. G. Skou, T. G. Skov, N. B. Jørgensen, K. K. Nielsen, A. Camacho-Guardian, T. Pohl, G. M. Bruun, and J. J. Arlt. “Non-Equilibrium Quantum Dynamics and Formation of the Bose Polaron”, en. *Nature Physics*, 1–5 (2021).
- [Söd99] J. Söding, D. Guéry-Odelin, P. Desbiolles, F. Chevy, H. Inamori, and J. Dalibard. “Three-Body Decay of a Rubidium Bose-Einstein Condensate”, *Applied Physics B* **69**, 257–261 (1999).
- [Spi09] F. M. Spiegelhalter, A. Trenkwalder, D. Naik, G. Hendl, F. Schreck, and R. Grimm. “Collisional Stability of  ${}^{40}\text{K}$  Immersed in a Strongly Interacting Fermi Gas of  ${}^6\text{Li}$ ”, *Physical Review Letters* **103**, 223203 (2009).
- [Spi10] F. M. Spiegelhalter, A. Trenkwalder, D. Naik, G. Kerner, E. Wille, G. Hendl, F. Schreck, and R. Grimm. “All-Optical Production of a Degenerate Mixture of  ${}^6\text{Li}$  and  ${}^{40}\text{K}$  and Creation of Heteronuclear Molecules”, *Physical Review A* **81**, 043637 (2010).
- [Sta98] D. M. Stamper-Kurn, H.-J. Miesner, S. Inouye, M. R. Andrews, and W. Ketterle. “Collisionless and Hydrodynamic Excitations of a Bose-Einstein Condensate”, *Physical Review Letters* **81**, 500–503 (1998).

- [Sta13] D. M. Stamper-Kurn and M. Ueda. “Spinor Bose Gases: Symmetries, Magnetism, and Quantum Dynamics”, *Reviews of Modern Physics* **85**, 1191–1244 (2013).
- [Str18] G. C. Strinati, P. Pieri, G. Röpke, P. Schuck, and M. Urban. “The BCS-BEC Crossover: From Ultra-Cold Fermi Gases to Nuclear Systems”, *Physics Reports* **738**, 1–76 (2018).
- [Str96] S. Stringari. “Collective Excitations of a Trapped Bose-Condensed Gas”, *Physical Review Letters* **77**, 2360–2363 (1996).
- [Sun17] M. Sun and X. Cui. “Enhancing the Efimov Correlation in Bose Polarons with Large Mass Imbalance”, en. *Physical Review A* **96**, 022707 (2017).
- [Suz08] K. Suzuki, T. Miyakawa, and T. Suzuki. “ $p$ -wave Superfluid and Phase Separation in Atomic Bose-Fermi Mixtures”, *Physical Review A* **77**, 043629 (2008).
- [Szy05] M. H. Szymańska, K. Góral, T. Köhler, and K. Burnett. “Conventional Character of the BCS-BEC Crossover in Ultracold Gases of  $^{40}\text{K}$ ”, *Physical Review A* **72**, 013610 (2005).
- [Taj18] H. Tajima and S. Uchino. “Many Fermi Polarons at Nonzero Temperature”, *New Journal of Physics* **20**, 073048 (2018).
- [Taj21] H. Tajima, J. Takahashi, S. I. Mistakidis, E. Nakano, and K. Iida. “Polaron Problems in Ultracold Atoms: Role of a Fermi Sea across Different Spatial Dimensions and Quantum Fluctuations of a Bose Medium”, *Atoms* **9**, 18 (2021).
- [Taj19] H. Tajima and S. Uchino. “Thermal Crossover, Transition, and Coexistence in Fermi Polaronic Spectroscopies”, *Physical Review A* **99**, 063606 (2019).
- [Tan10] L.-Y. Tang, Z.-C. Yan, T.-Y. Shi, and J. Mitroy. “Dynamic Dipole Polarizabilities of the Li Atom and the  $\text{Be}^+$  Ion”, *Physical Review A* **81**, 042521 (2010).
- [Tan19] L. Tanzi, E. Lucioni, F. Famà, J. Catani, A. Fioretti, C. Gabbanini, R. N. Bisset, L. Santos, and G. Modugno. “Observation of a Dipolar Quantum Gas with Metastable Supersolid Properties”, *Physical Review Letters* **122**, 130405 (2019).
- [Tie09] E. Tiemann, H. Knöckel, P. Kowalczyk, W. Jastrzebski, A. Pashov, H. Salami, and A. J. Ross. “Coupled System  $a^3\Sigma^+$  and  $X^1\Sigma^+$  of KLi: Feshbach Resonances and Corrections to the Born-Oppenheimer Approximation”, *Physical Review A* **79**, 042716 (2009).
- [Tie99] U. Tietze and C. Schenk. *Halbleiter-Schaltungstechnik*. Springer Verlag, Berlin (1999).
- [Tim01] E. Timmermans. “Degenerate Fermion Gas Heating by Hole Creation”, *Physical Review Letters* **87**, 240403 (2001).
- [Toj10] S. Tojo, Y. Taguchi, Y. Masuyama, T. Hayashi, H. Saito, and T. Hirano. “Controlling Phase Separation of Binary Bose-Einstein Condensates via Mixed-Spin-Channel Feshbach Resonance”, *Physical Review A* **82**, 033609 (2010).
- [Tra16] M.-I. Trappe, P. Grochowski, M. Brewczyk, and K. Rzążewski. “Ground-State Densities of Repulsive Two-Component Fermi Gases”, *Physical Review A* **93**, 023612 (2016).
- [Tra18] A. Trautmann, P. Ilzhöfer, G. Durastante, C. Politi, M. Sohmen, M. J. Mark, and F. Ferlaino. “Dipolar Quantum Mixtures of Erbium and Dysprosium Atoms”, *Physical Review Letters* **121**, 213601 (2018).
- [Tre12] C. Trefzger and Y. Castin. “Impurity in a Fermi Sea on a Narrow Feshbach Resonance: A Variational Study of the Polaronic and Dimeronic Branches”, *Physical Review A* **85**, 053612 (2012).
- [Tre11] A. Trenkwalder, C. Kohstall, M. Zaccanti, D. Naik, A. I. Sidorov, F. Schreck, and R. Grimm. “Hydrodynamic Expansion of a Strongly Interacting Fermi-Fermi Mixture”, *Physical Review Letters* **106**, 115304 (2011).
- [Tru01] A. G. Truscott, K. E. Strecker, W. I. McAlexander, G. B. Partridge, and R. G. Hulet. “Observation of Fermi Pressure in a Gas of Trapped Atoms”, *Science* **291**, 2570–2572 (2001).
- [Tun14] S.-K. Tung, K. Jiménez-García, J. Johansen, C. V. Parker, and C. Chin. “Geometric Scaling of Efimov States in a  $^6\text{Li}$ - $^{133}\text{Cs}$  Mixture”, *Physical Review Letters* **113**, 240402 (2014).

- [Ulm16] J. Ulmanis, S. Häfner, R. Pires, F. Werner, D. S. Petrov, E. D. Kuhnle, and M. Weidemüller. “Universal Three-Body Recombination and Efimov Resonances in an Ultracold Li-Cs Mixture”, *Physical Review A* **93**, 022707 (2016).
- [Val17] G. Valtolina, F. Scazza, A. Amico, A. Burchianti, A. Recati, T. Enss, M. Inguscio, M. Zaccanti, and G. Roati. “Exploring the Ferromagnetic Behaviour of a Repulsive Fermi Gas through Spin Dynamics”, *Nature Physics* **13**, 704–709 (2017).
- [VS08] B. Van Schaeybroeck. “Interface Tension of Bose-Einstein Condensates”, *Physical Review A* **78**, 023624 (2008).
- [VS09] B. Van Schaeybroeck and A. Lazarides. “Trapped Phase-Segregated Bose-Fermi Mixtures and Their Collective Excitations”, *Physical Review A* **79**, 033618 (2009).
- [Var02] C. M. Varma, Z. Nussinov, and W. van Saarloos. “Singular or Non-Fermi Liquids”, *Physics Reports* **361**, 267–417 (2002).
- [Ven17] W. N. Venables, D. M. Smith, and t. R. C. Team. *An Introduction to R* (2017).
- [Vic99] L. Vichi and S. Stringari. “Collective Oscillations of an Interacting Trapped Fermi Gas”, *Physical Review A* **60**, 4734–4737 (1999).
- [Vit08] M. Viteau, A. Chotia, M. Allegrini, N. Bouloufa, O. Dulieu, D. Comparat, and P. Pillet. “Optical Pumping and Vibrational Cooling of Molecules”, *Science* **321**, 232–234 (2008).
- [Viv00] L. Viverit, C. J. Pethick, and H. Smith. “Zero-Temperature Phase Diagram of Binary Boson-Fermion Mixtures”, *Physical Review A* **61**, 053605 (2000).
- [Vli13] J. Vlietinck, J. Ryckebusch, and K. Van Houcke. “Quasiparticle Properties of an Impurity in a Fermi Gas”, *Physical Review B* **87**, 115133 (2013).
- [Wac15] L. Wacker, N. B. Jørgensen, D. Birkmose, R. Horchani, W. Ertmer, C. Klempt, N. Winter, J. Sherson, and J. J. Arlt. “Tunable Dual-Species Bose-Einstein Condensates of  $^{39}\text{K}$  and  $^{87}\text{Rb}$ ”, *Physical Review A* **92**, 053602 (2015).
- [Wan15] F. Wang, X. Li, D. Xiong, and D. Wang. “A Double species  $^{23}\text{Na}$  and  $^{87}\text{Rb}$  Bose-Einstein Condensate with Tunable Miscibility via an Interspecies Feshbach Resonance”, *Journal of Physics B: Atomic, Molecular and Optical Physics* **49**, 015302 (2015).
- [Wan17] J. Wang, Y. Che, L. Zhang, and Q. Chen. “Enhancement Effect of Mass Imbalance on Fulde-Ferrell-Larkin-Ovchinnikov Type of Pairing in Fermi-Fermi Mixtures of Ultracold Quantum Gases”, *Scientific Reports* **7**, 39783 (2017).
- [Web03a] T. Weber, J. Herbig, M. Mark, H.-C. Nägerl, and R. Grimm. “Bose-Einstein Condensation of Cesium”, *Science* **299**, 232–235 (2003).
- [Web03b] T. Weber, J. Herbig, M. Mark, H.-C. Nägerl, and R. Grimm. “Three-Body Recombination at Large Scattering Lengths in an Ultracold Atomic Gas”, *Physical Review Letters* **91**, 123201 (2003).
- [Wen18] M. Wenzel, T. Pfau, and I. Ferrier-Barbut. “A Fermionic Impurity in a Dipolar Quantum Droplet”, en. *Physica Scripta* **93**, 104004 (2018).
- [Wil15] S. Will, D. Iyer, and M. Rigol. “Observation of Coherent Quench Dynamics in a Metallic Many-Body State of Fermionic Atoms”, *Nature Communications* **6**, 6009 (2015).
- [Wil08] E. Wille, F. M. Spiegelhalter, G. Kerner, D. Naik, A. Trenkwalder, G. Hendl, F. Schreck, R. Grimm, T. G. Tiecke, J. T. M. Walraven, S. J. J. M. F. Kokkelmans, E. Tiesinga, and P. S. Julienne. “Exploring an Ultracold Fermi-Fermi Mixture: Interspecies Feshbach Resonances and Scattering Properties of  $^6\text{Li}$  and  $^{40}\text{K}$ ”, *Physical Review Letters* **100**, 053201, 053201 (2008).
- [Wil09] E. Wille. “Preparation of an Optically Trapped Fermi-Fermi Mixture of  $^6\text{Li}$  and  $^{40}\text{K}$  Atoms and Characterization of the Interspecies Interactions by Feshbach Spectroscopy”. PhD thesis. Innsbruck University (2009).
- [Bla] “Window Function”, en. *Wikipedia* (2021).
- [Wöl18] P. Wölffe. “Quasiparticles in Condensed Matter Systems”, en. *Reports on Progress in Physics* **81**, 032501 (2018).

- [Wri07] M. J. Wright, S. Riedl, A. Altmeyer, C. Kohstall, E. R. Sánchez Guajardo, J. Hecker Denschlag, and R. Grimm. “Finite-Temperature Collective Dynamics of a Fermi Gas in the BEC-BCS Crossover”, *Physical Review Letters* **99**, 150403 (2007).
- [Wu11] C.-H. Wu, I. Santiago, J. W. Park, P. Ahmadi, and M. W. Zwierlein. “Strongly Interacting Isotopic Bose-Fermi Mixture Immersed in a Fermi Sea”, *Physical Review A* **84**, 011601 (2011).
- [Wu18] Y.-P. Wu, X.-C. Yao, X.-P. Liu, X.-Q. Wang, Y.-X. Wang, H.-Z. Chen, Y. Deng, Y.-A. Chen, and J.-W. Pan. “Coupled Dipole Oscillations of a Mass-Imbalanced Bose-Fermi Superfluid Mixture”, *Physical Review B* **97**, 020506 (2018).
- [Xu18] J. Xu and R. Qi. “Polaronic and Dressed Molecular States in Orbital Feshbach Resonances”, en. *The European Physical Journal D* **72**, 65 (2018).
- [Yan20a] Z. Z. Yan, Y. Ni, C. Robens, and M. W. Zwierlein. “Bose Polarons near Quantum Criticality”, *Science* **368**, 6487 (2020).
- [Yan19] Z. Yan, P. B. Patel, B. Mukherjee, R. J. Fletcher, J. Struck, and M. W. Zwierlein. “Boiling a Unitary Fermi Liquid”, en. *Physical Review Letters* **122**, 093401 (2019).
- [Yan20b] Z. Z. Yan. “From Strongly-Interacting Bose-Fermi Mixtures to Ultracold Molecules”. eng. Thesis. Massachusetts Institute of Technology (2020).
- [Yao16] X.-C. Yao, H.-Z. Chen, Y.-P. Wu, X.-P. Liu, X.-Q. Wang, X. Jiang, Y. Deng, Y.-A. Chen, and J.-W. Pan. “Observation of Coupled Vortex Lattices in a Mass-Imbalance Bose and Fermi Superfluid Mixture”, *Physical Review Letters* **117**, 145301 (2016).
- [Ye06] J. Ye, S. Blatt, M. M. Boyd, S. M. Foreman, E. R. Hudson, T. Ido, B. Lev, A. D. Ludlow, B. C. Sawyer, B. Stuhl, and T. Zelevinsky. “Precision Measurement Based on Ultracold Atoms and Cold Molecules”, *AIP Conference Proceedings* **869**, 80–91 (2006).
- [Yef13] T. Yefsah, A. T. Sommer, M. J. H. Ku, L. W. Cheuk, W. Ji, W. S. Bakr, and M. W. Zwierlein. “Heavy Solitons in a Fermionic Superfluid”, *Nature (London)* **499**, 426 (2013).
- [Yip01] S. K. Yip. “Collective Modes in a Dilute Bose-Fermi Mixture”, *Physical Review A* **64**, 023609 (2001).
- [Yu12] Z. Yu and C. J. Pethick. “Induced Interactions in Dilute Atomic Gases and Liquid Helium Mixtures”, *Physical Review A* **85**, 063616 (2012).
- [Yu10] Z. Yu, S. Zöllner, and C. J. Pethick. “Comment on “Normal Phase of an Imbalanced Fermi Gas””, *Physical Review Letters* **105**, 188901 (2010).
- [Yuv70] G. Yuval and P. W. Anderson. “Exact Results for the Kondo Problem: One-Body Theory and Extension to Finite Temperature”, *Physical Review B* **1**, 1522–1528 (1970).
- [Zac09] M. Zaccanti, B. Deissler, C. D’Errico, M. Fattori, M. Jona-Lasinio, S. Müller, G. Roati, M. Inguscio, and G. Modugno. “Observation of an Efimov Spectrum in an Atomic System”, en. *Nature Physics* **5**, 586–591 (2009).
- [Zac06] M. Zaccanti, C. D’Errico, F. Ferlaino, G. Roati, M. Inguscio, and G. Modugno. “Control of the Interaction in a Fermi-Bose Mixture”, *Physical Review A* **74**, 041605 (2006).
- [Zel19] T. Zelevinsky. “Ultracold and Unreactive Fermionic Molecules”, en. *Science* **363**, 820–820 (2019).
- [Zha15] H. Zhai. “Degenerate Quantum Gases with Spin-Orbit Coupling: A Review”, *Reports on Progress in Physics* **78**, 026001 (2015).
- [Zha12] Y. Zhang, W. Ong, I. Arakelyan, and J. E. Thomas. “Polaron-to-Polaron Transitions in the Radio-Frequency Spectrum of a Quasi-Two-Dimensional Fermi Gas”, *Physical Review Letters* **108**, 235302 (2012).
- [Zöl11] S. Zöllner, G. M. Bruun, and C. J. Pethick. “Polarons and Molecules in a Two-Dimensional Fermi Gas”, *Physical Review A* **83**, 021603 (2011).
- [Zür13] G. Zürn, T. Lompe, A. N. Wenz, S. Jochim, P. S. Julienne, and J. M. Hutson. “Precise Characterization of  $^6\text{Li}$  Feshbach Resonances Using Trap-Sideband-Resolved RF Spectroscopy of Weakly Bound Molecules”, *Physical Review Letters* **110**, 135301 (2013).

- 
- [Zwe12] W. Zwerger, ed. *The BCS-BEC Crossover and the Unitary Fermi Gas*. Springer, Berlin Heidelberg (2012).
- [Zwi05] M. W. Zwierlein, J. R. Abo-Shaeer, A. Schirotzek, C. H. Schunck, and W. Ketterle. “Vortices and Superfluidity in a Strongly Interacting Fermi Gas”, *Nature (London)* **435**, 1047–1051 (2005).
- [Zwi06a] M. W. Zwierlein, A. Schirotzek, C. H. Schunck, and W. Ketterle. “Direct Observation of the Superfluid Phase Transition in Ultracold Fermi Gases”, *Nature (London)* **442**, 54–58 (2006).
- [Zwi06b] M. W. Zwierlein, A. Schirotzek, C. H. Schunck, and W. Ketterle. “Fermionic Superfluidity with Imbalanced Spin Populations”, *Science* **311**, 492–496 (2006).
- [Zwi04] M. W. Zwierlein, C. A. Stan, C. H. Schunck, S. M. F. Raupach, A. J. Kerman, and W. Ketterle. “Condensation of Pairs of Fermionic Atoms near a Feshbach Resonance”, *Physical Review Letters* **92**, 120403 (2004).

# Acknowledgements

*“One’s life has value so long as one attributes value to the life of others,  
by means of love, friendship, indignation and compassion.”*

- Simone de Beauvoir

---

This thesis comprises the main part of what I did in my last six years, which was possible because of the boundless support of many people, be it of scientific or of personal matter. Therefore I want to thank all of you who joined me on my path.

First of all I want to thank Rudi for giving me the opportunity to do my PhD in his group, and for his great help in the course of our last publication. I learned a lot in the last year and I am very happy that I could do my PhD in the Grimm group. I also want to thank the former and present FeLiKx team members: Michale Jag, Marco Cetina, Rianne Lous, Emil Kirilov, Bo Huang, Tanner Grogan, Gregor Anich, Cosetta Baroni and Erich Dobler with whom I was lucky enough to work together and create a lot of scientific output. Thanks Michael, Marko and Rianne for introducing me to the FeLiKx experiment, giving me such a warm welcome and thanks for your support in all the questions I had. Thanks Michael, for being such an awesome office and lab mate. I will never forget the Feierabendbier sessions on the roof. Thanks Rianne for happy times in the lab and for being the strong woman who is never swayed and always helps people that are in need of help. I want to express my special gratitude to Cosetta who worked with me in the lab as it rapidly disintegrated and nearly buried us, for being a good friend and colleague, outside and inside the lab. I also want to thank Erich, who was the last one to join our team and brought in fresh spirit and motivation. Without you we would not be where we are now. Furthermore I want to thank Gregor, Erich and Cosetta for many movie nights with strange movies, after-work-drinks and discussions! The three of you made my every day life more fun and homey. Thank you.

In the beginning of my PhD I joined the Doktoratskolleg atoms, light and molecules (DK ALM), which was a great opportunity for me. Thanks Roland, Heide, Eric and Alex for all the time and work you invested into building up this project in Innsbruck and enabling such a great environment for the participants of this program. Amongst many other advantages the DK introduces the structure, job-security, and stability that the university of Innsbruck lacks to provide. I hope that all PhD students will some day experience similar treatment. I want to express my special thanks to Roland Wester who was (gladly) the head of the DK, for sharing knowledge with us, and for reminding some PIs to obey the rules. Furthermore I want to thank Heide Streicher for always being there and for her endless support.

Within the scope of the DK ALM I spent roughly two months working at LENS in Florence, Italy. I want to thank the whole team: Matteo Zaccanti, Giacomo Roati,

Francesco Scazza, Andreas Trenkwalder, Pedro Tavares, and Andrea Amico for welcoming me to your team as a guest PhD student. I will never forget the delicious sausages at Matteos home, the long nights in the lab with Pedro and Andrea, fun with Italian public transport, many overwhelming physics discussions with Matteo and Francesco, and of course the many delicious restaurants you guided me to. Thank you all for making this an amazing experience for me.

My second stay abroad was located in Paris, France, where I stayed for about four months at Collège de France in the Ytterbium-experiment of Fabrice Gerbier and Jérôme Beugnon. Thanks to Fabrice Gerbier, Jérôme Beugnon, Raphaël Bouganne, Manel Bosch Aguilera, and Alexis Ghermaoui for taking me into your team and introducing me to the world of lanthanides. I want to express my special thanks to Manel, with whom I spent about twelve hours a day in the lab. Thanks for introducing me to the world of old movies, the best street food in Paris, and thank you for being such a good friend. I will always remember to check for open fires in the lab, before getting a pizza and I will never forget the Libanese. Thanks also to Raphaël. With your constant good mood, and honest and happy attitude you enlightened my days. And finally thanks to Fabrice, for making this stay possible! Thanks to all of you and the rest of the ultracold team in Paris for the many wonderful scientific discussions and all the lab tours!

My big thanks also go to the students of the other ultracold atom experiments in Innsbruck. I want to thank the DyKs: Elisa, Vincent, Jeong Ho, Cornee, Marian, and Slava for their readiness to help in any possible situation. Thanks to the RbCs, the K(Cs), the CsIII, the Erbium, the Rare, the NewLanD and the T-REQS people, namely: Deborah, Camilo, Lukas, Silva, Govind, Charly, Krzysztof, Michael, Philipp, Milena, Sudipta, Katharina, Dani, Alex, Gabriele, Simon, Laurianne, Philipp, Giannmaria, Arno, Max, Claudia, Lauritz, Sandra, and Elena. Thank you all for forming such a motivated and friendly ultracold-group in Innsbruck, despite the circumstances.

I also want to thank the people in the workshop and the administrative team. Without you: Elisabeth, Klaus, Mr. Knabl, Christine, Silvia, Barbara, Verena, Valentin, David, Gerhard, Bernhard, Andreas, and Stefan. Thank you for all of your support and for the great quality, and enthusiasm with which you do your job. Without you, many tasks during my PhD would not have been possible!

I want to mention as well that without the open platforms [www.wikipedia.org](http://www.wikipedia.org), [www.arxiv.org](http://www.arxiv.org), [www.deepl.com](http://www.deepl.com), and [www.connectedpapers.com](http://www.connectedpapers.com) this thesis would not have been possible in this way. Thanks for all the people working on these platforms.

Besides the scientific and administrative staff, I want to thank my friends and family for their support throughout my time as a PhD student. Thanks to my family: Mama, Papa, Caro, Steve, Chris, Michi, Sahin, Cem, Çisem, Maxi, Sabine, Zissi, und Sebi. Each single one of you gave me in their own particular way, the support and backup I needed every single day. You are an exceptional family! Thank you!

I want to thank all the people that were there with me over the last six years. Thanks to Axl, for being an excellent friend, physicist and human being, with whom I was fortunate enough to meet already at the beginning of my physics degree and who joined my path

through the MSc degree, and PhD degree as well. Thanks to Luki, for weekend trips with your bus, dinner nights in your flat, parties at the Inn (or in the Bögen), or intense physics discussions at an after-work beer. It was always a lot of fun. Thanks to Lisa and Eva, for many girls nights with various topics and a looot of fun! Thanks to Nici and Fredl for always being there. Thanks to all the people from the Hütte for very fun weekends. Thanks to Cosetta, Erich and Gregor for fun nights! Thanks to Manel and Raphaël, and thanks to all of you who I did not mention so far. I want to thank you very much for being a part of my life and thus making it what it is today.

Finally I want to thank Chris, for everything you did for me! Without you I would probably sit in a padded cell right now. Thank you for being one of the kindest, most helpful, supportive and generous people I know. Thank you for the physics discussions that motivate to see things from a different perspective, thank you for your endless moral support and thank you for being the wonderful person that you are.